UNIVERSITÀ DEGLI STUDI DI PALERMO
Dottorato in Ingegneria Civile, Ambientale e dei Materiali
Dipartimento di Ingegneria
Settore Scientifico Disciplinare ING-IND/23

CORROSION RESISTANCE OF DIFFERENT STAINLESS STEEL GRADES IN FOOD AND BEVERAGE INDUSTRY

IL DOTTORE
GIADA TRANCHIDA

LA COORDINATRICE
PROF.SSA ANTONINA PIRROTTA

IL TUTOR
PROF.SSA MONICA SANTAMARIA

CICLO XXXII
ANNO 2020

UNIVERSITÀ DEGLI STUDI DI PALERMO
Dottorato in Ingegneria Civile, Ambientale e dei Materiali
Dipartimento di Ingegneria
Settore Scientifico Disciplinare ING-IND/23

CORROSION RESISTANCE OF DIFFERENT STAINLESS STEEL GRADES IN FOOD AND BEVERAGE INDUSTRY

IL DOTTORE
GIADA TRANCHIDA

LA COORDINATRICE
PROF.SSA ANTONINA PIRROTTA

IL TUTOR
PROF.SSA MONICA SANTAMARIA

CICLO XXXII
ANNO 2020

Abstract

According to their high corrosion resistance combined with their good mechanical properties, stainless steels are widely employed in chemical industries (refinery and petrochemistry), subsea solutions, oil and gas extraction, flowlines and piping systems, chemical tankers, desalination plants and water systems equipment. In particular, austenitic stainless steel grades establishing themselves also as materials of choice for food and beverage industries where a very high purity is required due to the more stringent regulamentation and consumer expectations. Actually, growth and survival of pathogenic micro-organisms in food processing represent one of the major concerns regarding poisoning of processed fluids and public health risk. Attachment of algae and/or bacteria is a surface phenomenon that occurs thanks to the production of a complex matrix termed extracellular polymeric substances (EPSs) mainly based on water and organic macromolecules as lipids, proteins, polysaccharides and nucleic acids providing mechanical resistance and all the nutrients necessary for bacteria proliferation for the formation of a three-dimension polymeric network. In addition, the presence of food-borne bacteria can induce spillage of materials and huge maintenance costs, increase drag resistance, and promote structural failure of metallic construction and devices. For this reason, in order to avoid contamination and ensure health and safety of consumers, cleaning operations are usually employed thanks to the physical action of high velocity flow jet spray, agitation and chemical action of cleaning agents enhanced by heat. Thus, SSs contact with aggressive media as chloride containing solutions, or highly concentrated organic and inorganic acidic solutions or hot alkaline electrolytes, typically employed in cleaning and processing operations, is unavoidable. On the other hand, due to the prolonged exposure to corrosive environments, storage vessel, distribution system and food contact materials can show red brown to dark violet deposits that are called *rouge*. Rouging is the macro scale symptom

of ongoing corrosion processes followed by the formation and precipitation of iron oxide or hydroxide compounds and Cr dissolution phenomena that could not only contaminate products but also negatively affect corrosion properties of the circuit's materials. Moreover, due the strong surface appearance caused by interference colors as a results of oxide growth, manufacturers can induce unplanned downtime of the plant in order to make necessary repairs and carry out routine cleaning, with consequent lost production time and damage of the business's bottom line, especially considering that many food and beverage operations have a high volume of products being produced continuously. In addition, the occurrence of dissolution phenomena, can threaten food quality due to the release of heavy metal ions from the substrate with consequent intoxication and poisoning of end consumers. Hence, the major challenges in food and beverage industry consist on ensure high hygiene and quality expectations, contain equipment maintenance cost and comply the demanding regulatory.

It is well accepted that corrosion resistance of stainless steels depends on the formation of a very thin chromium oxide rich passive film, typically 1 nm to 3 nm thick, whose composition, thickness, and protective action dynamically change with time and gradually adjust to the aggressive environments. Meanwhile, the significance of alloying elements such as Mo and N on stainless steel corrosion resistance is still not well understood. Mo, in particular, remains the most interesting alloying compound which has a beneficial effect toward localized corrosion phenomena such as pitting. Nevertheless, it still exists some ambiguity on its action mechanism and different models were provided in order to clarify its role on corrosion resistance of stainless steel. On the other hand, the presence of impurities, especially sulphur, have strong deleterious effect on pitting corrosion of SS due to the formation of MnS inclusions. The latter are less noble than the bulk of the alloy surface and thus oxidation processes can occur in the presence of chlorine media due to dissolution at MnS/SS boundary

and the onset of localized corrosion phenomena. For this reason, in the attempt to clarify the role of alloying elements and to gain more insight into corrosion resistance of SS, growth mechanism, composition and solid state properties of passive films grown on austenitic stainless steels in different aggressive solutions were widely studied. In addition, in the frame of food quality and safety, a lot of research works are mainly focused on the monitoring of release of heavy metal ions from chemical reactors and storage vessel mimicking the prolonged exposure of equipment to aggressive environments during working condition. On the other hand, just a few works are reported on the study of corrosion resistance of SSs as a consequence of their exposure to other media typically employed in food industry such as cleaning and disinfectant solutions.

Recently, Duplex has been proposed as alternative material to austenitic SSs when a compromise between corrosion and superior mechanical resistance and contained cost (due to the lower amount of Ni) is required. Duplex consists on a two-phase balanced microstructure due to the presence of Ni and N, promoting the stabilization of the austenite phase, and Cr and Mo, which act as ferritizing elements. The synergistic action of these alloying elements is fundamental since they induce the formation of a homogeneous Cr-oxide film on both phase, improving the corrosion resistance also at the grain boundaries. However, the prediction on how these two phases can interact or affect corrosion resistance of the steel is not straightforward and no general agreement exists on the mechanisms at the base of the improved corrosion resistance of duplex SS.

Pitting susceptibility of stainless steels is strongly affected by the alloying elements. The primary elements that contribute to the pitting and general corrosion resistance of both austenitic and duplex stainless steels are chromium (Cr), molybdenum (Mo), tungsten (W) (if present), and nitrogen (N). For this purpose, the Pitting Resistance Equivalent number (PREN) has been defined to correlate SSs composition to their relative corrosion resistance. PREN is defined according to the following relationship[1]:

PREN = % Cr + 3.3% (Mo + 0.5 W) + k % N

where k is a constant for which usually 16 is used. Basically, the higher the PREN, the higher the resistance of the steel to pitting is. Nevertheless, the calculation of PREN number refers to the average alloy composition and does not take into account the influence of phases morphology and structural inhomogeneities as well as differences in alloying elements distributions within the phases[2].

In this Ph.D. project, a ranking of different stainless steel grades usually employed in different selected aggressive environments typical of food and beverage industries was performed, with a special interest on metal release as a function of SSs composition and microstructure. The experimental activity is based on the study of physicochemical properties of passive films grown on their surface after immersion in simulating solutions based on electrochemical, photoelectrochemical and impedance measurements, in the attempt to correlate their electronic properties to their corrosion resistance.

In section 1 a general introduction on stainless steel is reported. Section 2 is devoted to the description of aggressive environments typically encountered in food and beverage industry. In section 3 the experimental part of this research work is reported explaining which materials and techniques were employed for the study of physicochemical properties of passive films and the monitoring of released metal ions. Section 4 will be devoted to the physicochemical characterization of passive films electrochemically grown on pure chromium, carbon steel and different stainless steel grades in different aqueous electrolytes as a function of the corresponding pH. In particular, passive films were first grown after potentiostatic passivation on pure chromium in order to have a reference and to better understand how far corrosion resistance of the latter is with respect to that of SSs. Moreover, since no general agreement exists on growth mechanism of passive films on chromium, as well as on their

semiconductive (p or n) or insulating character, a detailed investigation of their solid state properties was also performed proposing an alternative experimental approach that overcome the limitation of the Mott-Schottky theory. Since carbon steel contains only iron and carbon as main alloying elements and other elements such as Mn, Si, Al, S, P and Cr may also be present as traces, passivation was also performed on the latter in the attempt to study corrosion resistance of almost pure iron oxides grown both by potentiostatic polarization and after atmospheric exposure. Finally, two austenitic 304L / EN 1.4307 and 316L / EN 1.4404 with very close chromium content and a super duplex 2507 / EN 1.4410 SS with very high chromium content than that of two austenitic grades were studied in the attempt to understand how stainless steel composition and electrolyte pH can affect electronic properties and therefore corrosion resistance of passive layers covering their surfaces.

In section 5, the role of Mo and the effect of surface roughness (R_a) on passive films grown on SSs were also investigated. Moreover, in order to get more insight into the dissolution mechanisms, electrochemical conditions inducing rouging on the surface of stainless steel were investigated too. Section 6 is devoted to the study of corrosion properties of passive films grown on different stainless steels grades at the open circuit potential in selected aggressive environments typical of food and beverage industries, according to protocols and regulations found in the literature. In particular, the effect of long time exposure to food simulants, hot water, cleaning and disinfection solutions on corrosion resistance of passive films was evaluated, with a special interest on dissolution kinetic of SSs in food simulants. In Section 7 the effect of biofilm growth on corrosion resistance of SSs is reported. Sanitization protocols are also employed as a function of immersion time and temperature in order to estimate the effectiveness in bacteria removal.

1 Introduction

According to the European standard EN 10088, steel is classes as stainless when its chemical composition has a minimum chromium content of ~ 10%. The presence of chromium is responsible for the formation of a very thin oxide layer on steel surface mainly made up of Cr_2O_3. This passive film is adherent, compact and insoluble and protect the material on which it is formed. The worldwide yearly stainless steel production has been booming at an average growth of 6% since more than 50 years. In spite the production of SSs represents just a fraction of the overall production of steel (approx. 2% of all semi-finished products)[3,4], they are largely employed in a wide range of fields. Most of the structural applications occurs in the chemical and power engineering industries, which account for more than a third of the market (~ 34%). These applications include different range of use such as nuclear reactor vessels, heat exchangers, oil industry, components for chemical processing, pulp and paper industries and boilers used in fossil fuel electric power plants. Other applications of stainless steel are encountered in transportation sector (~ 9%), architecture (~ 5%) and food and beverage industry (~ 18%)[5].

Since many of the properties of SSs are strictly related to the crystalline structure established within the grains, a briefly description of the iron-carbon diagram is reported in this section.

1.1 Fe-C phase diagram

The study of steel structure and characteristics should first start from the knowledge of the Fe-C phase diagram that describes equilibrium phases related to the iron based alloys. The complete diagram should extend from 100% iron to 100% carbon, but it is normally studied up to around 6.67% carbon because iron alloys of practical industrial importance contain no more than 5% carbon. Actually, the normal equilibrium diagram reported in Fig. 1-1 represents the metastable equilibrium between iron and iron carbide (i.e. **cementite)**.

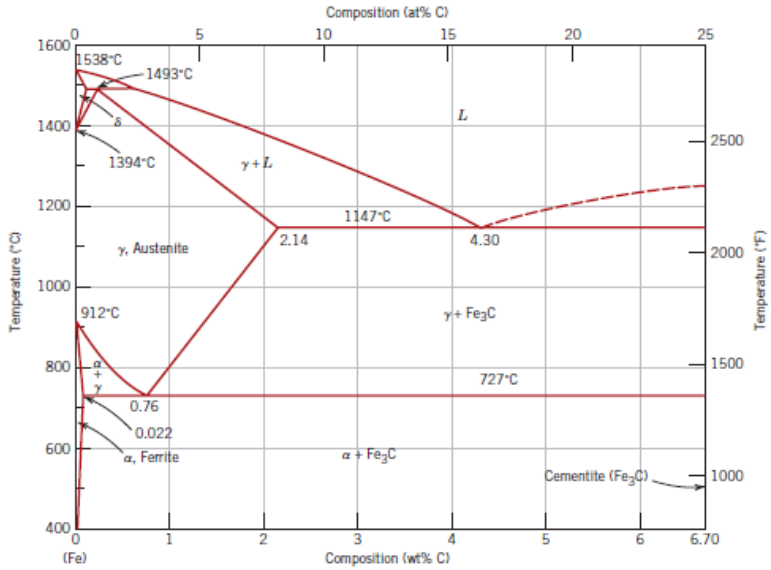

Fig. 1-1. Iron-iron carbide phase diagram[6].

Pure iron, upon heating, displays two changes in crystal structure before it melts. At room temperature the stable form is known as **ferrite**, or **α-Fe**, with a **body centered cubic** crystal structure (BCC), where atoms are located at each of the eight corners and one is at the center of the cube (see Fig. 1-2a). Ferrite in turn displays a polymorphic transformation to **austenite**, or **γ-Fe**, at 912°C characterized by a face centered cubic lattice where atoms are still in the corners

of the cube and also in the geometric center of each six faces (see Fig. 1-2b). Austenite persists to 1394°C at which temperature the FCC reverses back to a BCC phase known as **δ ferrite**, which finally melts at 1538°C.

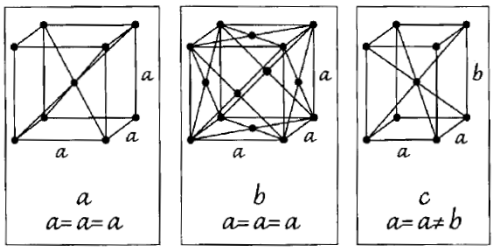

Fig. 1-2. Typical crystalline lattice structures of stainless steel where black dots represent atoms and the lines help the structure to be seen[7].

Carbon is an interstitial impurity in iron and forms solid solutions with each phases described above. In the BCC α-Fe the maximum solubility of C is 0.022 wt.% at 727°C. The limited C solubility can be explained considering the shape and size of the BCC interstitial positions that do not allow to receive carbon atoms. The low C concentration significantly influences mechanical properties of ferrite leading to the formation of a soft and ductile phase. **Austenite** phase, when alloyed only with C, is not stable at temperature below 727°C. The maximum solubility of C in austenite is 2.14 wt.% at 1147°C and it is much higher than that of C in ferrite due to the larger FCC interstitial positions (see Fig. 1-2b). Thus, the strains imposed on the surrounding iron atoms are much lower. On the other hand, C solubility decrease to 0.77 wt.% at 727°C. It becomes stable at room temperature if austenitizing alloying elements, such as N, Ni and Mg, are added to the base alloy. Austenite is soft, ductile tough and malleable due to the FCC crystalline structure. **δ-Ferrite** is the same of α-Fe but it is stable only at temperatures above 1394°C. In Fig. 1-3 the photomicrographs related to ferrite and austenite phases are reported. **Martensite** consists on a crystalline structure more similar to ferritic than to the austenitic. In fact, it has

also a body-centered cubic structure but one axis of the cube has been elongated to for a tetragonal structure (see Fig. 1-2c). It is the hardest and strongest of the three crystalline forms but the least workable[7].

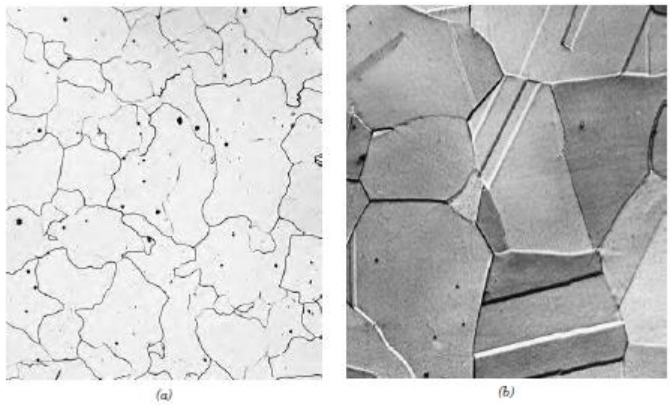

Fig. 1-3. Photomicrograph of a) ferritic and b) austenitic phases.

Finally, **Cementite** (Fe_3C) phase is formed when the solubility limit of C in α ferrite is exceeded below 727°C. It is very hard and brittle and its presence in some steel increase their strength.

Different microstructures may be produced in steel alloys depending on both the carbon content and heat treatments. Iron-carbon alloy containing between 2.14 wt.% and 6.70 wt.% C are classified as **cast irons**, conversely, when C content is lower than 0.008 wt.%, the iron-carbon alloy is considered pure Fe[6]. Iron-carbon alloys that contain between 0.008 and 2.14 wt.% C are classified as **steels**. Although a steel alloy may contain as much as 2.14 wt.% C, in practice, carbon concentrations rarely exceed 1.0 wt.%. Steels are iron-carbon alloy that can contain a certain amount of other alloying elements. Depending on composition and/or heat treatments, several different steel may exist. Mechanical properties are strongly affected by the carbon content and according to the latter one they are usually divided into low-, medium- and high-carbon types. On the other hand, subclasses of each groups can also exist depending on

the amount of alloying elements. Basically, **plain carbon steels** are considered iron-carbon alloy containing only residual concentrations of impurities, while in **alloy steels** alloying elements are intentionally added for a specific purpose. Among them, **stainless steels** are iron-carbon alloy where Cr is the predominant alloying element. As also showed in Fig. 1-4, depending on their room temperature microstructure, they can be divided in:

i. **martensitic stainless steels**, characterized by martensitic microstructure;
ii. **ferritic stainless steels,** characterized by ferritic microstructure;
iii. **austenitic stainless steels**, characterized by austenitic microstructure);
iv. **austen-ferritic stainless steels**, characterized by mixed austenitic and ferritic microstructure.

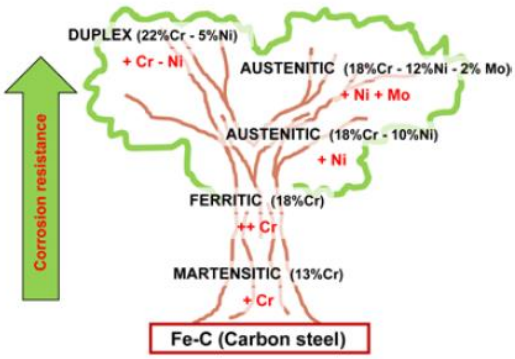

Fig. 1-4. Stainless Steel tree structure[4].

It is important to keep into account that these diagrams are only valid when the specified alloy is cooled very gradually in consecutive stages of equilibrium from the melting to the ambient temperature.

1.2 Alloying elements

In spite the presence of chromium, other alloying elements are often added in order to modify metallurgical characteristics as well as mechanical and corrosion resistance. In particular, **Carbon** is an *austenitising* element and it has a beneficial effect on steel hardness and mechanical resistance. Otherwise it has a close affinity with chromium with the consequent formation of chromium carbides, i.e. $Cr_{23}C_6$ that usually deposit on the grain boundary with consequent depletion of chromium content within the grain itself. If the amount of chromium falls below to the 10.5%, intergranular corrosion could occur.

Chromium is the chemical element that provides excellent corrosion resistance to different stainless steel grades and it is a *ferritising* agent. According to the Fe-Cr diagram reported in Fig. 1-5, a closed field related to the existence of γ phase is present with upper and lower limits respectively equal to 11.2% and 13.4%. This means that if the Cr amount is higher than 13.4%, the iron-chromium alloy will have a stable ferritic microstructure starting from the temperature of alloy solidification through to the ambient temperature, conversely, if the chromium amount is lower than 13.4%, the transition γ → α will occur.

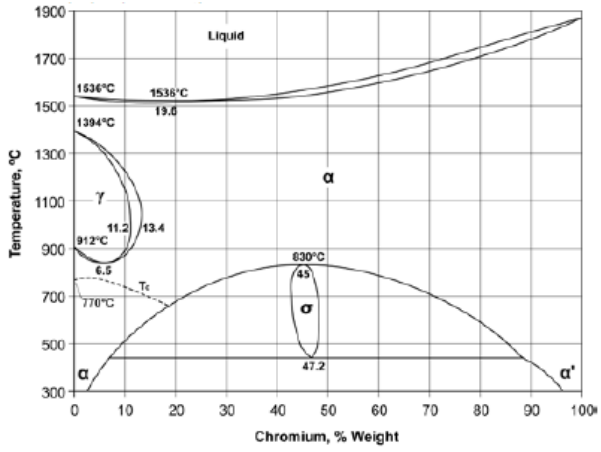

Fig. 1-5. Fe-Cr phase diagram[4].

If austenitising elements like Ni, Mn, C or N are added on the Fe-Cr alloy, γ field will expand and a shift to the right of the threshold limits will occur. In this way it is possible to have stable austenite at higher temperature (i.e. 900-1000°C) although a Cr content higher than 13.4%. Conversely, when chromium is ~ 16% and C is less than 0.1%, the steel will be ferritic due to the absence of structural transitions. When chromium content decreases (down to 13%) and the carbon amount ranges between 0.2% - 0.3%, the alloy undergoes the transformation γ→α with consequent formation of martensitic structure. Notably, σ phase related to the formation of intermetallic compounds with a tetragonal structure and a Cr content ranging between 40% and 50% could also occurs in the Fe-Cr alloy. The intermetallic deposits on the grain boundary result in higher hardness and brittleness of the steel but, conversely the corrosion resistance decreases due to the lower Cr content within the grain. This phenomenon is called "*embrittlement at 800°C*". In order to reduce carbide precipitation, it is recommended to not exposure the material to temperatures in the range 550°C-850°C for long time. The temperature range at which embrittlement occurs is affected by the presence of alloying elements: i.e. in the case of molybdenum, chromium carbide formation occurs at temperature up to 980°C. **Nickel** improves ductility and affords extremely high strength. It contributes to increase corrosion resistance of passive film promoting its re-passivation. Moreover, nickel tends to open the γ field pushing the critical point of γ→ α transition at very low temperature, leading to the formation of an austenitic structure also at room temperature. **Nitrogen** is a highly *austenitising* element (as well as Ni) and it is added to some stainless steel grades in order to improve both mechanical strength and localized corrosion resistance due to the precipitation of Cr_2N nitride instead of $Cr_{23}C_6$ carbide. Nitrogen is also added for Ni replacement since the higher cost and the allergenic behavior of the latter[8–10]. **Molybdenum** is another significant chemical element that behaves like a *ferritising* compound. In addition, it improves corrosion resistance, especially

towards localized attack such as pitting and crevice corrosion[11–14]. Mo also promotes the formation of secondary phases in ferritic, ferritic-austenitic and austenitic SSs. It has been suggested that the presence of Mo in passive films inhibits film breakdown and promotes the repair of the passive films[11,15]. It has also been proposed that dissolved Mo species reduce the active dissolution rate of bare stainless steel surfaces in highly acidic environments inside the pits[15–21]. **Manganese** is an *austenitising* element usually added in SSs at percentages lower than that 2 wt.%. Higher amount of manganese are used in order to replace nickel[10,22,23]. Manganese also increase the solubility of nitrogen[4,24,25]. **Titanium and niobium** are both *ferritising* element, but they are mainly used as stabilizing agents. They have a good affinity with carbon and carbides and carbonitrides of titanium or niobium, such as MC or $M_x(NC)_y$ (where M = Ti or Nb) are formed. They are added in order to increase the resistance to intergranular corrosion and mechanical properties reducing recrystallized grain size[7,24,26–28]. **Sulphur** is added to certain SSs in order to increase the machinability. At the levels present in SS grades, sulphur can reduce ductility and fabrication properties such as weldability, formability and corrosion resistance. In fact, the presence of inclusions of MnS or MnS/oxide behave like nucleation sites for pitting[29–31]. **Copper** it is another *austenitising* element that is added in small percentage (maximum 1%) to improve ductility (cold plastic deformability)[4]. Copper also improve corrosion resistance by reducing the corrosion rate in non-oxidizing environments, namely sulphuric acid[32–36].

1.3 Martensitic stainless steel

Martensitic stainless steel is characterized by limited chromium concentration, generally ranging from 11.5% to 18%, and by a very high carbon content (between 0.1% and 1%). As mentioned above, chromium is a strong ferritising element while carbon is austenitising but their amount in the alloy is balanced in order to have an austenitic structure at high temperature and a martensitic one at room temperature after tempering. Martensitic SSs are also named *self-tempering steels* since they can be hardened trough only air exposure. The higher carbon amount gives hardness and mechanical resistance for the steel but conversely, it tends to form chromium carbides. For this reason, martensitic stainless steels are the least resistant toward corrosion phenomena and therefore they are used only in slightly aggressive environments.

Mechanical properties of martensitic SS strongly depend on chemical composition and heat treatments to which they are subjected. Semi-finished parts must undergo heat treatments in order to become more workable. Usually *sub-critical annealing process* is employed through which the products are heated at temperatures between 730° - 830 °C for several hours and then gradually cooled. According to this process a pearlite structure characterized by a matrix based on α ferrite and globular carbides is formed. Subsequently, the semi-finished parts are roughly processed using machine tools in order to give them dimensions quite similar to the final products. After the mechanical treatment, hardening is performed in order to increase corrosion resistance and mechanical properties. Regarding hardening, some important considerations should be made. Thermal conductivity of stainless steel is not very high, therefore, in order to avoid permanent deformation or breakage of the parts, temperature must be carefully managed. Usually a gradual pre-heating up to about 800°C is performed especially when thicker parts are treated for a long time enough to be ensure that all parts of the material reached the pre-heating temperature[37]. In order to obtain the austenitic structure, temperature will be

increase high enough to allow the solubilization of carbides making C available for the solidification of martensite. Moreover, the austenitizing temperature will depend on Cr and C amount (i.e. it increases by increasing Cr and C percentages) but at the same time it shouldn't be too high in order to avoid grain enlargement and therefore worsening of mechanical properties of the finished pieces. Finally, tempering is performed in order to reduce brittleness and residual stress on the quenched pieces. It is important to stress that tempering must not be performed in the range 450°C to 600°C due to brittle fractures and worsening of corrosion resistance.

Semi-finished pieces made of martensitic stainless steel could be used either annealed or pre-hardened. In the industrial processing the most widely used are X30Cr13 (similar to AISI420B), characterized by higher C content and therefore higher hardness, and X12Cr13 (similar to AISI 410) with lower C content and therefore higher strength. They are quite resistant towards corrosion phenomena in rural environments, free-chloride fresh water, food grade substances, weak acids (such as organic acids), petrol products and oxidizing saline solutions (chromate, permanganates, etc.). They are also largely used for table and industrial cutting knives, surgical instruments, rasors, scissors, callipers and brake disks for motor vehicle. They are also employed for the manufacturing of power drive shafts in mildly aggressive environments, steam turbine blades or compressor blades, filters, handles, coins and medals. X17CrNi16-2, characterized by higher Cr content, is also used for shafts on marine engines, propeller shafts, pump parts, valves, turbine blades, and wear-resistant components in reforming oil plants.

1.4 Ferritic stainless steel

When chromium and carbon contents are respectively higher than 17% and lower than 0.1%, the ferritising effect of Cr is not balanced anymore by the presence of C and the stainless steel will have a ferritic structure at room temperature. There are different ferritic stainless steel grades, roughly divided into three main classes depending on chromium amount in the alloy:

- *Low Cr content ferritic SS* (Cr < 15%)
- *Medium Cr content ferritic SS* (15% < Cr < 18%)
- *High Cr content ferritic or "superferritic" SS* (Cr > 18%)

Although this classification, alloying elements are added such as aluminum and silicon to stabilize the ferritic structure, molybdenum to improve their corrosion resistance and titanium and niobium in order to avoid chromium carbide precipitation. In Fig. 1-6 the Fe-Cr diagram related to a base ferritic stainless steel grade with a carbon percentage of around 0.05% is reported (i.e. X6Cr17).

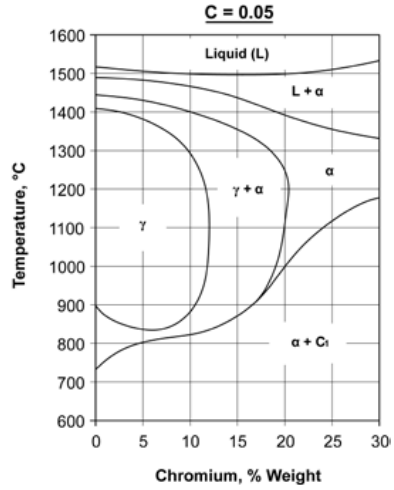

Fig. 1-6. Fe-Cr binary section of Fe-Cr-C ternary diagram for a steel containing 0.05% carbon.

Initial solidification occurs in phase α followed by a two phase transformation type α + γ. Subsequently, starting from about 900° – 950°C down to room temperature, the steel returns to a single phase state α with a ferritic grain structure. According to the phase diagram, there are no critical points to enable austenite → martensitic transformation, and therefore it is not possible to use heat treatments to increase tensile strength. Due to the high diffusion rate of atoms in the BCC lattice, ferritic stainless steels suffer of excessive enlargement of grains and consequently of increase in their embrittlement. At the same time, the existence of the α + γ phase at temperature higher than 900° - 950°C, where the T is strictly related to the amount of C and Cr, can lead to the presence of a little percentage of austenitic phase that could avoid the excessive enlargement of the crystalline grain during annealing treatment. On the other hand, a transition from austenite to martensite could occur if rapid cooling is performed causing *intergranular brittleness*. In order to ensure the formation of a stable ferritic phase and avoid the formation of the austenitic one, titanium and niobium are added, or stainless steel grades with higher Cr (more than 18%) content are used.

One of the major problems related to the use of stainless steel is the *precipitation of chromium carbide* that cannot be avoided in spite the very low solubility of carbon in the body-centered cubic lattice. In order to reduce chromium carbide precipitation, it is possible to add titanium and niobium to the alloy, reduce the C amount or perform a *complete annealing* heat treatment of the semi-finished products followed by rapid cooling before their use. As mentioned above, due to the absence of critical points at which phase transitions occur, the only possible heat treatment for ferritic stainless steel is *annealing* according to it is possible to improve their corrosion resistance due to Cr re-distribution in the crystalline lattice. Annealing is performed at different temperatures depending on the composition of the alloy while hold time will be carefully selected since they notably affect to the enlargement of the grain. On the other hand, heat treatments

can lead to the formation of *σ phase* and *embrittlement at 475°C*. σ phase formation is detrimental in terms of corrosion resistance and strength and it must be taken into account in the case of ferritic stainless steel grades with high amount of chromium and molybdenum (i.e. superferritic). In fact, the presence of Mo can lead to the formation of additional harmful phases. In order to reduce the occurrence of secondary phases, annealing treatment at 1050°C should be done followed by a rapid cooling of the semi-finished product in water.

Embrittlement at 475°C consists on the precipitation at the grain boundaries of α' phase characterized by higher Cr content with respect to the original α phase and it is significantly dangerous for all ferritic garades, with the exception of those with Cr amount less than 14%. This is mainly due to prolonged exposure or slow cooling within the temperature range between 400 to 525°C. Also in this case, annealing at 550°C – 600°C followed by rapid cooling is performed. Therefore, temperature and hold time are carefully selected according to the alloy composition. If the semi-finished part is in hardened state, annealing promotes also the re-crystallization of the microstructure with the formation of smaller grain originated from the first elongated due to the cold plastic deformation. This process is also known as *recrystallization annealing*.

Ferritic SS mechanical resistance is improved through cold plastic deformation processes, such as a *cold drawing* or *rolling*, following which the steel is hardened. Regarding the *strength*, the transition temperature increases by increasing chromium content in the alloy. Basically, ferritic stainless steels are used in the annealed state.

In industrial processing, the most used ferritic stainless steel are grades X6Cr17 (similar to AISI 430) and X2CrTi12 (similar to AISI 409). X6Cr17 is the traditional ferritic stainless steel. It has a good corrosion resistance (higher than that of martensitic) and it is largely used for machine parts for the production and transformation of nitric acid (tanks, condensers, pipelines, coils, etc.) for *cracking* and *reforming* plants in the oil sector production, for cutlery, household

appliances, decorative elements, accessories for interiors and kitchen extractor hoods. Applications of ferritic SSs are encountered also in the dairy industry and in components operating at 750° - 800°C due to their high resistance toward high temperature oxidation. X2CrTi12 is less resistant towards corrosion phenomena with respect the X6Cr17 but it is more deformable through cold plastic deformation and weldability is improved due to the stabilization with Ti. It is widely used in the automotive sector for the production of exhaust, catalytic converters and exhaust pipes for cars. In highly aggressive environments, ferritic SS grades with higher percentage of chromium and molybdenum are used, such as in the case of X2CrMoTi18-2 (similar to AISI 444), for heat exchangers, boilers and hot water storage tanks[4].

1.5 Austenitic stainless steel

Austenicic SSs are characterized by chromium content at least equal to 17% - 18% to which Ni is added to a percentage up to 8% - 9%. Moreover, C content is fixed at very low values (0.02% - 0.06%) in order to minimize chromium carbide formation. In spite the high Cr amount in the alloy, the austenitising effect of Ni ensure the formation of stable austenitic structure at room temperature with a FCC lattice. Austenitic stainless corrosion resistance is higher than that of martensitic and ferritic, specially towards atmospheric corrosion and water based solutions, even partially contaminated by chlorides. The base grade is represented by X5CrNi18-10 (similar to AISI 304) belonging to the family of *chromium – nickel stainless steel*. By adding molybdenum to values of 2 – 3%, it is possible to increase austenitic SS corrosion resistance. X5CrNiMo17-12-2 (similar to AISI 316) is the base grade of the second family of austenitic stainless steel called *chromium-nickel-molybdenum stainless steel*. In order to reduce production costs, Ni could be replaced with Mn, another austenitizing element, with the formation of SSs less resistant towards corrosion,

belonging to the *chromium-manganese-nickel* SS class. When nickel content is higher than 20%, austenitic stainless steels are called *superaustenitic.*

As in the case of ferritic stainless steel, critical points at which phase transitions could occur are not present due to the presence of carbon, nitrogen, nickel and manganese that thought their austenitizing effect are able to shift the transition temperature from austenite to martensite transformation to values well below the room temperature (see Fig. 1-7). This is the reason why heat treatments cannot be employed in order to improve their mechanical resistance. In spite C content is very low (usually in austenitic stainless steel is kept at values of 0.04% - 0.06%), the formation of chromium carbide is unavoidable. The phenomenon of carbide precipitation is also known as "*sensitisation*" and generally occurs at temperature ranging from 450°C and 900°C and the amount of precipitates depends on the exposure time during heat treatments.

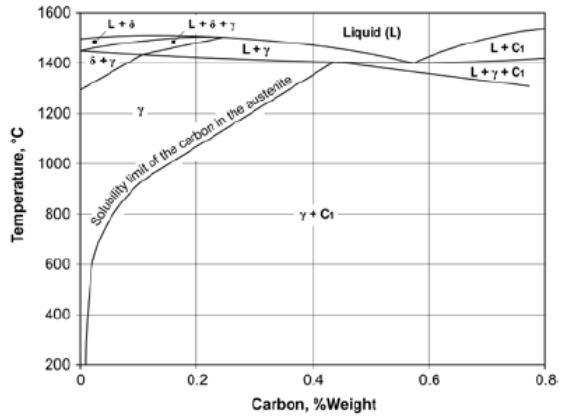

Fig. 1-7. Fe-C binary section of Fe-Cr-Ni-C quaternary diagram for a steel containing Cr = 18%, Ni = 8% and variable C content.

The most critical conditions are 700°C for just few contact minutes. Sensitization lead to the precipitation of chromium carbide in the boundaries of the crystalline grains (see Fig. 1-8) with the consequent depletion of chromium

content inside the grain at values lower than that necessary in order to have passivation of stainless steel surface.

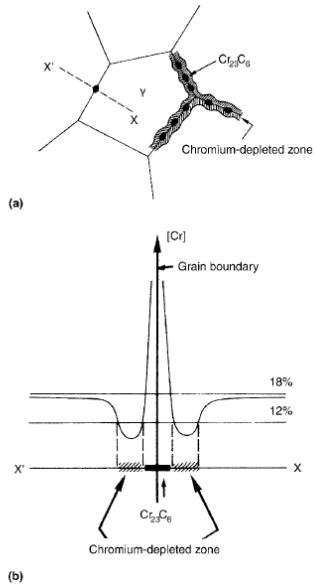

Fig. 1-8. Cr depletion from the austenite due to Cr carbide precipitation at the grain boundaries[38]**.**

Consequently, *local deterioration of corrosion resistance* and *inter-granular corrosion* occur also in slightly aggressive environments. In order to minimize the effect of chromium depletion, it is possible, as in the case of ferritic SSs, to add in the alloy stabilizing agents such as Ti or Nb that compete with Cr for the formation of stable carbides. The second possibility is to minimize C content in the alloy down to 0.02% - 0.03%. In this way, the sensitivity of austenitic SSs will be negligible even if the critical contact time is in the order of hours. Lastly, remembering that it is not possible to completely avoid chromium carbide precipitation, *solubilization* can be performed, that is annealing treatment at 1040° - 1050°C according to it is possible to dissolve any carbides present on the grain boundaries, to homogenize chemical composition and eliminate also microstructural irregularities. The option of solubilization often depends on the

dimension of the semi-finished parts. In fact, small parts are easily managed, while in the case of plant parts or welded structure heat treatment is not easy and therefore stabilized or low carbon content SS are preferred. Annealing is also named *quench annealing* because rapid cooling in water is necessary in order to preserve a uniform structure and composition and to prevent sensitization (except for stabilized and low carbon grades)[38].

Stabilized SSs usually undergo *stabilizing annealing* treatment after conventional annealing. They are maintained at temperatures between 850° - 950°C for a time that depends on the dimensions of the semi-finished parts and subsequently they are rapidly cooled. This further protective treatment is necessary in order to promote Ti and Nb carbides precipitation so that no C is available to fix with chromium. This process is usually employed when service conditions are highly severe. Although the adding of S, N and Cu, it is possible that a small amount of ferrite (1% - 5%) is present in the microstructure at room temperature due the rapid cooling from the melting point, as in the case of welding operations. It is possible to avoid the formation of the ferritic phase by increasing the amount of nickel (from 12% upwards) and nitrogen (0.10% - 0.25%) in the alloy.

Due to their FCC structure, austenitic stainless steels exhibit physical characteristics quite different than those of ferritic and martensitic. The linear heat expansion is 50 - 60% higher while the thermal conductivity is 40 - 50% lower than ferritic and martensitic SSs. They are also nonmagnetic and this makes them suitable for military applications. Mechanical characteristics are limited if compared to those of martensitic and ferritic grades due to the high deformability of the lattice structure. The only way to increase traction resistance is through hardening by cold working. One of the most interesting mechanical properties of austenitic SSs is the high resistance towards brittle fracture due to their FCC structure. In fact, their resilience curve never shows the transition to brittle fracture making them tough also at very low

temperatures. For this reason, austenitic SSs are the best candidates for cryogenic application.

Among austenitic SSs, AISI 304 is largely used in industrial, civil and military contests not for its mechanical properties but rather to its high corrosion resistance if compared with that of martensitic and ferritic grades. It is widely used in boilers, pressure tanks, vessels, heat exchangers, fluid transport pipes, plumbing, elevators and signs. It used also in buildings, urban furnishings, domestic utensils, sink and cabinets as well as in the chemical, petrochemical, nuclear and pharmaceutical industries, for the production of milk, beer, canned food, paper and pulp, colorants and explosive. Due to the absence of brittle fracture, it is largely employed in cryogenics sector for the storage and transport of liquefied gases. The stabilized versions with Ti and Nb have corrosion resistance quite similar than that of 304 and therefore they are used in the same applications especially for large size and thick items involved in welding operations. They are not suitable for decorative applications due to the precipitations of carbides that don't allow a satisfied surface finishing. Due to their higher mechanical properties, they are also used for making exhausting manifold, boiler bodies, chemical reactors, pressure vessels and pipe for armoured resistor. The low carbon version (AISI 304L) is used in order to avoid chromium carbide precipitation during welding operation and represents a good alternative to the stabilized versions in spite their mechanical resistance is lower with respect to the latter. Their surface finishing is very good and therefore are widely used for aesthetic applications. 304L is also largely employed for the realization of large-scale tanks and very thick reactors. Regarding the chromium-nickel-molybdenum stainless steel family, X5CrNiMo17-12-2 (similar to AISI 316) is the most widely used for the realization of components or parts of a plant operating in marine atmosphere or where severe corrosion phenomena could occur. Moreover, 316 is largely deformable and weldable. It displays highly corrosion resistance in presence of seawater, in contact to

process waters contaminated with halides (Cl^-, I^-, F^-), acid condensates and waste water. It is also largely employed in treatments with organic acids or alkaline solutions and also in dilute sulphuric, hydrochloric and phosphoric acid solutions. Due to their excellent corrosion resistance, 316 is used in chemical and petrochemical plants, in off-shore solutions and mostly in food and pharmaceutical industries where no contamination and high hygienic levels are recommended. Due to their nonmagnetic properties, they are also used for the realization of some military applications such as the manufacture of the hulls of submarines. As in the case of 304, the stabilized version with Ti and low carbon content versions are also available specially in welding operations. In order to improve corrosion resistance even more, some special stainless steels are used like “superaustenitc”. The type X1NiCrMoCu25-20-5 is characterized by a very high Ni content, and it is used for handling sulphuric and phosphoric acid solution as well as in the storage and transportation systems. Due to the very high Cr and Mo content, X1CrNiMoCuN20-18-7 SS is highly resistant towards chlorides attack, in fact, it is largely used in desalination plants and in chemical sectors or industrial operations (i.e. disinfection and sanitization processes) where bleach is extensively used.

1.6 Duplex Stainless Steel

Duplex SSs are characterized by a balanced dual-phase microstructure providing the best combination between mechanical and corrosion resistance properties. Typically, duplex stainless steels have a chromium content ranging from 22% to 25%, nickel content between 4% and 7%, with added molybdenum (3 - 4%) and nitrogen (0.1 - 0.25%) in many cases. This new generation of SSs developed due to a number of reasons. In fact, they possess the same, or even better, corrosion resistance as their austenitic counterparts, especially to stress corrosion cracking (SCC), higher strength, at least twice than that of austenitic grades, and are less

costly due to the lower contents of mainly nickel and molybdenum[2,3,39,40]. This microstructure is achieved due to the optimal balancing composition, allowing the stabilization of both phases at room temperature. On the other hand, phase precipitation in duplex stainless steel can occurs mainly due to Mo, Cr and W addition, making DDS grades more prone to transformation of ferritic phase to intermetallic phases (sigma and chi phases), nitrides, carbides or even to the alpha microstructure at lower temperatures (see Fig. 1-9).

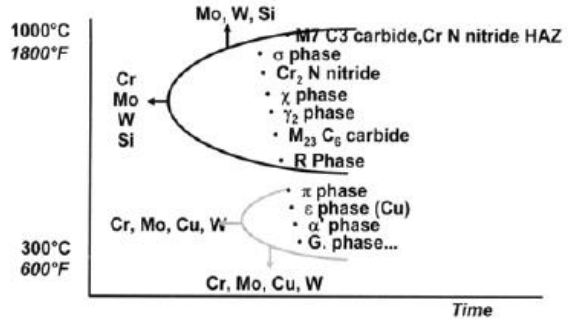

Fig. 1-9. Phase precipitations usually encountered in duplex grades[3].

Cupper addition can also allow epsilon-Cu precipitation at temperatures ranging from 600 to 300°C[36]. The formation of secondary phases can induce the reduction of toughness and corrosion resistance. Thus, all those technological processes that can induce significant modifications on DSS should be carefully handled such as welding or cooling after forging[4,41]. For this reason, after forming, semi-finished products undergo annealing treatment (i.e. solubilization) by holding the steel at temperatures ranging from 1050 to 1150°C and rapidly cooled in water in order to obtained the biphasic microstructure (i.e. austenite/ferrite ratio close to unity) and re-dissolve undesired compounds formed during manufacturing[2,4,42].

The Schaeffler diagram, reported in Fig. 1-10, displays the areas of stability of different stainless steel depending on the alloying elements.

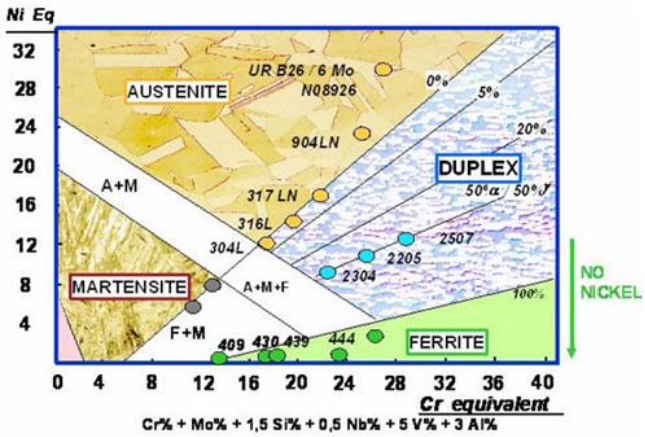

Fig. 1-10. Schaeffler diagram illustrating the areas of stability of stainless steel microstructure[3].

According to Fig. 1-10, most of duplex stainless steels have a typical 50% ferrite-50% austenite microstructure. The three main families of duplex grades are also plotted in the picture: the 2304 Mo free grades, the standard duplex type 2205 and the superduplex grades 2507 type. **Lean duplex** refers to all molybdenum free and nickel content lower than 3% stainless steel grades and represents less than 10% of the duplex volume. They are expected to replace 304L and 316L SSs since they are less alloyed in the expensive elements such as Ni and Mo. At the same time phase stability is ensured according to supplementary alloying of manganese, that is another austenitizing element, as discussed above. Higher amount of extra low cost nitrogen is added in order to promote the austenite stability and localized corrosion resistance. 2304 (Mo free grades) and 2101 are encountered in lean duplex grades. **Standard Duplex** (2205) replace 317 (LMN) and 904 grades due to the lower nickel content and higher mechanical properties if compared with those of austenitic grades allowing to reduce thicknesses. **Superduplex grade**s (SAF 2507) contribute about 10% of the total duplex amount and are considered the most suitable

materials for replacing 6Mo austenitic grades usually employed in severe environments. Since the progressive increasing of alloying element costs, new grades have been recently introduced. In fact, **Higher duplex grades** are new more alloyed grades characterized by higher corrosion resistance and structure stability than 2507 grades due to the higher Cr and N content. Moreover, partial replacement of Mo by Mo + W addition allows less sensitivity to intergranular phase precipitations on heating.

Duplex grades were generally employed in oil and gas application, i.e. sub-sea piping, manifolds, well applications and fire systems. They are also largely employed in desalination plant due to the severe chlorine containing environments, definitely replacing austenitic grades. Due to their cost advantages, by considering weight saving and maintenance costs, lean duplex can also be used for structural applications, such as bridges even in marine environments. DSS grades are also extensively used for chemical tankers, pressure vessels and storage tanks.

1.7 Stainless Steels Corrosion Resistance

Equipment manufacturing is based on the choosing of the optimum material to perform a given function reliably and safety, at the lowest cost, by taking into account technical needs, reliability, safety, imposed economic limits, and prescription imposed by regulatory agencies. Basically, fabricability, mechanical and physical properties and corrosion resistance are the main technical needs. *Fabricability* consists on the intrinsic ability of a material to be formed, cut, joined and heat treated and it is strongly related to mechanical, and thus composition of the material. Heat and mechanical treatments involved during manufacturing can also affect fabricability as well as the fabrication temperature. Surface finishing play also an important role, moreover in food and bioprocessing since its direct impact on cleanibility of processing equipment

during service and maintenance. *Physical properties* are strictly related to chemical and crystal structure of the material. The latter refer to density, melting point, magnetic properties and electrical and thermal conductivity, that strongly affect heat transfer in heat exchangers. *Mechanical properties* refer to strength, hardness and ductility of the material and depend on material composition, mechanical and thermal treatments performed during the fabrication and on service temperature. Minimum standards for mechanical properties of stainless steel referred to prescriptions reported in the American Society for Testing and Material (ASTM) and other national organization such as BSI and DIN. *Corrosion resistance* is the most important technical need that consists in the chemical or electrochemical interaction between the material and the surrounding environment. In fact, corrosion processes can induce surface modification, thus surface cleanability, and affect the life and the performance of processing equipment as well as the quality of products. A number of environmental factor play a key role on the onset of corrosion phenomena such as chemical composition, temperature, dissolved gases, suspended solids, flow rates, differential aeration, pH and the presence of microbial species. The design of the equipment (i.e. presence of crevice or traps that cannot be drained, radius curvature in piping system, etc.) and the excursion from normal operating conditions should be also considered. Materials should be ideally resistant to all type of corrosion processes both under normal and during excursion in operating conditions. Nevertheless, most materials after a certain period of time should be maintained or replaced. Corrosion can occur in many form and the knowledge of mechanisms and the environmental conditions that can induce the onset of degradation phenomena is fundamental in the choice of the suitable construction materials. General or uniform corrosion, pitting corrosion, crevice corrosion, stress corrosion cracking and galvanic corrosion are usually encountered when stainless steels are used. **General corrosion** consists in an uniform attack where the entire metal surface area is exposed to the corrosive environment and

converted into its oxide form. It is characterized by a uniform thinning of the metal which can be measured over time as millimetres per year (mm/yr).

The corrosion behaviour of multiphase alloys is strictly related to the electrochemical properties of the individual phases and on their galvanic interactions. **Galvanic corrosion** results due to the dissolution of less noble phase whose corrosion is enhanced by the presence of a nobler phase. High temperature of welding stainless steel can cause a depletion of alloying elements such as chromium. As a results of this depletion, weld metal area become less noble than it was originally. The relatively small surface area of the anodic weld metal coupled to the large surface area of stainless steel being joined establishes the onset on high current density at the anode and a consequent high corrosion rate[41]. **Crevice corrosion** is a kind of localized corrosion typically encountered in occluded area. It is usually the result of a depletion of dissolved oxygen in the obstructed area, which works as anodic site close to adjacent surfaces where oxygen is freely available to maintain a stable passive films. It occurs under deposits of biomass, organic film and inorganic residues as well as in welded joints, under washers or bolt heads, in poorly gasketed joints and geometrical discontinuities in which the electrolyte is stagnant with regards to the surrounding environment. Usually, high velocity streams tend to remove deposits or even better to prevent their formation (see Fig. 1-11).

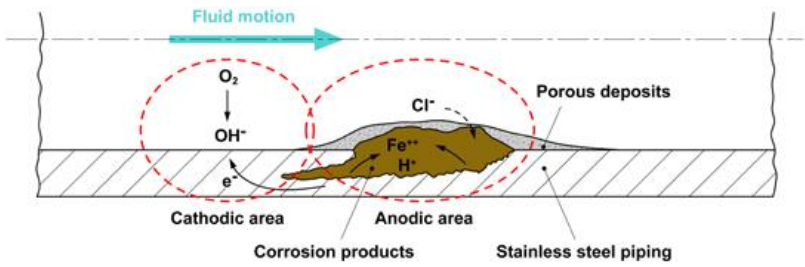

Fig. 1-11. Corrosion phenomenon under deposit in a pipe[4].

Thus, frequent cleaning of processes equipment may be beneficial.

Since the electrochemical properties of grain boundaries often differ from those of the bulk metal, a corrosion cell can form between a grain boundary and the rest of the surface. The result is a localized attack known as **intergranular corrosion**. In SSs it is a result of chromium depletion at the grain boundaries in heat-affected zones due to inappropriate heat treatments which induce segregation or precipitation phenomena referred as *sensitizing heat treatment*[43] (as already discussed in section 1.4).

Stress corrosion cracking (SCC) is caused by the combined action of a static tensile stress and corrosion. The stress may originate from external loading or be the result of a thermal or mechanical treatment that generate residual stresses in the material. Depending on the environmental conditions, SCC can induce the growth of intergranular cracks which may follow the gain boundaries (i.e. intergranular cracking) or pass through the grains (i.e. transgranular cracking)[43], as reported in Fig. 1-12. Austenitic stainless steels can be subjected to SCC in hot chloride solutions, in hot caustic soda and in chloride solutions containing sulphides or polythionates.

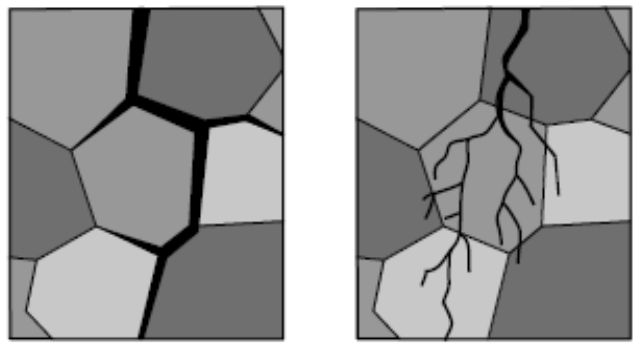

Fig. 1-12. Schematic representation of stress corrosion cracking: a) intergranular cracking and b) transgranular cracking[43].

Pitting corrosion is one of the most frequently seen forms of localized corrosion on SS consisting on the formation of cavities or holes in the material

whose growth eventually leads to perforation of a metal plate or pipe wall. Thus pitting corrosion can be quite important even if the absolute amount of corroded material is small. Pitting is likely occur on localized sites where the protective oxide film breaks down due to low dissolved oxygen concentrations or acidic environments which make the protective layer less stable, coupled with high concentration of chloride. The presence of surface non–uniformities such as surface roughness and inclusions play an important role on pitting initiation. Typical shape of corrosion pits are showed in Fig. 1-13: a) deep narrow pits exhibiting crystalline attack; b) occluded pits growing under a cover constituted of corrosion products or non-corroded metal; c) hemispherical pits with a polished surface usually encountered during potentiostatic tests in concentrated electrolytes[43].

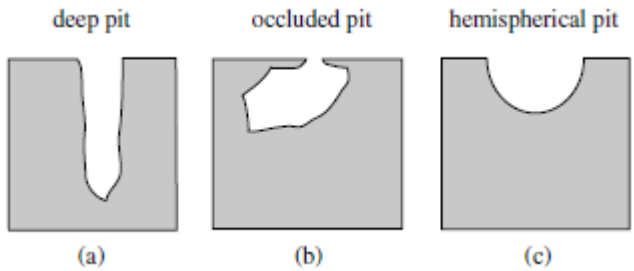

Fig. 1-13. Shape of corrosion pits: a) deep pit; b) occluded pit; and c) hemispherical pit[43].

It is considered to be more dangerous with respect to generalized corrosion since the difficulties on the prediction of the onset of pitting initiation and on the detection of the process.

2 Stainless Steels in Food and Beverage Industry

Good Manufacturing Practises (GMPs) consist on a combination of manufacturing and management practises, based on the experience, concerning food safety and quality, where *food quality* refers to nutritional, sensory and compositional of food products, while *food safety* concerns the microbial, chemical or physical hazard. These rules are mainly regulated by different agencies such as FDA (Food and Drug Administration), USDA (U.S. Department of Agricolture), EPA (Environmental Protection Agency), FTC (Federal Trade Commission), and CS (Custom Service). Meanwhile, the European Union is also developing a uniform text regarding food plant hygiene for its 14 member countries. These regulations are usually encountered in food plant and equipment design in order the guarantee food products specification and costumer expectations. Hygienic design of food processing equipment is also focused on the use of effective construction materials in order to avoid poisoning and contamination due to the release of metals from the substrate[44]. In fact, materials must be corrosion resistant, cost-effective, easily cleaned and not dangerous for operators and should also comply with the hygienic requirements regarding food safety. For this reason, austenitic stainless are the most used materials for food and beverage processing since they meet the strictest quality, safety and environmental prescriptions, including 3-A sanitary standards and relevant national authorizations[45]. The widespread use of SSs in food and drink industries is due to their high corrosion resistance in most food and beverages since no flavors or discoloration is imparted to processed fluids. In addition, they are easily and readily cleanable, ensuring high hygienic environments during both processing and handling. They can be also formed into necessary shapes suitable for fluid processing, movement and storage[45], as disclosed in Fig. 2-1. Nevertheless, production equipment such as fermentators, pasteurizators, mixer tanks, distillation columns, extractor and evaporators usually come in contact

with aggressive and corrosive environments due to the prolonged exposure to acidic, fatty or alcoholic foods.

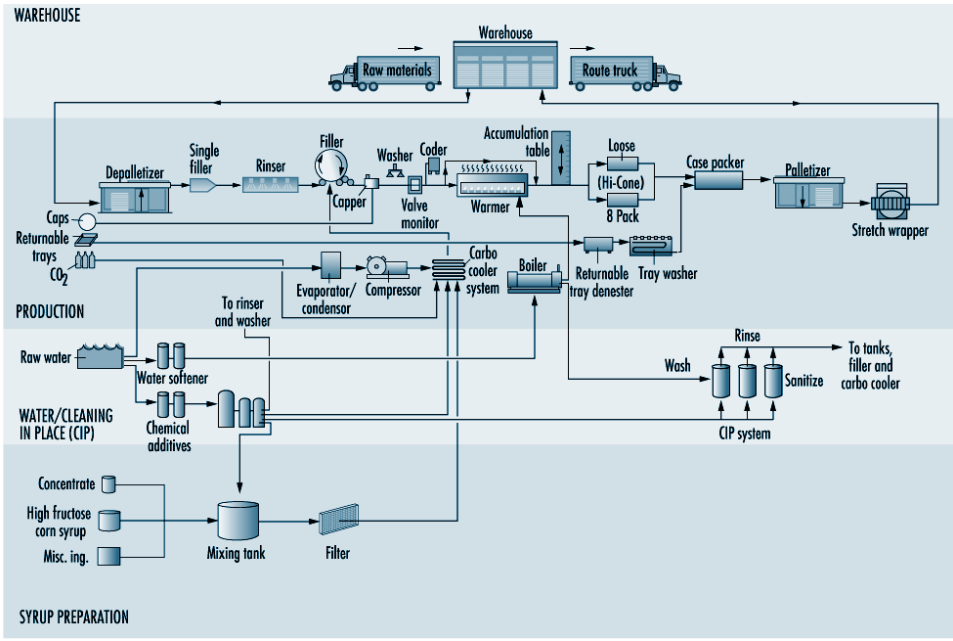

Fig. 2-1. Flow chart for soft drink manufacturing.

Moreover, since one of the major concerns regarding food processing consists on microbial contamination, *Cleaning*, *Disinfection* and *Sterilization* are usually employed after industrial processing, in order to ensure food safety and to avoid poisoning of consumers. For this reason, plant design should also provide appropriate equipment for the preparation of cleaning solutions and CIP piping (see Fig. 2-1).

Recently, duplex stainless steels are increasingly the material of choice for a wide variety of food and drink applications. Primarily used in chemical and desalination plants and in piping applications, their high strength makes them suitable for the construction of storage tanks due to thickness and cost reduction. A schematic representation of thickness distributions for a storage tank made of

both AISI 304 and Lean Duplex stainless steel is reported in Fig. 2-2a. In Fig. 2-2b, new storage tanks made with Outokumpu patented LDX 2101, in collaboration with the Spanish storage tank builder Emypro, are reported. The total saving achieved was about 350 tons, or 16% of the total weight[45].

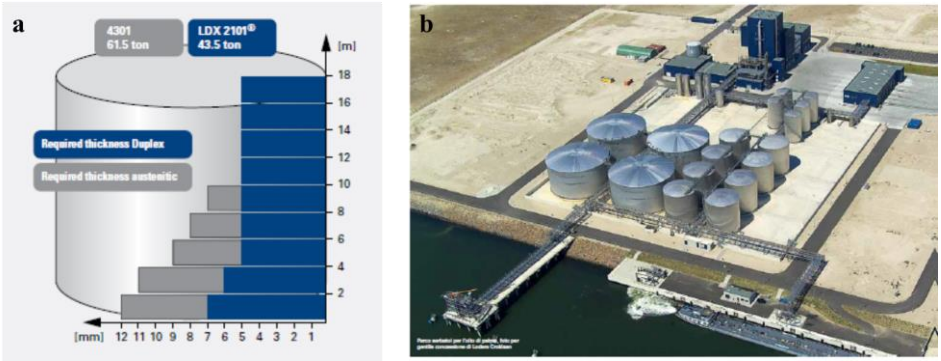

Fig. 2-2. a) schematic representation of thickness distribution for a storage tank made of AISI 304 (in grey) and Lean Duplex (in blue) stainless steel. b) palm oil tank farm located in the port of Barcelona[45].

Moreover, their high corrosion resistance, which is similar or even higher than austenitic grades, allows to use them for mustard, vinegar-making, cheese dairies or fish-canning processing. They are also widely employed for the production of natural tartaric acid as by-product of grape pressing, in distillation column for acetic acid recovery, in distillery and in wine and probiotic drink fermentation[45–49]. In addition, their superior resistance toward stress corrosion cracking makes them the perfect choice whenever steam is present.

In any case, every food and beverage process is characterized by specific demands thus materials should be chosen with care. EN 1.4301 (AISI 304) grade is used in a wide range of applications from brewing vessels to milk tankers (see Fig. 2-3)[50].

Fig. 2-3. Tank for low-fat milk production.

In particular, in the case of beer kegs, the neck and bottom of the vessel are usually made of tempered rolled 301LN in order to improve toughness and allowing to load several kegs on top of each other (see Fig. 2-4).

Fig. 2-4. Beer kegs[50].

EN 1.4401 (AISI 316) stainless steel grade is widely used for more aggressive foods. In particular, it is more resistant to high levels of chloride or sulphur dioxide in the operating environments making it suitable for processing of salty foods and aggressive media such as the pectin used in jam-making and the storage of white wines (see Fig. 2-5)[50].

Fig. 2-5. Wine storage tanks[45].

Super-austenitic stainless steel grades are typically employed for the realization of evaporator tubes and ice cream moulds due to their higher resistance towards pitting and stress corrosion cracking with respect to 316L grades. In very corrosive environments as in the case of syrup tanks where process conditions are very aggressive (Cl^- 10 000 ppm, pH ~ 5, T ~ 80°C) duplex stainless steel grades are more suitable. The latter can also be used for cooking tomato, barbecue and soy sauces (see Fig. 2-6).

Fig. 2-6. Heat exchanger made of duplex stainless steel grades.

Nevertheless, SSs are not immune toward corrosion phenomena as a consequence of the long term exposure to aggressive environments typical of food and beverage industries. A description of typically corrosive environments which SSs usually face with during processing, cleaning and storage operations is reported below.

2.1 Rouging

Rouging is the macroscale symptom of the onset of dissolution phenomena that can occur with the formation of undesirable particles. This process is characterized by the formation of a thin yellow surface film that, if allowed to grow, can develop to black when the oxide is thick enough, followed by release of particles downstream[51]. It is usually encountered in the internal surfaces of storage tanks, distillation columns, process vessels and distribution systems consisting on piping, valves, pump housings, fittings, etc. of HPW and WFI usually stored and handled at temperatures above 60°C[52,53]. Rouge consists basically on stainless steel corrosion products and it could be roughly divided into three main classes. **Class I Rouge** is a *deposited corrosion product*. This consists of iron oxides and hydroxides originated elsewhere in the water system and deposited downstream. The underlying stainless-steel surface beneath such deposits usually remains unaltered. It appears as an orange/magenta film comprising particles that are electrostatically attached to the surfaces. This rouge deposit can be wiped away, provided that this part of the system can be accessed, or by ultrasonic cleaning. **Class II Rouge** typically occurs in the presence of chlorides. It consists on an *adherent corrosion product* originating *in-situ* on un-passivated or improperly passivated stainless steel surface. Due to this kind of rouging, the passive-protective film on the stainless-steel surface is altered resulting in a red discoloration. Class II rouging is usually induced by Cr dissolution and can be removed by mechanically or chemical means. In this case

both chromium and iron are active species in the degradation phenomenon. **Class III Rouge** is the result of an iron oxide corrosion product called magnetite (Fe_3O_4) leading to a blue or black deposit that cannot be removed by simple cleaning. On electropolished surfaces, corrosion deposit may be glossy black, stable, and adherent. In contrast, on un-passivated mechanically polished surfaces, the corrosion deposit may be powdery black, and it may be detached[54,55]. This product is usually formed on surfaces in high-temperature steam systems.

Since rouging mainly occurs due to iron oxidation, passivation steps are crucial in order to increase the corrosion resistance, provide a contaminant-free environment and ensure the longevity and purity of the system. Nevertheless, rouging can occur quickly even after passivation treatments and the onset of degradation phenomena can occur at a speed much faster than usual under certain aggressive industrial environments. Such a kind of dissolution mechanism is extremely insidious since the difficulty in detecting the corrosion event[51].

One of the most susceptible component to rouging in a WFI loop is the circulation pump. As reported in Fig. 2-7a, rouging occurs on both the cover and the impeller. The pronounced generation and deposition of rouge in pumps is the macroscale representation on how rouging is strongly affected by flow rate. Rouging is also encountered within the section of the pharmaceutical plant where formulation tanks and CIP equipment are installed and on the internal wall of WFI buffer ranks. According to Fig. 2-7b, rouge floating particles deposit in horizontal lines on the shell as a result of alternating water level. Piping is also affected by rouging since fine particles can be released from the origin place (see Fig. 2-7c).

Fig. 2-7. Rouging build-up on a) the house pump b) in the buffer tank in the storage section and c) in piping through movement equipment[53].

As mentioned above, rouging usually occurs at high temperatures, but it could be also visible at lower operating temperature such as in buffer tank for cold water (~10°C), where surface discoloration occurs in the splash area close to the spray ball, as reported in Fig. 2-8a. Rouging is also visible in processing equipment since periodically sanitization with WFI, clean steam or CIP solutions usually employed at high temperatures. Steam generators are also affected by rouging since equipment work at 120 – 130°C and a dark deposit will be formed on the surface, according to class III rouging (see Fig. 2-8b)[53].

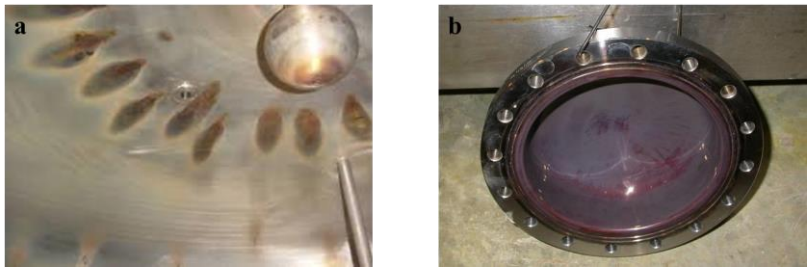

Fig. 2-8. Rouging visual appearance in a) splash areas close to the spray ball on the top of a buffer tank for cold water storage and b) in the generator operating at 120°C[53].

Many hypotheses have been proposed regarding causes and propagation of rouging, but it is generally believed that it is based on a combination of several factors. According to *Klapper at al.*[56] rouging is a surface phenomenon and it could be related to localized corrosion in weak point of passive film. This film

can breakdown as a consequence of exposure to ultra pure water which is devoid of ions and consequently alloying elements will be release to media depending on the composition and substrate finishing of stainless steel. Cyclic de-passivation and re-passivation will occur due to iron further oxidation with oxygen dissolved in water and incorporation of very low concentration of nickel, chromium and molybdenum coming from the bare alloy will take place too, leading to a distribution of corrosion products characterized by different surface colorations. This mechanism needs to happen different time in order to make rouge visible[54]. Not properly welded parts, where heat tints formation occurs, or not well cleaned areas could be weak points of rouging onset. It can be also affected by surface contaminations as mild steel particles, grinding dust and residues from emery wheels. Rouging strongly depends on the processing environment: in fact, materials are repeatedly exposed to corrosive fluids such as halides of bleach, temperature and pressure gradients, mechanical stresses, high shear environments, stagnant flow areas, etc. Water oxygen content and pH also could induce rouging[56]. In fact, pH influences water solubility of Fe^{2+} and Fe^{3+} and therefore the range of formed colors (i.e. thicknesses). Moreover, at elevated temperature dissolved oxygen in aqueous solutions is lower with respect to cold water and de-passivation will be enhanced. Iron diffusivity to the surface will also increase and reaction with the dissolved oxygen to form oxide and hydroxide will enhanced too[54]. High flow rates can increase dissolution rate and therefore corrosion kinetic.

Rouging monitoring is not straightforward, especially in the initial stage and visual appearance could be a qualitative evaluation of the onset of dissolution phenomena. Surface discoloration could be visible within some months after plant starts up to some years, but when interference colors are visible, production downtime of the plant is carried out in order to make necessary repairs and carry out routine cleaning. Sensors are usually installed to measure the reflectance of stainless steel surfaces or to perform interval sampling for

quality evaluation of processed fluids. As soon as rouging occurs, mechanically cleaning could be performed for poorly adhesive rouging particles removal. Unfortunately, manual cleaning is limited to parts easily accessible. Thus, de-rouging is carried out with inorganic acids and chelating agents. Among inorganic acid, nitric acid is one of the most used, although other acids are employed such as phosphoric or citric acid that are able to promote re-passivation and restore corrosion resistance of stainless steel. Organic acids are not used due to their lower solubilizing capacity. Chelants are chemical compounds based on a metal ion and a chelating agent able to remove particular cations such as iron in the case of de-rouging treatments. On the other hand, chelants are used for a limited time since to their tendency to dissolve metal surface even after rouge removal. Nevertheless, rouging is an unavoidable process that can occurs repeatedly even after removal. According to the US FDA (Food and Drug Administration), no regulations are reported on rouging prevention or remediation methods and generally, it is not considered critical for the quality of water. Conversely it may represent a potential risk due particulate contamination because particles of rust can be removed from the surface and dispersed throughout the piping distribution system. Particulate spread can also cause equipment maintenance problems due to blockages in filters. Moreover, since the surface morphology change as a consequence of ongoing dissolution phenomena, bacterial attachment and soil accumulation can be enhanced[54]. Although no specific regulations are provided, FDA established standards of quality for equipment construction (21CFR, Chapter I, Part 211, Subpart D, Sections 211.65), and cleaning and maintenance of the latter (21CFR, Chapter I, Part 211, Subpart D, Sections 211.67)[57]. For this reason, food and pharmaceutical equipment should be prepared according to the highest standards[53,54]. In particular, it is necessary to select the appropriate stainless steel avoiding low grades due to their lower corrosion resistance. The minimum specifications for processing hot highly pure water recommended the use of

304L and 316L due to their higher chromium content. Surface finishing has also a strong effect on the onset of rouging. In particular, electropolishing has a beneficial effect due to the lower surface contamination. Surface imperfections should be avoided because they could represent weakness points were passive film can be easily damaged becoming preferential sites were rouging can develop[58].

2.2 Biofilm

One of the major concerns on food industry consists on the adhesion of microorganisms to food contact surfaces from the viewpoint of food safety and quality[59,60]. In 1684 *Leeuwenhoek*, using his primitive light microscope, found that microbes attach to tooth surfaces and form sessile communities, which could be considered as the first observation of microbial biofilms. The concept of biofilms was first introduced not until the 1920s, when *Angst* in 1923, observed that the number of marine bacteria on the surface of ships' hull was higher than that of surrounding floating cells, and proposed that bacterial biofilm led to serious corrosion of ships' hulls. By the 1980s, bacteria were observed on the solid surfaces of many ecological environments including waste water treatment systems, equipment used to manufacture vinegar, in industrial water systems, tooth decay, urinary tract and other implanted medical devices[61,62]. The attachment of pathogenic microorganisms leads to the formation of a complex microbial ecosystem known as biofilm which can induce potential hygienic problems due to contamination of processed food. In fact, each year 48 million cases of food illnesses are identified in the United States, resulting in 128 000 hospitalizations and around 300 deaths revealing shortages in the current food safety standards and regulations[63]. Food processing facilities usually encounters warm and wet environments that, in the case of poor sanitation or improperly surface cleaning and soil buildup, can encourage bacterial growth in centrifuges,

pipelines, tanks, pasteurizers and packing tools[64]. In addition, bacterial colonization of food processing equipment represents one of the major concerns in damaging metal surfaces (i.e. pitting and corrosion) and can also contribute to decrease heat transfer, lose sensor sensitivity and filters plugging. For this reason, biofilm-associated effects such as corrosion of metal surfaces, alteration of organoleptic properties and risk to consumers health are of critical importance in food industry where numerous processes and equipment are involved as active surface substrate[60,65,66]. Biofilm consists on the accumulation of reproducing, metabolically active cells associated with solid substrata, embedded in a complex matrix termed extracellular polymeric substances (EPSs). EPS is mainly based on water and organic macromolecules as lipids, proteins, polysaccharides and nucleic acids and represents the 85-95 % of the weight of the biofilm providing mechanical resistance during bacteria attachment and all the nutrients necessary for biofilm growth, leading to the formation of a three-dimension polymeric network. Biofilm can form quickly in food industry environments, conferring advantages to the microbial cells such as physical resistance against desiccation, mechanical resistance against liquid streams in pipelines and chemical protection against chemicals, antimicrobials and disinfectans[66–68]. In Fig. 2-9, the sequence of events in biofilm formation on food-contact surfaces is reported. The first step of biofilm growth, also known as *surface conditioning*, consists on the deposition of organic molecules from food (i.e. milk, beef, kitchen, etc.) on equipment surfaces within seconds of exposure to an aqueous environment. Some microbial cells remain even after cleaning and sanitizing and initiate their growth being attracted on surfaces. Adhesion is a time dependent process and can roughly be divided into two phases: the reversible and the irreversible attachment. The reversible phase, where microorganisms are near but not in actual contact with the surface, mainly includes various long-distance interactions such as electrostatic, hydrophobic and Van der Waals forces. Conversely, in the irreversible phase, where binding

to the surface are various short range forces including dipole-dipole, hydrophobic, ion dipole, ion-ion, covalent bonds and hydrogen interaction, the microbes are irreversibly bound after they scanned the surface to detect whether the nutrient level is sufficient enough to live on. After irreversible attachment, microcolonies formation will proceed accompanied by EPS production and the aggregation of planktonic cells from the surrounding medium will occur as a result of cell-to-cell communication known as *quorum sensing*. Lastly, larger biofilms are formed. Due to dispersion phenomena, further attachment occurs on metallic substrate starting from mature biofilm and other micro-colonies are formed[61,65,67,68].

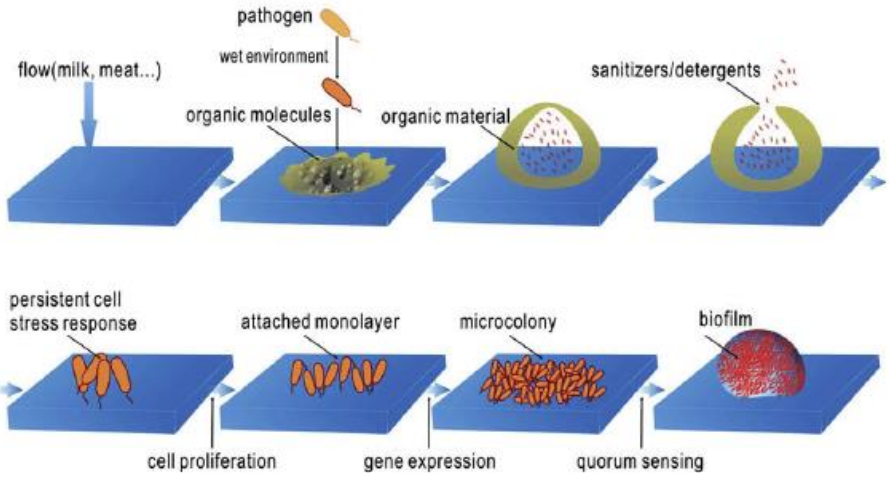

Fig. 2-9. Sequence of events in biofilm formation on food- contact surfaces[61].

Most of the microorganisms in biofilm are aerobic but anaerobic bacteria can also be present depending on their localization due to oxygen gradients onset through the biofilm and the formation of anoxic zones where anaerobic conditions prevail and where fermentative bacteria are particularly active.

The formation of microbial biofilm is a very complex continuous process and mainly depends on the type of bacterial strain (i.e. cell hydrophobicity, motility

and structure), on the environmental conditions (i.e. pH and temperature) and on the surfaces where attachment occurs[67,68]. In particular, abraded surfaces can accumulate soil and reduce surface cleanability. Moreover, surface defects can provide protection against the removal of soil and bacteria where surviving microorganism can regrow and produce a biofilm. For this reason, surface roughness (R_a) values below 0.8 μm, are the recommended values used for describing "hygienic" surface and it is the minimum accepted for food contact materials according to 3-A sanitation standards[58,69,70].

2.3 Food processing environments

In the frame of Good Manufacturing Practice (GMP), food contact materials (FMC) employed in food and beverage processing plant must be manufactured according to high quality and hygienic requirements. In fact, metals and alloy are potential source of contamination since they are largely employed as FCM both in process equipment production in the food industry and in household utensils. Therefore, declaration of compliance (*DoC*) and supporting documentation are necessary in order to reduce contamination and to guarantee the compliance with the legislation. The guideline limits for metal release from food contact materials may be different between the countries[71] and uniform guidance and interpretations are necessary. The guideline is based on the work of the Council of European and other authorities that provide useful information regarding risk assessments (European Food Safety Authority, EFSA), Food Additives (WHO/FAO), plastic food materials (EU regulation 10/2011) and contaminants (EU regulation 1881/2006) [72].

Harmonized legislation on FCM is applied to materials that:

- could be brought in contact with food;
- are already used for food contact processes;

- can release their constituents to food under normal working conditions[72].

Metal release occurs due to corrosion and it can induce adverse effects on human health (diseases and allergies) or induce modifications in the organoleptic characteristics of processed food[73]. For this reason, migration and release tests on FCM materials made of metals and alloys must be done by employing mimicking solutions able to simulated the prolonged exposure of processing equipment to aggressive environments typically encountered in food and beverage industry. Nevertheless, FCMs made of metals and alloys are not covered by a specific EU legislation but different regulations, restrictions and technical guidelines can be used to ensure high quality levels and safety of products by also taking into account storage time, temperature, thermal processing and residual oxygen. According to the literature, the *Italian law text*, stipulated on 23rd March 1973, and the *CoE protocol*, implemented in the European Union in 2003, are the reference tests largely used for the evaluation of metal release in mimicking solutions from FCMs usually employed in food processing. Testing methodologies and limiting values are also regulated. In particular, the most modern analytical method used for the determination of trace elements is the Inductively Coupled Plasma Mass Spectroscopy (ICP-MS) that replaces the traditional Atomic Absorption Spectroscopy (AAS) in many countries due to improved sensitivity (i.e. lower detection limits) and the possibility to perform multi-element analysis. Criteria that must be evaluated in release tests are accuracy, applicability (matrix and concentration range), limit of detection (LOD), limit of quantification (LOQ), precision, repeatability, reproducibility, recovery, selectivity and sensitivity and the initial concentration of metals in food simulants when migration/released tests are performed should also be determined[72]. Moreover, metal ions release must be evaluated as single elements considering that FCMs are affected by pH, salt, acid, fat and alcohol content in processed fluids.

2.3.1 *Italian Ministerial Decree of 21 March 1973*

The Italian Ministerial Decree of 21 March 1973, concerning the "*Hygienic requirements of packages, containers and other tools destined to come into contact with food or other substances for personal use*", refers exclusively to stainless steels used as food contact materials. The aforementioned Decree is mainly divided into two Titles. **Title I**, namely "*general provisions*", provides general guidelines regarding hygiene requirements of materials that come into contact with food. The enterprises engaged in the production of such materials have the obligation to control regularly the proper implementation of the provisions of the Decree. **Title II**, namely "*provisions concerning individual materials",* establishes hygiene requirements referred to specific substances that could be released from materials used for the production of packages, containers and tools destined as a consequence of their contact with food. Title II is dived in:

- item I – plastic equipment;
- item II – rubber equipment;
- item III – regenerated cellulose equipment;
- item IV – paper and cardboard equipment;
- item V – glass equipment;
- item VI – stainless steel equipment;
- item VII – final and transitional provisions.

Item VI of Title II is based on general provisions regarding the use of stainless steel as food contact material. Only stainless steel listed in Section 6 of Annex II

are suitable for food processing (i.e. Article 36). According to the Ministerial Decree, *overall migration tests* are necessary in order to ensure stainless steel suitability as food contact material (methods are reported in Section 1 of Annex IV). *Specific migration tests* of chromium and nickel release from SS are regulated according to the methods reported in Sections 2.3 and 2.5 of Annex IV; manganese migration is covered using the methods set out in Section 2.10 of Annex IV.

Food simulants are classified depending on features of foodstuff as follow:

- SIMULANT A: aqueous foodstuff with pH > 4.5 simulated with distilled water of water with equivalent quality;
- SIMULANT B: acidic foodstuff with pH < 4.5 simulated with aqueous solution with 3% w/v acetic acid;
- SIMULANT C: alcohol base foodstuff simulated with aqueous solution with 10% v/v ethanol;
- SIMULANT D: fatty based foodstuff simulated with sunflower oil or other fatty simulants.

In the case of reusable objects, specific migration tests are performed after three successive "attacks" of equal duration on the desorb solution coming from the third "attack". Following simulation tests are considered the most reliable in order to establish suitability of stainless steel:

- For equipment characterized by long time exposure at room temperature, aqueous solution of acetic acid at 3 % w/v for 10 days at 40 °C is used;

- For equipment used for short periods at high or at room temperature, aqueous solution of acetic acid at 3 % w/v at 100 °C for 30 minutes is used;

- For equipment exposed for short periods at high or at room temperature, that can only be used in contact with water, assessment of suitability is based on the use of distilled water or water of equivalent quality at 100 °C for 30 minutes.

Specific migration limits are also covered by this article. Both trace chromium (trivalent ion) and nickel content should not exceed 0.1 ppm. Manganese must be lower than 0.1 ppm too.

2.3.2 *Council of Europe protocol (CoE protocol)*

An innovative approach based on a new technical guideline text regarding suitability and safety of metals and alloys as food contact materials has been established in 2003 by the European Council and implemented by the European Union with the aim to ensure the safety and suitable quality of food contact materials[71,73–76]. It differs from the Italian law text in the use of artificial tap water and 5 g/L (0.3 vol %) citric acid mimicking solutions since they are considered more realistic simulants than distilled water and acetic acid. In fact, since release from metals and alloys is based on electrochemical mechanism, the use of acid is questionable considering the onset of dissolution phenomena that can provide misleading results from release tests. Moreover, most of alkaline and acidic food contains citric acid. In fact, it is present in most of fruits (i.e., apples, passion fruits, limes, strawberries, tangerines, plums, grapes, etc.) and vegetables (beans, carrots, mushrooms, potatoes, rhubarb, broccoli, etc.). For this reason, citric acid is also considered a versatile and innocuous alimentary additive and its use is covered by the Joint FAO/WHO Expert Committee on

Food Additivities[77]. Particularly, citric acid is largely employed to provide a pleasant, tart flavour to foods and beverages. It is highly used as acidic additive in:

- soft drinks and syrups to provide tartness, simulate natural fruit flavour and as acidulant in carbonated based beverages;
- wine and ciders to prevent and reduce turbidity due to tannin - iron or phosphate – iron complexes and for pH adjustments;
- candies as acidulant, to provide tartness and enhance fruits flavour. It avoids also crystallization of sucrose;
- canned fruits and vegetables;
- gelatin desserts, jams and jellies to adjust pH;
- dairy products to improve microbiological stability. It is also used as antioxidant and as emulsifier in ice creams and processed cheese;

In pharmaceutical industry it is largely employed:

- as effervescent in powders and tablets coupled with bicarbonates;
- as anticoagulant;
- to enhance active ingredients dissolution;
- as buffering agent, metallic – ion chelator in cosmetics and for pH adjustment.

It is finally employed as cleaner of metal oxides in order to remove ferrous and non-ferrous metals from the surface due to complexing action toward heavy metal ions[77]. According to the CoE protocol, some innovative provisions regarding specific maximum metal release limits (SRLs) for each alloying element, analytical methods and simulant solutions are introduced. In particular, a solution of artificial tap water (according to DIN 10531) of pH ~ 7.5 with 0.12 g/L $NaHCO_3$, 0.07 g/L $MgSO_4 \cdot 7H_2O$ and 0.12 g/L $CaCl_2 \cdot 2H_2O$ is used for the simulation of aqueous, alcoholic or fatty food type of food, while a 5 g/L of citric acid (pH ~ 2.4) solution is used to mimic the acidic food environments

with a pH ≤ 4.5. Following the protocol, passivation cycles are carried out to simulate the heating and cooling cycles typical of the food and beverage industry by immersion for:

- 2 h at 70°C;
- 2 h at 70°C + 24 h at 40°C;
- 2 h at 70°C + 238 h at 40°C.

In the Italian text law, 3% vol. acetic acid (pH 2.4) was considered as the worst case for simulation tests for foods with a pH lower than 5, while in the CoE protocol, 5 g/L is used for food with a pH ≤ 4.5. Despite the same pH, their abilities to complex metal ions are different, resulting in higher amounts of released ions according to the prescription reported in the CoE protocol compared to the Italian text. This finding can be explained considering the higher complexation ability of citric acid with respect to that of acetic acid considering that at pH 4.5 citrate ion ($HCit^{-2}$) are predominant and can form bi- or polydentate metal complexes, while acetate can only form monodentate. Therefore more stable complexes are formed in the case of simulation with citric acid[73].

2.4 Hot Purified Water (HPW)

Water is one of the major commodities used in chemical plants since it is widely employed as a service fluid for vessels or containers washing, and for providing and absorbing heat in heat exchangers. It can be also used as *raw material* for preparing cleaning solutions and as *Active Pharmaceutical Ingredient* (APIs) in pharmaceutical plant[78]. According to the US Pharmacopeia (USP), two grades of purity water are defined: Hot Purified Water (HPW) and Water For Injection (WFI).

HPW is use as an excipient in the production of non-parenteral preparations and, in specific, for pharmaceutical preparations and assays, for which water is indicated. In particular, HPW is one of the few raw materials that is normally prepared on site. In fact, it does not exist in the pure form in nature due to its ability to absorb, suspend or dissolve various compounds. Drinking water is the minimal source of feed water to produce PW, through deionization, distillation, ion exchange, reverse osmosis, filtration or other appropriate procedures.

HPW is also a starting material in the WFI and pure steam preparations. WFI is water of extra high quality without significant contamination. USP admits purification processes that are equivalent or superior to distillation in the removal of chemicals and microorganisms, such as reverse osmosis coupled with electro-deionization, nanofiltration and, downstream, ultrafiltration (see Fig. 2-10). As defined in the Ph. Eur. and the USP, WFI is mainly used for the preparation of medicinal products and parental solutions for injectable administration where water is used as a vehicle. Since microorganism that are prone to spread in the water produce endotoxins, all the equipment used by the production lines to purify, store and distribute WFI must prevent the build-up of endotoxin and minimize microbial contamination in the system[79].

Clean Steam differs from steam produced by a conventional boiler and it is used as utility in chemical plant. In contrast with water, no pharmacopoeia standard is required for clean steam and usually manufacturers refer to HPW and WFI specifications since clean steam purity is related to its condensate. It is largely employed in pharmaceutical and healthcare industry for equipment sterilization. Basically, HPW, WFI and clean steam are important supplies for product formulation, cleaning and sterilization in chemical plant.

The layout for high purity water and clean steam production, coupled to CIP facilities, is reported in Fig. 2-10. HPW, WFI and clean steam production usually takes place in the utility facilities where distillation columns and steam

generator are located. From this point HPW, WFI and clean steam are distributed to the user points all over the plant through the piping system.

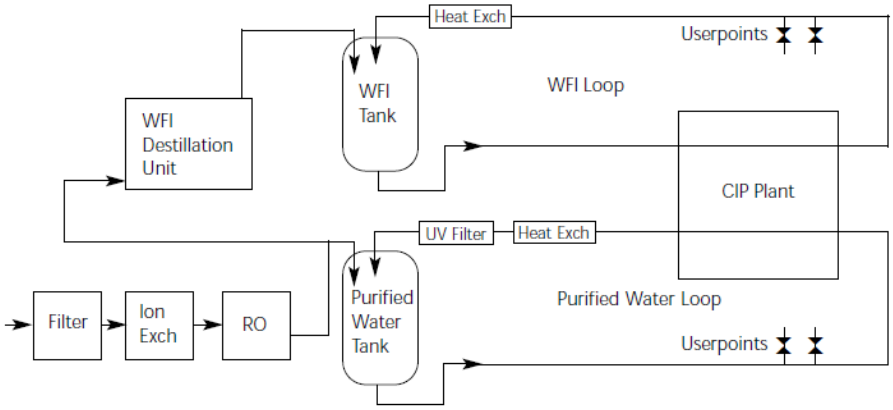

Fig. 2-10. Schematic representation of HPW, WFI and clean steam production plant integrated to a CIP system[52].

Notably, WFI is circulated constantly trough a buffer tank at about 80°C to keep the system self-sanitizing. Due to highly demanding purity requirements, water used for cleaning and sterilization processes should have a specific conductivity below 1.25 µS cm^{-1} at room temperature (according to the Pharmacopeia) which makes water and its condensate poorly concentrated in ions[52]. Moreover, HPW and WFI are usually stored at high temperature (~ 60°C). Considering the high purity and high storage and processing temperature, dissolution phenomena are usually encountered in storage tank, piping and pumps employed for water treatment, storage and distribution (i.e. rouging).

2.5 Cleaning In Place

Cleaning In Place (CIP) refers to all those mechanical and chemical treatments that are necessary to prepare equipment for food processing, either for removal of normal fouling after a processing run or when switching the production line

from one recipe to another. The main advantage in CIP processing consists on a substantial reduction in the time that the plant is out of production and on the ability to use more aggressive cleaning chemicals in a contained environment which cannot be safely handled with manual cleaning. CIP consists in an integrated and hygienic design which is part of the complete process. In fact, it consists of vessels for preparation and storage of cleaning chemicals, pumps and valves for circulation of the CIP chemicals throughout the plant, instrumentation to monitor the cleaning process and vessels to recover the chemicals. In the simplest application, single-use CIP can be employed and subsequently dismiss the solutions to drain, but this is very expensive in term of cleaning chemicals, water use and effluent costs. Moreover, this operation is not environmentally friendly and can only be justified if it is essential to apply a single use system to prevent microbiological cross-contamination of different areas of the process plant. Conversely, it is more usual to recover cleaning solutions in a recovery tank and restore the original concentration of the cleaning fluid, and then to re-use the recovered solutions[80].

As reported in Fig. 2-11, after production the plant is more or less soiled with the food products that have been inside the plant.

Fig. 2-11. Visual appearance of a tank filled with yogurt (first two pictures on the left) and of a tubular heat exchanger in a UHT plant that has been heating white milk at 120°C (last picture on the right)[81].

How to clean a chemical plant depends on what type of food and processing conditions are employed, as well as on the knowledge of how acids and detergents affect different type of soiling in the attempt to find the optimal operating conditions able to improve their interaction. Nevertheless, it is difficult to predict how fouling occurs and subsequently to identify the best way to perform cleaning, since the wide distribution of contaminants, soils and operating conditions. For this reason, cleaning protocols are semi-empirically developed in industry. A rough classification based on the relationship between the nature of fouling, type of cleaning employed and cost is reported in Fig. 2-12[82].

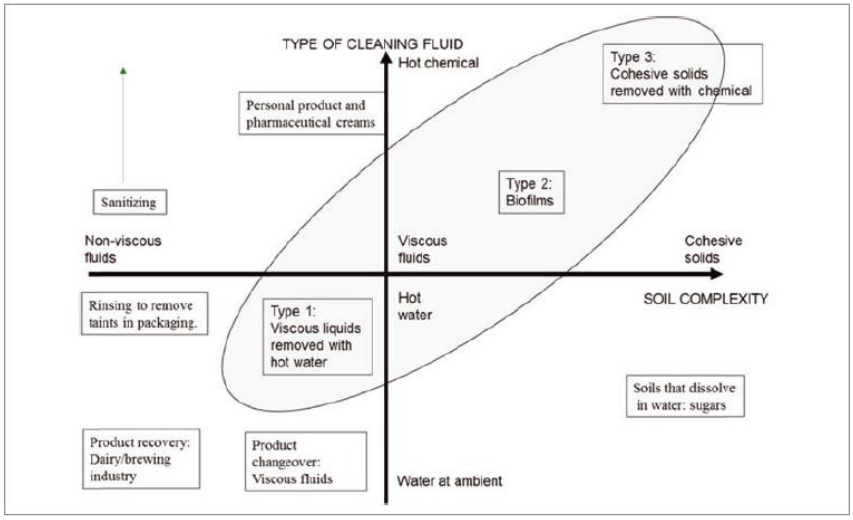

Fig. 2-12. Classification of cleaning problems based on soil type and cleaning chemical use[82].

Basically, soils are divided in those that are soluble and those that are not soluble in water. Sugars and some minerals for instance are soluble in water and therefore it is easier to remove them. Conversely, water-insoluble soils are harder to remove and there are usually divided in **organic** and **inorganic** soils (see Fig. 2-13). Organic soil includes fats, oils, grease, protein, starch and other

carbohydrates. If these compounds have been heated during processing, the heat may have induced reactions in the soil matrix, making them harder to remove. For instance, protein may denature and promote further cross-linking reactions with other proteins and also react with carbohydrates. Usually, organic soils are dissolved by alkaline detergents. Inorganic soils include mineral and salt deposit usually derived from limescale precipitation due to high water hardness. They are easily removed by acids (nitric or phosphoric acid).

In order to improve cleaning efficiency, mechanical force, heat, chemical force and contact time must be evaluated. The mechanical force consists on shear forces created by flow. As a general CIP rule, the minimum flow velocity through the CIP and transfer piping should be at least 1.5 m s^{-1}, but a higher value of 2 m s^{-1} is recommended if obstruction in lines occurs.

Fig. 2-13. Representation of protein fouling on the left and mineral fouling on the right.

In addition, the Reynolds number of the flow must be well in turbulent regime in order to ensure good radial mixing, heat transfer (i.e. uniform heating), mass transfer (i.e. of cleaning chemicals and soils) and momentum (i.e. scouring action of eddies)[58]. Moreover, CIP system design and construction requires piping to be free of dead space and pockets as much as possible; if not possible,

the dead zone should be less than two pipe diameters and the dead legs should also face the oncoming flow, as reported in Fig. 2-14.

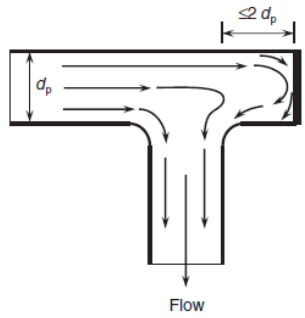

Fig. 2-14. Preferred arrangement of dead legs in pipework.

The chemical force is represented by the solution employed for soil removal. As mentioned before, alkaline detergents are largely used in order to remove the major part of organic soils. Basically, sodium hydroxide is typically employed at 0.5 – 2 wt.% for most applications, but higher levels could be used for some food applications[80,81,83]. On the other hand, excessive levels of NaOH may induce crosslinking of proteins in some food systems. Roughly, a typical CIP sequence includes: (i) washing with process water, (ii) rinsing with an acidic solution, (iii) washing with purified water, (iv) rinsing with a caustic solution, and (v) washing with purified water[81,82].The third force to use is heat. In this way, molecules move faster and therefore the effectiveness of cleaning increases. As a general rule, a plant should be cleaned at the same temperature as that used during processing. If higher temperature is employed, denaturation and crosslinking could occur, making cleaning more difficult to perform[81]. Typically, alkaline cleaning is performed at 75-80°C[58].

The last parameter is time, that is strictly related to the type of processed food and employed detergents.

CIP solutions are injected inside the tank or in other food processing equipment by spray devices. Static spray head (see Fig. 2-15a) has no moving parts and are

considered “self-cleaning” sanitary devices. These devices spray the fluid onto the tank surface from a fixed position and the effectiveness of cleaning strongly depends on the flow rate and on the size and the pattern of the holes. Conversely, dynamic spray balls are driven by liquid flow (see Fig. 2-15b-c). The fluid is injected onto the tank surface using larger pressure, that can in turn induce wall shear stresses, and rotation in order to ensure full vessel coverage. It should be note that impingement jets from a rotatory device or from small jets in a static device can induce rouging due to the worn of small iron particles that can further deposit on the tank wall[82].

Fig. 2-15. Commercial available a) spray ball static device, b) rotary spray head dynamic device and c) rotary jet head dynamic device[82].

Suitable materials of construction are stainless steel type 304L and 316L even if CIP component systems used directly in food processing are made of higher-grade type such as 316L.

When cleaning is performed, the plant appear visible cleaned but further treatment are required. CIP is a methodology able to remove product residues from a process plant and not a means for micro-organisms removal from the system. This is the role of the post CIP sanitization or sterilization processes by using either chemical sanitizers (*disinfection*) or the application of heat to destroy micro-organisms (*sterilization*)[80].

2.6 Disinfection

It is a process by which microorganisms are reduced to a level that doesn't compromise food safety or suitability and it is done with chemical and/or physical methods. Disinfectants can act both as *killing media* (bactericidal, fungicidal or virucidal effect) or as *growth inhibitor* (bacteriostasis, fungistasis), although, in the frame of sterility of food contact materials and purity of processed products, lethality is the only way of action. In contrast to antibiotics, that have distinct cellular targets within the microorganism, disinfectants don't work in a specific manner and therefore their mode of action is still not clear. Moreover, environmental factors such as temperature, pH, salinity, kind of target microorganisms and the state in which the latter are, could also affect their activity[84]. Disinfectants differs depending on how they interact with the microorganism. They can act:

- **on the external membrane** of the bacterial wall that protect bacterium from the surrounding environment. Usually bacterial membrane consists on basic compounds such as phospholipids and lipopolysaccharides stabilized by Mg^{++} and Ca^{++} cations. Therefore, surface interactions will play an important role during initial contact and absorption stages between cells and disinfectants;
- **on the bacterial wall** that is different between Gram-positive and Gram-negative bacteria;
- **on the cytoplasmic membrane** due to transport phenomena trough;
- **on energy metabolism** (i.e. some disinfectants could affect ATP production);
- **on the cytoplasm and nucleus** at chromosomic level;
- **on bacterial spores:** since the surface composition and structure of spores make them more resistant if compared with vegetative bacteria

towards disinfectants, highly oxidizing chemicals such as hydrogen peroxide and chlorine are usually recommended.

For the use in food processing equipment, disinfectant must be non-toxic to humans and it must not give any offensive odor to the food. It must be not corrosive to the circuit's materials and it should be stable and active during its action. Sensitivity towards the presence of organic matter should be also taken into account. A lot of compounds could be used in order to perform chemical sanitization but they must be approved by FDA (Food Drug Administration) as no-rinse, food-contact surface sanitizers. Among them the more common are ozone, chlorine compounds (i.e. sodium hypochlorite and sodium dichloroisocyanurate (NaDCC)) and quaternary ammonium compounds (QACs). Novel disinfectants such as electrolyzed water (EO), reactive oxygen species as dichloro-dihydro-fluorescein diacetate (DCFH-DA) and peroxides as hydrogen peroxide (HP) and peroxyacetic acid (PAA) could also be used[85–87].

NaClO is the most widely disinfectant employed in food processing plant, especially for the control of microbially levels in drinking water treatment due to its broad antimicrobial spectrum, rapid bacterial action, solubility in water, low cost and non-toxicity to humans at use concentrations. The effectiveness of NaClO as disinfectant is mainly related to the pH and the amount of available chloride in the solution. In fact, when NaClO is added in water, hypochlorous acid and sodium hydroxide are formed, as follow[88,89]:

$$NaClO + H_2O \leftrightarrow HClO + NaOH \qquad (2.1)$$

Hypochlorous acid is a weak acid in aqueous solutions and as soon as it is formed, it dissociates to hyplochlorite ion and H^+, depending on the pH of the solution:

$$HClO \leftrightarrow ClO^- + H^+ \qquad (2.2)$$

$$HClO + H^+ + Cl^- \leftrightarrow Cl_2(aq) + H_2O \qquad (2.3)$$

According to the equilibria 2.2 and 2.3, hypochlorous acid (HClO), hypochlorite ion (ClO^-) and hydroxide ion (OH^-) are the principal compounds present in sodium hypochlorite solution, where HClO is the active specie in the germicidal activity, while ClO^- plays an important role during cleaning action. Therefore, as it is displayed in Fig. 2-16, the optimal pH region of the germicidal activity differs from that of its cleaning action although both HClO and ClO^- are strong oxidizing agents able to interact with the organic soils and therefore with the EPS matrix.

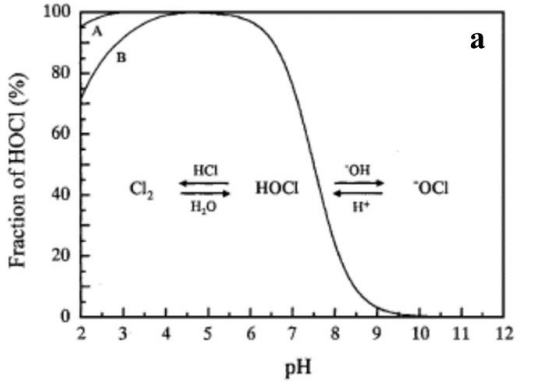

Fig. 2-16. HClO equilibria in aqueous solution as a function of pH[89].

Nevertheless, it is possible to perform both organic soil removal and microbes control in a single process. The action mechanism of both HClO and ClO^- is until now under investigation, but it is well accepted that it is mainly related to their ability to react with a large number of organic molecules. Basically, their germicidal action is based on the presence of Cl^+ in both chemical species that behaves like electrophile allowing it to react with high electronic density substrates. Among the biological molecules, C=C double bond, peptide bond, amino groups, and thiol groups are present, susceptible to the electrophilic attack by Cl^+. On the other hand, their ability in the germicidal action differs due to the presence of a lipid layer on the bacteria cells membrane. As reported in the literature[90–93], this lipid layer behaves like a hydrophobic substrate and therefore

ClO^- will not diffuse trough the membrane while, due to its electro-neutrality, HClO will do performing its germicidal action both inside and outside the cell, as showed in Fig. 2-17:

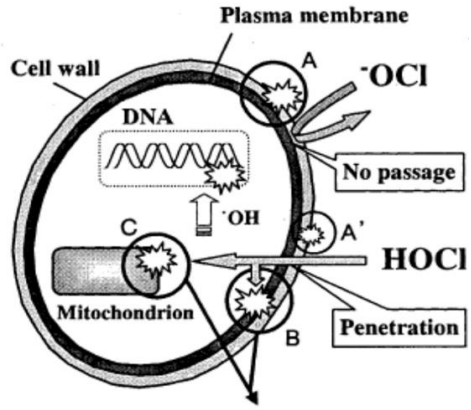

Fig. 2-17. Representation of the mechanisms of the germicidal actions of HClO and ClO^-[89].

As mentioned above, highly concentrated sodium hypochlorite solutions are mainly used when cleaning operations are involved. In spite the higher amount of the latter, the resulting OH^- (see equilibrium 2.1) can display germicidal action due the interaction with the membrane cell causing protein denaturation and destruction of the superficial structure. It is also important to perform cleaning operations before disinfection since the germicidal action of NaClO is lowered by the presence of organic soil residual.

2.7 Sterilization

If cleaning and disinfection are not able to remove all the microorganisms from equipment surfaces, sterilization step is usually performed since any bacterial residue, coupled with typical food processing conditions, can enhance biofilm

formation. Sterilization is defined as a process according to the complete destruction or elimination of all living microorganism, viable spores, viruses and viroids is achieved. It can be accomplished by physical (dry or moist heat) and/or chemical methods, but usually steam under pressure at high temperature is preferred. Saturated steam is usually employed because it contains the maximum amount of moisture without liquid condensate presence allowing to exploit water latent heat evaporation. The germicidal action efficiency of steam sterilization depends on the combination of heat and moist able to promote oxidation reactions that kill bacteria, thus a good compromise between temperature and time must be evaluated. Sterilization is often performed at 121°C for 20 minutes, but depending on contamination level, it could be also realized at 134°C for about 5 minutes. The important is that if temperature is increased, contact time must be decrease in order to avoid damage on passive film covering SSs surface. Every SIP cycle consists on the use of steam to elevate the temperature of the equipment, maintaining it at a minimum temperature for a specific time and finally cooling-down the system[88,94–97].

Cleaning, sterilization and disinfection of processing lines are performed before production re-starts. Nevertheless, it is important to clarify that cleaning must precede disinfection and sterilization because it is able to remove the great part of soils making further sanitization operations easier, as shown below in Fig. 2-18.

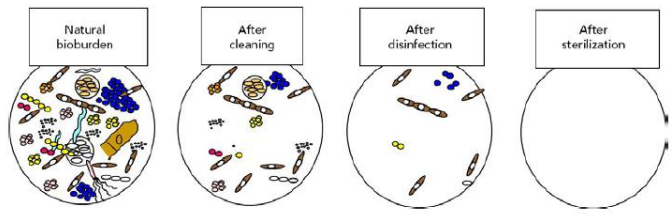

Fig. 2-18. Soil distribution after each cleaning step[81].

3 Materials and methods

The experimental activity of this research project is mainly focused on the study of solid state properties and corrosion resistance of passive films grown on different stainless steel grades as a function of the bulk alloy and electrolyte compositions. Different stainless steel grades, kindly provided by Outokumpu Company, were used. The corresponding composition is reported below in Table 3-1, where surface finishing and the pitting resistance equivalent number are also reported.

Table 3-1. As supplied stainless steel compositions (wt. %).

SS	**AISI 304L EN / 1.4307**	**AISI 316L EN / 1.4404**	**Super Duplex 2507 EN / 1.4410**
C	0.02	0.02	0.02
Cr	18.1	17.2	25.0
Ni	8.1	10.1	7.0
Mn	0.94	0.94	0.84
Mo	/	2.1	4.0
N	/	/	0.3
S	0.005	0.010	0.015
P	0.045	0.045	0.035
Si	0.75	0.75	0.26
Fe	balance	balance	balance
Surface finishing	2B	2B	2E
PRE	18	24	43

2B surface finishing refers to cold rolled, heat treated and pickled surfaces. It is characterized by a reflective surface and represents the most common finish for a wide range of steel types since it ensures good corrosion resistance, smoothness and flatness. Conversely, 2E surface finishing consists on a cold rolled and heat treated surface followed by pickling and appears as rough and dull[98,99].

Potentiostatic passivation was performed by applying a constant potential difference between anode and cathode. The process is carried out by forcing the current to flow from the cathode to the anode using an external power source, i.e. a potentiostat. A three-electrode configuration was used consisting on the metal substrate, where the oxide growth occurs, as the working electrode, a DSA (Dimensionally Stable Anode) electrode as a counter and silver/silver chloride electrode as a reference.

Passivation at the open circuit potential was performed by different immersion time in mimicking solutions. In particular, passive films were grown on food simulants, hot water, cleaning, disinfectant and sterilization environments. Simulating protocols will be discussed in detail in section 6. Notably, sample preparation and characterization was partially carried out at the "*Institute for Surface Science and Corrosion, Department of Materials Science"* at the Friedrich Alexander University of Erlangen-Nuremberg under the supervision of Prof. Dr. Sannakaisa Virtanen.

Biofilm growth was simulated in a fed-batch fermenter dedicated for the production of recombinant protein in E. coli, whose experimental set-up will be described in detail in section 7. This part of the research activity was performed at the "*Scienze e Tecnologie Biologiche Chimiche e Farmaceutiche*" department, at the University of Palermo.

Mirror surface finishing of different stainless steel grades was carried out with grinding papers P320, P500, P800 and P1000 grit. SSs samples were then treated

with a polishing cloth coupled with alumina suspension of 1 and 0.3 μm. Finally, the coupons were ultrasonically cleaned in ethanol and rinsed with deionized water.

In order to study growth mechanism, structure, solid state properties and corrosion resistance of passive films, *in-situ* end *ex-situ* techniques were employed. *In-situ* physico-chemical characterization was carried out in an exploited potential range very narrow to the open circuit potential and in quasi-neutral solutions (0.1 M ABE, pH ~ 8) in order to not modify passive films. *Ex-situ* characterization was also performed gaining more insight about oxide films properties. The techniques used for the characterization of passive films will be discussed in the following sections.

3.1 Photocurrent Spectroscopy (PCS)

Physiochemical characterization of passive films and corrosion layers is a preliminary task for a deeper understanding of the corrosion behaviour of metals and alloys. In particular, corrosion mechanism is based on electron and ion transfer reactions at the metal/oxide and oxide/electrolyte interfaces depending on the nature of the redox couple in the solution (i.e. redox potential, $E_{red/ox}$), on the corrosion potential (E_{corr}), on the flat band potential (U_{fb}) of the semiconductive passive film and on its conductivity type (*p* or *n*-type)[100]. For this reason, the knowledge of solid state properties of passive films is a fundamental tool for the location of the characteristic energetic levels of the *SS/passive film/electrolyte* interfaces, allowing the study of corrosion processes at a molecular level.

PCS is a non-destructive technique based on the analysis of the electrochemical response, in terms of photocurrent and photopotential intensity, of the metal/passive film/electrolyte interfaces under irradiation with photons of suitable energy and intensity. The choice of analyzing under potentiostatic control is recommended due to the relevant role of the electrode potential in the

establishment of electrochemical equilibria involving different metal oxidation states and reactivity of the passive films[101–103].

Beside the possibility related to the use of a very simple experimental set-up, PCS provides useful information on:

i. energetics at the metal/passive film/electrolyte interfaces in terms of determination of passive film flat band potential (U_{fb}), internal photoemission thresholds and location of conduction and valence band edges;
ii. the oxide electronic structure and indirectly determination *in situ* of the chemical composition of passive films through the knowledge of the optical band gap (E_g)[104].

Moreover, photocurrent response of passive film/electrolyte interface is strictly related to the number of absorbed photons. Therefore, PCS does not need special requirements in terms of surface finishing, allowing to monitor also long-term corrosion processes, where large changes in surface reflectivity are expected due to the formation of rough surface as a consequence of corrosion products covering. Finally, the risk of electrode modifications under illumination can be minimized by improving the sensitivity of the signal detection by using a lock-in amplifier, coupled to a mechanical light chopper, which allows to study very thin films (1 to 2nm thick) also under relatively low-intensity photon irradiation[102].

Conversely, the main limitations in the use of PCS are related to the following issues:

i. only passive films having semiconducting or insulating properties can be investigated;
ii. surface layers with a band gap lower than 1 eV or higher than 5.5 eV require a more complex experimental set-up or are not accessible in aqueous solutions;

iii. complementary investigation based on the use of other techniques is necessary for the determination of structure and chemical composition of passive films.

The first two limitations are more apparent than real. In fact, according to the optical band gap values reported in the literature for amorphous or crystalline oxide films grown on a wide range of sp- and d- metals, most common metal oxides have bandgap values ranging within the optical limits of the PCS experimental set-up. Moreover, with the exception of noble metals (i.e. Ir, Ru, etc.) where passive film growth occurs only at very high polarizing voltages, most metals are unstable in aqueous solutions and therefore photoactive films with insulating or semiconducting properties will spontaneously grow after immersion in the electrolytes. The third limitation is the principal one. Nevertheless, PCS can provide useful information regarding structure and composition of passive films if more realistic interpretative models are taken into account based on the valuation of the more complex electronic structure of amorphous passive layers[101–103].

PCS experimental set-up employed for the measurements performed in this Ph.D. work is reported in Fig. 3-1. It consists on a 450 W UV-Vis xenon lamp coupled with a Kratos monochromator. According to the lamp-monochromator system, working electrode is radiated with a photon flux at variable wavelength in a wide range of photon energies (5.5 to 1.5 eV) through a quartz window in the cell.

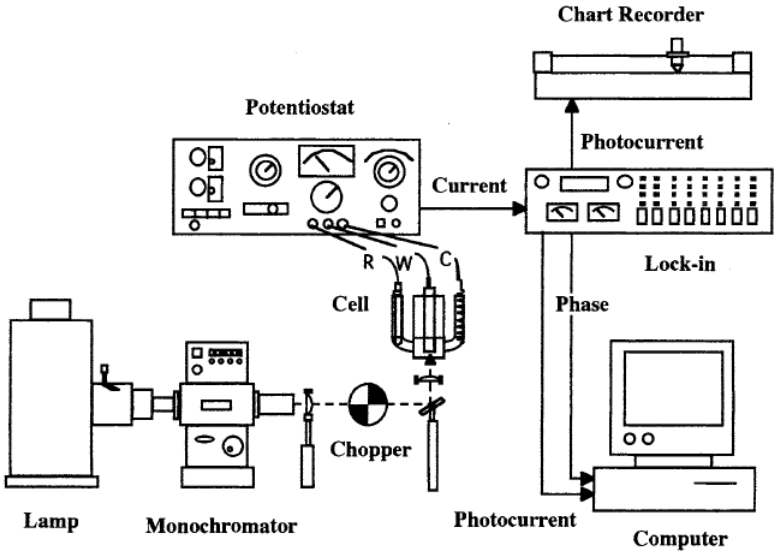

Fig. 3-1. Experimental set-up employed for the Photocurrent Spectroscopy measurements[101].

In order to detect weak photocurrent signals in the presence of large dark current, a chopper together with a lock-in amplifier is used. When the photocurrent is measured by means of the lock-in technique the illumination of the junction is interrupted several times per second (periodically chopped photon flux). In this case, the lock-in measures a signal whose intensity depends on the ratio between the chopping angular frequency, ω_c, and the time constant of the electrical equivalent circuit of the junction, τ, including also the electrolyte resistance ($\tau = R_tC_t$, with R_t and C_t representing the total resistance and capacitance of the junction respectively)[102].

3.1.1 *Photoelectrochemical behaviour of a Semiconductor/Electrolyte interface under illumination*

In order to better understand the photoelectrochemical behaviour of a semiconductor/electrolyte junction under illumination, a briefly discussion regarding the main features and differences between a crystalline and an amorphous material is reported.

The structure of a semiconductor/electrolyte interface (SC/El) differs from that of the metal/electrolyte (M/El) interface due to the different mobile carriers concentration. In addition, the potential drop, in the case of the metal/electrolyte interface, occurs mainly across the electrolytic double layer thus a change in the electrode potential U_E with respect to the reference electrode moves the Fermi level of the metal with respect to the electronic levels in the solution changing the photoemission threshold E_{th} as follow:

$$E_{\mathrm{th}} = E_{\mathrm{th},0} + eU_{\mathrm{E}} \qquad (3.1)$$

where $E_{th,0}$ represents the photoemission threshold at an arbitrary zero electrode potential value. Conversely, the potential drop at the SC/electrode interface occurs mainly across the space charge region inside the semiconductor. For the latter, the onset photocurrent energy threshold coincides with the band gap of the SC (E_g) that is independent of the electrode potential. The total potential drop across the SC/El interface can be written as:

$$\Delta\Phi_{SC/El} = \{\phi_{SC}(\infty) - \phi_{SC}(0)\} + \{\phi_{SC}(0) - \phi_{El}(-\infty)\} \qquad (3.2)$$

where the first term in the right-hand side represents the Galvani potential drop from the bulk (zero electric field) to the surface of SC/El junction, whilst the second term represents the Galvani potential drop occurring into the compact and diffuse double layer (if any) of the electrolytic solution. According to the

Galvani potential profile across the SC/El interface reported in Fig. 3-2, the region of the semiconductor, where the potential drop occurs, is defined as the space-charge region (i.e. X_{SC}).

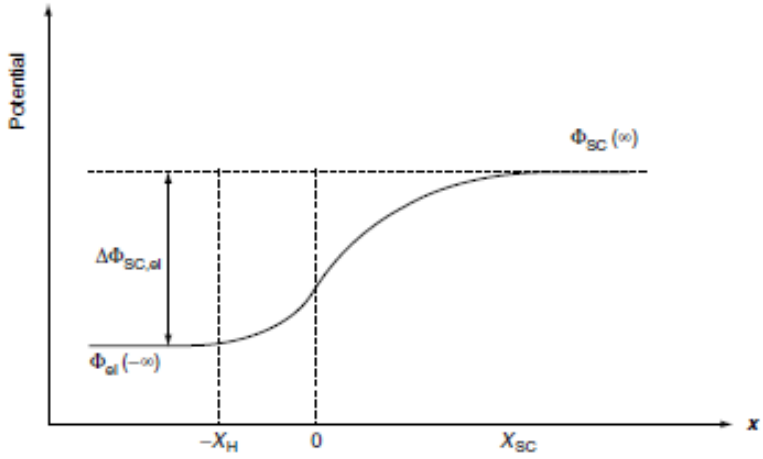

Fig. 3-2. Galvani potential profile across the semiconductor/electrolyte (SC/El) interface[102].

X_{SC} thickness change by changing the electrode potential according to the following equation:

$$X_{SC} = X_{SC}^{0}(|\Delta\Phi_{SC}| - kT/e)^{1/2} \qquad (3.3)$$

where X_{SC}^{0} is the space charge width in the semiconductor at 1 V of band bending and its value depends on the concentration of mobile carriers in the SC that is function of the doping level.

In Fig. 3-3, a schematic diagram of an n-type SC/electrolyte interface, in the energy-distance coordinates under slightly depleted (i.e. anodic polarization, $\Delta\Phi_{SC} > 0$) and flat band conditions (i.e. $X_{SC} = 0$), is also reported.

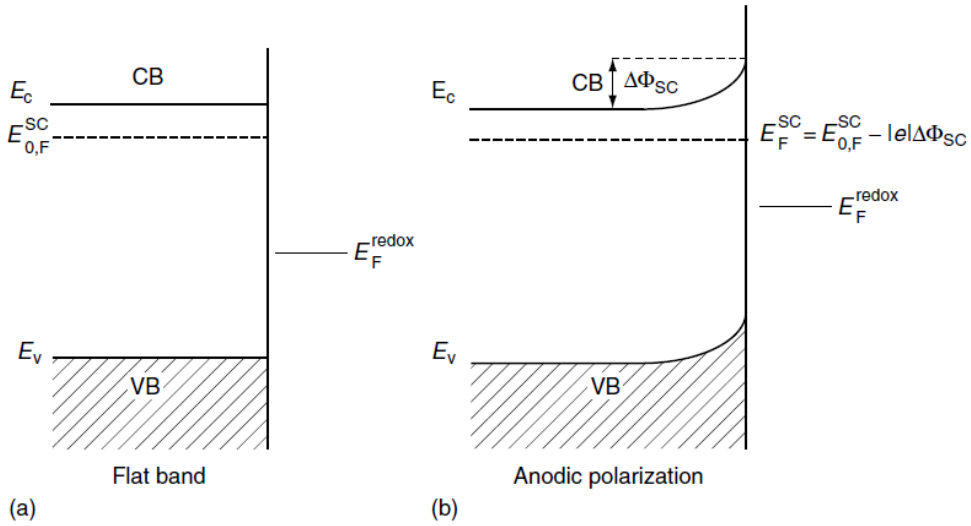

Fig. 3-3. Electron energy levels in the SC/El junction a) at the flat band potential and b) under anodic polarization for an n-type semiconductor.

When the potential drop within the semiconductor is zero (i.e. $\Delta\Phi_{SC} = 0$) the electrode potential U_E will be equal to U_{fb}, thus:

$$\Delta\Phi_{SC} = U_E - U_{fb} \qquad (3.4)$$

According to the Gärtner-Butler model, the absorption process of incident light in the bulk of the SC can be schematically represented as reported below in Fig. 3-4:

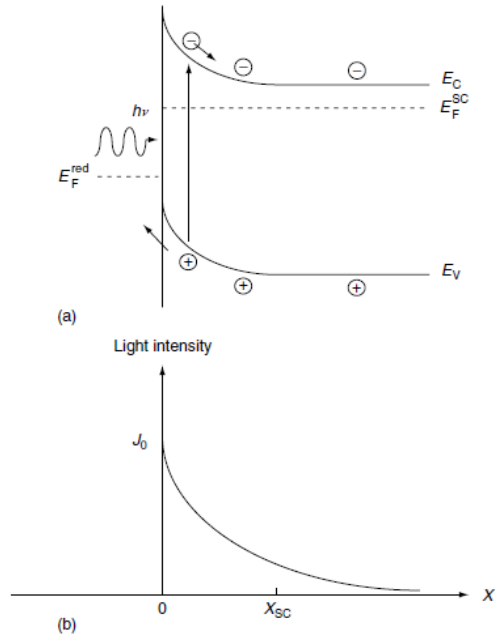

Fig. 3-4. Schematic representation of a crystalline n-type SC/El interface under illumination where the generation of the electron-hole pair is also reported[102].

where J_0 (cm^{-2} sec^{-1}) is the photon flux entering the SC corrected for the reflection losses at the SC/El interface which absorbed according to the *Lambert-Beer* law. By assuming that each absorbed photon with energy $hv > E_g$ forms a free electron-hole couple, the number of electron-hole pairs generated per second and unit volume at any distance from the surface, *g(x)*, is given by:

$$g(x) = J_0 \alpha e^{-\alpha x} \qquad (3.5)$$

where the light absorption coefficient α (cm^{-1}) is a function of the incident light. According to the Gärtner-Butler model, the total photocurrent collected in the external circuit consists of two terms consisting on a migration, I_{drift}, and a diffusion term, I_{diff}. The first one takes into account the contribution of the minority carriers generated into the space-charge region, while the second accounts for the minority carriers entering the edge of the space charge region from the bulk field region ($x > X_{SC}$) of the SC. No light reflection at the rear

interface is assumed, so that the light entering is absorbed within the SC. In addition, it is assumed that no recombination of the minority carriers occurs within the space-charge region due to the presence of an electric field which separates efficiently the photogenerated carriers, as well as for the carriers at the surface of the SC (i.e. the minority carriers coming at the depletion edge from the bulk region of the SC). According to the aforementioned assumption, the following equation, for a n-type SC, can be written as follow:

$$I_{ph} = I_{drift} + I_{diff} = eJ_O \left[\frac{1 - \exp(-\alpha X_{SC})}{1 + \alpha L_h}\right] + ep_0 \frac{D_h}{L_h} \qquad (3.6)$$

where D_h and L_h are respectively the hole diffusion coefficient and the diffusion length and p_0 represents the hole equilibrium concentration. The same equation can also be written for a p-type semiconductor with D_n and L_n instead of D_h and L_h and n_0 (i.e. electron equilibrium concentration) instead of p_0[102]. For wide band gap SCs, where the concentration of minority carriers is very small into the bulk, the equation reported above can be simplified by neglecting the last term. Moreover, according to the definition of X_{SC}, and by assuming $\alpha X_{SC} << 1$ and αL_h, Butler derived the equation reported below for the photocurrent at a crystalline SC/El junction:

$$I_{ph} = eJ_0 \alpha X_{SC}^0 \left(U_e - U_{fb} - \frac{kT}{e}\right) \qquad (3.7)$$

Eq. 3.7 displays a quadratic dependence of the photocurrent on the electrode potential, that allow to find the flat band potential, U_{fb}, of the junction[102]. In fact, by neglecting the term kT/e, a plot $(I_{ph})^2$ vs. U_E may intercept the voltage axis at the flat band potential regardless of the employed λ as long as the assumption $\alpha X_{SC} << 1$ is respected. It is important to stress that all the equations discussed above pertain to the steady-state values of the *dc* photocurrent. The equation

obtained for steady-state remain valid also for chopped conditions provided that the lock-in measured signal remains proportional to the steady-state chopped value[103].

In addition, according to Eq. 3.7, a direct proportionality between the measured photocurrent and the light absorption coefficient can also be derived. In fact, in the vicinity of the optical absorption threshold of the SC the relationship between the absorption coefficient and the optical band gap of the material, E_g, can be written as:

$$\alpha = A\frac{\left(h\nu - E_g^{opt}\right)^{n/2}}{h\nu} \tag{3.8}$$

Thus, it is possible to derive the following equation:

$$Qh\nu = A\left(h\nu - E_g^{opt}\right)^{n/2}\left(X_{SC}^0\sqrt{|U_e - U_{fb}|}\right) \tag{3.9}$$

$Q = (I_{ph})/eJ_0$ represents the photocurrent collection efficiency and E_g^{opt} the optical threshold for the onset of photocurrent at the illuminated electrode. In fact, at constant electrode potential, it is possible to get the optical band gap of the material from the dependence of the photocurrent on the wavelength (i.e. the photocurrent spectrum of the junction) of the incident light at constant photon flux. In fact, by plotting $(Q_{hv})^{2/n}$ vs. $h\nu$ at constant electrode potential ($U_E - U_{fb}$ = const.), it is possible to get a characteristic photon energy $h\nu_0 = E_g^{opt}$ where, for an ideal SC/El junction, E_g^{opt} is equal to the minimum distance in energy between the filled states of VB and empty states of CB, i.e. the band gap E_g. n can assume different values depending on the nature of the optical transitions between states of both the VB and the CB. In fact, optical transitions at the energies near E_g of a crystalline material can be direct or indirect. In the first case other particles do not participate apart from the incident photon and the

electron of the VB while for the latter, the optical transition is assisted by the participation of lattice vibration. By assuming a parabolic electronic density of states distribution, i.e. DOS ($N(E) \propto E^{1/2}$) near the band edges, in the case of direct transition n is equal to 1 or 3, depending on whether the optical transitions are allowed or forbidden in the quantum mechanical sense[105]. Conversely, in the case of indirect optical transitions, the value of n is equal to 4. It is important to underlying that in the presence of strong surface recombination effects, the onset of photocurrent will occur at much higher band bending than that predicted by Gärtner-Butler equation[102].

On going from crystalline thick SC electrodes to very thin insulating or semiconducting corrosion films on metals, new interpretative models should be employed. In particular, the two models of DOS (i.e. density of states) usually considered for the interpretation of optical and electronic behaviour of insulating or semiconducting amorphous materials are showed in Fig. 3-5.

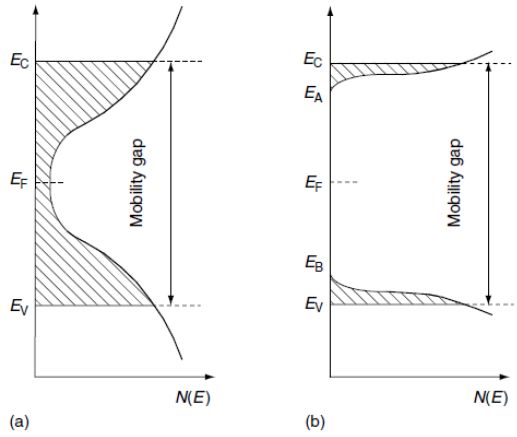

Fig. 3-5. Representation of the density of electronic states as a function of energy according to different amorphous semiconductor models: a) Cohen-Fritzsesche-Ovinsky model and b) Mott and Davis model. The dotted areas represent the localized state while E_C and E_V are respectively the conduction and valence band mobility edges[102].

The main feature of amorphous materials is the absence of long-range order in spite usually they retain the same short-range order with respect to the

crystalline counterparts. Nevertheless, the band structure model can also be applied in the absence of long-range lattice periodicity. This means that the long-range disorder perturbs but does not annihilate the band structure allowing the presence of a finite density of states within the so called "mobility gap" (E_C – E_V) of the amorphous semiconductor (a-SC) or insulator. The DOS distribution reported in Fig. 3-5a (CFO model) accounts the presence of defect states within the semiconductor that induce a continuous distribution of electronic states within the mobility gap. Conversely, the DOS distribution proposed by Mott and Davis can be attributed to an ideal amorphous material where only a long-range lattice disorder in considered (see Fig. 3-5b). The different electronic structure described for an amorphous semiconductor affects the generation and transport processes of photocarriers in amorphous materials and therefore the photoelectrochemical response of the a-SC/El junction.

In the case of amorphous material, by assuming a parabolic DOS distribution in the vicinity of the mobility edges of both conduction and valence bands, the following relationship holds:

$$\alpha h\nu = \text{const}(h\nu - E_g^m)^2 \qquad (3.10)$$

where $E_g^m = E_C - E_V$ is the mobility gap of the a-SC. The exponent 2 is reminiscent of the indirect optical transitions in crystalline material but now photons interact with the solid as a whole. This type of transition in amorphous materials is termed non direct. Because some tailing of states is theoretically foreseen for an a-SC by any proposed model of DOS, E_g^m represents an extrapolated rather than a real zero in the density of states. Notably, in the absence of appreciable differences in short-range order of amorphous and crystalline counterpart, the mobility gap of amorphous anodic films should be equal or larger than the band gap of the crystalline counterpart. Such a difference in optical band gap value can be assumed as a measure of the influence of lattice

disorder. The difference $\Delta E_{am} = (E_g^{m} - E_g^{cryst})$ in the range of 0.1 to 0.35 eV, is in agreement with the expected extension of the localized states regions near the band edges due to the lattice disorder. Conversely, a mobility gap of passive film lower than the band gap of the crystalline counterpart must be interpreted as an indication that differences are present in the short-range order of the two phases due to the formation of a defective structure with a high density of localized states within the mobility gap as well as changes in the density of the passive film, which is known to affect also the value of the optical gap in amorphous materials[102].

3.1.2 *Semiempirical Correlation between Optical Band Gap Values of Oxides and the Difference of Electronegativity of the Elements*

As discussed above, photocurrent spectroscopy is an optical technique that allow the estimation of solid state properties of photoconductive passive films. PCS can also be used as an analytical tool for the identification of the nature of corrosion and passive films based on a semi-empirical correlation between optical band gap of oxides and composition of passive films grown on metal and alloys[103].

Starting from the Pauling's equation for the calculation of single-bond energies and heats of formation of inorganic compounds, based on the concept of electronegativity, different authors tried to overcome the difficulties in applying theoretical models based on very complex quantum mechanical calculations by proposing semiempirical models and correlations for the prediction of physico-chemical properties of inorganic compounds[106,107]. Starting from the correlations proposed by *Manca* and *Vijh*, based on the relationship between the standard heat of formation ($\Delta H_f^0{}_{eq}$) and the band gap of inorganic compounds, *Di Quarto et al.* proposed a semiempirical correlation between the optical band gap of crystalline oxides and the difference of electronegativity of their constituents (in

the Pauling's scale) in order overcome the limitations of previous models making PCS suitable for corrosion studies. In fact, by considering a polyatomic oxide molecule MO_y and taking into account Pauling's equation for the average bond energy $D_{A\text{-}B}$[104], the proposed correlation can be written as follow:

$$E_g = 2[E_I(\chi_M - \chi_o)^2 + \Xi] \qquad (3.11)$$

where, E_I is the extra-ionic energy unit orbitally dependent whose value change due to the different atomic coordination in different crystal structure. χ_M and χ_o are the electronegativities of metal and oxygen respectively and Ξ is defined as:

$$\Xi = \frac{1}{2y}[(D_{M-M} + yD_{O-O}) - R] \qquad (3.12)$$

where $D_{M\text{-}M}$ and $D_{O\text{-}O}$ are the bond energy of diatomic molecule in the gas phase, y is the stoichiometric coefficient and is R an energy parameter that take into account the lattice energy. By plotting the band gap values of different oxides as a function of $(\chi_M - \chi_O)^2$, the proposed correlation can be separated for sp- and d-metals according to the two different extrapolate interpolating lines displayed in Fig. 3-6:

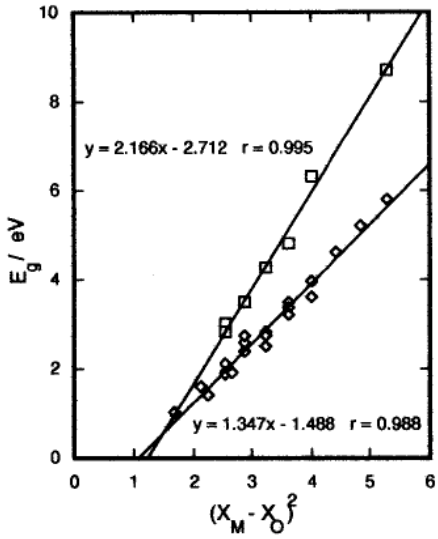

Fig. 3-6. Optical band gap values E_g vs the square of difference of Pauling's electronegativity of binary oxides: (□) sp-metal oxides and (◊) d-metal oxides[104].

$$E_g - 1.35(\chi_M - \chi_O)^2 - 1.49 \qquad \text{in eV}$$

$$E_g = 2.17(\chi_M - \chi_O)^2 - 2.71 \qquad \text{in eV}$$

Notably, Cr_2O_3, FeO, Fe_2O_3 are well interpolated as d-metal oxides.

Starting from the same assumptions, the proposed correlations was also extended to ternary oxides, oxyhydroxides and hydroxides (as well as hydrated oxides). In fact, by considering a generic oxyhydroxide ($MO_{(y-m)}OH_{2m}$), it is possible to define the average electronegativity of the anionic groups due to the knowledge of those of oxygen and hydroxyl groups. Generally, lower optical band gap values are measured for hydrate oxide or oxyhydroxide films[104].

The proposed correlation can also be extended to the mixed oxides, i.e. $A_aB_bO_o$, by the introduction of an average electronegativity parameter (χ_{av}) defined as the arithmetic mean between the electronegativities of the metal partners in the oxides (χ_A and χ_B), as reported below:

$$\chi_{av} = \frac{a\chi_A + b\chi_b}{a + b} \quad (3.13)$$

Therefore, the relationship for d metal oxides can be written as follow:

$$E_g - \Delta E_{am}\,(eV) = 1.35\,(\chi_{av} - \chi_O)^2 - 1.49 \quad (3.14)$$

where χ_O is oxygen electronegativity (3.5 in the Pauling scale). Generally, ΔE_{am} = 0 for crystalline oxides, whilst increasing values are expected if the lattice disorder affects density of states distribution both near the valence and conduction band edges[104,108,117,118,109–116]. Considering the system under investigation, according to the Pauling scale, χ_{Cr}^{3+} = 1.6 and χ_{Fe}^{3+} = 1.9[119], therefore knowing E_g it is possible to get χ_{av} and the a and b according to Eq. 3.13. Notably, according to Eq. 3.10 a band gap decreasing from 3.4 eV (reported in the literature for pure Cr_2O_3)[55,109] to 2.0 eV (reported in the literature for pure Fe_2O_3) is expected[115,122] by increasing the iron content into the passive films.

3.2 Electrochemical Impedance Spectroscopy and Differential Capacitance Measurements

It is well recognized that electronic properties of passive films play a fundamental role in the study of dissolution and breakdown phenomena as well as in the estimation of the rate of localized corrosion (i.e. pitting). For this reason, Electrochemical Impedance spectroscopy (EIS) and Differential Capacitance measurements are the most popular used tools for the study of semiconductor/electrolyte interfaces[123]. These techniques are based on the perturbation of the cell with an alternating signal of small amplitude (*stimulus*),

where a potential perturbation is typically used, and on the observation of the frequency response of the system under investigation, that can be considered pseudo-linear. Under this condition, the output response (i.e. current) will also be a signal containing the same frequencies of the stimulus. The main advantages of pseudo-steady state techniques are that they allow to perform high-precision long lasting measurements since the system may be indefinitely steady, the system response can be described by linearized current-potential characteristics and the measurements can be performed by spanning a wide range of frequencies. The amplitude of the alternating signal is fundamental for the preservation of the linearity of the system, thus linear model for the interpretation of the experimental results can also be used making kinetic and diffusion studies easier. The correct value of the signal amplitude depends on the system under investigation and it is derived by the optimization between both the minimization of noise in the impedance response (by using a large amplitude) and the minimization of the non-linear response of the system (by using a small amplitude)[124,125].

Electrochemical Impedance spectra are recorded at constant electrode potential by spanning the a.c. signal frequency. A purely sinusoidal voltage can be expresses as:

$$E = E_0 \sin(\omega t) \tag{3.15}$$

where ω is the angular frequency, which is 2π times the frequency in Hz. The voltage signal can also be thought as a rotating vector (or *phasor*) quantity whose length is the amplitude *E* and whose rotating frequency is ω[124]. The output signal will be a current response that usually is not in phase with the potential, thus the current is given by:

$$I = I_0 \sin(\omega t + \varphi) \tag{3.16}$$

where φ is the phase angle. The impedance is defined as a kind of generalized resistance as follow:

$$Z = \frac{E}{I} \tag{3.17}$$

The impedance response can be also described as having real and imaginary components, as follow:

$$Z = Z_{re} + jZ_j \tag{3.18}$$

When the input and output are in phase, the imaginary part of the impedance has a value of zero and the impedance will have only a real contribution, Z_{re}. If the input and the output are out of phase, the real part of the impedance has a value zero and the impedance has only imaginary contribution Z_j. The relationship between the complex impedance and the phase angle is shown more clearly in the use of phase diagrams, as reported below:

$$Z = |Z|\exp(j\varphi) \tag{3.19}$$

Where |Z| represents the magnitude of the impedance vector and φ is the phase angle[125]. However, critical issues in the interpretation of the EIS data consist on the determination of the most suitable equivalent circuit able to model the impedance results and on the physical meaning of the passive elements used for the equivalent circuit[100,123,126]. Basically, resistor, inductor and capacitor are the main passive components of an electrical circuit. The impedance of a resistor consists only of the real part, which is equal to the resistance of the resistor itself. When a voltage is applied across it, the current flowing through will be in phase with the applied potential. Capacitors are components that introduce capacitance into a circuit and thus are used for electrical energy storage in the form of electric field. The impedance of a capacitor consists only of the

imaginary part and it increases by decreasing both the capacitance and the frequency of the applied signal. The current will be shifted of -90 degrees with respect to the applied voltage. An inductor is a component that introduce an inductance into a circuit and it is used for electrical energy storage in the form of a magnetic field. The impedance of an inductor increases by increasing the frequency of the applied voltage and the current through it will be shifted of 90 degrees with respect to the applied voltage. When the assumption of a uniformly active electrode is not valid, a time-constant dispersion can be observed due to the variation along the electrode surface of reactivity or of current and potential, resulting in a 2-dimensional distribution. Time-constant dispersion can also be caused by a distribution of time constants reflecting a local property of the electrode, resulting in a 3-dimensional distribution. This variation can be modelled by a constant-phase-element (CPE), whose impedance can be expressed as follow:

$$Z_{\mathrm{CPE}} = \frac{1}{(j\omega)^{\alpha} Q} \qquad (3.20)$$

where ω is the frequency of the applied signal. Notably, the parameters α and Q are independent of frequency. When α is equal one, *Q* has units of a capacitance and represents the capacity of the interface. Conversely, when α differs from one, the system shows behavior that has been attributed to surface heterogeneity or to continuously distributed time constants for charge-transfer reactions[125].
The variation of the impedance with frequency can be displayed in different ways. In *Bode plo*t log |Z| and φ are plotted as a function of log ω, while when the imaginary component Z_j is displayed as a function of the real one Z_{re}, an alternative representation of impedance is provided namely *Nyquist plot*[125].

In Differential Capacitance measurements, the d.c. potential is spanned (for an n-type SC) from anodic polarization (according to the stability of the oxide film) down to a polarizing potential approaching the flat band potential, while the a.c.

signal frequency is kept constant during the measurement. Vice-versa for a p-type SC. In terms of equivalent electrical circuit, the oxide/electrolyte interface can be expressed by two capacitors in series:

$$\frac{1}{C_m} = \frac{1}{C_{SC}} + \frac{1}{C_H} \tag{3.21}$$

where C_H is the capacitance of the Helmholtz compact double layer and C_{SC} is the capacitance of the space charge region in the semiconductor. By assuming $1/C_H << 1/C_{SC}$, under the simplifying assumption reported below:

i. crystalline semiconductor electrode homogeneously doped under depletion regime;
ii. fully ionized single donor (or acceptor, for p-type SC) level;
iii. absence of deep lying donor (or acceptor) levels in the forbidden gap of the SC;
iv. negligible contribution of surface states and minority carriers to the measured capacitance;
v. absence of Faradic processes at the SC/El interface;
vi. width of space-charge layer much lower than the semiconductor thickness;

a simplified expression for the space charge capacitance, C_{SC}, is obtained, known as Mott-Schottky equation:

$$\left(\frac{1}{C_{SC}}\right)^2 = \left(\frac{2}{\varepsilon_{ox}\varepsilon_0 |e| N_D}\right)\left(\Delta\Phi_{SC} - \frac{kT}{|e|}\right) \tag{3.22}$$

where $\Delta\Phi_{SC}$ is the potential drop into the semiconductor and N_D is the density of ionized donors in the n-type SC. An equivalent expression can be also derived for a p-type SC with the minus sign in front of $\Delta\Phi_{SC}$ and N_A instead of N_D. The

extrapolation to zero of the first term in M-S equation provides the value of the intercept with voltage axis U_0 (namely flat band potential), whilst from the slope it is possible to derive the concentration of donor (or acceptor) in the SC. In spite the validity of the aforementioned equation was tested for several SC/El interfaces, in many cases a misuse has been made of such equation. A strong limitation in the application of classical M-S analysis to passive films come out from the strong frequency dependence usually observed in the differential capacitance values of the junction affecting considerably both the slope (N_D, N_A) and the flat band potential values[103]. Possible explanation of such a behavior is due to the presence of deep lying donor (or acceptor) level and/or the presence of surface states, usually encountered in the case of crystalline semiconductors and semiconducting passive films. In the case of thin passive film, the presence of a frequency dependent capacitance is intrinsic to the formation of a layer having an amorphous or strongly disordered nature. In fact, the electronic states lying into the gap do not follow instantaneously the imposed ac signal, but they need a finite response time. The latter depends on the energy position with respect to the Fermi level and it can be much longer than the period of the ac signal having angular frequency ω. This means that by changing ω at constant band bending the levels able to follow the signal change. On the other hand, by changing the band bending at constant ac frequency, deeper levels of depleted region lying below a critical level will not change the occupancy with ac signal[123]. For this reason, differential capacitance measurements are usually performed in a large range of frequencies in order to get reliable information on both the flat band potential and donor or acceptor concentration of passive films[103,123].

Unless otherwise stated, Electrochemical Impedance Spectroscopy and Differential Capacitance measurements were carried out in 0.1 M ABE solution (pH ~ 8) by using a Parstat 2263 (PAR), controlled by a computer via Electrochemistry PowerSuite software. A three-electrode arrangement was used,

consisting of the specimen, a Pt net having a very high specific area and a silver/silver chloride (Sat. KCl, U_0 = 0.197 V vs SHE) as a reference electrode. The impedance spectra were generated by applying a sinusoidal signal of amplitude 10 mV over the frequency range 0.1 Hz-100 kHz and were finally analysed with Zview software.

3.3 Inductively Coupled Plasma – Optical Emission Spectroscopy (ICP-OES)

ICP – OES is one of the most powerful and popular analytical tools used for the determination of trace elements in environmental, metallurgical, geological, petrochemical, pharmaceutical, materials and food safety applications[120].

The technique is based on the spontaneous emission of photons from atoms and ions produced thought the RF discharge. The emission of light can be explained considering the Bohr model according to the electrons travel around the nucleus in discrete orbitals characterized by discrete energy levels. When they are in the orbitals closest to the nucleus, they are in their *ground state*. Conversely, when energy is added to the electrons due the absorption of light or though collisions with other particles, the atom becomes *excited*. If excitation occurs, electrons are promoted from the ground state to further orbitals with higher energy. In this situation the atoms are not stable, and the electrons are prone to release the energy as electromagnetic radiation or photon, decaying back to their ground state. If the energy is high enough, the electron can be completely dissociated from the atom, leaving it positively charged. This process is known as *ionizatio*n, and the energy necessary for the ionization changes by changing the element under investigation. Excitation, ionization and emission processes are displayed below in Fig. 3-7.

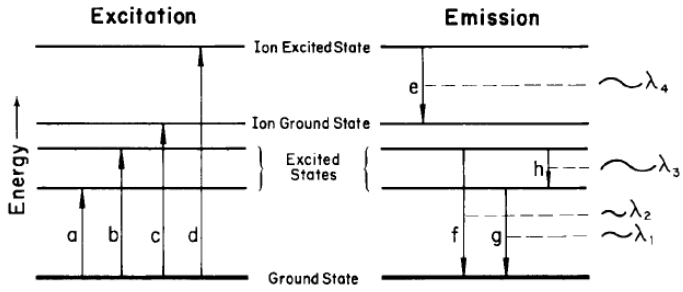

Fig. 3-7. Energy level diagram[127].

The energy difference between the upper and the lower energy levels represents the wavelength of the radiation involved in the transitions. Since every element is characterized by its own set of absorption or emission lines, the wavelength of the photons can be used for the elemental determination. Moreover, the intensity of the emitted light at specific wavelengths provides the concentrations of the elements under investigation[127]. According to the physical description of the processes described above, in OES high temperatures are necessary in order to promote not only the dissociation into atoms but also their excitation and ionization. For this reason, the inductively coupled plasma discharge (ICP) is used nowadays for OES.

The ICP system was first developed for optical emission spectroscopy (OES) by *Fassel et al.* at Iowa State University in the US and by *Greenfield et al*. at Albright & Wilson in the UK in the mid-1960. It was commercialized for the OES system in 1974 and now it represents the most widely employed source for the OES)[128]. In Fig. 3-8, a schematic representation of the torch is reported. The argon gas is injected trough the torch, which is a system consisting of three concentric tubes made of fused silica where the sample is carried though the inner tube.

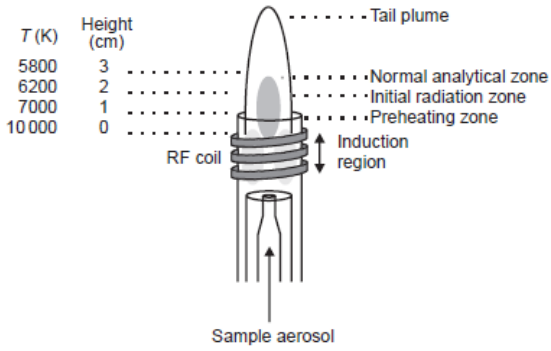

Fig. 3-8. Schematic representation of the ICP assembly where the torch with the three concentric tubes, the RF coil, the different plasma regions and the temperature gradient are displayed[128].

A copper coil, called **load coil**, envelops the top of the torch that is connected to a RF generator. By applying a RF power ranging from 700 to 1500 watts, an alternating current moves though the coil causing electric and magnetic fields on the top of the torch. When the outer argon flow (10 – 15 L min^{-1}) is injected though the torch a spark will be applied with consequent ionization of the gas. The electrons are further accelerated by the magnetic field and in turn will collide with other argon atoms sustaining the ICP discharge and the formation of the plasma (consisting of electrons and argon atoms and ions)[127].

Sample aerosol is carried by the inner argon flow (0.5-1.5 L min^{-1}) into the centre of the plasma through a pneumatic nebulizer (i.e. peristaltic pump), while the intermediate argon flow (0 – 1.5 L min^{-1}) is injected in order to lift the plasma and dilute the inner gas flow when organic solvents are injected[127]. As displayed in Fig. 3-9, by reaching the plasma, the sample is sequentially *desolvated*, *vaporized* and *atomized* though collisional excitations at high temperature with the formation of a cloud consisting of hot gases mainly based on free atoms and ions[127,128].

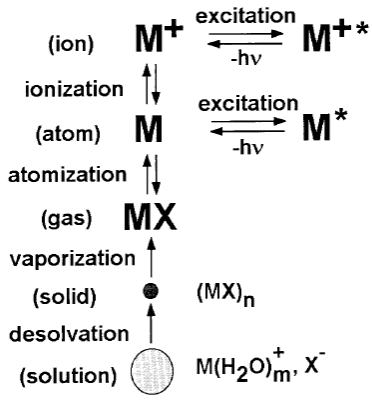

Fig. 3-9. Processes that take place when the sample is injected into the ICP discharge[127].

As also displayed in Fig. 3-9, these steps occur mainly in the preheating zone (PHZ) and in the initial radiation zone (IRZ). The normal analytical zone (NAZ) represents the part of the torch where the analytical emission is collected. The emission from the NAZ zone of the torch (see Fig. 3-9) can be detected by two different configurations. The *radial view* is the standard operating mode usually employed for ICP – OES system where the plasma works with a vertical configuration and the analysis is performed from the side of the plasma itself. Conversely, in the *axial view* the torch is horizontal and the NAZ zone is observed from the end of the plasma. Axial configuration is employed in order to improve the sensitivity of the signal[128].

The emitted photons are then collected by a lens or a concave mirror. Since the excited species emit light at different wavelengths, the emission from the plasma will be polychromatic. A monochromator allows the separation into different wavelengths and the light measurement at one wavelength at a time. Finally, the signal coming from the monochromator is converted by a photodectector in an electrical signal that is further displayed by a computer software. A representation of the layout of a typical ICP – OES instrument is reported in Fig. 3-10.

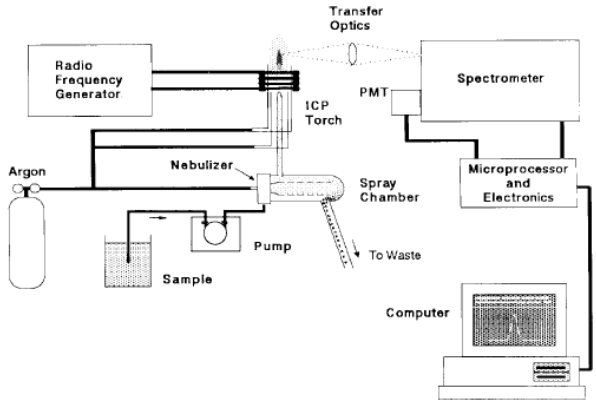

Fig. 3-10. Schematic representation of the layout of ICP – OES equipment[127].

The main advantage related to OES technique is strictly related to the excitation properties of the high temperature source since a large number of different energy levels for several elements can be detected. It is also possible to choose from different emission wavelengths for each element and the emitted lines from several elements can be detected simultaneously for up to 70 elements. Moreover, it is a system able to reproduce vaporization, atomization, excitation and ionization steps for a wide range of elements in different sample matrices[128]. Solid samples can also be detected in spite they need extraction or digestion with acidic media in order to have the analytes in a liquid solution. Conversely, by increasing the number of emission wavelengths, the probability that interference phenomena can occur will increase due to the overlapping of the emitted lines that cannot be measured separately.

In this Ph.D. work, the estimation of the heavy metal ions released by different SS grades by immersion in mimicking solutions was carried out by PerkinElmer Optima 2100 DV ICP-OES. Before analysis, a calibration line was recorded for each metal by using properly standard solutions.

3.4 X-ray Photoemission Spectroscopy (XPS)

X – ray Photoelectron Spectroscopy (XPS) was developed in the mid-1960s by the Nobel Prize in Physics *Kai Siegbahn*, at the university of Uppsala, Sweden. According to the development of commercial manufacturing of surface analysis equipment, XPS starts to be employed in laboratories in the early 1970s[129].

XPS, also known as ESCA (Electron Spectroscopy for Chemical Analysis), is a surface technique that provides direct information on the electronic structure of matter, without restrictions on the type of sample. XPS works by irradiation of the samples by monoenergetic soft X – ray (200 – 2000 eV) causing electrons to be ejected from the **core levels**, according to the photoelectron effect where incident photons with energy *hv* knock out photoelectrons from atoms[129–132]. The analysis of the emitted electrons is carried out due to the knowledge of their kinetic energy given by:

$$E_k = h\nu - BE - \Phi_s \qquad (3.23)$$

where hν is the energy of the photon, BE is the binding energy of the atomic orbital from which the electrons are kicked out and Φ_s is the spectrometer work function, as displayed in Fig. 3-11.

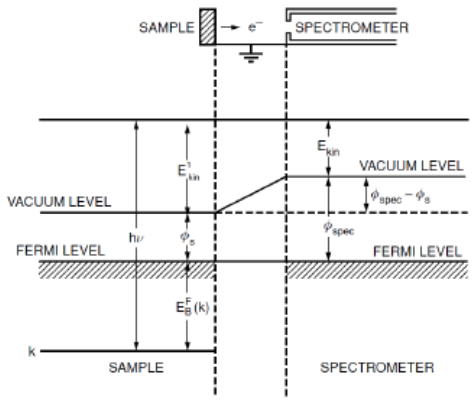

Fig. 3-11. Schematic representation of the photoemission[131].

According to Eq. 3.23, by the knowledge of the photon energy (*hv*), it is possible to estimate the binding energy for all core level electrons with BE < hν - Φ_s.

As a consequence of the photoelectric process, Auger electrons can be also emitted due to the relaxation of the excited electrons. Auger emission is the result of a three – electron process, where, after the core electron emission, an outer electron decays in the inner orbital vacancy and the exceeding energy allows a second electron (namely Auger electron) to be emitted from the outer core levels, as displayed in Fig. 3-12. The Auger region in the XPS spectrum allows to gained useful information on sample composition.

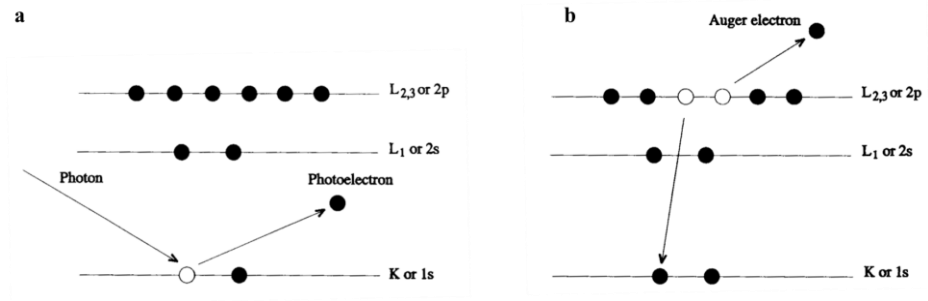

Fig. 3-12. Photoelectron emitted due to incident photons in a) XPS emission process and b) in the relaxation process with the consequent Auger electron emission[129].

Fig. 3-13 displays the schematic representation of the experimental set-up employed for XPS measurements. The sample is introduced in a chamber under ultra – high vacuum (UHV) consisting of a turbo molecular pump where a final pressure lower than 10^{-9} mbar is achieved. The UHV condition is necessary in order to avoid contamination of adsorbed gas on the solid surface that can affect the XPS signal, minimize the photoelectron scattering and maximize the main free path, allowing electrons to be injected in the spectrometer analyser with the same kinetic energy.

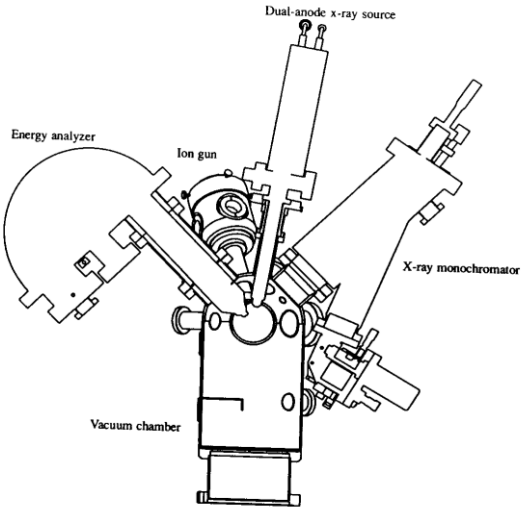

Fig. 3-13. Representation of the UHV chamber coupled with the photoemission equipment[129].

The X-ray source consists of a cathodic filament which emits thermal electrons through heating due to an emission current of about 30 mA. Electrons are then accelerated toward an anode by applying a high voltage ranging from 9 to 12 keV. The energy of the X-ray beam strongly depends on the anode material used as X-ray source: Mg Kα (1253.6 eV) and Al Kα (1486.6 eV) are usually employed to knock out electrons from atoms, molecules or solid[129–131] and the diameter of the X-ray beam usually ranges from 5 mm to 1 – 5 μm. Nevertheless, XPS for condensed matter is a very surface sensitive technique. In fact, only photoelectrons coming from a thin surface layer (in order of tens of angstroms) can escape from the sample without energy loss although the penetration depth of the incident photons is in the order of micrometers (depending on the wavelength of the incident X-ray beam and on the sample material). An important parameter for the description of the surface sensitivity is the **mean escape depth (λ)**, defined as the mean free path of a photoelectron in a solid, that is a function of E_k and of the photons beam incident angle[131]. Optimal

surface sensitivity is obtained for electron kinetic energy ranging from 25 to 200 eV. The scattered photoelectrons only contribute to the background[130].

Photoelectrons are finally collected and measured by an **electron analyser** where the intensity of the photoemitted electrons is measured. The "survey" X-ray photoelectron spectrum will display a series of signals related to all the electrons with binding energy lower than *hv*, overlapped to a background signal. The identification of the elements in the sample is performed directly from the estimation of the kinetic energy of the ejected photoelectrons. Moreover, since every element have a unique set of bind energy, it is possible to get more insight into the chemical state and composition of the sample under investigation through the chemical shifts arising from the difference between the chemical potential and the polarizability of compounds. The relative concentrations of elements are determined through the photoelectron intensities by to the knowledge of the peak area[129].

All the elements, with the exception of hydrogen and helium, and a wide range of materials (including no conducting samples) can be analysed through XPS (i.e. polymer, ceramics, plastics and metals) as long as they are stable in vacuum environment. Depth profiling can also be coupled with ion etching (sputtering) and oxide thickness measurements can also be carried out. In addition, the incident photon beam is less destructive if compared with other techniques where electrons are used to bombard samples, especially when organic materials are investigated. Conversely, samples that decompose under X-ray irradiation cannot be studied. Nevertheless, it is largely used in biomedical and biotechnology, semiconductor, pharmaceutical, electronic and solar photovoltaics applications[133].

The experimental set-up employed for XPS analysis reported in my Ph.D. work consists of a Physical Electronics 5600 spectrometer (PHI 5600 XPS device) with a monochromated Al Kα radiation (1486.6 eV, 300 W). A take-off angle of the emitted photoelectrons of 45° relative to the surface has been set and

charging of the sample was corrected by using the C1s signal. Background subtraction and data evaluation were done by the MultiPak-Software (MultiPakV6.1A, 99 June 16, copyright Physical Electronics Inc., 1994–1999).

4 Passive Films Growth on Chromium, Carbon Steel and Different Stainless Steel Grades

The study of corrosion resistance of SS is not straightforward due to their heterogeneous composition. In fact, SSs are iron based alloy containing a large amount of Cr and other elements (Ni, Mo, N, Mn, etc.) able to enhance their mechanical and corrosion resistance. According to the literature, corrosion resistance of austenitic and duplex SS strongly depends on the formation of a few nanometres thick passive layer mainly consisting of chromium oxide whose composition, structure, thickness and electronic properties could affect their corrosion resistance[55,117,134–137]. For this reason, a lot of published research works are focused on the study of passive films properties grown on pure chromium[138,139,148,140–147] in order to get more insight into electronic properties, and therefore corrosion resistance, of SSs. Nevertheless, there is no general agreement on growth mechanism and on semiconductive (n or p) or insulating nature of chromium oxide that some authors try to explain according to the Mott and Schottky model even if the hypothesis underlying the theory are not satisfied.

For this reasons, this part of my Ph.D. thesis is focused on the study of corrosion resistance and electronic properties of passive films grown on pure sputtered chromium under potentiostatic polarization in acidic (pH ~ 2) and alkaline (pH ~ 13) aqueous solution.

4.1 Passive film grown on pure sputtered chromium

Polarization curves were first recorded in acidic and alkaline solutions by sweeping the potential at 2 mV s^{-1} in the anodic direction from the equilibrium potential related to the H_2 evolution reaction at the corresponding pH. According to Fig. 4-1a, a wide passive range ending at ~ 0.8 V vs Ag/AgCl is evident in acidic solution according to the onset of oxidation reaction of Cr^{3+} to chromate ions. Moreover, a low passivity current of ~ 120 nA cm^{-2} was registered in agreement with the formation of a compact and stable passive film in spite the thermodynamic predictions. On the other hand, in alkaline solution, a narrower passivity region and a passivity current increasing by increasing the polarizing potential were displayed (see Fig. 4-1b).

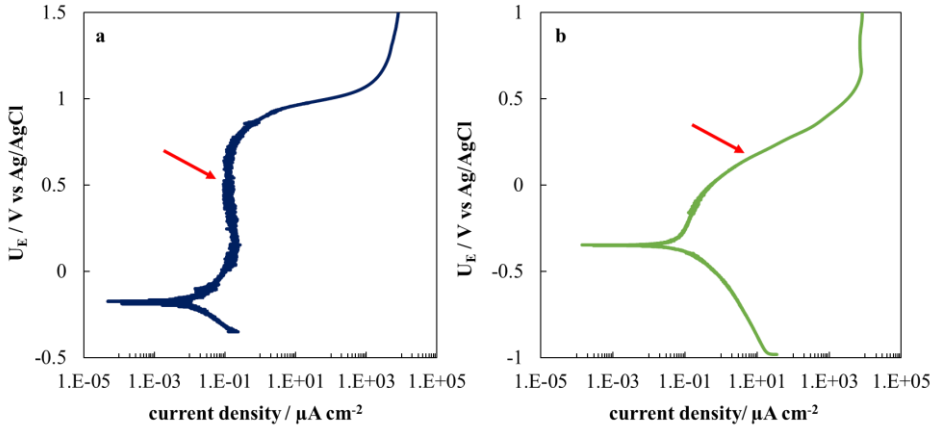

Fig. 4-1. Polarization curves for pure sputtered Cr recorded recorded at 2 mVs^{-1} in a) 5 mM H_2SO_4 solution (pH ~ 2) and b) 0.1 M NaOH solution (pH ~ 13).

According to the polarization curves (see the arrows in Fig. 4-1a and Fig. 4-1b), pure sputtered chromium was passivated under potentiostatic polarization at 0.5 V vs Ag/AgCl in H_2SO_4 solution and at 0.1 V vs Ag/AgCl in NaOH solution in order to get more insight into growth mechanism of passive films. As reported in Fig. 4-2a, the recorded current density monotonically decreases until stationary

condition is reached after ~ 10 h of polarization, while the current density in the case of passivation in alkaline solution does not reach a stationary value even after 15 h of polarization (see Fig. 4-2b).

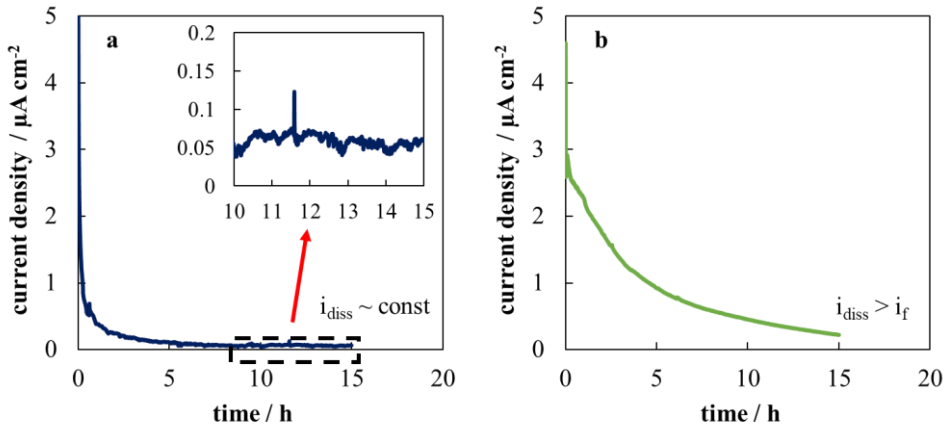

Fig. 4-2. Current density vs time curves under anodic polarization at c) U_E = 0.5 V vs Ag/AgCl in 5 mM H_2SO_4 solution (pH ~ 2) and d) U_E = 0.1 V vs Ag/AgCl in NaOH solution (pH ~ 13).

4.1.1 *Differential Capacitance and Impedance Measurements*

The measured capacitance, C_M, vs. the electrode potential curves recorded in phosphate buffer solution (pH ~ 7) at three different frequencies of the a.c. signal for passive films grown on pure sputtered Cr in both acidic and alkaline solutions, were reported in Fig. 4-3. According to the experimental results, C_M strongly depends on potential and frequency, suggesting the presence of energy levels within the band gap. This means that the use of the Mott-Schottky model as a tool for the studying of electronic properties of chromium oxide is not suitable. Moreover, the differential capacitance recorded for passive films grown in alkaline solution is not monotonic. Such behavior occurs when Fermi level pinning lead an n-type surface inversion layer on p-type films or vice versa, thus it is not possible to definitely discriminate between the formation of a n-type or p-type passive film[149] by the knowledge of C_M.

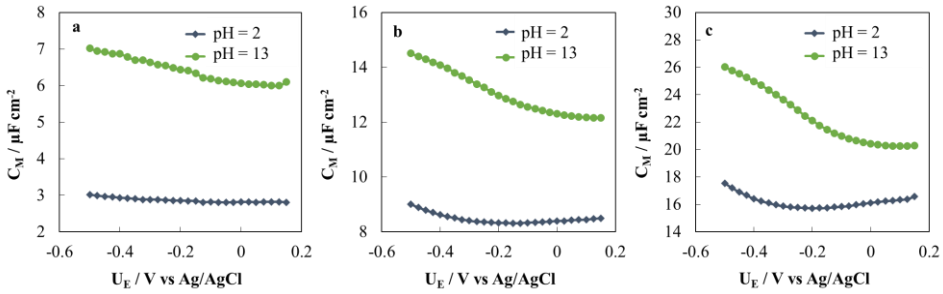

Fig. 4-3. Measured series capacitance (C_M) vs. potential curves recorded in phosphate buffer solution (pH ~ 7) for passive films grown on Cr under anodic polarization in acidic (pH ~ 2) and alkaline (pH ~ 13) solution at a) 10 kHz, b) 1 kHz and c) 100 Hz.

4.1.2 *Photoelectrochemical Measurements*

Photocurrent spectrum recorded at the open circuit potential (U_{OC} ~ 0.2 V vs SSC) in 1 mM $FeSO_4$, related to passive film grown on pure chromium at pH 2 after anodic polarization at 0.5 V vs SSC is reported. $FeSO_4$ was used in order to provide a kinetically easier photo-oxidation process (Fe^{2+} / Fe^{3+}) and therefore enhance the photocurrent to current ratio since passive films grown on Cr are poorly photoactive. According to Eq. 3.10, a band gap of ~ 3.4 eV was estimated, according to the value reported in the literature for Cr_2O_3[55,117]. Notably, a red shift in the light absorption threshold is evident even using a 400 nm cut off filter corresponding to an indirect optical transition at 2.40 eV (see Fig. 4-4b) that is in agreement with the formation of $Cr(OH)_3$.

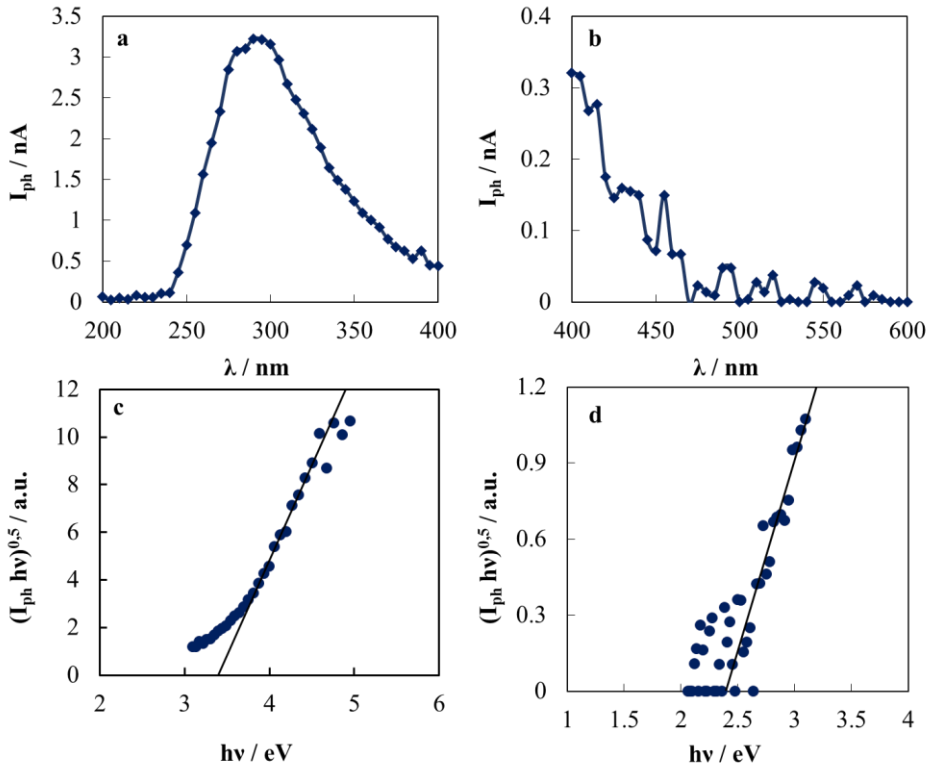

Fig. 4-4. Raw photocurrent spectra for passive film grown on Cr after anodic polarization in 5 mM H_2SO_4 solution (pH ~ 2) recorded 1mM $FeSO_4$ at U_E = 0.2V vs Ag/AgCl a) without and b) with a cut off filter (λ > 400nm). c) and d). $(Q_{ph}\ h\nu)^{0.5}$ vs hν plots.

According to the experimental results, passive film grown on pure chromium in acidic solution (pH ~ 2) has a bilayered structure with an inner layer consisting of chromium oxide and an outer layer based on chromium hydroxide, in agreement with[141], where the authors confirm this structure on the basis of XPS results. Conversely, as displayed in Fig. 4-5, only one optical transition was revealed for passive film grown in 0.1 M NaOH solution corresponding to the formation of $Cr(OH)_3$ (i.e. 2.4 eV) according to the Pourbaix diagram where chromium hydroxide is thermodynamically stable at pH ~ 13[150].

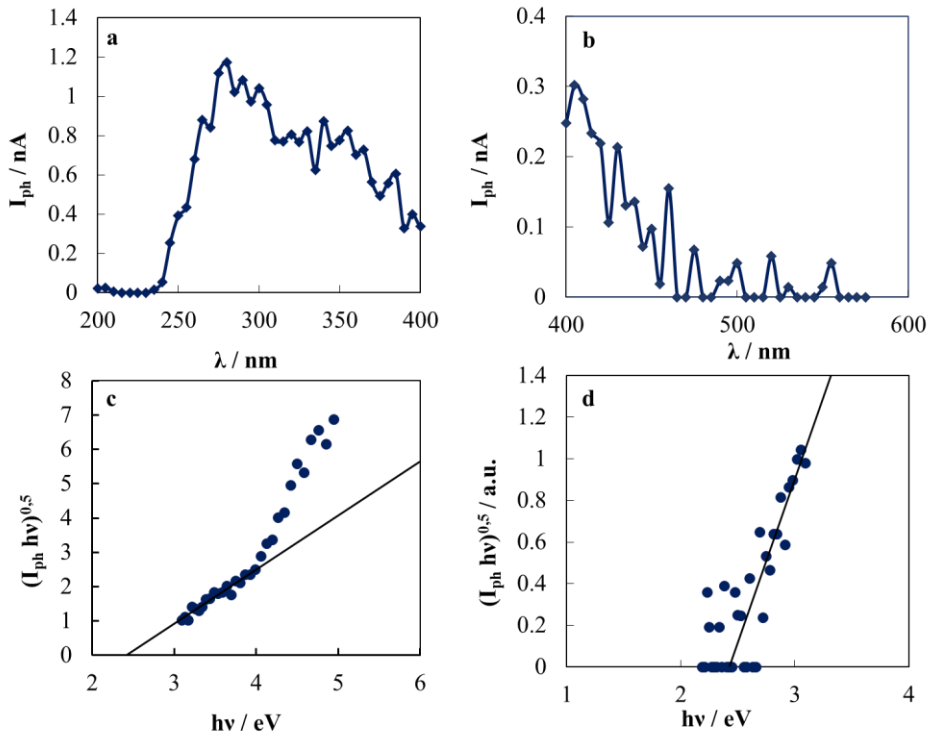

Fig. 4-5. Raw photocurrent spectra for passive film grown on Cr after anodic polarization in 0.1 M NaOH solution (pH ~ 13) recorded 1mM $FeSO_4$ at U_E = 0.2V vs Ag/AgCl a) without and b) with a cut off filter (λ > 400 nm) c) and d) $(Q_{ph}\ h\nu)^{0.5}$ vs hν plots.

Finally, in order to check the real sign of the photocurrent, current vs. time curves were recorded by manually chopping sample irradiation under monochromatic light at λ = 280 nm. According to the current transients reported in Fig. 4-6, recorded photocurrent is cathodic for both passive films grown in acidic and alkaline solutions, suggesting that the passive films are insulator or a p-type semiconductor with a flat band potential more anodic than 0.2 V vs Ag/AgCl. This experimental finding suggests that passive films grown on pure chromium are poorly resistant toward anodic dissolution and therefore toward corrosion phenomena since the energy distance between the Fermi level and the valence band edge is very low.

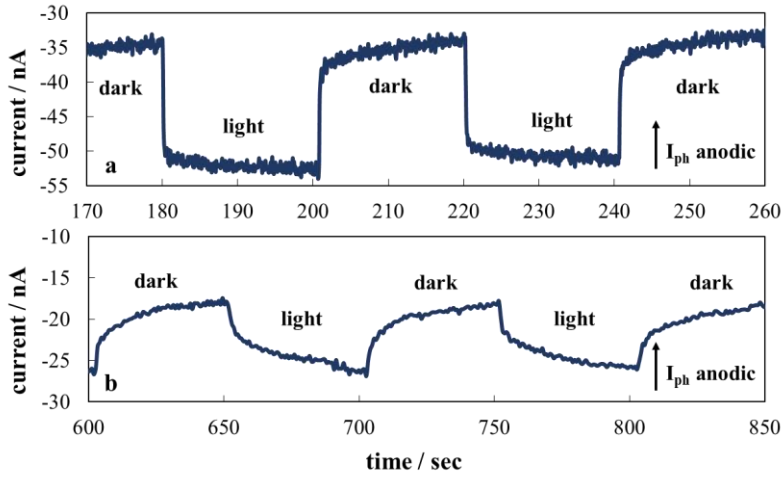

Fig. 4-6. Current vs time curves recorded at U_E = 0.2 V vs Ag/AgCl in 1 mM $FeSO_4$ at λ = 280 nm for passive film on Cr after passivation under anodic polarization in a) 5 mM H_2SO_4 solution (pH ~ 2) and b) 0.1 M NaOH solution (pH ~ 13).

4.1.3 *Growth Mechanism*

As mentioned in the introduction of this section, passive film formation on chromium has been extensively discussed in a large number of published papers. In fact, passivity of metals is a critical issue when corrosion resistance is studied and therefore, understanding growth kinetic mechanism require the detailed knowledge of the involved interfacial reactions and transport mechanisms. Phenomena typically established when metal passivation occurs are the *growth of the oxide layer*, the *dissolution of the oxide film* and the *precipitation of dissolving species from the solution*. Oxide film growth is generally due to solid-state diffusion on metals and some authors try to explain passivation of Cr through the *High Field Mechanism* (HFM)[138,140] while other researchers use the *Point Defect Model* (PDM)[151,152], where the first is generally used for thermally air grown passive films while the latter is employed when oxide layers are grown electrochemically. When passivation occurs, the driving force (i.e. the applied potential V through the metal/oxide/solution interfaces) is divide into

three parts: the potential drop at the metal/oxide interface ($\Phi_{m/f}$) that controls the internal reactions at the metal/oxide interface, the potential drop in the oxide film (Φ_f) that control the transport mechanism through the oxide itself and the potential drop at the film/solution interface ($\Phi_{f/s}$) that regulate the reaction across the layer, as reported below in Fig. 4-7:

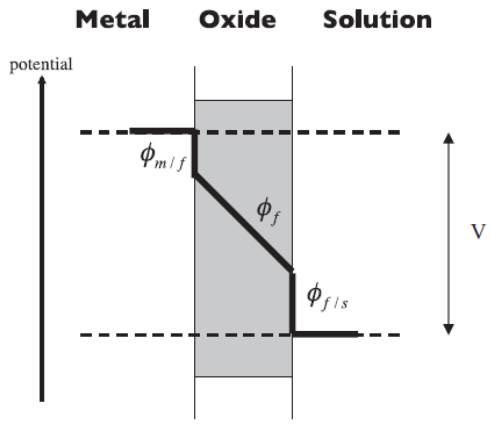

Fig. 4-7. Schematic representation of the potential drops in the metal/oxide/electrolyte interfaces[153].

The thickening of the corresponding oxide will be a combination of transport and reaction through the described interfaces and the modelling of the oxide growth will depend on the physical hypothesis underlying the aforementioned models. More in detail, the HFM is based on the assumption that the growth mechanism is due to migration of interstitial cations where the activation energy of the rate-limiting step is reduced by the electric field which in turn depends on the thickness layer. Conversely, in the PDF model it is believed that oxide thickening is due to the transport of anionic vacancies across the oxide layer, where the electric filed is assumed constant (i.e. thinning of the oxide layer due to dissolution phenomena is not considered)[153].

According to the experimental results reported below, the growth mechanism of pure sputtered chromium in both acidic (pH ~ 2) and alkaline (pH ~ 13) environments was studied. As reported in Fig. 4-2 where current vs. time curves are showed, the measured current density could be considered the sum of the current related to the growth process (i_f) and the current dissolution (i_{diss}) of passive film during the potentiostatic polarization, when the capacitance charging current could be neglected[55]. According to the experimental results, the high field mechanism was proposed to explain the dependence of the current on time during the anodic polarization, based on *Strehblow* and *Moffat* considerations[138,140]. The proposed model stated that the formation current depends on potential according to the equation reported below:

$$i_f = A \exp \beta X = A\ exp \frac{\beta \Delta \varphi_{film}}{d} \qquad (4.1)$$

where A is a temperature dependent constant, β is the field strength coefficient, X the electric field strength across the growing oxide film, $\Delta\varphi_{film}$ the potential drop inside the passive layer and d its thickness. Basically, the potential different across the metal/passive film/electrolyte interfaces ΔV consists of $\Delta\varphi_{film}$ that is the potential drop in the chromium oxide layer and the $\Delta\varphi_H$ that represents the potential drop across the passive film/electrolyte interface and that represent the key factor in the estimation of the dissolution current related to the oxidation of Cr^{3+} to soluble higher oxidation state species that, according to ref.[140], could be written as follow:

$$i_d = i_d^0 \exp \frac{\alpha n F \Delta \varphi_H}{RT} \qquad (4.2)$$

where i_d^0 is the exchange current density for the dissolution process, α is the transfer coefficient and n the number of electrons. By assuming the constancy of

the displacement vector at the passive film/electrolyte interface, it is possible to assume:

$$\Delta\varphi_H = \Delta V\left(1+\frac{d\varepsilon_{dl}}{\delta\varepsilon_{film}}\right)^{-1} = \frac{\Delta V}{\left(1+\frac{C_{dl}}{C_{film}}\right)} \qquad (4.3)$$

where ε_{dl} is the dielectric constant of oriented water in the Helmholtz double layer and δ its thickness. Eq. 4.3 described the dependence of $\Delta\varphi_H$ from the passive film capacitance. Notably if the film capacitance changes significantly, the potential drop inside the double layer could not be considered constant.

Moreover, according to the differential capacitance measurements (see Fig. 4-3) recorded in phosphate buffer solution (pH ~ 7) where, according to the Pourbaix diagram chromium oxide is stable[150] and in the exploited potential range where no charge transfer reactions occur, C_M could be expressed as the series of the film (C_{film}) and the double layer capacitance (C_H), as below:

$$\frac{1}{C_M} = \frac{1}{C_{film}} + \frac{1}{C_H} \qquad (4.4)$$

By considering a parallel plate capacitor model for the film capacitance, its thickness can be estimated as follow:

$$C_{film} = \frac{\varepsilon\varepsilon_0}{d} \qquad (4.5)$$

with ε_0 is the vacuum permittivity and ε is the passive film permittivity. Notably the estimation of d is allowed at high frequencies and high band bending where C_M could be considered not affected by the states inside the gap and thus the space charge region coincides with the oxide thickness[100].

By the knowledge of the film capacitance, it is possible to estimate the potential drop inside the passive film according to Eq. 4.3 and the film thickness

according to Eq. 4.4 and 4.5 where a dielectric constant of 12 was used for passive film grown in acidic solution considering that Cr_2O_3 is formed (according to its band gap value) while a dielectric constant of 25 was employed for passive film grown in alkaline solution considering that $Cr(OH)_3$ is formed (according to its band gap value)[140]. C_H value of 35 μF cm^{-2} was assumed according to ref.[140] while ΔV in Eq. 4.3 is defined as the difference between the applied potential (E_{appl}) and the equilibrium potential (E_{eq})[150]. Finally, the electric field strengths were estimated whose values, listed in Table 4-1, are in agreement with those reported in the literature[138,140,154,155].

During anodic polarization at 0.5 V vs SSC in acidic solution a steady state condition is reached after 10 h, where the equilibrium between the formation and the dissolution current is established, $i_f = i_d$ = 50 nA cm^{-2}. Substituting in Eq. 4.1 the electric field strength, previously estimated, and $\beta = 7.19 \cdot 10^{-7}$ cm V^{-1}, a pre-exponential factor $A = 2.8 \cdot 10^{-9}$ A cm^{-2} is obtained in agreement to the values reported in the literature[138,140]. Finally, substituting the dissolution current in Eq. 4.2, an exchange current density i_d^0 of 11 nA cm^{-2} is estimated, quite similar to the value reported by *Strehblow*[138]. Thus, the experimental results are in good agreement with the hypothesis of the high field mechanism.

Table 4-1. Kinetic parameters for growth mechanism of pure Chromium in 5 mM H_2SO_4 (pH ~ 2) and 0.1 M NaOH (pH ~ 13) solutions.

Solution	**E_g** **eV**	**ε**	**d_{ox}** **nm**	**$\Delta\phi_H$** **mV**	**X** **MV cm^{-1}**	**i_{diss}** **A cm^{-2}**	**i_{0diss}** **A cm^{-2}**
H_2SO_4 (pH 2)	3.40	12	3.5	0.11	3.99	$50 \cdot 10^{-9}$	$50 \cdot 10^{-9}$
NaOH (pH 13)	2.40	25	3.0	0.30	4.74	/	/

4.1.4 *Concluding Remarks*

Potentiostatic polarization of pure chromium in acidic (pH ~ 2) and alkaline (pH ~ 13) solutions induces the formation of thin passive films behaving as p-type semiconductor or insulator material. The growth kinetic follows a high filed mechanism with an efficiency < 1 due to the onset of dissolution phenomena. According to PCS measurements, 3.4 eV was estimated that is the value reported for Cr_2O_3 and a photocurrent tail at low photon energy corresponding to 2.4 eV was recorded, related to the formation of $Cr(OH)_3$. This experimental finding suggests that a bilayered structure is formed on Cr after passivation at pH ~ 2, with an inner layer of Cr_2O_3 an outer layer of $Cr(OH)_3$ whose thickness depends on the hydration degree. Conversely, only ~ 2.4 eV was recorded after passivation of pure chromium in alkaline solution, suggesting that only $Cr(OH)_3$ is formed. According to current vs time measurements, cathodic photocurrent was measured for both samples at polarizing voltage very close to that used for potentiostatic passivation, suggesting that Fermi level is very near to the VB edge, making them poorly stable towards anodic dissolution phenomena.

4.2 Passive Films grown on Carbon Steel

Nowadays Weathering Steel are considered a good compromise between Carbon Steel, in terms of their higher corrosion resistance, and Stainless Steel, in terms of their lower price due to the presence of a very little amount of particles as Cu, Cr, P and Ni that account for less than three percent weight but that positively affect corrosion processes. They are also commercially known as CorTen from the union of corrosion resistance and mechanical strength, allowing builders to reduce materials thicknesses. It is widely reported in the literature that their corrosion behaviour is related to their ability to passivate themselves with the formation of an adherent and thick passive film consisting on a distribution of iron oxyhydroxides such as Lepidocrocite (γ-FeOOH), Akaganeite (β-FeOOH), Goethite (α-FeOOH), Magnetite (Fe_3O_4), and other products resulting from corrosion processes. Thanks to the formation of this passivation layer, their use allows a reduction in terms of maintenance costs during the years, due to the possibility to avoid the use of protective paints or galvanizing processes, and so an increase of exercise life. Rust film formation lead also to combine functionality with aesthetics thanks to the different colours that they can take depending on growth conditions. Indeed, they are widely used in buildings, as guardrails, bridges, transmission tower and lighting poles, or in decorative contexts as ornamental sculptures, facades, roofs and so on[156–158], but the most important application of WS is in aggressive and coastal atmosphere due to their higher corrosion resistance.

Growth mechanism of passive films on WS and their effect on corrosion resistance are still not completely understood. It is also widespread opinion that solar light can positively affect corrosion processes improving growth kinetics and leading to the formation of a very thick rust film able to protect substrate against aggressive agents[159–163]. Many authors suggest that this effect is due to the presence of semiconducting phases inside passive film that can exhibit photovoltaic effects with the formation of photo-generated electron-hole pairs

with reducing and oxidizing capacity, respectively. *Song et al.*[159] reported studies about the role of the photovoltaic effect of Lepidocrocite and Akaganeite on the corrosion of WS under visible light affirming that they have an n-type SC behaviour bur reporting a counterintuitive positive photo-potential[164].

In the present work, growth mechanism and corrosion resistance of passive films grown after potentiostatic polarization in quasi neutral aqueous solution and after different exposure time in atmosphere were studied in the attempt to gain more insight into the corrosion resistance of low alloy steel. In order to have a reference and to make a comparison with atmospheric films in terms of their electrical and corrosion properties, in the first part of this work a physico-chemical characterization of passive film prepared in laboratory thought an electrochemical process by imposing a constant polarizing potential is reported. As it has seen during the experimental experience, rust film growth is strictly related to atmospheric conditions such as humidity, temperature, daily wet-dry cycles that can obviously change as seasonal change, so it becomes almost impossible to reproduce the same experimental conditions when a comparison between physical-chemical properties of specimens grown after the same exposure time is carried out. Since the best approach to study corrosion process consists on considering the substrate degree of rusting and not time exposure in atmosphere as the real variable to take into account, the second part of this work is focused on the study of electrical and solid state properties of several WS specimens characterized by different degree of rusting based on corrosion products. In addition, in order to clarify the role of light (if any) during growth process and to verify if it can positively affect growth kinetics, photo-electrochemical investigation on specimens characterized by different degree of rusting was also carried out. Polarization curves were recorded in order to estimate rust film polarization resistance and to verify its corrosion behaviour by simulating coastal atmosphere using chloride containing solution. Finally, all the experimental findings were used to suggest a growth mechanism.

Notably, due to their lower corrosion resistance than that of both austenitic and duplex SSs, all the measurements were carried out by employing Hg/HgO as reference electrode in order to avoid the presence of chlorides and thus the onset of pitting.

4.2.1 *Passive film growth*

WS coupons (0.07 wt.% C, 0.51 wt.% Si, 0.45 wt.% Mn, 0.098 wt.% P, 0.007 wt.% S, 0.033 wt.% Al, 0.29 wt.% Cu, 0.8 wt.% Cr, 0.17 wt.% Ni, Fe balance) were mechanically treated as already described in section 3.1. According to Fe Pourbaix diagram[150], anodic films were grown in Borate Buffer (0.42 M H_3BO_3 and 0.08 M $Na_2B_4O_7$, pH ~ 8) aqueous solution by potentiostatic polarization at 0.6 V vs Hg/HgO for 30 minutes. As reported in Fig. 4-8a, the current density recorded at 0.6 V vs Hg/HgO monotonically decreases towards an almost stationary value where growth current is balanced by dissolution current, according to the high field growth mechanism[55].

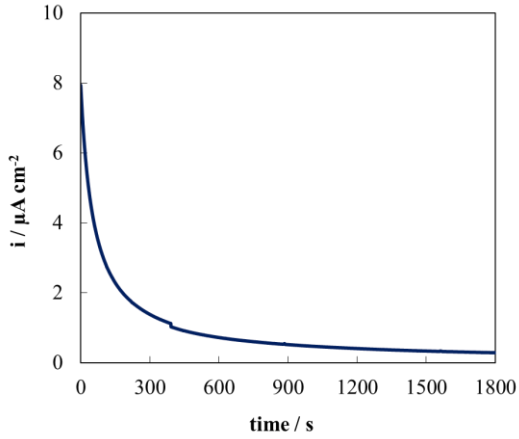

Fig. 4-8. Current density vs time curve recorded in Borate Buffer aqueous solution (pH ~ 8) for 30 minutes at U_E = 0.6 V vs Hg/HgO.

In Fig. 4-9 photocurrent spectrum recorded at 0.4 V vs Hg/HgO (i.e. below the formation potential in order to limit passive film modification) in Borate Buffer

(pH ~ 8) for passive films grown on WS after potentiostatic polarization at 0.6 V is reported. According to Fig. 4-9b, a photocurrent tail is also recorded at low photon energy by using a cut off filter for λ > 400 nm, corresponding to an indirect optical transition of ~ 2 eV (see Fig. 4-9c) very close to the band gap reported for α-Fe_2O_3 (see Table 4-2)[115]. This experimental finding suggests that potentiostatic polarization of WS allows the formation of passive films mainly consisting of hematite. Current vs time transients were also performed by manually chopping samples irradiation under monochromatic light. The recorded photocurrent at 0.4 V vs Hg/HgO under λ = 320 nm was anodic as expected for n-type semiconductor (see Fig. 4-9d).

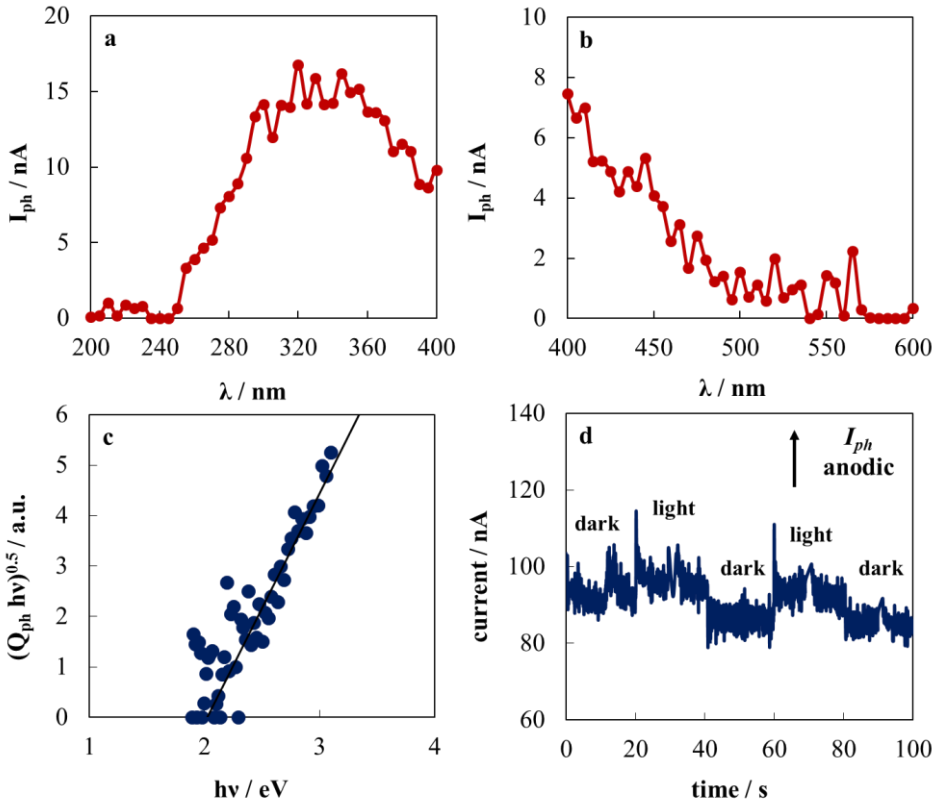

Fig. 4-9. Raw photocurrent spectrum recorded in Borate Buffer solution (pH 8) at U_E = 0.4 V vs Hg/HgO for passive film grown in Borate Buffer at 0.6 V vs Hg/HgO for 30 minutes for a) 200 nm < λ < 400 nm and b) λ > 400 nm. c) $(Q_{ph}\ h\nu)^{0.5}$ vs hν plot. d) Current vs time curve recorded at U_E = 0.4 V vs Hg/HgO in Borate Buffer solution at λ = 320 nm.

Table 4-2. Band gap value for passive film grown at 0.6 V vs Hg/HgO in Borate Buffer solution.

Passivation conditions	**E_g / eV**
0.6 V vs Hg/HgO	2.03

Differential capacitance measurements at three different frequencies of the a.c. signal recorded in Borate Buffer for passive film grown at 0.6 V vs Hg/HgO are reported in Fig. 4-10a. C_M was recorded starting from a potential lower than the passivation potential (in order to not modify samples), down to a polarizing voltage higher than the equilibrium potential for the hydrogen evolution reaction. It is important to note that C_M values strongly depend on frequency and polarizing potential as usual for a semiconductor, and that, for all frequencies, the measured capacitance is constant until ~ 0.1 V vs Hg/HgO and increases when the polarizing voltage decreases, confirming the formation of n-type SC passive film.

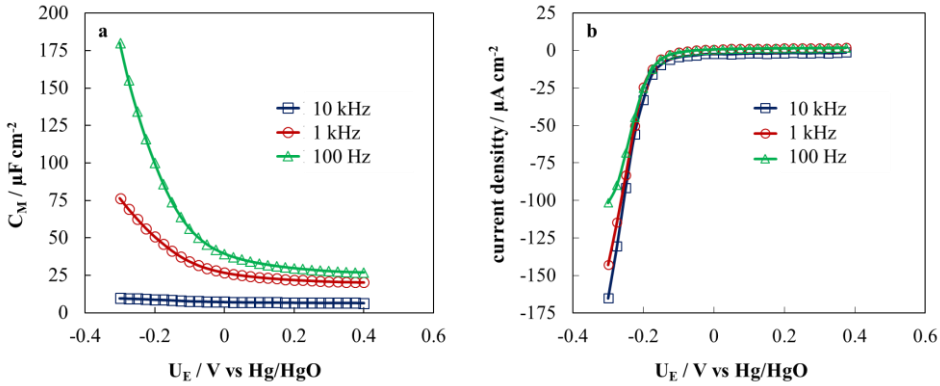

Fig. 4-10. a) Differential capacitance and b) current density vs potential curves recorded in Borate Buffer solution (pH 8) at 10 kHz, 1 kHz and 100 Hz for passive films grown under potentiostatic polarization at U_E = 0.6 V vs Hg/HgO in Borate Buffer solution for 30 minutes.

Notably, the values recorded for C_M are much higher than the Helmholtz double layer capacitance in aqueous solutions (20 – 30 μFcm^{-2}). This means that for the interpretation of the dependence of the measured capacitance from the potential a more appropriated equivalent circuit should be used to model the alloy/passive film/electrolyte interfaces.

According to the literature[55], different charge contributions could affect the measured equivalent capacitance at a semiconductor/electrolyte interface, as describe below:

i. The space charge due to the ionized donor (or acceptor) in the semiconductor (C_{sc});
ii. The charge trapped in the surface states (C_{ss}) due to the presence of localized electrons levels within the band gap related for instance to dangling bonds;
iii. The charge due to the adsorbed ions or ionized surface groups (C_{ad}) as a consequence of chemical reaction with the electrolyte;
iv. The ionic counter charge in the electrolyte (C_H).

The equivalent circuit corresponding to the physical description is reported in Fig. 4-11[55].

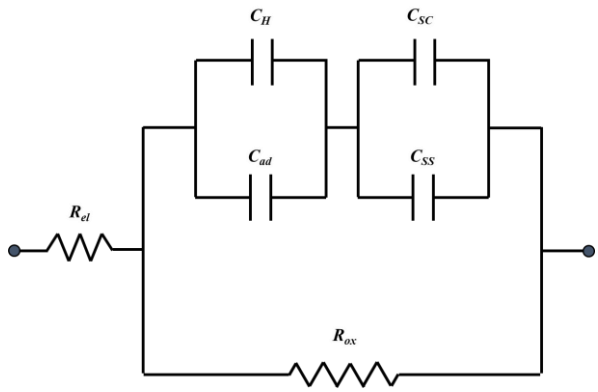

Fig. 4-11. Equivalent circuit employed for the investigation of passive film/electrolyte interface where several charge contributions to the overall measured capacitance are displayed.

It is also important to take into account that when a.c. voltage is externally applied to a SC, in order to perform impedance measurements, electron exchange between bulk and surface states, ions adsorption and ionic group formation take a finite time and therefore they will follow the perturbation signal depending on the frequency of the a.c. signal. In fact, according to the experimental results, at 10 kHz, that is the highest investigated frequency, a C_M lower than C_H was measured, suggesting that $(C_H + C_{ad}) >> (C_{SC} + C_{SS})$ and C_M almost coincident with $(C_{SC} + C_{SS})$ is obtained. Nevertheless, the estimation of the C_{SC} from the equivalent measured capacitance, C_M, is not straightforward since it is not possible to estimate the contribution arising from the surface states[55]. Thus, the Mott-Schottky model cannot be used in order to gain information regarding the density states of passive films under investigation.

Nevertheless, impedance spectra can be fitting by using the equivalent circuit reported in Fig. 4-12 where R_{el} is the electrolyte resistance, R_{ox} the resistance of the corresponding oxide film grown on 316L SS, *CPE* the constant phase element introduced in order to model the non ideal capacitance of the oxide and α is the exponent of the *CPE* element[55]

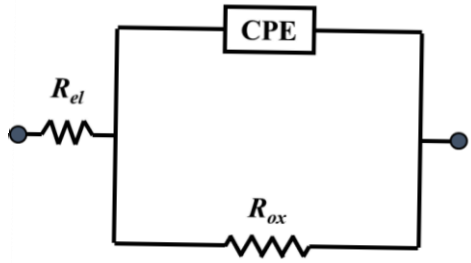

Fig. 4-12. Equivalent circuit employed to model the passive film/electrolyte interface.

In Fig. 4-10b the dependence of current density on potential during the potential scans of Fig. 4-10a is reported. The current keeps almost constant in a wide

electrode potential range, where no Faradic processes are occurring. However, when the polarizing voltage is more negative than -0.1 V Hg/HgO, an electronic current starts to circulate due to the degeneration of the semiconductor with the onset of a reduction process (O_2 reduction, see Fig. 4-10b).

Fig. 4-13 shows the EIS spectra in the Nyquist representation recorded in Borate Buffer solution (pH 8) at different polarizing potentials. The dependence of the imaginary impedance component on real component is described by a portion of a depressed semicircle. Hence, EIS spectra were fitted according to the electrical equivalent circuit reported above in Fig. 4-12. The fitting parameters are listed in Table 4-3. The oxide resistance is very high (in the order of 10^5 Ω cm^2) suggesting the formation of a blocking layer. The best fitting exponent of the constant phase element is high ($\alpha = 0.89$) but still < 1.

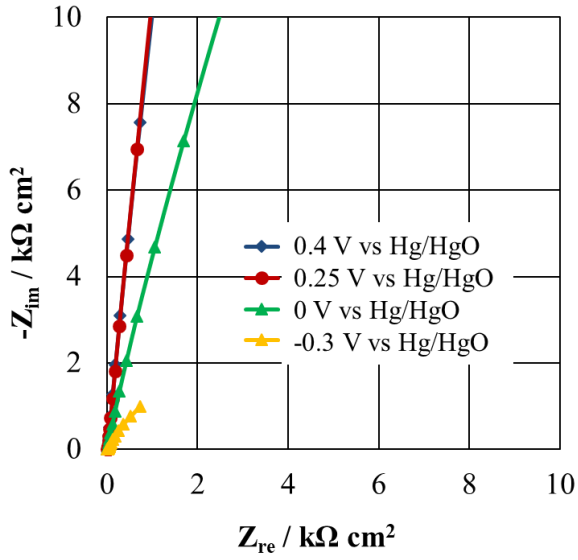

Fig. 4-13. EIS spectra in the Nyquist representation recorded in Borate Buffer solution (pH 8) at different polarizing potentials for passive films grown for 30 minutes at U_E = 0.6 V vs Hg/HgO in the same solution.

Table 4-3. Fitting parameters of EIS spectra recorded at different polarizing potentials for passive films grown on WS surface at different passivation potentials in Borate Buffer aqueous solution (pH ~ 8) for 30 minutes. The equivalent circuit reported in Fig. 4-12 was employed.

Passivation condition	Potential V vs Hg/HgO	R_{el} Ω cm^2	R_{ox} Ω cm^2	Q_{CPE} S s$^{\alpha}$ cm^{-2}	α	χ^2
0.6 V vs Hg/HgO for 30 minutes	0.4	16	$1.8 \cdot 10^6$	$3.41 \cdot 10^{-5}$	0.94	$3.30 \cdot 10^{-2}$
	0.25	16	$4.5 \cdot 10^6$	$3.71 \cdot 10^{-5}$	0.94	$3.33 \cdot 10^{-2}$
	0	16	$1.8 \cdot 10^5$	$8.81 \cdot 10^{-5}$	0.89	$3.26 \cdot 10^{-2}$
	-0.3	16	$9.2 \cdot 10^3$	$1.04 \cdot 10^{-3}$	0.69	$3.03 \cdot 10^{-2}$

4.2.2 *Passive films grown due to atmospheric exposure*

Fig. 4-14a-e show the surfaces of WS samples with different degree of rusting corresponding to different exposure times ranging from a few days (i.e. not macroscopic evidence of corrosion, see Fig. 4-14a) to 1-3 months (i.e. fully covered by corrosion products, see Fig. 4-14e).

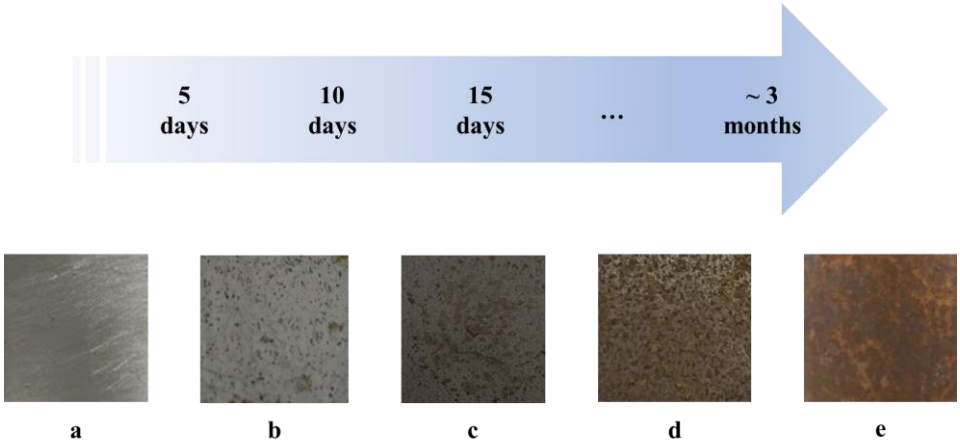

Fig. 4-14. Representation of the rust film formation after atmosphere exposure on WS surface characterized by different degree of rusting.

SEM micrographs reveal that passive films of Fig. 4-14e have a porous structure mainly constituted by globular and laminar agglomerates, as "*bird's net shape*" and "*flower petal shape*" providing a cauliflower morphology (Fig. 4-15a-d). Cross section reported in Fig. 4-15e reveales that after long time exposure in atmosphere a very thick (18 μm) and adherent passive film is present.

Composition of this rust layer was determined by Raman Spectroscopy and X-ray diffraction. Raman spectrum reported in Fig. 4-16a reveals significant peaks at 247, 381, 530 and 650 cm^{-1} that can be attributed to the presence of Lepidocrocite (γ-FeOOH). The other peaks at 224, 290, 408, 497, 611 and 1330 cm^{-1} are typical of hematite. The remaining peak at 499 cm^{-1} can be attributed to akaganeite[165]. No peaks associated to the presence of magnetite are detected, but this does not exclude the presence of Fe_3O_4 in the rust, since it is usually present in the inner part of rust film adhering to the steel surface and can be transformed into hematite by laser irradiation. According to the XRD pattern reported in Fig. 4-16b, rust film formed on Weathering Steel surface after very long time exposure (i.e. Fig. 4-14e) consists mainly of Lepidocrocite, Hematite, Akaganeite and Magnetite[166,167].

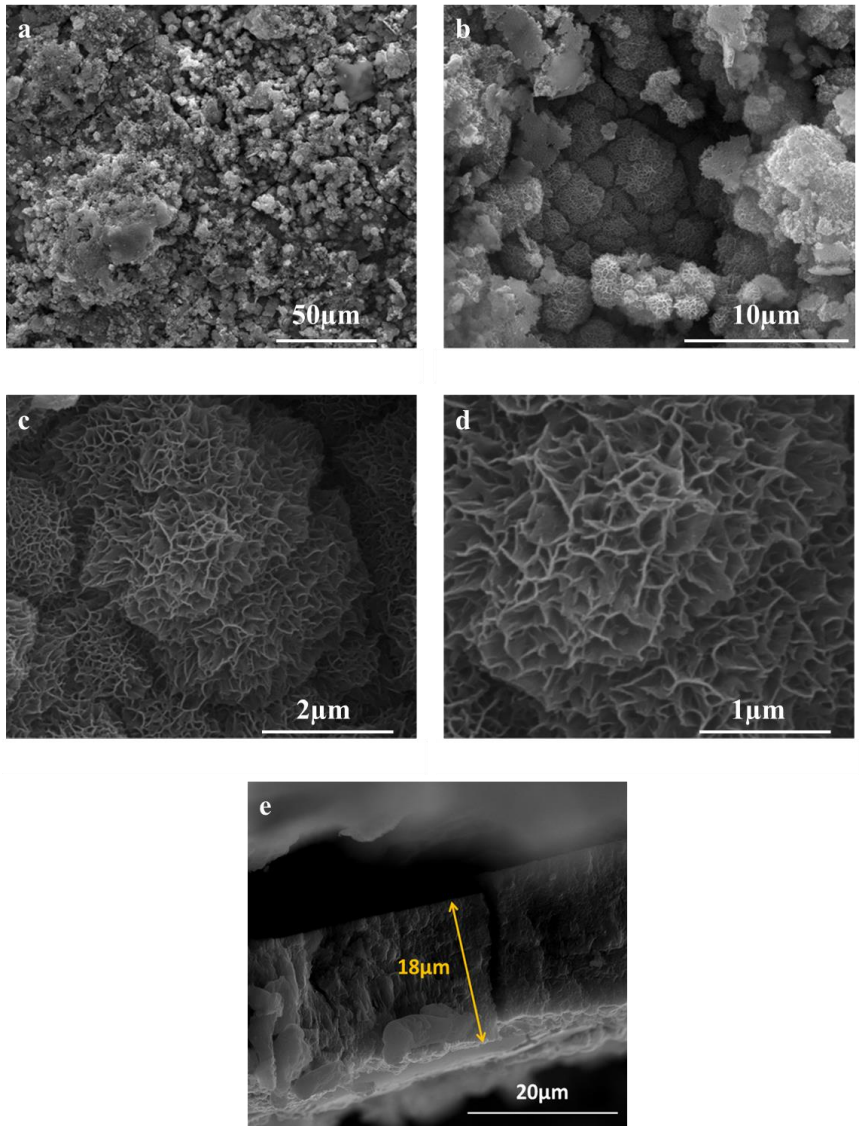

Fig. 4-15. SEM view of passive rust film formed on totally covered Weathering Steel (i.e. Fig. 4-14e) a) 50µm b) 10µm c) 2µm d) 1µm. e) View of the cross section and thickness estimation.

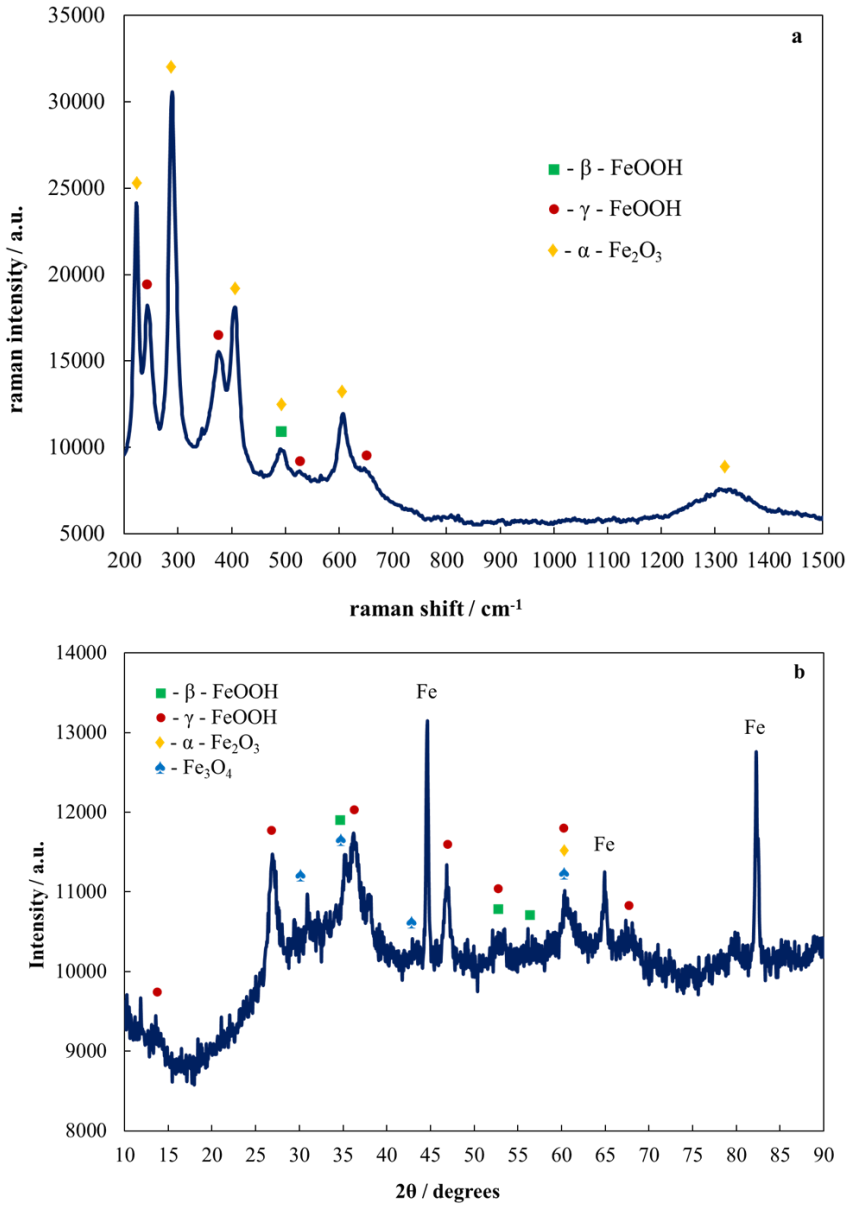

Fig. 4-16. a) Raman spectrum and b) XRD pattern related to rust film formed on WS after atmospheric exposure with a totally covered surface (i.e. Fig. 4-14e).

In Fig. 4-17 photocurrent spectrum for WS after 5 days of atmospheric exposure (see Fig. 4-14a) recorded in Borate Buffer at the open circuit voltage (~ 0 V vs SSC) is reported.

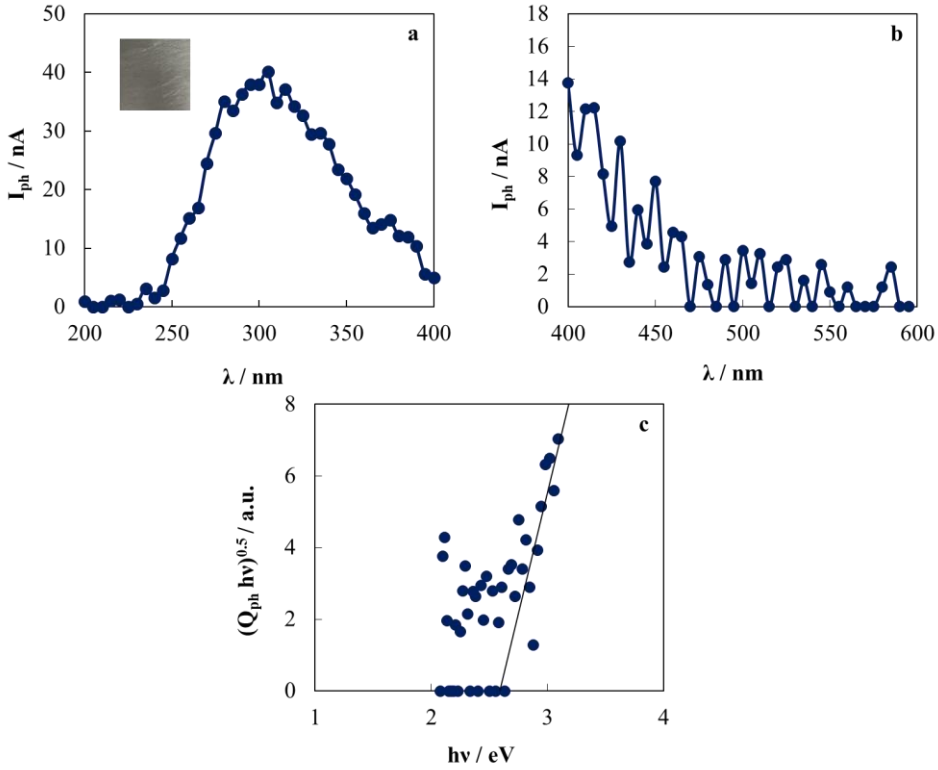

Fig. 4-17. Photocurrent spectrum related to rust film formed on WS surface during the early growth stage (i.e. Fig. 4-14a) recorded in Borate Buffer solution at the open circuit potential (U_{OC} ~ 0V vs SSC) for a) $200 < \lambda < 400$ nm and b) $\lambda \geq 400$ nm. c) $(I_{ph}\ h\nu)^{0.5}$ vs hν plot.

According to Eq. 3.10, an optical band gap of ~ 2.6 eV is estimated (see Fig. 4-17c), which is significantly higher than that estimated for the passive films grown after potentioastatic polarization at 0.6 V (Hg/HgO). Notably, the estimated E_g is very close to the value reported in the literature for γ-Lepidocrocite[159–163]. For higher exposure time a photocurrent tail was recorded at low photon energy by using a cut off filter for $\lambda > 400$ nm, corresponding to a band gap value of 2.3 eV (see Fig. 4-18).

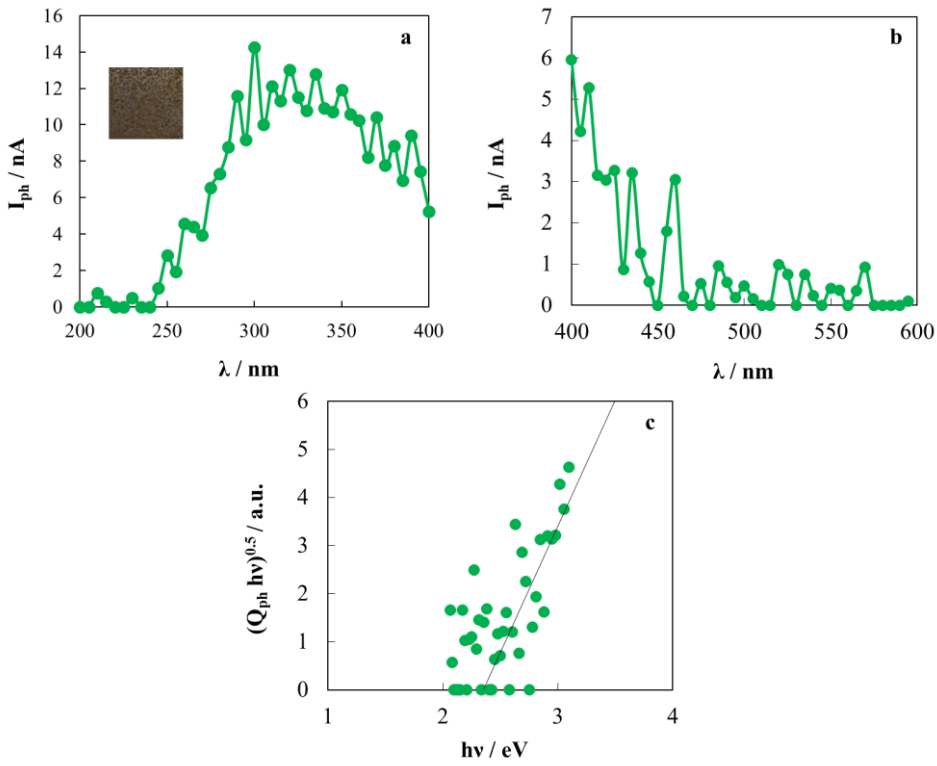

Fig. 4-18. Photocurrent spectrum related to rust film formed on WS surface during the early growth stage (i.e. Fig. 4-14d) recorded in Borate Buffer solution at the open circuit potential (U_{OC} ~ 0V vs SSC) for a) $200 < \lambda < 400$ nm and b) $\lambda \geq 400$ nm. c) $(I_{ph}\ h\nu)^{0.5}$ vs hν plot.

Optical band gap of passive films on samples after different degree of rusting are listed in Table 4-4. According to the reported values, optical band gap of passive film decreases by increasing the exposure time in atmosphere but no photocurrent is recorded after long exposure time, when the surface of the WS is completely covered by rust.

Table 4-4. Band gap values of rust film on WS samples with different degree of rusting.

Passivation conditions	E_g / eV
a – early growth stage (no coverage)	2.59
b – onset coverage	2.35
c – higher degree of rusting	2.29
d – much higher degree of rusting	2.35
e – totally degree of rusting	No photocurrent

Current versus time curves were also recorded for WS samples after different exposure time by manually chopping light irradiation at the open circuit potential (~ 0 V vs SSC). The measured photocurrent is anodic (see in Fig. 4-19a), suggesting that passive films on WS have n-type SC behaviour. This is also confirmed by the potential versus time curve recorded under constant irradiation at 300 nm.

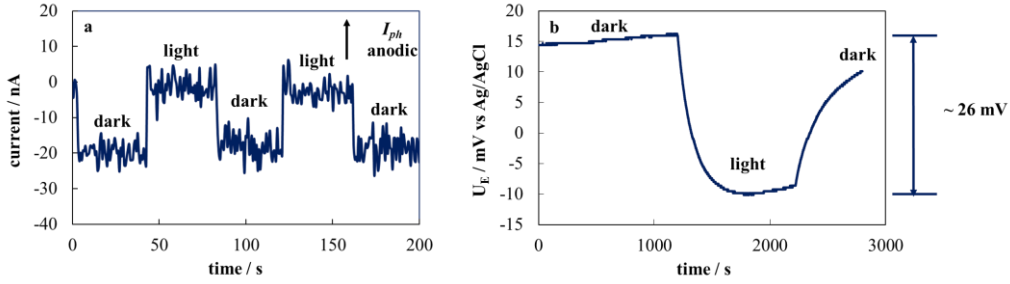

Fig. 4-19. a) Current vs time curve recorded in Borate Buffer solution at U_{OC} ~ 0 V vs Ag/AgCl at 300 nm related to rust film formed on WS surface (i.e. Fig. 4-14a). b) Potential vs time curve recorded in Borate Buffer solution at λ = 300 nm at the open circuit potential (~ 0 V vs SSC).

According to Fig. 4-19b, potential shifts in the cathodic (negative) direction soon after irradiation as expected for a n-type SC[164]. Photo-potential arises in a direction to reduce potential across the space charge layer, so in the case of an n-type SC bend bending bends upwards so photo-generated electrons are available

to further oxygen reduction improving corrosion kinetics. We also tried to record photo-potential in the case of degree of rusting but no effect was appreciable.

Electrochemical Impedance spectra were also recorded in order to estimate the oxide resistance of atmospheric layers. Nyquist representation of the EIS spectra recorded at the open circuit potential (~ 0 V vs SSC) is reported in Fig. 4-20.

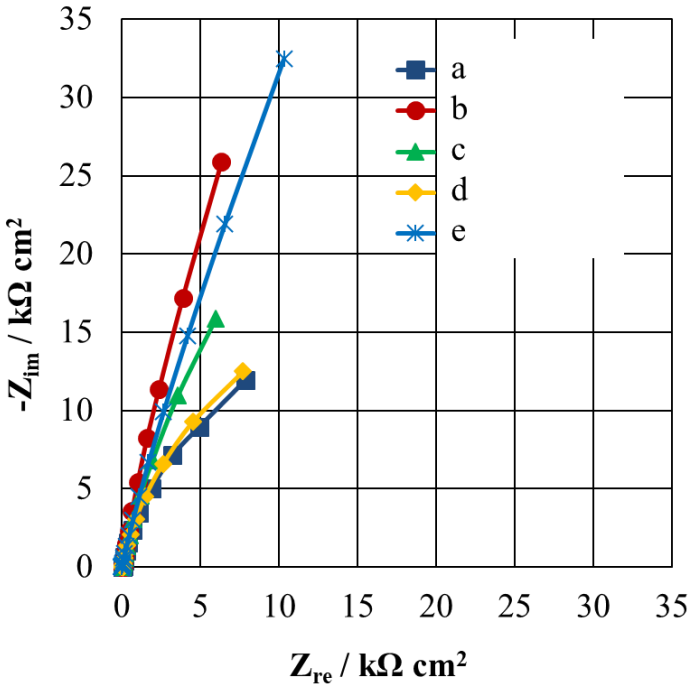

Fig. 4-20. EIS spectra in the Nyquist representation recorded at the open circuit potential (U_{OC} ~ 0 V vs Ag/AgCl) in Borate Buffer solution for WS samples with different degree of rusting.

Experimental results were fitted according to the equivalent circuit of Fig. 4-12, and fitting parameters are reported in Table 4-5. Oxide resistance of WS samples strongly depends on the amount of rust products on WS surface. In particular, in the early growth stage, polarization resistance is very low and increases by increasing the exposure time in atmosphere.

Table 4-5. Fitting parameters of EIS spectra recorded at the open circuit potential (U_{OC} ~ 0 V vs Ag/AgCl) in Borate Buffer (pH 8) for WS samples with different degree of rusting.

Passivation conditions	R_{el} Ω cm^2	R_{ox} Ω cm^2	Q_{ox} S s^n cm^{-2}	α	χ^2	δ nm
a – early growth stage (no coverage)	82	$3.17 \cdot 10^4$	$7.78 \cdot 10^{-5}$	0.90	$1.93 \cdot 10^{-3}$	1.27
b – onset coverage	82	$2.25 \cdot 10^5$	$5.12 \cdot 10^{-5}$	0.91	$1.99 \cdot 10^{-3}$	1.41
c – higher degree of rusting	57	$9.13 \cdot 10^4$	$8.74 \cdot 10^{-5}$	0.88	$7.12 \cdot 10^{-4}$	1.44
d – much higher degree of rusting	60	$4.00 \cdot 10^4$	$8.76 \cdot 10^{-5}$	0.88	$2.18 \cdot 10^{-4}$	1.59
e – totally degree of rusting	13	$3.27 \cdot 10^5$	$4.21 \cdot 10^{-5}$	0.86	$1.87 \cdot 10^{-3}$	4.83

Moreover, the exponent n < 1 of the constant phase element suggests a not ideal behaviour of the oxide capacitance. According to the literature[125,168–170], this can occur when the passive film resistivity is not constant across on going from the metal to the electrolyte, thus the power-law model can be used.

As stated in section 3.2, when the assumption of a uniformly active electrode is not valid, a time-constant dispersion along the electrode surface or in normal direction can be observed[170], as showed in Fig. 4-21.

This variation can be modelled by a constant-phase-element impedance (CPE), whose expression, for a blocking system, can be written as a function of model parameters α and *Q*, as follow[140]:

$$Z_{\mathrm{CPE}} = \frac{1}{(j\omega)^{\alpha} Q} \qquad (4.6)$$

When α = 1 the system is described by a single time-constant and the parameter

Q has units of a capacitance. Conversely, *Q* has units of $s^{\alpha} / \Omega\ cm^2$.

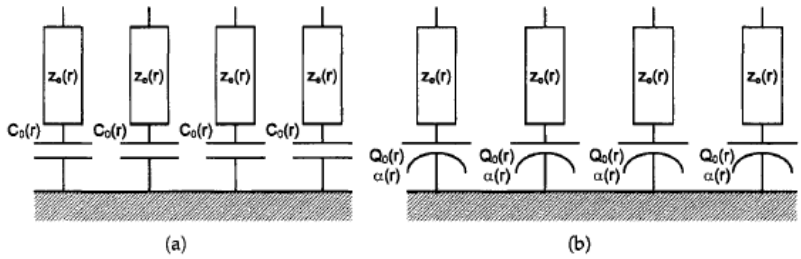

Fig. 4-21. Schematic representation of time constant distribution for a blocking electrode in a) 2-dimensional and b) combined 2-dimensional and 3-dimensional distribution.

According to previous works reported in the literature[157,158], the power law model provides physical meaning to the CPE behavior observed for passive films where a normal distribution of resistivity is assumed (i.e. 3D distribution), thus allowing to extract the corresponding capacitance. The effective capacitance associated to the CPE can be expressed as:

$$C_{\text{eff}} = \frac{\epsilon\epsilon_0}{\delta} \qquad (4.7)$$

where ε is the dielectric constant and ε_0 is the permittivity of vacuum equals to 8.8542×10^{-14} F/cm.

By assuming a dielectric constant independent on position into the passive film, the distribution of resistivity along the film thickness it was found to follows a power-low profile as reported below:

$$\frac{\rho}{\rho_\delta} = \xi^{-\gamma} \qquad (4.8)$$

The parameter ξ is the dimensional position ξ = y/δ, where δ represents the film thickness and y is the position through it. ρ_δ is the resistivity corresponding to ξ

= 1 and γ is a constant that describes the variation of the resistivity. A distribution of resistivity that provides a bounded value for resistivity was proposed to be[168]:

$$\frac{\rho}{\rho_\delta} = \left(\frac{\rho_\delta}{\rho_0} + \left(1 - \frac{\rho_\delta}{\rho_0}\right)\xi^\gamma\right)^{-1} \quad (4.9)$$

where ρ_0 and ρ_δ are the boundaries values of resistivity at the interfaces.
The relationship between the CPE parameters *Q* and α, the dielectric constant ε and the resistivity ρ_δ was found to be:

$$Q = \frac{(\epsilon\epsilon_0)^\alpha}{g\delta\rho_\delta^{1-\alpha}} \quad (4.10)$$

where g is the interpolation formula defined as:

$$g = 1 + 2.88(1-\alpha)^{2.375} \quad (4.11)$$

According to Eq. 4.7 and 4.10, the effective capacitance of the passive film can be written as follow:

$$C_{\text{eff,PL}} = (gQ)^{1/\alpha}(\delta\rho_\delta)^{(1-\alpha)/\alpha} \quad (4.12)$$

When α and g are equal to 1, the CPE parameter Q represents the capacitance of passive films, where Q and α can be obtained due to the fitting of the EIS spectra, while ε can be obtained through independent measurements[169]. The application of Eq. 4.12 to CPE parameters given in Table 4-5 allows to estimate the film thickness of passive films grown after atmospheric exposure, by assuming ε = 12 and limiting value of resistivity of 500 Ohm cm taken from calibration of Fe17Cr stainless steel[170].

The resulting thickness is very low suggesting that the recorded capacitance is due to a space charge region significantly thinner than the rust layer.

Notably the power law model can be a useful tool for the estimation of oxide thicknesses. Nevertheless, it does not provide straightforward information regarding their corresponding corrosion resistance, that in turn is affected by many other parameters such as composition, morphology and electronic properties of passive films in terms of band gap (E_g), flat band potential (U_{fb}) and the presence of localized states in the gap.

In Fig. 4-22a differential capacitance versus potential curves recorded in Borate Buffer (pH ~ 8) are reported.

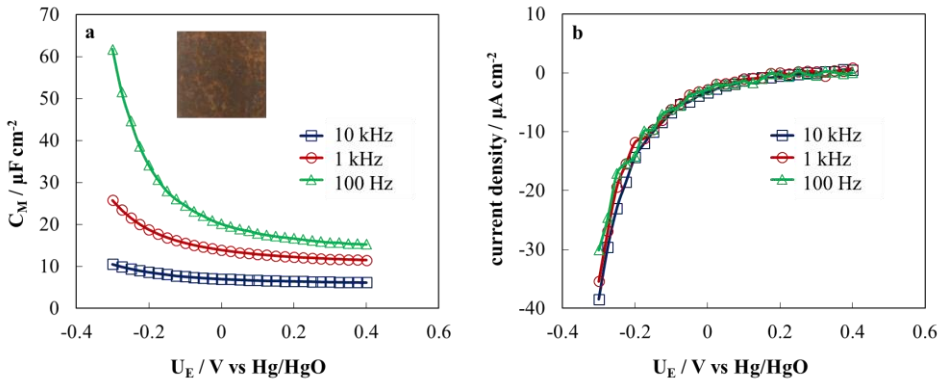

Fig. 4-22. a) Differential capacitance and b) current density vs potential curves recorded in Borate Buffer solution at 10 kHz, 1 kHz and 100 Hz for totally covered WS sample (i.e. Fig. 4-14e).

As in the case of anodic films, capacitance appears strongly dependent on polarizing potential and frequency, in agreement with the not ideal capacitance suggested by the constant phase elements used to model the electrochemical behaviour of the metal/passive film/electrolyte interface. It is higher at negative potentials and decreases moving towards more anodic potentials until it becomes constant, as usually for an n-type SC. In Fig. 4-22b the dependence of current density on potential during the potential scans of Fig. 4-22a is reported. A

cathodic current starts at ~ 0.2 V vs Hg/HgO, suggesting the occurrence of Faradic processes, thus the interface does not behave as a blocking interface.

Polarization curves were recorded in order to better understand corrosion properties of both films in terms of their corrosion current density, corrosion potential and pitting potential in the case of chloride containing solutions. As disclosed in Fig. 4-23a, in chloride free solution passive films grown in aqueous solution exhibit a wider passivity range and more anodic corrosion potential than that of the atmospheric film.

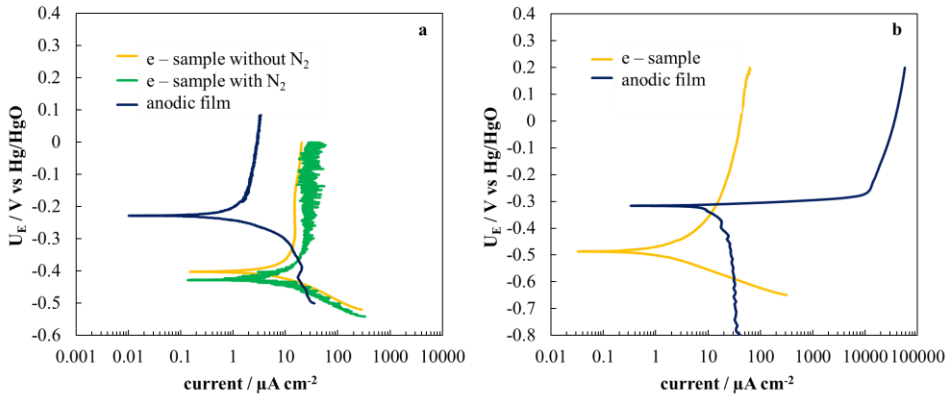

Fig. 4-23. Polarization curves for passive film grown at 0.6 V vs Hg/HgO on WS sample in Borate Buffer solution (blue line) and for atmospheric layer (i.e. Fig. 4-14e) (yellow line) recorded in a) Borate Buffer solution (pH 8) and b) 0.6 M NaCl. Polarization curve related to the totally covered WS sample recorded in free chloride deaerated solution is also reported (green line).

Conversely atmospheric layer reveals the presence of an oxidation peak due to the oxidation of Fe^{2+} to Fe^{3+}. According to Fig. 4-23b, corrosion behaviour in chloride containing solution is different because atmospheric film presents a more cathodic corrosion potential but a pitting potential much higher with respect to anodic film where pitting immediately occurs. This experimental finding suggests that in the case of passive film grown in aqueous solution, chloride can easily diffuse towards the substrate, while in the case of atmospheric corrosion the porous layer is able to work as a physical barrier

against oxygen diffusion. In this way oxygen transport to the uncovered areas is slowed down or hindered protecting the substrate. Moreover, the cathodic branch of the polarization curve for WS after rusting under atmospheric conditions is not sustained by O_2 reduction, as confirmed by recording the same curve in deaerated solution. This implies that the cathodic current is due to the reduction of Fe^{3+} to Fe^{2+} in the passive film.

In previous works the growth mechanism of rust layers on weathering steel has been extensively studied[157,158,172–174]. There is a general agreement on the role of wet-dry cycles in determining the rate of rust thickening[157], which is affected by the kinetic of both anodic process (i.e. iron oxidation) and cathodic process (O_2 reduction). According to *Stratman et al.*[173] O_2 reduction takes place within the oxide scale and not at the metal/electrolyte interface, thus electrons left by iron oxidation at the metal/film interface must reach the oxide/electrolyte interface. And considering that iron oxides are usually n-type semiconductors, some authors suggested that a role can also be played by light irradiation[160]. This implies that the electronic properties of the rust layers play a key role in the growth mechanism, as confirmed by the large numbers of papers devoted to their characterization[159–163,175]. However, the employed approach is sometimes questionable.

The experimental findings of this work show that the behavior of WS changes as a function of the rusting degree, which in turn depends on exposure time as well as on the effective climate conditions. The samples of this study were selected at different degree of rusting in order to get information on WS/passive film/electrolyte interface at different stages of the rusting process. When there is no macroscopic evidence of rust (see Fig. 4-14a), the passive film on WS is a n-type semiconductor with a band gap of 2.6 eV, very close to the value reported in the literature for γ-lepidocrocite[159–163], but higher than that estimated for passive films on the same steel grown by anodic polarization (see Fig. 4-9) and

than that reported for hematite (2.0 – 2.2 eV)[115]. Conversely, the polarization resistance at OCP of passive films on WS grown by atmospheric corrosion and polarization resistance in chloride free environment of anodic films are comparable (see Table 4-3 and Table 4-5).
As far as the surface is not completely covered by rust it is possible to record photocurrent and the passive films have a band gap of 2.3 eV. However, when the surface is fully covered, films are no more photoactive.

The film on the WS surface consists of several layers with different composition and electronic properties. The XRD patters indicate the presence of Fe_3O_4 and lepidocrocite inside the rust layer. The presence of the latter is also confirmed by Raman Spectroscopy, which is more sensitive to the composition of the outer layer. Moreover, the polarization curve reported in Fig. 4-23, shows a passivity current density significantly higher than that measured for anodic film on WS (see Fig. 4-23a). According to the scheme of Fig. 4-24, an inner layer of magnetite is present in direct contact with the metal, which can accept the iron ions but also electrons due to its electronic conductivity. These electrons can reach the outer layer of the passive film mainly constituted by FeOOH where O_2 can accept the electrons and provide OH^- ions and, thus, the formation of lepidocrocite. According to the literature[157], oxygen reduction occurs at the passive film/electrolyte interface. This multi layered structure allows the rust thickening up to values significantly higher than those usually reported for passive films grown on steel. As for the case of anodic films on WS, the formation of Fe_2O_3 (i.e. iron oxide with Fe^{3+}) occurs with a very low passivity current density and very poor pitting corrosion resistance (see Fig. 4-23a). In spite the presence of Fe^{2+} the thick rust layer grown by atmospheric corrosion on the surface of the WS works as a good barrier against diffusion of aggressive species such as chloride ions, thus resulting very effective in the prevention of localized corrosion phenomena such as pitting. Indeed, the pitting potential

according to Fig. 4-23b, is significantly higher than that measured for anodic films of WS.

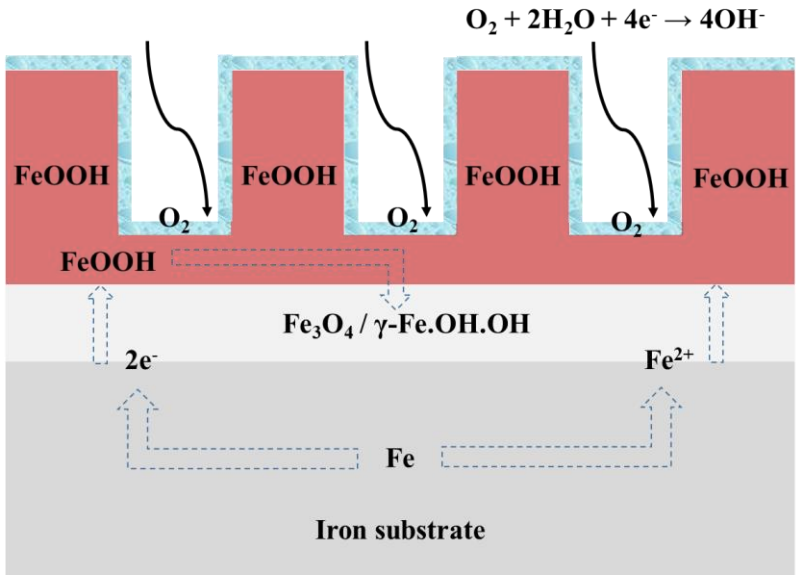

Fig. 4-24. Simplified schematic representation of the proposed growth mechanism of rust film on Weathering Steel substrate due to atmospheric exposure.

The electronic conductive layer at the metal/passive film interface is stable during atmospheric corrosion since Fe^{2+} ions are introduced from the metal/passive film interface, while Fe^{2+} is oxidized at the megnetite/lepidocrite interface. Due to the high band gap of lepidocrocite the portion of absorbed light from the solar spectrum is not significant, thus the light irradiation does not play a significant role on the kinetic of the corrosion processes. It is more likely that light irradiation plays a role in the duration of the dry/wet cycles during atmospheric corrosion since the corrosion process goes on only when the surface of the rust layer is wet[157,173].

Finally, it important to stress that using Mott-Schottky plot to get information on the electronic properties of passive films on WS grown by atmospheric

corrosion can lead to misleading information, since one of the main assumption behind the use of this approach, i.e. dealing with a not Faradic interface, is not correct, since at high anodic potential the film is oxidized thank to the imposed potential. This makes the films no more representative of the rust layer grown by atmospheric corrosion. Moreover, the strong dependence on frequency of the superimposed a.c. signal poses several questions about the quantitative interpretation of the obtained results.

More reliable information is provided by the EIS spectra recorded at the OCP (see Fig. 4-20), since the immersion at the open circuit potential in not aggressive environment does not change the electronic properties of the passive films. The R_{ox} raises as far as the surface is completely covered, while it starts to decrease when the surface is fully covered, due to the formation of a more conducive layer.

4.2.3 Concluding remarks

In this work the growth kinetic of atmospheric films grown on low alloy steel was studied in order to understand how growth mechanism and electronic properties of the corresponding passive films can improve their corrosion behavior. For this reason, in the first part a physico-chemical characterization of passive film grown on weathering steel samples under potentiostatic polarization in aqueous solution was reported. According to the HFM passive film growth is due to the balance between formation and dissolution processes that induce the formation of a thin, compact and adherent passive film mainly consisting of hematite (i.e. Fe^{3+}). Unlike passive films grown on pure chromium, they are n-type semiconductor. Nevertheless, passive films grown after anodic polarization are poorly resistant towards corrosion phenomena since they easily come in contact with aggressive ions such as chloride.

Conversely, according to photo-electrochemical and morphological characterization, atmospheric exposure of WS samples induces the formation of a distribution of iron oxyhydroxides consisting of hematite, akaganeite, lepidocrocite and magnetite (Fe^{2+} / Fe^{3+}) that in turn increases the conductibility of the rust film. Unlike stainless steels, where their corrosion resistance is addicted to the formation of a thin protective passive film mainly based on Cr_2O_3, the improved corrosion resistance of WS can be explained by considering the formation of conductive paths on going from the metal to the rust film surface allowing the balance between Fe^{2+} oxidation and Fe^{3+} reduction reactions, sustaining the thickening of the rust film that in turn is able to hinder the diffusion of aggressive species.

Finally, the photo-electrochemical measurements on WS samples characterized by different degree of rusting suggest that the light affect the seasonal cycles rather than improve the growth kinetic of rust film.

4.3 Passive Films on Different Stainless Steel grades

A large part of published papers is mainly focused on the study of electronic properties and composition of passive films grown on Fe-Cr model alloys and on austenitic and duplex stainless steels. Moreover, most of this experimental works investigate passivity of SS in acidic solution, where iron and chromium oxides are not thermodynamically stable, according to the Pourbaix diagram, and where defective $Cr_{2+x}O_{3-y}$ may exist as a metastable phase[150]. However, as already discussed in the description of the industrial aggressive environments, SS can also come in contact with alkaline solutions such as cleaning and disinfectant solutions in CIP cycles or in fine chemical specialty industries. For this reason, in this work the results of a physicochemical characterization of passive films on different stainless steel usually employed in food and pharmaceutical processing in both acidic (pH ~ 2) and alkaline (pH ~ 13) solutions.

4.3.1 *Passive films growth*

In Fig. 4-25 current density vs. potential curves were recorded for 304L, 316L and Duplex stainless steel in 5 mM H_2SO_4 (pH ~ 2) and 0.1 M NaOH (pH ~ 13) are reported. The anodic branches of the polarization curves for 316L and Duplex are very similar, except for the height of the anodic peak due to chromate ions formation, which is larger for duplex in agreement with the corresponding higher Cr content. Conversely, an oxidation peak is present at less noble potential for 304L in acidic solution, that can be attributed to iron species dissolution (see Fig. 4-25a). Notably, the noisy on polarization curves recorded in 0.1 M NaOH for different stainless steel grades can be addicted to the sensitivity of the instrument.

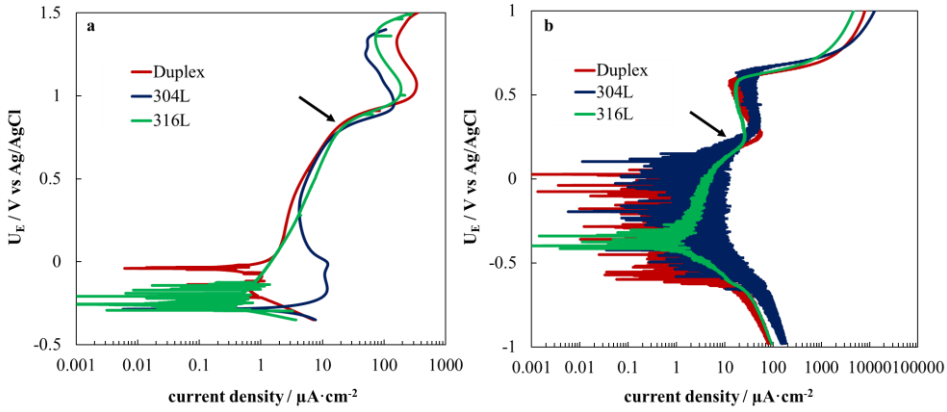

Fig. 4-25. Polarization curves recorded for different SS grades at 2 mV s^{-1} in a) 5 mM H_2SO_4 solution (pH ~ 2) and b) 0.1 M NaOH solution (pH ~ 13).

SSs were passivated by anodic polarization below the equilibrium potential of further oxidation of Cr^{3+} to chromate ions respectively at 0.85 V vs SSC in acidic solution and at 0.2 V vs SSC in alkaline solution. Fig. 4-26a displays that in acidic solution current density decreases during the polarization until a steady state condition is reached for 316L and Duplex SS suggesting the formation of passive films whose thickness is almost constant, with the exception of 304L. Notably, the current density recorded during polarization in alkaline solution is significantly lower if compare to that recorded during passivation of pure chromium (see Fig. 4-26b), suggesting the formation on SS surfaces of a passive layer more stable towards corrosion reactions.

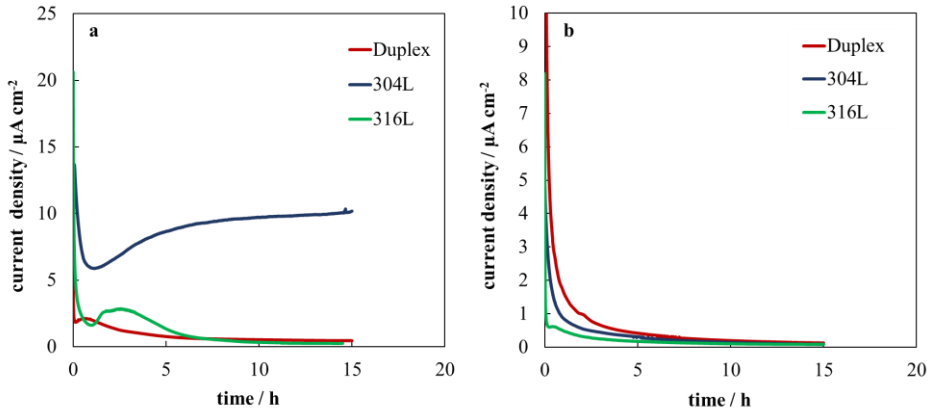

Fig. 4-26. Current density vs time curves recorded under anodic polarization at a) 0.85 V vs SSC in 5 mM H_2SO_4 solution (pH ~ 2) and b) 0.2 V vs SSC in 0.1 M NaOH solution (pH ~ 13).

4.3.2 *Differential Capacitance and Impedance Measurements*

The dependence of the overall impedance on potential at constant frequency of the stimulus a.c. signal was studied in order to get more insight into SS/passive film/electrolyte interfaces. Differential capacitance curves recorded in Phosphate Buffer solution (pH ~ 7) are reported in Fig. 4-27. C_M strongly depend on frequency, as also reported in the case of passive films grown on pure chromium and on low alloy steel, and its dependence from the potential in the exploited range suggests that passive films grown on SS surfaces are n-type SC.

Notably, the experimental data range from 16 µF cm^{-2} to values that are significantly higher than 35 µF cm^{-2}, that is the Helmholtz double layer capacitance estimated in aqueous solution, as also found for passive films grown on weathering steel after potentiostatic polarization.

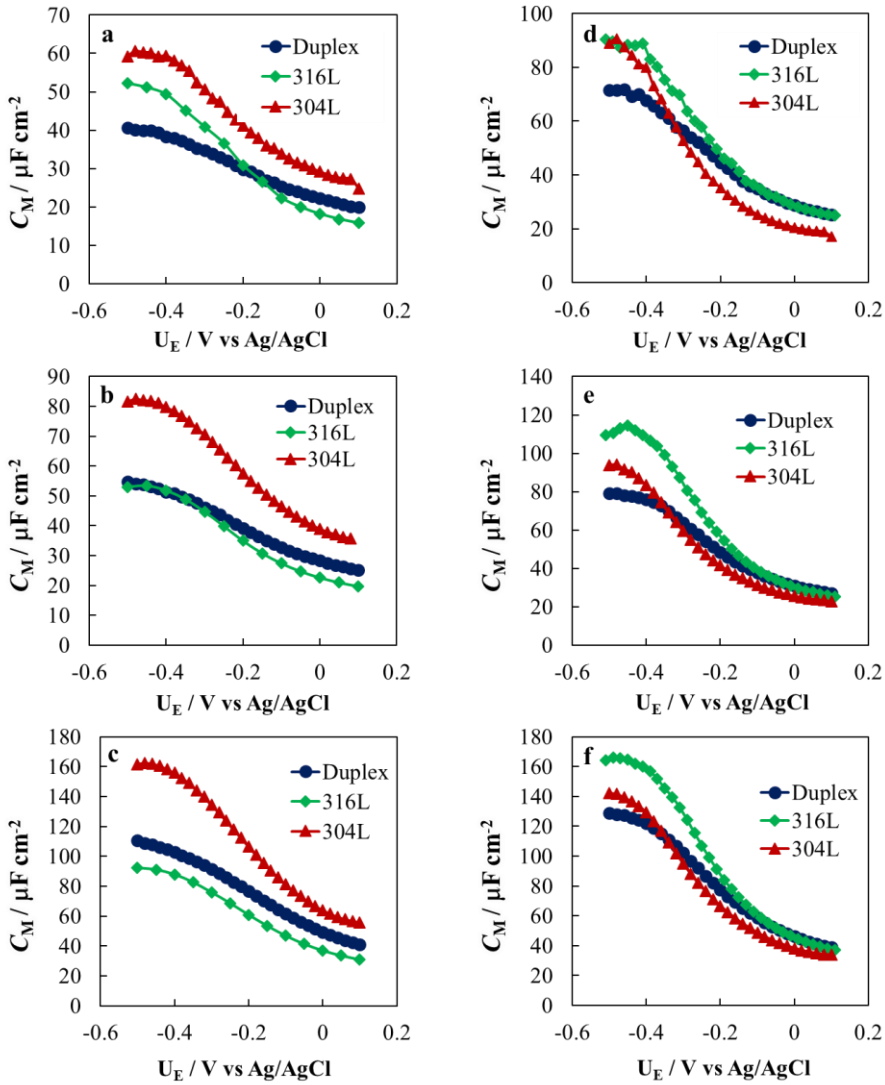

Fig. 4-27. Measured series capacitance vs. potential curves recorded in Phosphate Buffer solution (pH ~ 7) for passive films grown on different stainless steel grades surfaces after 15 h of anodic polarization in 5 mM H_2SO_4 at a) 10 kHz, b) 1 kHz and c) 100 Hz and in 0.1 M NaOH at d) 10 kHz, e) 1 kHz and f) 100 Hz.

Impedance spectra, recorded in Phosphate Buffer solution (pH ~ 7) in the same exploited potential range for differential capacitance measurements, are displayed in Fig. 4-28 in the Nyquist representation for DSS after anodic polarization in both acidic and alkaline solutions.

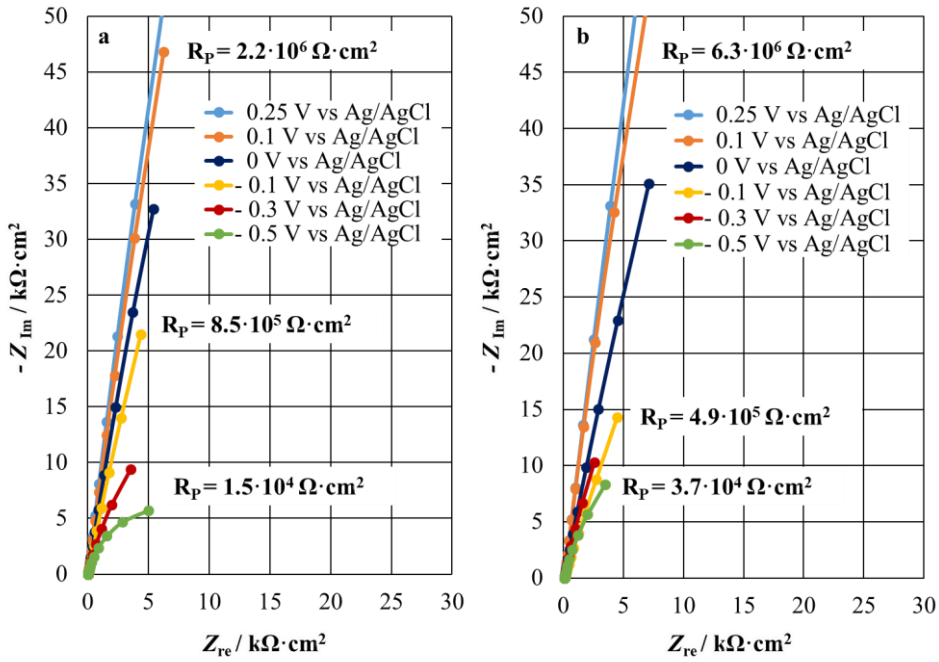

Fig. 4-28. EIS spectra in the Nyquist representation recorded in Phosphate Buffer solution (pH ~ 7) at several potentials, for passive films grown on Duplex SS after passivation under anodic polarization in a) H_2SO_4 solution (pH ~ 2) and b) NaOH solution (pH ~ 13).

The dependence of the imaginary impedance component on the real one is described by a portion of depressed semicircle as also expected according to the measured capacitance, where a strong dependence on frequency was revealed. Experimental data were finally fitted by employing the equivalent circuit reported in Fig. 4-12. Fitting parameters for passive films grown on SSs under investigation, reported in Table 4-6, Table 4-7 and Table 4-8, suggest that the resistance of passive films decreases by decreasing the polarizing potential, as expected for n-type SC. Moreover, the constant phase element Q is strongly affected by the potential since it ranges between 30 and 210 μS s^{α} cm^{-2} with α ranging from 0.80 to 0.94, as expected when the source of CPE is the frequency dependent equivalent capacitance of the passive film/electrolyte interface.

As reported in the literature, some authors tried to explain the CPE behaviour considering a not constant resistivity through the passive film thickness[170,171]. With the same approach, by assuming ε = 12 and limiting value of resistivity of 450 Ω taken from calibration of Fe17Cr stainless steel, thickness in order of ~ 2 nm were estimated.

Table 4-6. Fitting parameters of EIS spectra recorded at different polarizing potentials in Phosphate Buffer solution (pH ~ 7) after 15 h of anodic polarization in both acidic and alkaline solutions for 304L SS.

Passivation conditions	**Applied potential V vs Ag/AgCl**	R_{el} **Ω cm²**	R_{ox} **Ω cm²**	Q_{CPE} **S sⁿ cm⁻²**	**α**	χ^2
0.85 V vs SSC for 15 h in 5 mM H_2SO_4	0.2	137	$5.00 \cdot 10^5$	$3.80 \cdot 10^{-5}$	0.95	$2.74 \cdot 10^{-3}$
	0.1	138	$7.20 \cdot 10^5$	$3.30 \cdot 10^{-5}$	0.96	$2.30 \cdot 10^{-3}$
	0	138	$2.79 \cdot 10^5$	$4.60 \cdot 10^{-5}$	0.94	$2.24 \cdot 10^{-3}$
	-0.1	137	$1.12 \cdot 10^5$	$8.50 \cdot 10^{-5}$	0.88	$2.54 \cdot 10^{-3}$
	-0.3	137	$1.72 \cdot 10^4$	$1.52 \cdot 10^{-4}$	0.89	$2.77 \cdot 10^{-3}$
	-0.5	137	$2.37 \cdot 10^4$	$1.20 \cdot 10^{-4}$	0.90	$2.80 \cdot 10^{-3}$
0.2 V vs SSC for 15 h in 0.1 M NaOH	0.2	100	$6.70 \cdot 10^5$	$3.04 \cdot 10^{-5}$	0.91	$4.80 \cdot 10^{-4}$
	0.1	104	$5.30 \cdot 10^5$	$3.40 \cdot 10^{-5}$	0.94	$4.40 \cdot 10^{-4}$
	0	107	$3.50 \cdot 10^5$	$4.40 \cdot 10^{-5}$	0.92	$4.30 \cdot 10^{-4}$
	-0.1	110	$1.85 \cdot 10^5$	$8.72 \cdot 10^{-5}$	0.87	$6.44 \cdot 10^{-4}$
	-0.3	94	$7.03 \cdot 10^3$	$1.80 \cdot 10^{-4}$	0.88	$1.80 \cdot 10^{-4}$
	-0.5	95	$7.28 \cdot 10^3$	$2.05 \cdot 10^{-4}$	0.86	$1.14 \cdot 10^{-4}$

Table 4-7. Fitting parameters of EIS spectra recorded at different polarizing potentials in Phosphate Buffer solution (pH ~ 7) after 15 h of anodic polarization in both acidic and alkaline solutions for 316L SS.

Passivation conditions	**Applied potential V vs Ag/AgCl**	$\mathbf{R_{el}}$ **Ω cm²**	$\mathbf{R_{ox}}$ **Ω cm²**	$\mathbf{Q_{CPE}}$ **S sⁿ cm⁻²**	**α**	χ^2
0.85 V vs SSC for 15 h in 5 mM H_2SO_4	0.2	59	$2.30 \cdot 10^6$	$3.00 \cdot 10^{-5}$	0.94	$6.40 \cdot 10^{-4}$
	0.1	50	$2.20 \cdot 10^6$	$3.40 \cdot 10^{-5}$	0.93	$6.40 \cdot 10^{-4}$
	0	45	$1.14 \cdot 10^6$	$4.50 \cdot 10^{-5}$	0.92	$6.80 \cdot 10^{-4}$
	-0.1	41	$8.51 \cdot 10^5$	$7.00 \cdot 10^{-5}$	0.89	$1.37 \cdot 10^{-4}$
	-0.3	38	$5.40 \cdot 10^4$	$1.50 \cdot 10^{-4}$	0.89	$6.30 \cdot 10^{-4}$
	-0.5	36	$1.47 \cdot 10^4$	$1.60 \cdot 10^{-4}$	0.89	$4.38 \cdot 10^{-4}$
0.2 V vs SSC for 15 h in 0.1 M NaOH	0.2	89	$2.35 \cdot 10^5$	$5.40 \cdot 10^{-5}$	0.91	$8.14 \cdot 10^{-4}$
	0.1	78	$3.16 \cdot 10^5$	$4.70 \cdot 10^{-5}$	0.94	$1.52 \cdot 10^{-3}$
	0	72	$2.90 \cdot 10^5$	$4.91 \cdot 10^{-5}$	0.92	$6.24 \cdot 10^{-4}$
	-0.1	68	$1.10 \cdot 10^5$	$1.00 \cdot 10^{-4}$	0.87	$6.12 \cdot 10^{-4}$
	-0.3	60	$2.75 \cdot 10^4$	$1.27 \cdot 10^{-4}$	0.88	$2.30 \cdot 10^{-4}$
	-0.5	60	$7.65 \cdot 10^3$	$1.60 \cdot 10^{-4}$	0.86	$2.79 \cdot 10^{-4}$

Table 4-8. Fitting parameters of EIS spectra recorded at different polarizing potentials in Phosphate Buffer solution (pH ~ 7) after 15 h of anodic polarization in both acidic and alkaline solutions for Duplex SS.

Passivation conditions	**Applied potential V vs Ag/AgCl**	$\mathbf{R_{el}}$ **Ω cm²**	$\mathbf{R_{ox}}$ **Ω cm²**	$\mathbf{Q_{CPE}}$ **S sⁿ cm⁻²**	**α**	χ^2
0.85 V vs SSC for 15 h in 5 mM H_2SO_4	0.2	155	$2.42 \cdot 10^6$	$2.72 \cdot 10^{-5}$	0.92	$1.61 \cdot 10^{-3}$
	0.1	145	$2.41 \cdot 10^6$	$3.03 \cdot 10^{-5}$	0.92	$1.57 \cdot 10^{-3}$
	0	139	$6.01 \cdot 10^5$	$3.73 \cdot 10^{-5}$	0.91	$1.63 \cdot 10^{-3}$
	-0.1	134	$1.66 \cdot 10^5$	$5.60 \cdot 10^{-5}$	0.89	$1.60 \cdot 10^{-3}$
	-0.3	131	$6.80 \cdot 10^4$	$1.32 \cdot 10^{-4}$	0.89	$2.07 \cdot 10^{-3}$
	-0.5	129	$1.38 \cdot 10^4$	$1.60 \cdot 10^{-4}$	0.88	$1.25 \cdot 10^{-3}$
0.2 V vs SSC for 15 h in 0.1 M NaOH	0.2	144	$1.26 \cdot 10^6$	$3.93 \cdot 10^{-5}$	0.91	$4.34 \cdot 10^{-4}$
	0.1	140	$1.50 \cdot 10^6$	$4.75 \cdot 10^{-5}$	0.91	$9.20 \cdot 10^{-4}$
	0	136	$6.03 \cdot 10^5$	$5.20 \cdot 10^{-5}$	0.91	$1.02 \cdot 10^{-4}$
	-0.1	135	$1.56 \cdot 10^5$	$8.75 \cdot 10^{-5}$	0.92	$9.10 \cdot 10^{-4}$
	-0.3	134	$1.86 \cdot 10^4$	$2.10 \cdot 10^{-4}$	0.89	$2.37 \cdot 10^{-4}$
	-0.5	133	$1.68 \cdot 10^4$	$1.36 \cdot 10^{-4}$	0.90	$1.80 \cdot 10^{-4}$

4.3.3 *Photoelectrochemical Measurements*

In order to gain more insight into electronic properties of passive films grown on SS surfaces, photoelectrochemical investigation was carried out. Photocurrent spectrum recorded in 0.1 M ABE (pH ~ 9) at U_E = 0.1 V vs SCC for passive film grown on DDS after 15 h of anodic polarization at 0.85 V vs SSC in acidic solution is reported in Fig. 4-29. By assuming non direct optical transition, a band gap value of 2.9 eV was estimated for passive film grown on duplex stainless steel, while 3.0 eV was obtained for that grown on 316L. Conversely, a lower band gap was estimated for the oxide film grown on 304L (see Table 4-9).

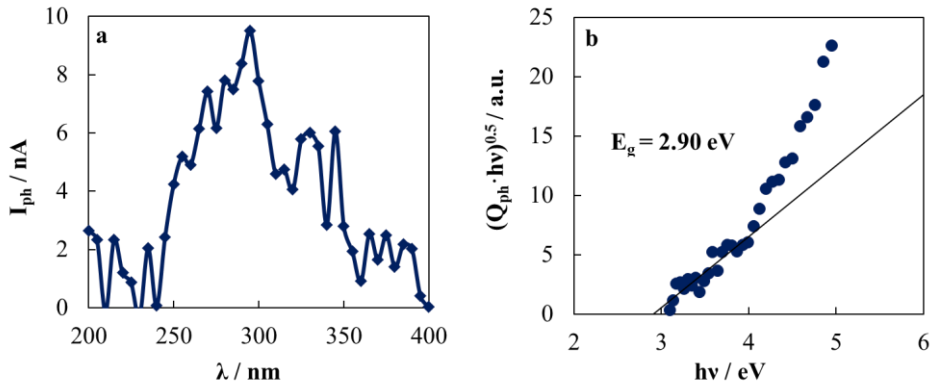

Fig. 4-29. a) Raw photocurrent spectrum for passive film grown on Duplex SS after 15 h anodic polarization at 0.85 V vs SSC in 5 mM H_2SO_4 solution recorded at U_E = 0.1 V vs SSC in 0.1 M ABE (pH ~ 8). b) $(Q_{ph}\ hv)^{0.5}$ vs hv plot.

The same photoelectrochemical investigation was carried out for passive films grown on SSs sample after 15 h of anodic polarization at 0.2 V vs SSC in alkaline solution. According to the photocurrent spectrum reported in Fig. 4-30, the band gap value estimated for passive film grown on Duplex SS after 15 h of polarization at 0.2 V vs SSC in 0.1 M NaOH is 2.9 eV, quite similar to that estimated after passivation in acidic solution. Conversely, E_g values very close to

that reported for Fe_2O_3 were estimated for passive films grown on 316L and 304L SS (see Table 4-9).

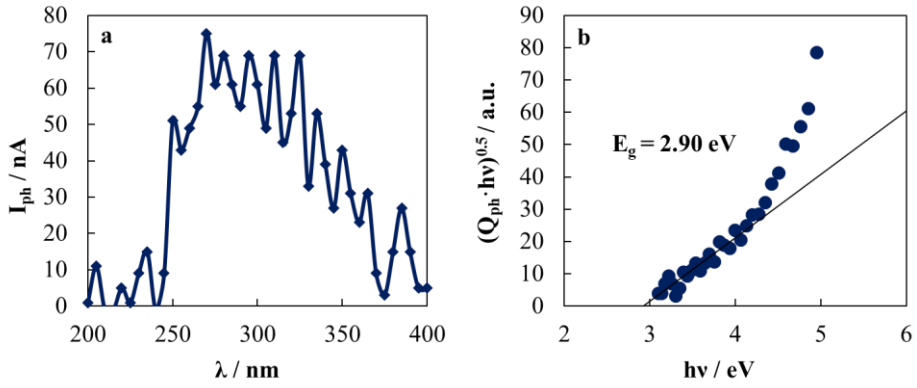

Fig. 4-30. a) Raw photocurrent spectrum for passive film grown on Duplex SS after 15 h anodic polarization at 0.2 V vs SSC in 0.1 M NaOH solution recorded at U_E = 0.1 V vs SSC in 0.1 M ABE (pH ~ 8). b) $(Q_{ph}\ hν)^{0.5}$ vs hν plot.

The measured photocurrent is anodic, according to the current transient recorded under constant irradiating wavelength (λ = 280 nm) reported in Fig. 4-31, suggesting that passive films grown on different stainless steel grades in both acidic and alkaline solutions behave like n-type semiconductor. Anodic spikes were also recorded as displayed in Fig. 4-31b, suggesting a strong recombination of the photo-generated charge carriers as usually could happen with iron oxide based electrode.

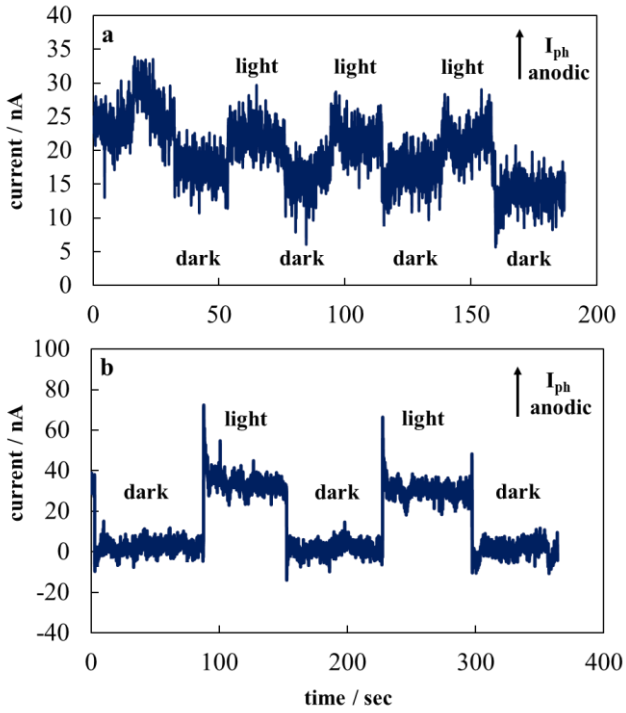

Fig. 4-31. Current vs time curves recorded at U_E = 0.1 V vs. SSC in 0.1 M ABE at λ = 280 nm for passive films grown after 15 h of anodic polarization in a) 5 mM H_2SO_4 and b) 0.1 M NaOH.

Band gap values estimated for all passive films are listed below in Table 4-9:

Table 4-9. Band gap values for passive films grown on different stainless steel grades after anodic polarization at pH ~ 2 and pH ~ 13.

Passivation conditions	Stainless Steel	E_g / eV
0.85 V vs SSC in 5 mM H_2SO_4 for 15 h	304L	2.70
	31L	3.00
	Duplex	2.90
0.2 V vs SSC in 0.1 M NaOH for 15 h	304L	2.20
	316L	2.40
	Duplex	2.90

According to Eq. 3.10, passive film grown on 304L are characterized by higher iron content if compared with those grown on duplex and 316L SS, as expected considering that passive films with different structure and composition are grown for SS containing and not containing Mo. In fact, according to *Marcus et al*. passive films grown on 316L SS in acidic solution by potentiostatic polarization, display a bilayered structure with an inner layer mainly based on Cr_2O_3 and an outer Mo containing iron oxide layer. The latter has a thickness of ~ 5 Å that decreases during the anodic polarization, while the inner layer is ~ 18 Å thick[176]. Therefore, the optical band gap estimated for 316L and Duplex SS (both containing Mo) refers to the inner film due to the very low thickness of the outer layer. Moreover, a lower band gap is reported for passive films grown on SS surfaces if compared with pure Cr_2O_3 (i.e. 3.4 eV) since small amount of Fe are present in the oxide layer reducing the band gap of passive films. This effect is more evident if passive films grown on 304L are considered. In fact, anodic polarization of FeCrNi alloys in acidic solution lead to the formation of a bilayered structure with an inner thicker Cr – Fe mixed oxide layer and an outer thin chromium hydroxide layer[177]. This finding suggests that the measured band gap for passive films grown on 304L is in agreement with the formation of an iron-chromium mixed oxide film, with a Cr/Fe ratio close to 1 according to Eq. 3.10, while no optical transitions related to the outer thin hydroxide layer are obtained. Conversely, when anodic polarization is performed in alkaline solution, an optical band gap very close to that reported for Fe_2O_3[115] was estimated for passive films grown on 304L and 316L SS. Moreover, the higher measured photocurrent with respect to that recorded in the case of passivation in acidic solution (see Fig. 4-29 and Fig. 4-30) and the photocurrent transients are in agreement with the formation of a passive film consisting of iron oxide[178], that is stable at pH 13 according to the Pourbaix diagram[150]. Notably, the optical band gap reported for passive film grown on duplex is higher if compared with E_g values estimated for passive films grown on austenitic stainless steel,

suggesting the formation of an iron-chromium mixed oxide film, in agreement with the higher Cr content of this steel. Independently on the passivation solution, the n-type semiconducting behavior of passive films grown on different SS grades is in agreement with the formation of an iron doped Cr_2O_3 or an iron-chromium mixed oxide. Moreover, the presence of iron in the passive film shifts the Fermi level toward cathodic direction near the conductive band edge, as expected for an extrinsic n-type semiconductor. This experimental finding suggests that iron doping makes passive films grown on austenitic and duplex SS more stable toward anodic dissolution.

4.3.4 *Concluding Remarks*

According to the experimental results, band gap values of passive films grown on different SS grades after anodic polarization depend on both SS composition and electrolyte pH. Potentiostatic polarization of different stainless steel grades below the transpassive potential in both acidic and alkaline solution induces the formation of passive films behaving as n-type semiconductors and, therefore, they result stable against anodic dissolution with a passive region wider with respect to pure chromium. For 304L and 316L polarization at pH 2 induces the formation of thin passive films with a high band gap value, suggesting the formation of an iron containing C_2O_3 layer. Conversely, a lower band gap was measured after passivation in alkaline solution, due to the formation of an almost pure iron oxide. Passive films on duplex SS have a band gap of 2.9 eV independently of the pH of the solution. A Cr_2O_3 rich passive film is formed in both cases due to the high Cr content of this steel, behaving as n-type semiconductor due to the presence of iron.

5 Effect of Molybdenum and Surface Roughness on Corrosion Resistance of Different Stainless Steel Grades

Highly alloyed stainless steels (SSs) are usually employed as construction materials that are expected to come in contact with aggressive environments where localized corrosion is likely to occur. They usually contain significant concentration of chromium and molybdenum since these alloying metals reduce the susceptibility of the steels toward localized corrosion phenomena such as pitting. However, there are environments where SSs suffer general corrosion due to transpassive dissolution promoted by highly oxidizing environments (such as those in pulp bleaching processes) or by high temperature electrolytes under irradiation[179]. In such cases a large concentration of Cr and Mo can enhance transpassive dissolution with detrimental effect on the degradation rate of the steels[179–181].

In previous published literature[20,179–183] the transpassive dissolution mechanism of several austenitic SSs was studied. The authors proved that a key role is played by the transpassive dissolution of Cr, which causes a reduction of chromium concentration in the passive films and a consequent iron enrichment. According to[179] a secondary passivation can start when the iron in the outermost layer is higher than that of chromium, thus the presence of elements other than Cr and Fe can hinder the establishment of a secondary passivation. However, the authors did not explicitly mention how the electronic properties of the films change during the switching from passive to transpassive region and how they affect the electrochemical processes occurring at the metal/film and film/electrolyte interfaces.

In this work we studied the change in the band gap, flat band potential and impedance of passive films grown on different stainless steel grades (AISI 304L, AISI 316L and Duplex SS) as a function of the polarization potential. Passive films were grown in quasi neutral solution (pH ~ 7) at different polarizing

potentials, in order to get more insight into dissolution phenomena on equipment materials typically involved in food and beverage industries. Since surface roughness plays an important role in the frame of good manufacturing practises, passivation was also performed on the same stainless steel grades with a standard surface finishing, in order to assess the effect of R_a on electronic properties, composition, thickness and structure of passive films.

Photoelectrochemical measurements were carried out to estimate the band gap of the films grown on these steels, while impedance measurements were carried out to evaluate their overall impedance. The results were used to rationalize the mechanism of transpassive dissolution of SSs as a function of their composition, and to sketch the potential distribution across the metal/passive film/electrolyte interface.

5.1 Passive films growth on mechanically treated SS samples

Polarization curves for SS samples with a mirror surface finishing recorded in Phosphate Buffer solution (pH ~ 7) are reported in Fig. 5-1a. The potential was scanned at 2 mV s^{-1} in the anodic direction starting from a polarizing potential slightly higher with respect to the equilibrium potential for hydrogen evolution at pH 7 (i.e. ~ - 0.6 V vs Ag/AgCl). A careful inspection of the polarization curves (see Fig. 5-1b) reveals the presence of an anodic current peak at potential higher than 0.5 V vs Ag/AgCl for 316L and duplex SSs, which is less pronounced for 304L. This peak is due to the oxidation of Cr_2O_3 to Cr(VI) containing species, which are highly soluble in aqueous solutions. Indeed, the equilibrium potential for the corresponding processes can be calculated according to the following eqs.[150]:

a. $Cr_2O_{3(hydroxide)}/CrO_4^{2-}$

   $U_{eq} = 1.386 – 0.0985\ pH + 0.0197 \log[CrO_4^{2-}] = 0.38$ V vs. Ag/AgCl

b. $Cr_2O_{3(oxide)}/CrO_4^{2-}$

$U_{eq} = 1.311 - 0.0985\ pH + 0.0197 \log[CrO_4^{2-}] = 0.30$ V vs. Ag/AgCl

c. $Cr_2O_{3(hydrated\ hydroxide)}/CrO_4^{2-}$

$U_{eq} = 1.244 - 0.0985\ pH + 0.0197 \log[CrO_4^{2-}] = 0.24$ V vs. Ag/AgCl

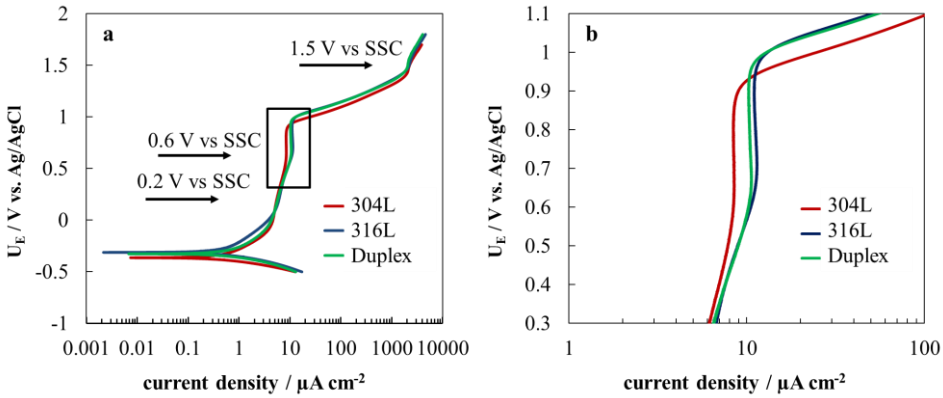

Fig. 5-1. a) polarization curves for mirror finished 304L, 316L and Duplex SS recorded at 2 mV s^{-1} in phosphate buffer solution (pH 7) and b) magnification of the recorded polarization curves.

Moreover, by further increasing the polarizing potential oxygen evolution starts to occur on all the SSs, at a current density exponentially increasing by increasing the potential. The corresponding Tafel lines (see Fig. 5-1b) have the same slope but the intercept on the Y axis is lower for 304L.

In order to follow the change in the passive films properties on going from the passive to the transpassive region, the SSs were potentiostatically polarized at 0.2 V, at 0.6 V and at 1.5 V. At 0.2 V vs Ag/AgCl chromium dissolution as chromate ions is not thermodynamically possible, since the equilibrium potential for the corresponding half-cell reaction is between 0.38 V vs. SSC and 0.24 V vs. SSC according to the above reported equilibria. Conversely, at 0.6 V vs. SSC chromate ions formation is thermodynamically allowed and at 1.5 V vs. SSC

oxygen evolution can occur.

In Fig. 5-2 the current density vs time curves recorded during potentiostatic polarization at 0.2 V and 0.6 V vs. SSC on SS samples are reported.

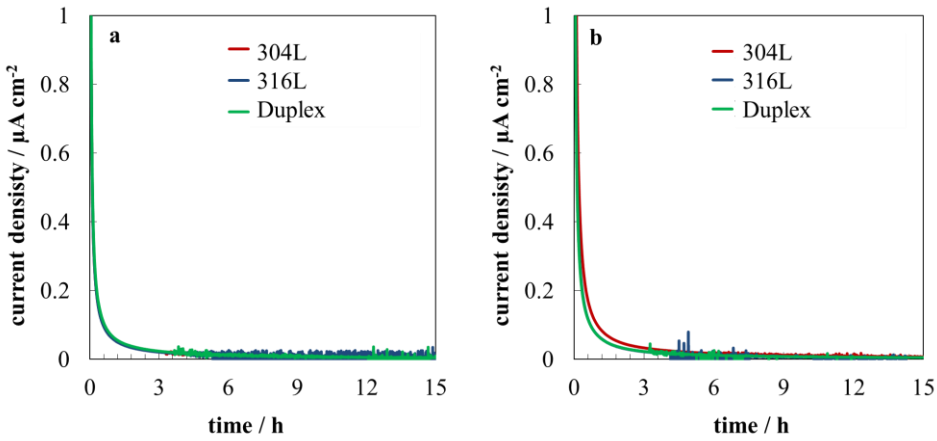

Fig. 5-2. Current vs time curves recorded under potentiostatic polarization at a) U_E = 0.2 V vs Ag/AgCl and b) U_E = 0.6 V vs Ag/AgCl in Buffer Phosphate solution (pH ~ 7) for SSs samples with a mirror surface finishing.

The current density decreases monotonically to zero for long polarization time. At 0.2 V vs Ag/AgCl the circulated charge per unit surface, *q*, is not appreciable different for the different SS grades (in the order of ~ 2.8 mC cm^{-2}), whilst during the polarization at 0.6 V vs Ag/AgCl it is higher for 304L than that measured for the other steels.

According to the current vs. time curves reported in Fig. 5-3, current density recorded in transpassive condition is much higher if compared with that recorded at 0.6V and 0.2V vs SSC, even after very long polarization time. At this potential O_2 evolution occurs with consequent local decrease of the pH close to the surface of SS samples. Notably, after 15 h of anodic polarization at 1.5 V vs SSC, SSs surface appears yellow (see Fig. 5-4**Fig. 5-4**). These findings suggest that after potentiostatic polarization at 1.5 V vs Ag/AgCl, passive films are thicker than those grown at 0.6 V and 0.2 V vs SSC.

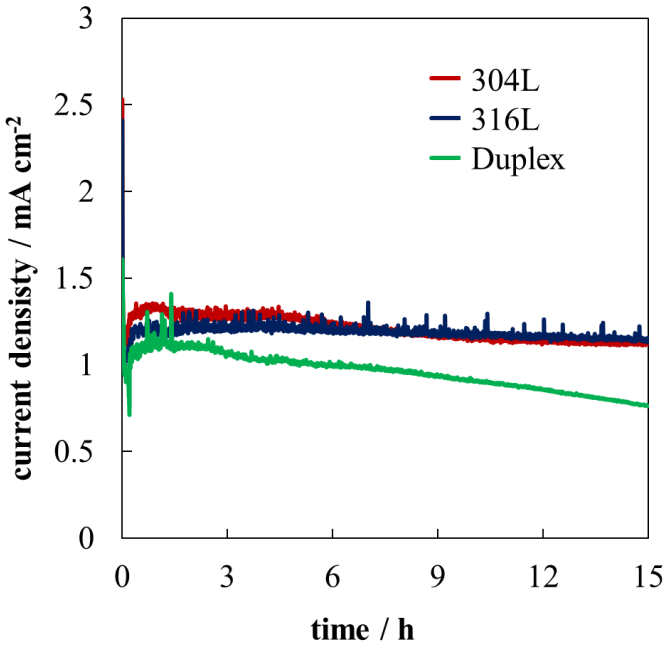

Fig. 5-3. Current vs time curves recorded under potentiostatic polarization at U_E = 1.5 V vs Ag/AgCl in Buffer Phosphate solution (pH ~ 7) for SSs samples with a mirror surface finishing.

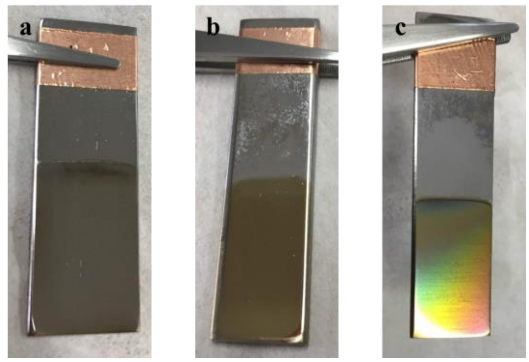

Fig. 5-4. Photos related to mirror finished different stainless steel samples after polarization at U_E = 1.5 V vs Ag/AgCl in Buffer Phosphate solution (pH ~ 7).

5.1.1 *Photoelectrochemical characterization*

Photoelectrochemical measurements were carried out in order to gain more insight into solid state properties of passive films as a function of the passivation conditions. Primarily, in order to have a reference, photocurrent spectra related to native oxide grown by air exposure on different SS grades were reported. In Fig. 5-5 photocurrent spectra recorded in Phosphate Buffer solution (pH ~ 7) at the open circuit potential (U_{OC} ~ -0.2 V vs SSC) are reported. By assuming non direct optical transitions, a band gap value of ~ 3.0 eV was estimated for the native oxide grown on 316L and 304L SSs coupons while a slightly higher value (~ 3.1 eV) was estimated for the native oxide grown on Duplex SS (see Table 5-1). No marked differences are observed in the measured photocurrent for all passive films under investigation.

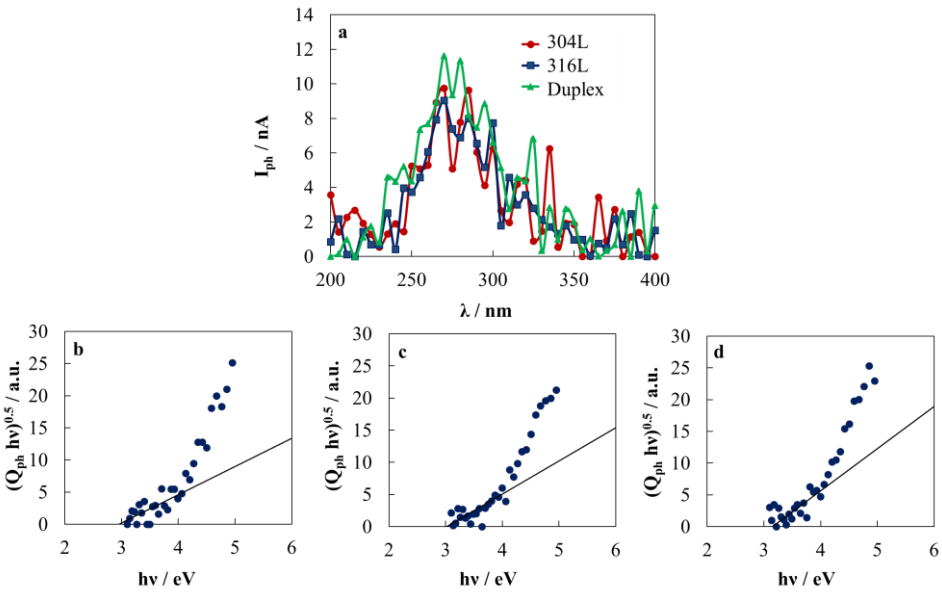

Fig. 5-5. a) Raw photocurrent spectra recorded at the open circuit potential (U_{OC} ~ -0.2 V vs SSC) in Buffer Phosphate solution for native oxide grown on 304L, 316L and Duplex stainless steel with a mirror surface finishing by air exposure. $(Q_{ph}\ h\nu)^{0.5}$ vs hν plot is reported for b) 304L c) 316L and d) Duplex stainless steels.

Table 5-1. Band gap values for native oxide grown by air exposure on SSs samples with a mirror surface finishing.

native oxide	E_g / eV
304L	2.95
316L	3.02
Duplex	3.14

Fig. 5-6 displays the photocurrent spectra for passive films grown after potentiostatic polarization at 0.2 V vs SSC in Phosphate Buffer solution (pH ~ 7), recorded in the same solution at 0.1 V vs SSC.

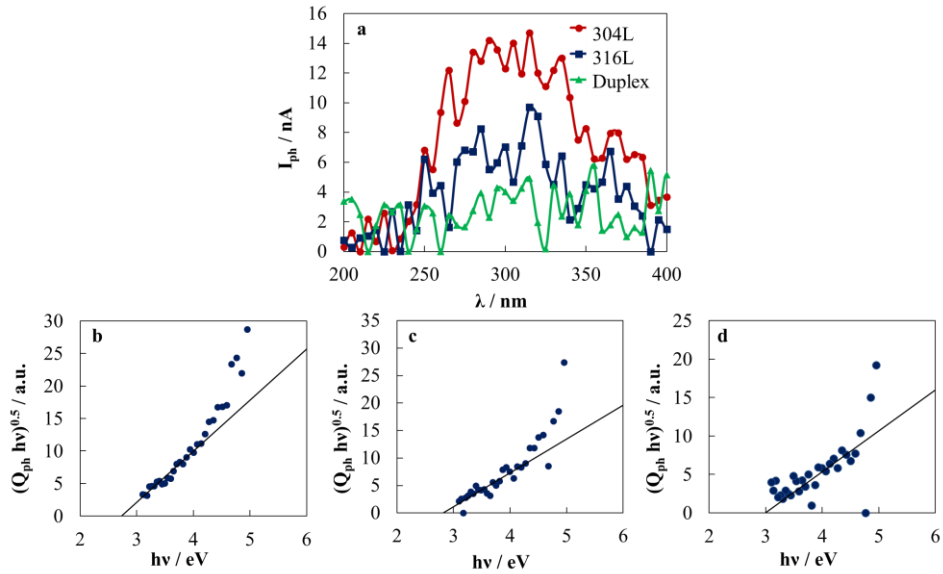

Fig. 5-6. a) Raw photocurrent spectra recorded at 0.1 V vs SSC in Buffer Phosphate solution for passive films grown on 304L, 316L and Duplex stainless steel with a mirror surface finishing passivated at 0.2 V vs SSC in Phosphate Buffer solution (pH ~ 7). $(Q_{ph}\ hv)^{0.5}$ vs hv plot is reported for b) 304L c) 316L and d) Duplex stainless steels.

According to Eq. 3.10, a band gap value of ~ 2.8 eV was estimated for passive films grown on 304L and 316L, while a higher value was estimated for passive films grown on Duplex SSs (~ 3.00 eV) (see Table 5-2). In order to check the

real sign of the measured photocurrent, current vs time curves were recorded at 0.1 V vs. SSC in Phosphate Buffer solution by manually chopping sample irradiation under monochromatic irradiation (λ = 280 nm). According to the current transients reported in Fig. 5-7, anodic photocurrent was measured, in agreement with the formation of a n-type SC.

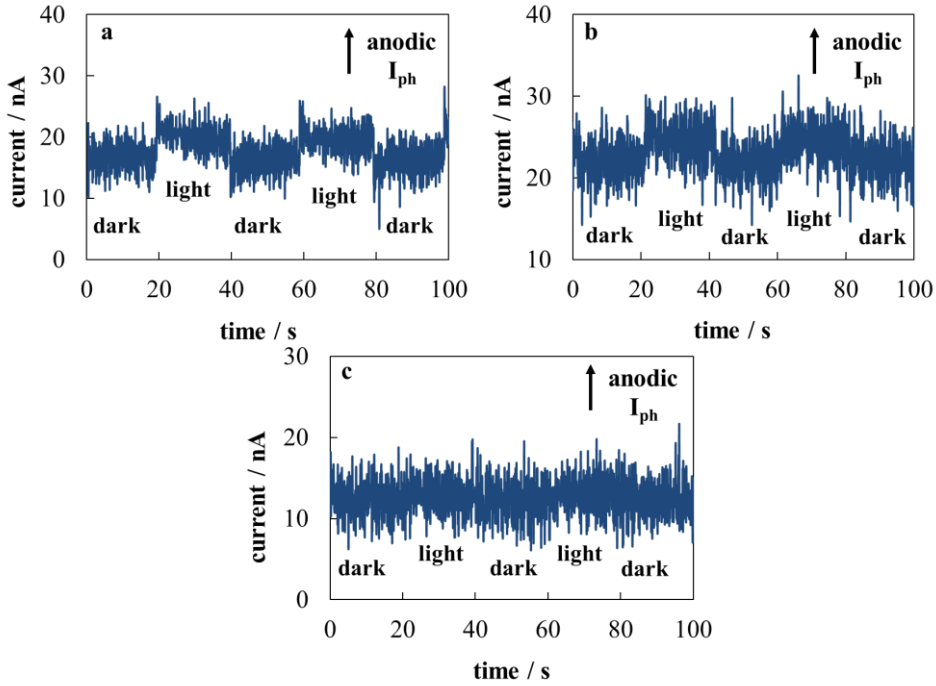

Fig. 5-7. Current vs time curves recorded at U_E = 0.1 V vs SSC in Phosphate Buffer solution (pH ~ 7) at λ = 280 nm for passive grown after 15 h of anodic polarization at U_E = 0.2 V vs SSC in Phosphate Buffer solution on a) 304L, b) 316L and c) Duplex mirror finished stainless steels.

Notably, extremely low photocurrent was measured in the case of passive films grown on DSS suggesting the formation of a thin layer if compared to those grown in the austenitic grades.

The same photoelectrochemical investigation was carried out for passive films grown on different stainless steel grades after anodic polarization at 0.6 V vs SSC. The raw photocurrent spectra recorded at 0.2 V vs. SSC are reported in Fig. 5-8. By assuming a non direct optical transition, a band gap of 2.4 eV was

estimated for oxide layer grown on 304L, while 2.9 eV and 3.3 eV were obtained for 316L and Duplex SSs, respectively (see Table 5-2).

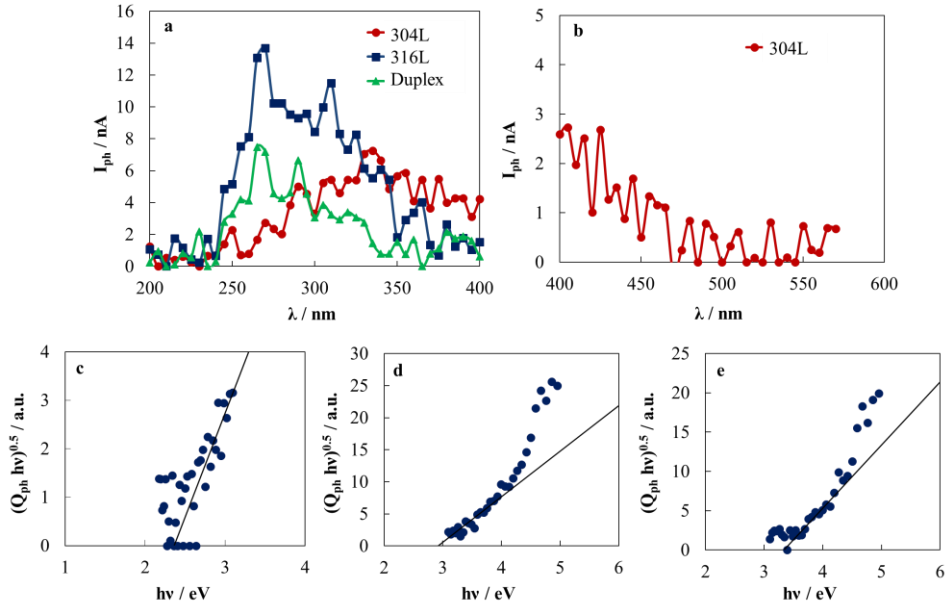

Fig. 5-8. a) Raw photocurrent spectra recorded at 0.2 V vs SSC in Buffer Phosphate solution for passive films grown on 304L, 316L and Duplex stainless steel with a mirror surface finishing passivated at 0.6 V vs SSC in Phosphate Buffer solution (pH ~ 7) a) without a cut-off filter b) with a cut-off filter. $(Q_{ph}\ h\nu)^{0.5}$ vs hν plot is reported for b) 304L c) 316L and d) Duplex stainless steels.

According to the current transient under constant irradiating wavelength (i.e. λ = 280 nm), the measured photocurrent is anodic (see Fig. 5-9), in agreement with the formation of n-type semiconductor passive films.

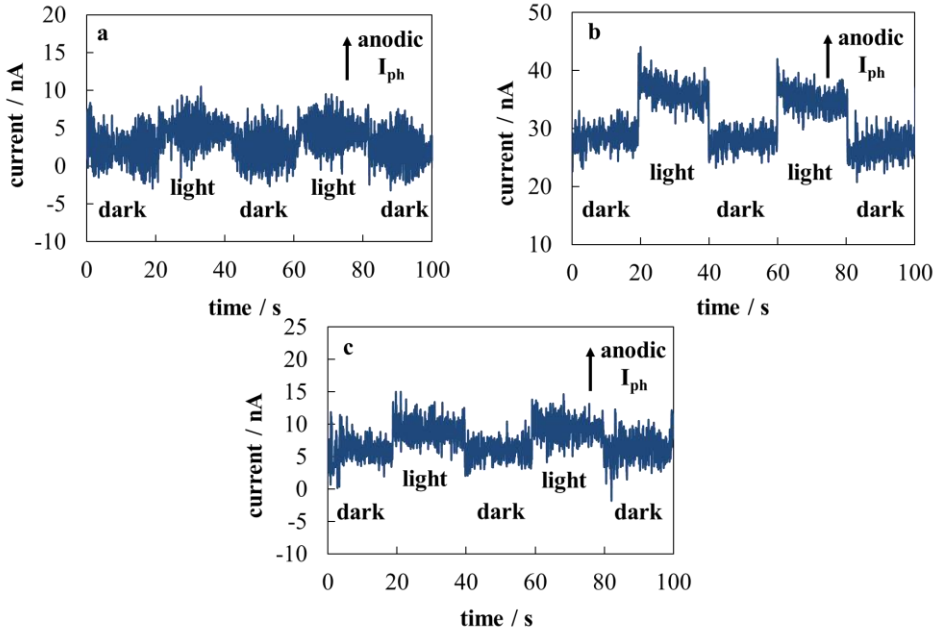

Fig. 5-9. Current vs time curves recorded at U_E = 0.2 V vs SSC in Phosphate Buffer solution (pH ~ 7) at λ = 280 nm for passive grown after 15 h of anodic polarization at U_E = 0.6 V vs SSC in Phosphate Buffer solution on a) 304L, b) 316L and c) Duplex mirror finished stainless steels.

Finally, raw photocurrent spectra for passive films on mirror surface finished SS grown at 1.5 V vs. SSC in Buffer Phosphate solution and recorded at 0.2 V vs. SSC in the same electrolyte are displayed in Fig. 5-10. The measured photocurrent is significantly higher than that recorded for passive films grown at 0.6 V vs SSC and a red shift of the light absorption threshold is present (see Fig. 5-10b) corresponding to optical band gap values significantly lower (i.e. ~ 2.4 eV) for passive films grown both on austenitic and duplex grades (see Table 5-2). As displayed in the current transients reported in Fig. 5-11, anodic photocurrent was measured confirming that passive films behave like n-type SC.

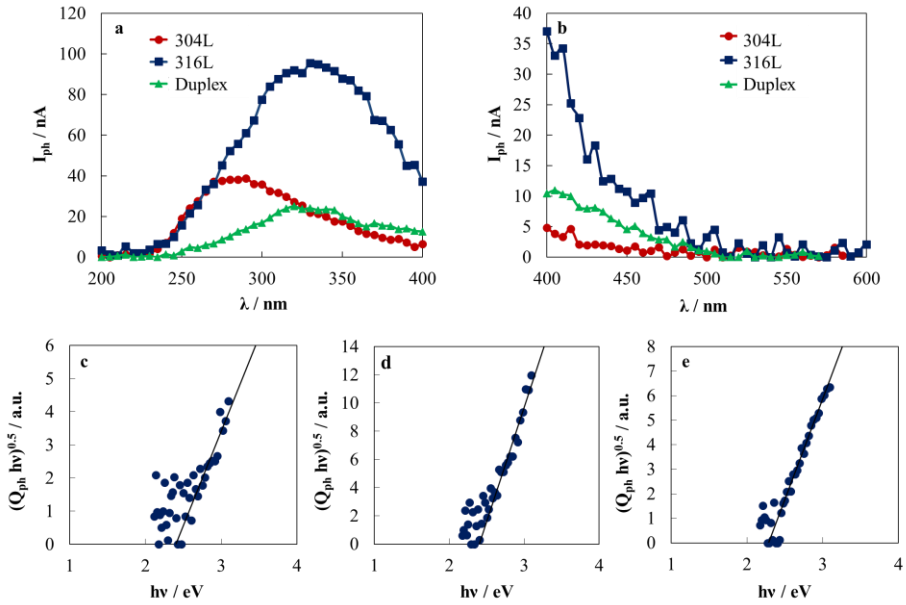

Fig. 5-10. Raw photocurrent spectra recorded at 0.2 V vs SSC in Buffer Phosphate solution for passive films grown on 304L, 316L and Duplex stainless steel with a mirror surface finishing passivated at 1.5 V vs SSC in Phosphate Buffer solution a) without a cut-off filter b) with a cut-off filter. $(Q_{ph}\ h\nu)^{0.5}$ vs hν plot is reported for c) 304L d) 316L and e) Duplex stainless steels.

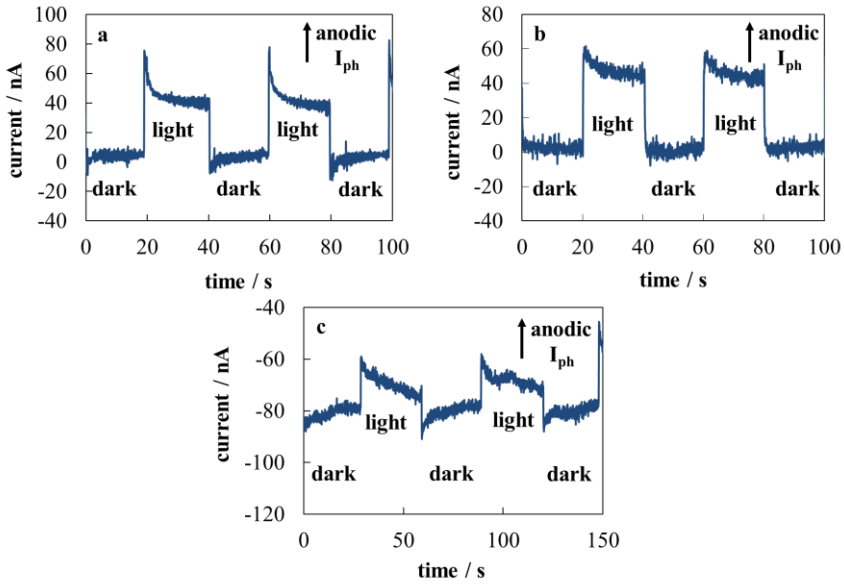

Fig. 5-11. Current vs time curves recorded at U_E = 0.2 V vs SSC in Phosphate Buffer solution (pH ~ 7) at λ = 280 nm for passive grown after 15 h of anodic polarization at U_E = 1.5 V vs SSC in Phosphate Buffer solution on a) 304L, b) 316L and c) Duplex mirror finished stainless steels.

Table 5-2. Band gap values for passive films grown on SSs samples under different polarizing potentials in Buffer Phosphate solution (pH ~ 7) on SS samples with a mirror surface finishing.

Passivation conditions	SS	Eg / eV	colour
0.2 V vs Ag/AgCl for 15 h	304L	2.44	No
	316L	2.81	No
	Duplex	3.00	No
0.6 V vs Ag/AgCl for 15 h	304L	2.73	No
	316L	2.92	No
	Duplex	3.34	No
1.5 V vs Ag/AgCl for 15 h	304L	2.4	light yellow
	316L	2.4	yellow
	Duplex	2.29	yellow

5.1.2 *Impedance measurements*

In Fig. 5-12, the impedance spectra in the Nyquist representation recorded at 0.15 V vs SSC (i.e. under anodic polarization with respect to U_{FB}) in Buffer Phosphate solution are reported. The dependence of the imaginary impedance component on the real component is described by a portion of a depressed semicircle. In order to estimate the resistance of passive films, impedance spectra were fitted according to the equivalent circuit reported in Fig. 4-12. The parameters provided by the best fitting procedure according to the equivalent circuit of Fig. 4-12 are reported in Table 5-3. For comparison, fitting parameters for the native oxide grown on mirror finished SSs by atmospheric exposure are also reported. In spite the strong Cr depletion in the oxide layer induced by passivation at 1.5 V vs. SSC, passive films grown on austenitic and Duplex SSs

display a very high oxide resistance.

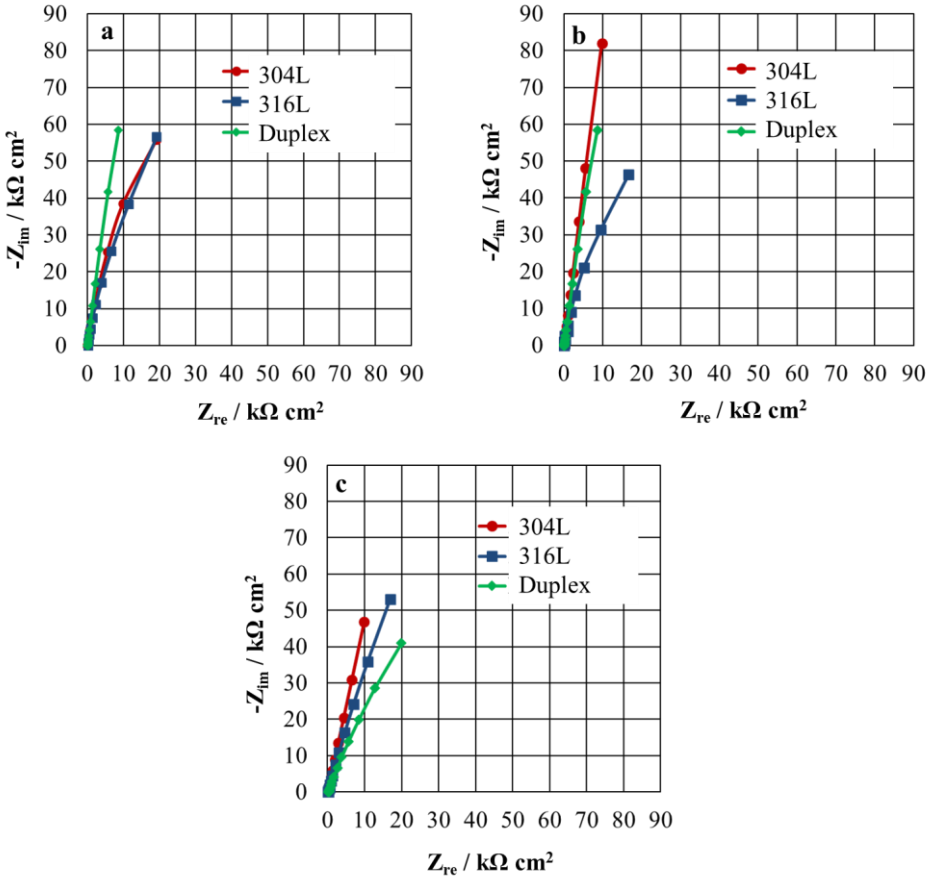

Fig. 5-12. EIS spectra in Nyquist representation recorded at U_E = 0.15 V vs Ag/AgCl in buffer phosphate solution (pH ~ 7) for passive films grown after 15 h of anodic polarization at a) U_E = 0.2 V vs Ag/AgCl, b) U_E = 0.6 V vs Ag/AgCl and c) U_E = 1.5 V vs Ag/AgCl in Buffer Phosphate solution (pH ~ 7).

Other interesting information can be obtained by the constant phase element modulus and exponent, α, reported in Table 5-3. Q_{CPE} values are significantly lower than that measured for the native oxide on SSs samples, and the corresponding best fitting are higher[55]. The causes of the non ideal capacitive behaviour of these passive films can be different. In previous papers[55,184] for

passive films grown on as supplied 316L SS, such behaviour was explained by the charge accumulation due to surface states and/or adsorption phenomena involving the oxide surface.

Table 5-3. Fitting parameters of EIS spectra on passive films grown on different stainless steel grades at different polarizing potential in buffer phosphate solution (pH ~ 7) according to the equivalent circuit reported in the inset of Fig. 4-12.

Passivation conditions	**SS**	R_{el} $\Omega\ cm^2$	R_{ox} $\Omega\ cm^2$	Q_{CPE} $S\ s^{\alpha}\ cm^{-2}$	**α**	χ^2	**δ** nm
native oxide	**304L**	57	$1.2 \cdot 10^5$	$7.5 \cdot 10^{-5}$	0.89	$3.16 \cdot 10^{-3}$	1.5
	316L	165	$1.3 \cdot 10^5$	$8.1 \cdot 10^{-5}$	0.88	$5.60 \cdot 10^{-3}$	1.64
	Duplex	219	$1.2 \cdot 10^6$	$5.9 \cdot 10^{-5}$	0.87	$5.68 \cdot 10^{-3}$	2.8
0.2 V vs Ag/AgCl for 15 h	**304L**	92	$3.1 \cdot 10^5$	$2.4 \cdot 10^{-5}$	0.92	$1.24 \cdot 10^{-3}$	2.7
	316L	127	$2.5 \cdot 10^5$	$2.4 \cdot 10^{-5}$	0.92	$2.30 \cdot 10^{-3}$	2.4
	Duplex	154	$5.9 \cdot 10^5$	$2.2 \cdot 10^{-5}$	0.93	$2.03 \cdot 10^{-3}$	2.2
0.6 V vs Ag/AgCl for 15 h	**304L**	262	$3.1 \cdot 10^6$	$2.0 \cdot 10^{-5}$	0.94	$1.51 \cdot 10^{-3}$	1.9
	316L	90	$2.5 \cdot 10^5$	$3.0 \cdot 10^{-5}$	0.91	$4.15 \cdot 10^{-3}$	2.6
	Duplex	111	$1.4 \cdot 10^6$	$2.5 \cdot 10^{-5}$	0.93	$2.04 \cdot 10^{-3}$	1.8
1.5 V vs Ag/AgCl for 15 h	**304L**	92	$6.0 \cdot 10^6$	$3.2 \cdot 10^{-5}$	0.86	$1.15 \cdot 10^{-3}$	6.2
	316L	173	$1.2 \cdot 10^6$	$2.7 \cdot 10^{-5}$	0.84	$2.31 \cdot 10^{-2}$	11.4
	Duplex	318	$2.2 \cdot 10^5$	$3.0 \cdot 10^{-5}$	0.83	$2.39 \cdot 10^{-3}$	13.5

Due to the improved surface finishing of these steels as well as encouraged by the lower modulus of the constant phase elements, we suggested to explain the not ideal capacitive behaviour of the passive films assuming a not constant resistivity across the oxides[170,171]. In such case we can use the power-law model. Assuming $\varepsilon = 12$ and limiting value of resistivity of 500 $\Omega \cdot$ cm taken from calibration of Fe17Cr stainless steel[170], it is possible to estimate the passive films

thickness reported in Table 5-3. According to the power law approach passive films grown in Phosphate Buffer solution are thicker than those grown by atmospheric exposure. The data also show that the film grown at 1.5 V vs SSC on 304L is thinner than those grown on 316L and duplex. This is in agreement with the colour shown by the samples soon after the anodic polarization (see Fig. 5-4).

In Fig. 5-13Fig. **5-15** Mott- Schottky curves (C_M^{-2} vs. U_E) recorded at different frequencies of the a.c. signal for passive films grown at 0.2 V, 0.6 V and 1.5 V vs Ag/AgCl on austenitic and duplex SS in Phosphate Buffer solution are reported. The exploited potential range is between the equilibrium potential for hydrogen evolution at pH 7 and the equilibrium potential of Cr(III) oxidation to chromate ions (see Eqs. a-c). The measured capacitance is sensitively influenced by the a.c. signal frequency thus the interpretation of the differential capacitance curves by a classic Mott-Schottky approach is not suitable to get any reliable information on the donor density (N_d) of the investigated passive film[100,117]. However, a few qualitative information can be obtained from the curves of Fig. 5-13Fig. **5-15**. The capacitance increases when the polarising voltage shifts toward the cathodic direction, i.e. toward the flat band potential, confirming that all the passive films behave like n-type semiconducting materials. Notably, the comparison of the C_M^{-2} vs potential curves for the investigated passive films suggesting, at all frequencies, a U_{FB} more cathodic for passive films on 304L with respect that of passive films formed on AISI 316L and duplex SSs.

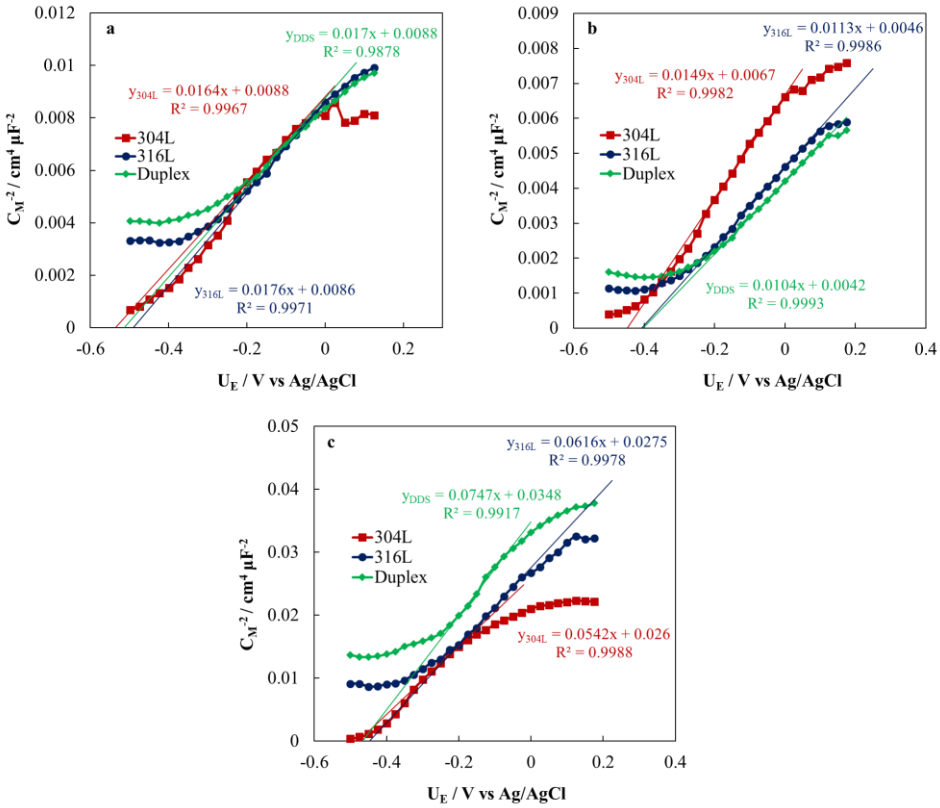

Fig. 5-13. Mott – Schottky plot and linear regression at 5 kHz in phosphate buffer solution (pH 7) for passive films grown on different stainless steel grades at a) U_E = 0.2 V vs Ag/AgCl, b) U_E = 0.6 vs Ag/AgCl and c) U_E = 1.5 V vs Ag/AgCl in phosphate buffer solution (pH 7).

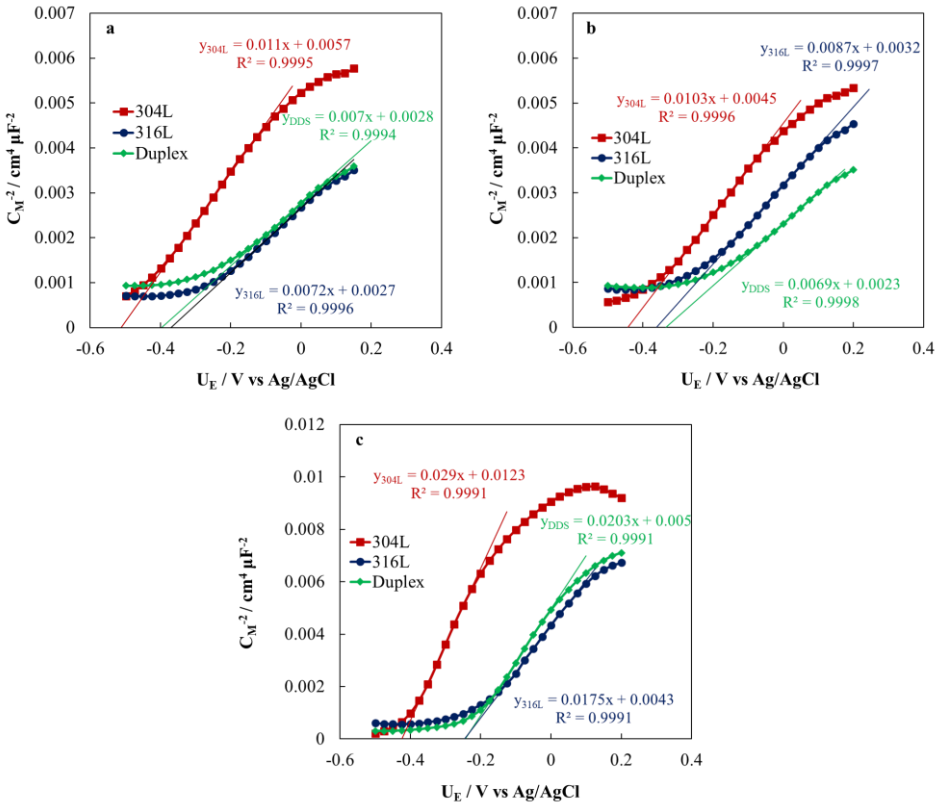

Fig. 5-14. Mott – Schottky plot and linear regression at 1 kHz in phosphate buffer solution (pH 7) for passive films grown on different stainless steel grades at a) U_E = 0.2 V vs Ag/AgCl, b) U_E = 0.6 vs Ag/AgCl and c) U_E = 1.5 V vs Ag/AgCl in phosphate buffer solution (pH 7).

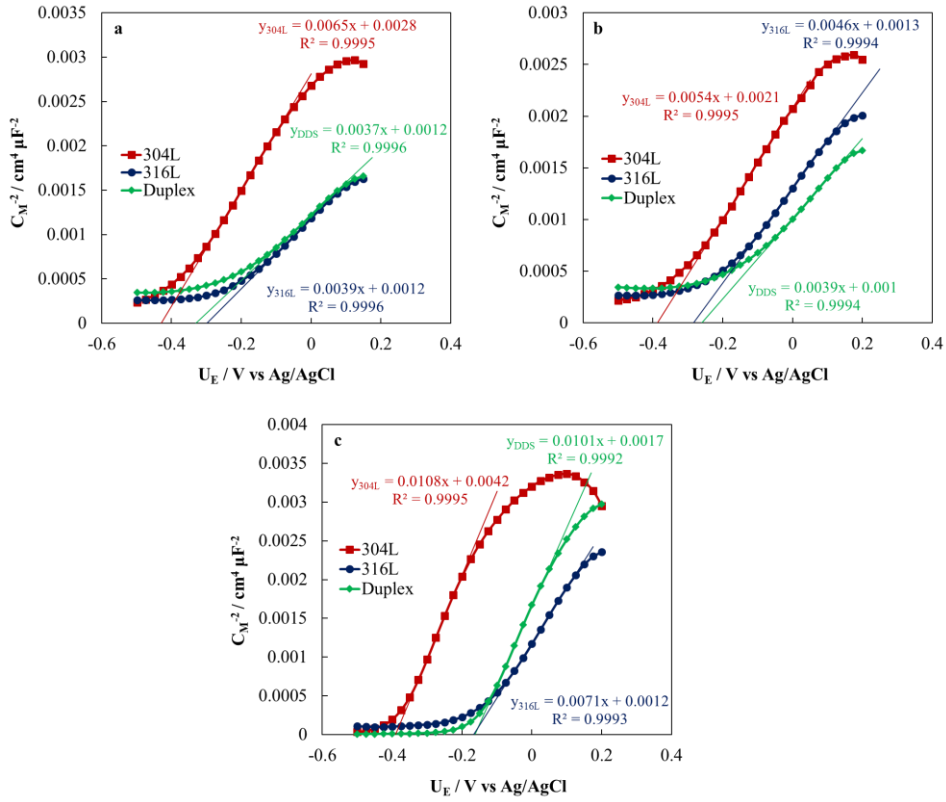

Fig. 5-15. Mott – Schottky plot and linear regression at 100 Hz in phosphate buffer solution (pH 7) for passive films grown on different stainless steel grades at a) U_E = 0.2 V vs Ag/AgCl, b) U_E = 0.6 vs Ag/AgCl and c) U_E = 1.5 V vs Ag/AgCl in phosphate buffer solution (pH 7).

The current vs time transients recorded by polarizing the SSs at 0.2 V and 0.6 V va Ag/AgCl can be interpreted in the frame of a high field mechanism (HFM)[185]. Taking into account the resistance and the capacitance of the native oxides (see Table 5-3), the corresponding time constant $\tau = RC$ is in the order of 10 s, thus after the first minute of polarization the circulating current is Faradic and it can be associated to alloy metals oxidation inducing a film thickening and/or a change in the film composition.

During the potentiostatic transient the potential drop across the metal/oxide electrolyte interface is distributed according to the scheme of Fig. 5-16, where

$\Delta\varphi_{SC}$ and $\Delta\varphi_{H}$ represent the potential differences at the SS/passive film and passive film/electrolyte interfaces, respectively.

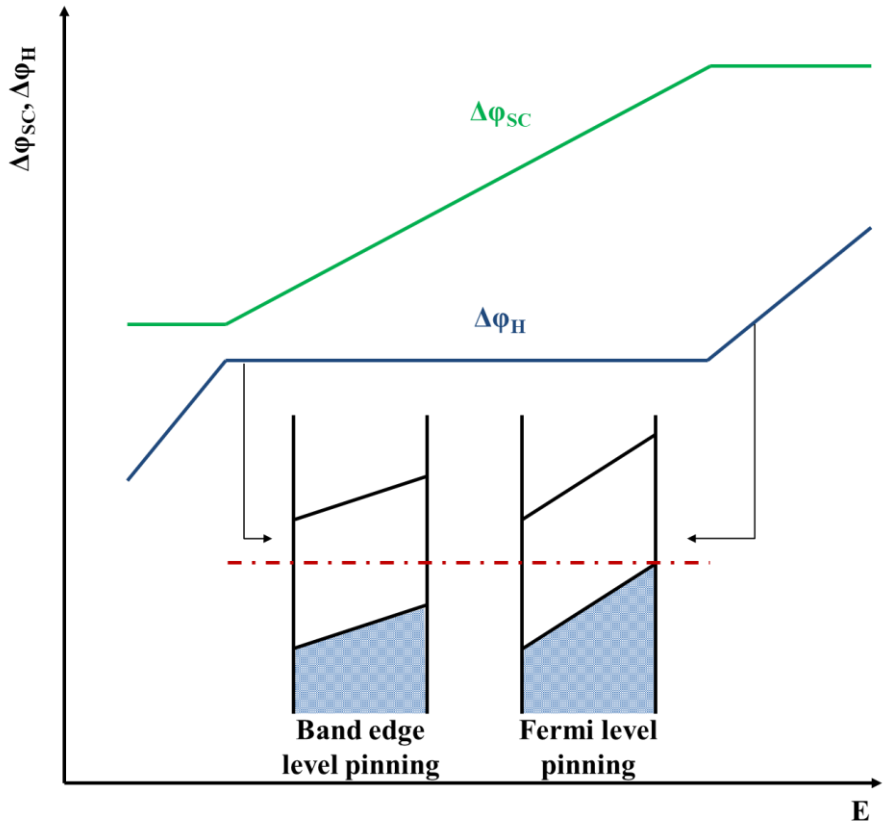

Fig. 5-16. Schematic representation of the variation of the potential across the passive film (adapted from Sato)[164].

In the range of potential of the passive state, the oxide film is in the condition of band edge level pinning at the film/solution interface. Hence, the potential difference $\Delta\phi_{H}$ across the oxide/electrolyte interface is constant independently on the potential of the passive state. This implies that by increasing the anodic polarization, $\Delta\varphi_{SC} = U_{E} - U_{FB}$ increases with consequent increasing of the electric field across the oxide.

The photoelectrochemical investigation suggests that the polarization at 0.2 V vs Ag/AgCl slightly reduces the band gap of the passive films on all the SSs with

respect to the corresponding native oxides, suggesting an increase in the Fe/Cr ratio in the passive film due to the oxidation of iron from the alloy. Since at pH 7 the passive films are stable and below the thermodynamic equilibrium potential for chromate formation (i.e. at 0.2 V vs SSC) the circulated charge induces a film thickening. Using the Faraday's law, the thickening of the oxide with respect to the native is in the order of 0.5-1.5 nm:

$$d = \frac{M_{ox} q}{zF\rho_{ox}} \qquad (5)$$

where M_{ox} is the molar mass of the oxide layer (g mol^{-1}), q is the total circulating charge (C cm^{-2}), z represents the number of electrons transferred per ion, F is the Faraday's constant (96480 C mol^{-1}) and ρ_{ox} and d are the density (g cm^{-3}) and the thickness (cm) of the oxide layer, respectively. Since the densities of the main oxide metals are quite similar, the density of Cr_2O_3 was used for the estimation of the oxide thickening. This is confirmed by the results of Table 5-3 where the application of the power law model provides a film thickness in the order of 1 nm higher than that of the native oxide. Finally, the dependence of the capacitance on potential suggests that passive films on 304L have a flat band potential more cathodic than that of passive films on 316L and duplex. This experimental finding can be explained considering that passive films on 316L and duplex SSs contain molybdenum as Mo(IV) or Mo(VI)[15]. The incorporation of these species with a higher valence state with respect to Cr(III) and Fe(III) in the passive films creates acceptor levels close to the valence band edge according to scheme presented in Fig. 5-17.

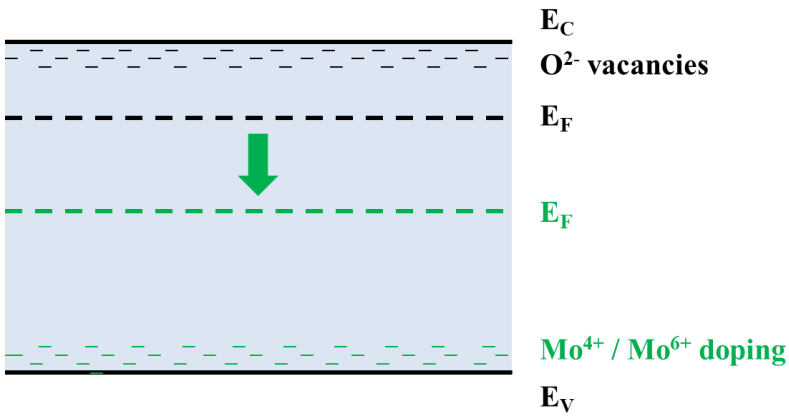

Fig. 5-17. Schematic representation of the band energy levels in the passive films grown on 316L and duplex stainless steel after Mo doping.

These states compensate the donors levels induced by the iron incorporation responsible of the n-type character of Cr_2O_3 passive films[185], thus shifting the oxide Fermi level toward the mid gap.

When the passivation is carried out at 0.6 V vs Ag/AgCl the behaviour of the passive films on the investigated SSs is different. The circulated charge during the potentiostatic transient is higher than that measured for the passive film grown at 0.2 V but the film thickness provided by the power law are comparable or lower, suggesting that the circulated charge is wasted for the formation of soluble Cr(VI) containing species.

In spite the similar behaviour of the different SSs grades, the resulting bang gaps are different. Indeed, the potential drop inside the passive film, $\Delta\Phi_{SC} = U_E - U_{FB}$ is higher for 304L with respect to those containing molybdenum. Since the passive films thicknesses are comparable the corresponding electric field strength is higher, thus allowing the oxidation of Cr(III) to Cr(VI) at lower potential**.** This explains also why for 304L the secondary passivation with the formation of an iron rich passive film (with a band gap of 2.4 eV) occur at 0.6 V vs Ag/AgCl, while higher potentials are necessary to induce Cr depletion of

passive films on 316L and duplex SSs, whose band gap is very close to that reported for Cr_2O_3 even after 15 h at 0.6 V vs Ag/AgCl. For the passive films grown at 1.5 V vs Ag/AgCl, the higher potential is enough for all steels to induce a strong chromium depletion lowering their band gap (see Table 5-3)

5.2 Passive films on rough stainless steel

In order to get more insight into the role of surface roughness on growth kinetic and on electronic and corrosion properties of passive films, potentiostatic passivation was also carried out on different stainless steel grades with a standard surface roughness.

Current vs time curves recorded in Phosphate Buffer solution at 0.6 V and 1.5 V vs SSC are displayed in Fig. 5-18.

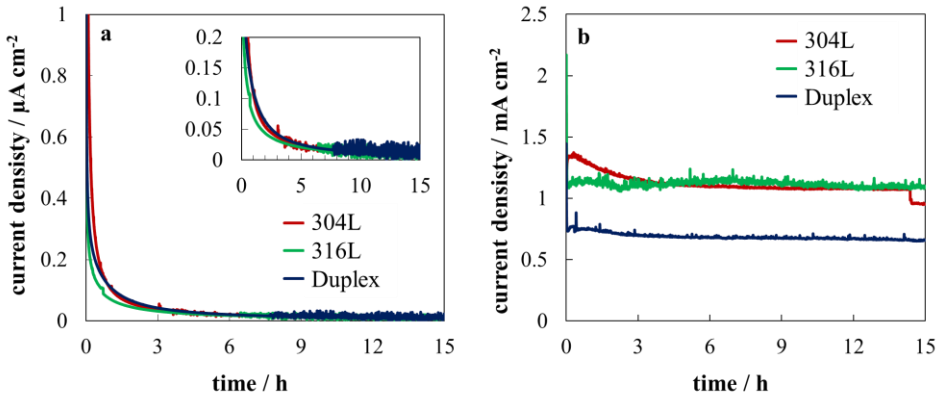

Fig. 5-18. Current vs time curves recorded for 15 h under potentiostatic polarization at a) U_E = 0.6 V vs SSC and b) U_E = 1.5 V vs SSC in Buffer Phosphate solution (pH ~ 7) for SSs samples with a standard surface finishing.

The current density recorded during polarization at 0.6 V vs. SSC monotonically decreases with time reaching an almost stationary value after ~ 7 h of polarization (see Fig. 5-18a). Conversely, as displayed in Fig. 5-18b, after 15 h of anodic polarization at 1.5 V vs SSC, the recorded current density is higher than that recorded under passive condition and a surface discoloration also

occurs due to the onset of rouging (see Fig. 5-19). Notably, 316L appears light yellow with respect to 304L and Duplex suggesting the formation of passive films with different thicknesses.

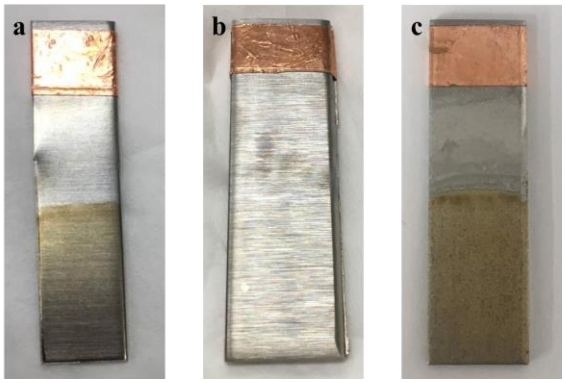

Fig. 5-19. Samples pictures after 15 h under anodic polarization at 1.5 V vs, SSC for a) 304L, b) 316L and c) Duplex stainless steel with a standard surface finishing.

5.2.1 *Photoelectrochemical characterization*

Photoelectrochemical investigation was carried out in order to assess the role of surface roughness on electronic properties of oxide layers grown under different growth conditions. Also in this case, in order to have a reference, raw photocurrent spectra, reported in Fig. 5-20, were recorded for as supplied samples in Phosphate Buffer solution (pH ~ 7) at the open circuit potential (U_{OC} ~ 0 V vs. SSC).

The corresponding optical band gaps for 304L, 316L and Duplex SSs are 2.9 eV, 3.1 eV and 3.2 eV respectively, as reported in Table 5-4. According to Eq. 3.10, passive films on duplex and 316L have a band gap very close to that reported for Cr_2O_3, while the lower E_g for passive film on 304L suggests higher iron content. Notably, the measured photocurrent for passive films grown on as supplied austenitic grades is significantly higher with respect to that measured for the native oxide grown on the corresponding mirror finished samples suggesting the

formation of thicker passive layers. Passive films on 304L and 316L are more photoactive than that grown on duplex SS.

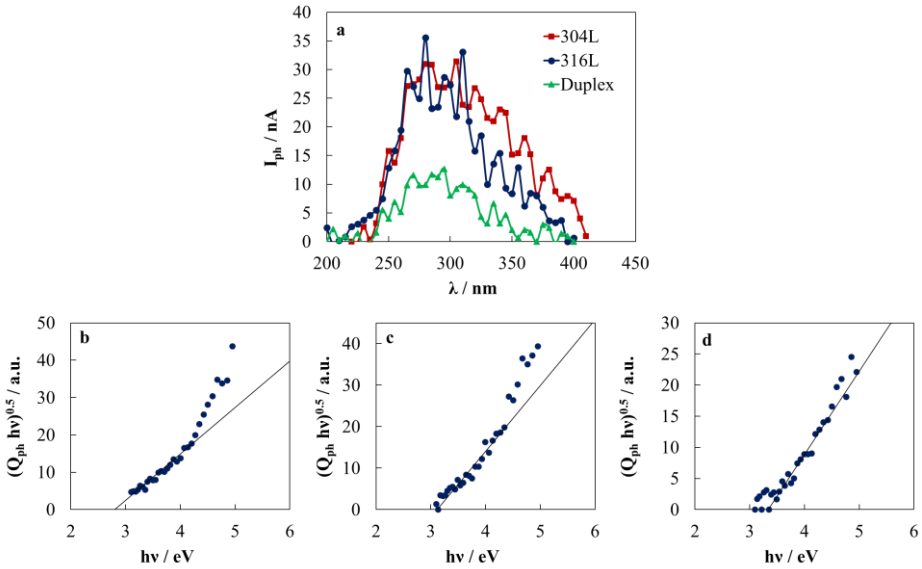

Fig. 5-20. Raw photocurrent spectra recorded at the open circuit potential (U_{OC} ~ 0 V vs. SSC) in Buffer Phosphate solution for passive films grown on as supplied different stainless steel samples. $(Q_{ph}\ hν)^{0.5}$ vs hν plot is reported for b) 304L c) 316L and d) Duplex stainless steels.

Table 5-4. Band gap values for native oxide grown by air exposure on as supplied SS samples.

as supplied SS	**E_g / eV**
304L	2.9
316L	3.1
Duplex	3.2

In Fig. 5-21 the raw photocurrent spectra related to passive films grown on SS samples at 0.6V vs. SSC in Buffer Phosphate solution and recorded at 0.2 V vs SSC, are reported.

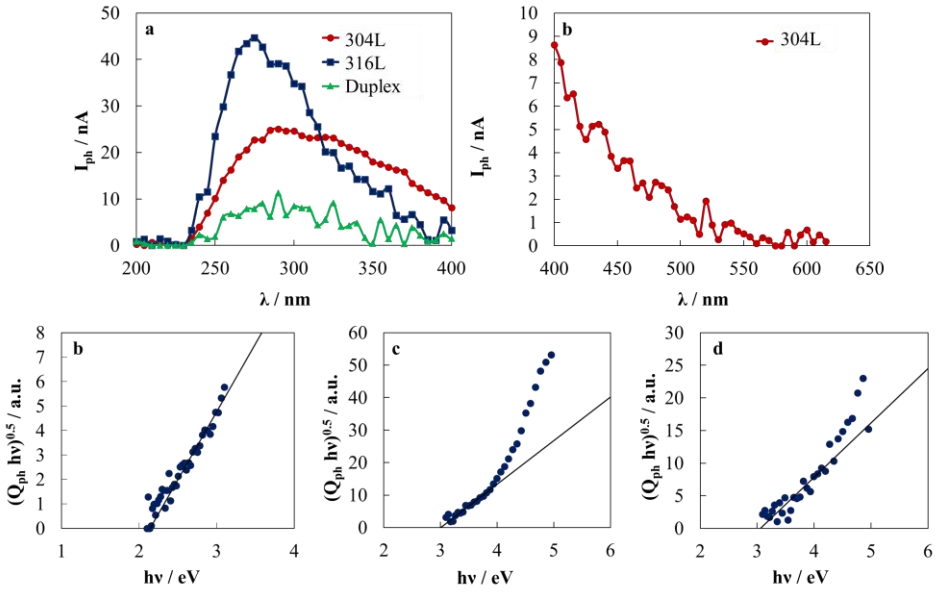

Fig. 5-21. a) Raw photocurrent spectra recorded at 0.2 V vs SSC in Buffer Phosphate solution for passive films grown on 304L, 316L and Duplex stainless steel with a standard surface finishing passivated at 0.6 V vs SSC in Phosphate Buffer solution. $(Q_{ph}\ h\nu)^{0.5}$ vs hν plot is reported for b) 304L c) 316L and d) Duplex stainless steels.

A band gap of ~ 3.00 eV was estimated for both passive films grown on 316L 2B and Duplex 2E. In the case of 304L 2B SS, a photocurrent tail is recorded at low photon energy, even using a 400 nm cut off filter, corresponding to an optical band gap value of 2.14 eV. The same photoelectrochemical characterization was performed for passive films grown at 1.5 V vs. SSC. According to the raw photocurrent spectra reported in Fig. 5-22a, the measured photocurrent is higher than that recorded for passive films grown at 0.6 V vs. SSC and a red shift of the light absorption threshold is present for all SS grades under investigation (see Fig. 5-22b).

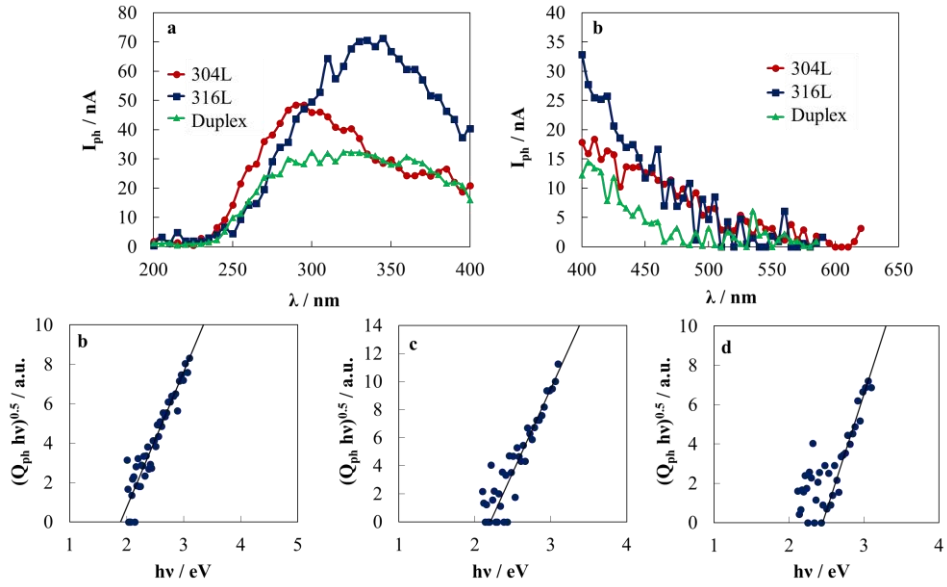

Fig. 5-22. Raw photocurrent spectra recorded at 0.2 V vs SSC in Buffer Phosphate solution for passive films grown on 304L, 316L and Duplex stainless steel with a standard surface finishing passivated at 1.5 V vs SSC in Phosphate Buffer solution a) without a cut-off filter b) with a cut-off filter. $(Q_{ph}\ h\nu)^{0.5}$ vs hν plot is reported for b) 304L c) 316L and d) Duplex stainless steels.

According to the values reported in Table 5-5, by assuming a non direct optical transition, the estimated band gap ranges between 2 - 2.2 eV for passive films grown on 304L and 316L while a slightly higher value was obtained for Duplex SS (2.45 eV). These experimental findings are in agreement with a strong chromium depletion on all passive films and the consequent formation of iron rich oxide layers.

Table 5-5. Band gap values for passive films grown on SSs samples with under anodic polarization in Buffer Phosphate solution (pH ~ 7) on SS samples with a standard surface finishing.

Passivation conditions	SS	E_g / eV	colour
0.6 V vs Ag/AgCl for 15 h	304L	2.14	No
	316L	3.00	No
	Duplex	3.06	No
1.5 V vs Ag/AgCl for 15 h	304L	1.9	yellow
	316L	2.2	light yellow
	Duplex	2.45	yellow

Finally, in order to check the real sign of the measured photocurrent, current vs. time curves were recorded at 0.2 V vs. SSC in Phosphate Buffer solution by manually chopping sample irradiation under monochromatic light (λ = 280 nm). The measured photocurrent is anodic (see Fig. 5-23) suggesting that passive films grown both in passive and transpassive conditions behave line n-type SC.

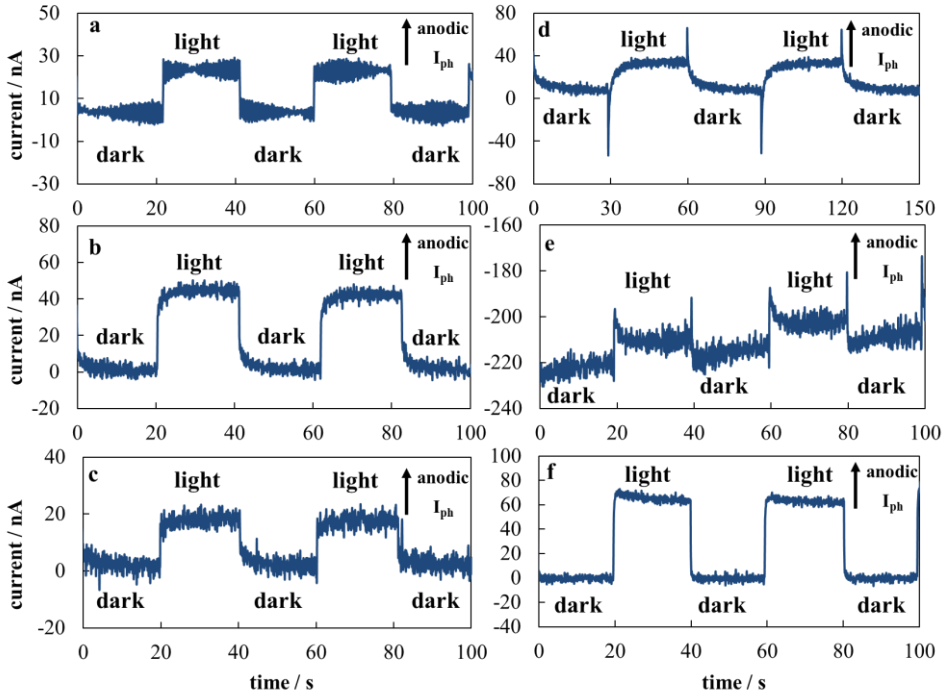

Fig. 5-23. Current vs time curves recorded at U_E = 0.2 V vs SSC in Phosphate Buffer solution (pH ~ 7) at λ = 280 nm for passive grown after 15 h of anodic polarization at U_E = 0.6 V vs SSC in Phosphate Buffer solution on a) 304L, b) 316L and c) Duplex stainless steel and for passive films grown in the same passivation solution at U_E = 1.5 V vs SSC on d) 304L, e) 316L and f) Duplex stainless steel.

According to Eq. 3.10, the estimated E_g values for passive films grown after 15 h of anodic polarization at 0.6 V vs. SSC suggest the formation of almost pure hematite for 304L (2.14 eV), while chromium rich passive films are formed on both 316L and duplex SSs (~ 3.0 eV). Conversely, strong chromium depletion occurs for the latter by increasing the polarizing potential (i.e. 1.5 V vs. SSC), in agreement with the formation of iron rich passive films (i.e. 2.2 – 2.4 eV).

5.2.2 *Impedance measurements*

In order to get more insight into corrosion resistance of passive films grown under potentiostatic polarization on SS samples with a standard surface finishing, differential capacitance vs. potential curves and EIS spectra were recorded.

According to the curves reported in Fig. 5-24, the measured C_M ranges from ~ 5 μF cm^{-2} to significantly higher values than the Helmholtz double layer capacitance recorded in aqueous solutions for passive films grown both in passive and tranpassive conditions. As in the case of SS samples with a mirror surface finishing, the measured capacitance is strongly dependent on frequency and potential, as expected for a semiconductor and a more cathodic flat band potential was detected in the case of 304L grade.

In Fig. 5-25, the impedance spectra in the Nyquist representation recorded at 0.2 V vs SSC in Buffer Phosphate solution are reported. The dependence of the imaginary impedance component on the real one is described by a portion of a depressed semicircle, as expected due to the strong influence of C_M on frequency. Experimental data were finally fitted according to the equivalent circuit reported in Fig. 4-12.

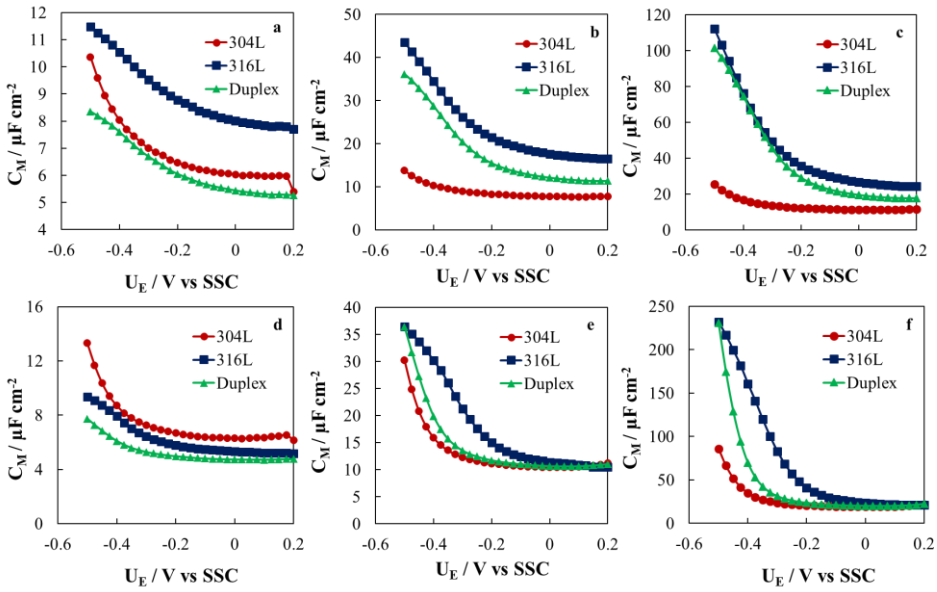

Fig. 5-24. Measured series capacitance vs. potential curves recorded in Phosphate Buffer solution (pH ~ 7), for passive films grown on different stainless steel grades after passivation under anodic polarization at U_E = 0.6 V vs SSC at a) 5 kHz, b) 1 kHz and c) 100 Hz and at U_E = 1.5 V vs SSC at d) 5 kHz, e) 1 kHz and f) 100 Hz.

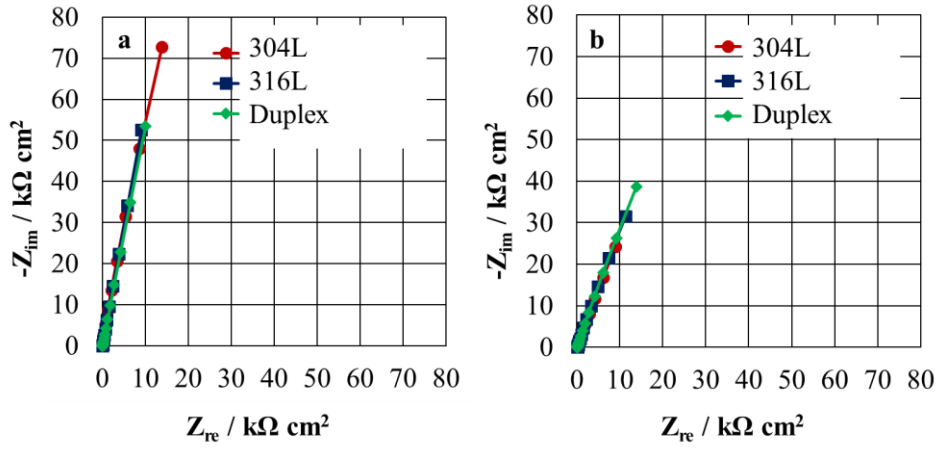

Fig. 5-25. EIS spectra in Nyquist representation recorded in buffer phosphate solution (pH ~ 7) for passive films grown after 15 h of anodic polarization at a) U_E = 0.6 V vs SSC and b) U_E = 1.5 V vs SSC vs SSC in Buffer Phosphate solution (pH ~ 7).

According to the values listed in Table 5-6, the polarization resistance of passive films grown after anodic polarization at 0.6 V and 1.5 V vs. SSC is higher if compared to that of the corresponding as supplied samples. Moreover, R_{ox} estimated for passive films grown in transpassive conditions are slightly lower than those estimated for SS samples passivated at 0.6 V vs SSC for austenitic grades, while no significantly differences are reported in the case of duplex SS suggesting that passive films grown on the latter are highly resistant toward dissolution phenomena in spite Cr dissolution. In order to estimate the thickness of passive films grown after 15 of anodic polarization in Phosphate Buffer solution on rough SS samples, the power law model analysis[170,171] was applied to CPE parameters provided in Table 5-6 by assuming $\varepsilon = 12$ and limiting value of resistivity of 500 Ohm · cm taken from calibration of Fe17Cr stainless steel[170].

Table 5-6. Fitting parameters of EIS spectra on passive films grown on different stainless steel grades at different polarizing potential in buffer phosphate solution (pH ~ 7) according to the equivalent circuit reported in the inset of Fig. 4-12.

Passivation conditions	**SS**	$\mathbf{R_{el}}$ $\mathbf{\Omega\ cm^2}$	$\mathbf{R_{ox}}$ $\mathbf{\Omega\ cm^2}$	$\mathbf{Q_{CPE}}$ $\mathbf{S\ s^{\alpha}\ cm^{-2}}$	**α**	$\mathbf{\chi^2}$	**δ** **nm**
As supplied	**304L**	41	$7.8 \cdot 10^5$	$3.23 \cdot 10^{-5}$	0.97	$2.06 \cdot 10^{-2}$	0.6
	316L	49	$3.2 \cdot 10^5$	$5.81 \cdot 10^{-5}$	0.93	$2.72 \cdot 10^{-2}$	0.8
	Duplex	48	$4.0 \cdot 10^6$	$4.87 \cdot 10^{-5}$	0.90	$3.99 \cdot 10^{-2}$	1.7
0.6 V vs Ag/AgCl for 15 h	**304L**	38	$3.1 \cdot 10^7$	$2.06 \cdot 10^{-5}$	0.89	$3.76 \cdot 10^{-3}$	5.3
	316L	93	$1.5 \cdot 10^6$	$2.80 \cdot 10^{-5}$	0.91	$3.63 \cdot 10^{-4}$	2.7
	Duplex	86	$1.3 \cdot 10^7$	$2.79 \cdot 10^{-5}$	0.88	$3.62 \cdot 10^{-4}$	4.3
1.5 V vs Ag/AgCl for 15 h	**304L**	40	$8.0 \cdot 10^6$	$5.63 \cdot 10^{-5}$	0.77	$5.64 \cdot 10^{-3}$	24.8
	316L	137	$8.3 \cdot 10^5$	$4.35 \cdot 10^{-5}$	0.81	$2.58 \cdot 10^{-4}$	13
	Duplex	92	$7.0 \cdot 10^7$	$3.64 \cdot 10^{-5}$	0.79	$8.57 \cdot 10^{-4}$	25

According to the power-law approach, thickness of passive films grown on different SS grades increases by increasing the polarizing potential. This finding is also supported by the strong surface discoloration of samples after polarization at 1.5 V vs. SSC in agreement with the formation of a very thick passive layers. Notably, the thickness of passive films grow on 316L is the lowest if compared to 304L and duplex SS as also suggested according to the surface discoloration (see Fig. 5-19). In spite the strong Cr depletion, the estimated oxide resistances are slightly higher if compared with those obtained for passive films grown on mirror finished SS samples. Notably, passive films grown on rough SSs are thicker than those grown on samples with a mirror surface finishing, in spite the surface roughness. On the other hand, the oxide layer is non homogenous as suggested by the values of the exponential factor of the CPE, that are lower than those estimated for passive films grown on SS samples with a mirror surface finishing. This experimental finding can be explained assuming a 2-dimensional time constant distribution in addition to the variation of resistivity through the thickness as well as supposed in the power low model.

According to the experimental results, no marked differences were obtained in the case of passive films grown on as supplied different stainless steel grades if compared to those grown on the corresponding SS samples with a mirror surface finishing. This finding suggests also that a key role is played by the presence (if any) of Mo in the bare alloy that in turn affects electronic properties of passive films and therefore their corrosion resistance.

5.3 Concluding remarks

Potentiostatic passivation of different stainless steel grades with a mirror surface finishing in Phosphate Buffer solution (pH ~ 7) was carried out at different polarizing potentials. According to the photoelectrochemical characterization, passivation at 0.2 V vs Ag/AgCl induces an iron enrichment in the passive films (more pronounced for 304L). Conversely, when passivation at 0.6 V vs Ag/AgCl induces a chromium depletion in the films grown on 304L, while Cr rich passive layers are present on the surface of 316L and duplex SS according to their high band gap values. In contrast, when polarization is performed at 1.5 V vs. SSC, iron rich passive films are formed on all stainless steel grades under investigation.

In spite growth condition and alloy composition, passive films grown on different stainless steel grades are n-type semiconductor, according to the current transient, and thus highly resistant towards corrosion phenomena. However, the more cathodic flat band potential for passive films on 304L is responsible of a higher potential drop inside the oxide, which in turn induces chromate formations (and thus dissolution) at potential lower than that necessary for 316L and duplex SSs. The more anodic flat band potential of passive film on Mo containing SSs has been rationalized assuming the formation of acceptors levels in the mobility gap of the passive film due to incorporation of Mo(IV) and/or Mo(VI) species, able to compensate the donor levels (oxygen vacancies), responsible on the n-type character of the oxides.

According to the experimental findings, surface roughness dos not significantly affect electronic properties and thus corrosion resistance of passive film.

6 Passive Films Grown in Simulating Solutions

Consumer and retailer expectations are increasing, price constraints are hardening, regulatory demands are more stringent - these are major challenges that food and beverage manufacturers face today. The occurrence of corrosion phenomena can threaten the food quality and the integrity of processing plant equipment. The corrosion environment in the food and beverage industry involves moderately to highly concentrated chlorides, often mixed with significant concentrations of organic acids. Moreover, importance of cleanliness in food processing plants is extremely high. Therefore, it is mandatory to adopt effective cleaning and sanitization programs to eliminate bacteria and viruses from surfaces and equipment. Compared to austenitic, duplex stainless steels exhibit higher mechanical strength, comparable corrosion resistance and lower cost due to the reduced Ni content. However, they have a two-phase microstructure, where comparable volumes of both ferrite and austenite are present, and the interaction between these two phases must be taken into account to explain/predict the corrosion resistance of this alloy. Indeed, segregation of elements such as Cr, Mo, Ni and N, determining the corrosion resistance of the steel, induces a Cr and Mo enrichment in the ferritic phase and a Ni and N enrichment in the austenitic phase, thus a different corrosion resistance is expected[186,187]. Therefore, predicting the behaviour of a duplex in a specific environment is not straightforward. This explains why a large number of paper is focused on the use of local electrochemical techniques to identify the weak points of the duplex SS (if any) in different aggressive environments[188–192].

Due to the relevant impact of passive film dissolution on the quality of processed fluids in the food and beverage industry, several works have been published in the last few years studying the amount of metal ions released in chemical reactors or storage vessels made in SSs in contact with aggressive environments mimicking the operating conditions. A special attention has been

paid toward the effect of acidic food on the metal release rate of different SS grades[46,193–195], while less information is available on the effect of other fluids usually employed in the food and beverage industry[196]. Moreover, papers focused on the assessment of the corrosion resistance of SSs in the corresponding environments are just a few[46,197–200].

A specific approach on how mimicking food and beverage industry is described in ref.[196], where the authors refer to a new test guideline recently been published by the Council of Europe (CoE) to ensure safety of metals and alloys in food contact[76]. In this work, the corrosion resistance of austenitic 304L and 316L and duplex 2507 in aggressive solutions simulating environments typical of food and beverage industry according to the CoE protocol was studied, as well as in high temperature purified water and 0.25 M NaOH solutions, usually employed for the cleaning in place (CIP). The effect of prolonged exposure to NaClO containing solutions, typically used as disinfectants for the removal of all the living microorganisms on food contact materials, was also studied.

6.1 Passive films grown on SSs after immersion in Food Simulants

Food simulants were prepared according to the CoE protocol recently published by the European council[76], and to the prescriptions necessary to maintain an acceptable hygiene level in the plant. To simulate the aqueous, alcoholic, or fatty food environments a solution of artificial tap water (according to DIN 10531) of pH ~ 7.5 with 0.12 g/L $NaHCO_3$, 0.07 g/L $MgSO_4 \cdot 7H_2O$ and 0.12 g/L $CaCl_2 \cdot 2H_2O$ was prepared. To mimic the acidic food environments, a solution of 5 g/L of citric acid (pH ~ 2.4) was used. Following the protocol, passivation cycles were carried out by immersion for 2 h at 70°C, for 2 h at 70°C + 24 h at 40°C and for 2 h at 70°C + 238 h at 40°C to simulate the heating and cooling cycles typical of the food and beverage industry.

6.1.1 *Photoelectrochemical results*

Passive films on the investigated stainless steels after immersion in food simulants were characterized by photoelectrochemical measurements. In order to minimize the change in the passive films composition and properties, the measurements were performed in a non aggressive solution (0.1 M ABE, pH ~ 9) exploiting a very narrow electrode potential range around the open circuit potential. To assess the effect of food simulants on passive film on the investigated SSs and following the CoE protocol, we recorded photocurrent spectra and impedance spectra soon after the three immersion steps described above. Fig. 6-1 shows the photocurrent spectra recorded in 0.1 M ABE at 0.10 V vs Ag/AgCl for SSs after immersion for 2 h at 70°C and 238 h at 40°C in 5 g l^{-1} citric acid solution (i.e. acidic food)

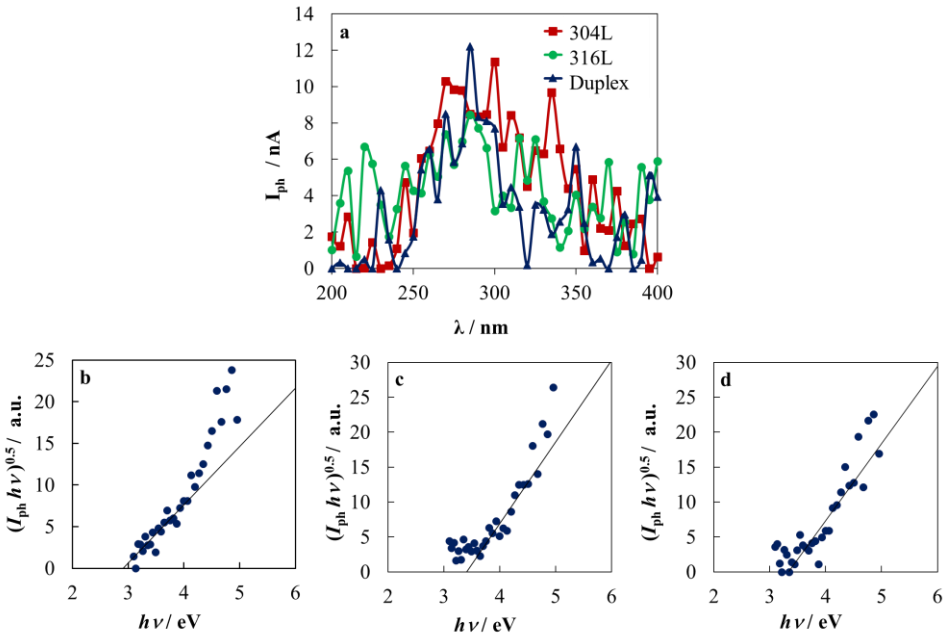

Fig. 6-1. Raw photocurrent spectra related to passive films grown on different stainless steel grades after 2 h at 70 °C and 238 h at 40°C in 5 gL^{-1} citric acid (pH 2.4) recorded in 0.1 M ABE solution (pH ~ 8) at U_E = 0.1 V vs Ag/AgCl. $(Q_{ph}\ h\nu)^{0.5}$ vs hν for passive grown by air exposure on b) 304L, c) 316L and d) duplex stainless steels.

As summarized in Table 6-1, the band gap values are almost constant during the three steps of immersion and very close to the band gap value reported in the literature for Cr_2O_3[201]. The photocurrent transients recorded by manually chopping monochromatic light irradiation indicate the formation of passive film with a n-type semiconductor behaviour (see Fig. 6-2). Notably, the photocurrent is very low suggesting the formation of very thin oxide layers.

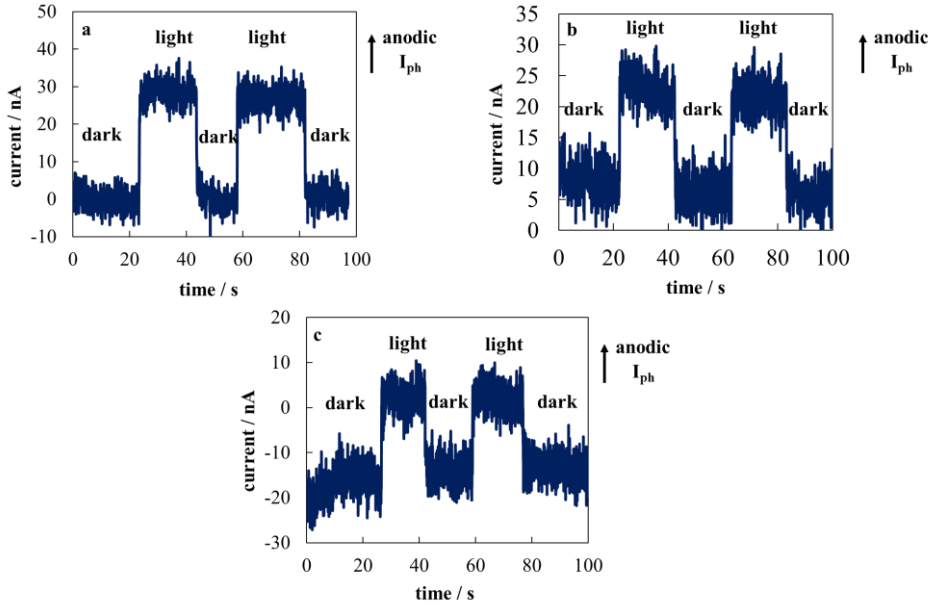

Fig. 6-2. Current vs time curves recorded at U_{OC} ~ 0 V vs Ag/AgCl in 0.1 M ABE solution (pH ~ 8) for passive grown on a) 304L, b) 316L and c) duplex stainless steel at λ = 300 nm after 2 h at 70°C and 238h at 40°C of immersion in 5 gL^{-1} citric acid (pH 2.4).

Conversely, the passive films composition and properties change significantly during immersion in high temperature tap water, mimicking fatty food. In Fig. 6-3 the photocurrent spectra recorded after 2 h of immersion at 70°C and 238 h of immersion in 40°C tap water for 304L, 316L and Duplex SSs are reported.

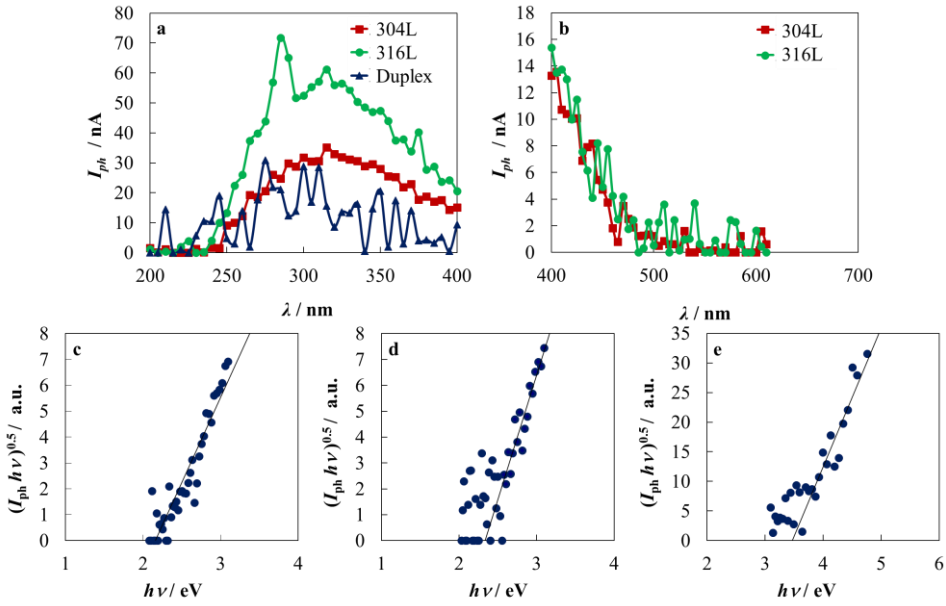

Fig. 6-3. Raw photocurrent spectra related to passive films grown on different stainless steel grades after 2 h at 70 °C and 238 h at 40°C in artificial tap water (pH 7.5) recorded in 0.1 M ABE solution (pH ~ 8) at U_E = 0.15 V vs Ag/AgCl. $(Q_{ph}\ h\nu)^{0.5}$ vs hν for passive grown by air exposure on b) 304L, c) 316L and d) duplex stainless steels.

The band gap decreases to 2.3 eV for passive films on 304L and 316L, while a higher value of 3.4 eV is estimated for passive film on duplex (see Table 6-1). This means that passive films on austenitic SSs formed during immersion at the open circuit potential in high temperature tap water are enriched in iron, while those grown on duplex SS are still very rich in chromium. Independently on their band gap and according to the recorded photocurrent transients, passive films in fatty food simulants behave as n-type semiconductors (see Fig. 6-4), thus they are highly stable against anodic dissolution.

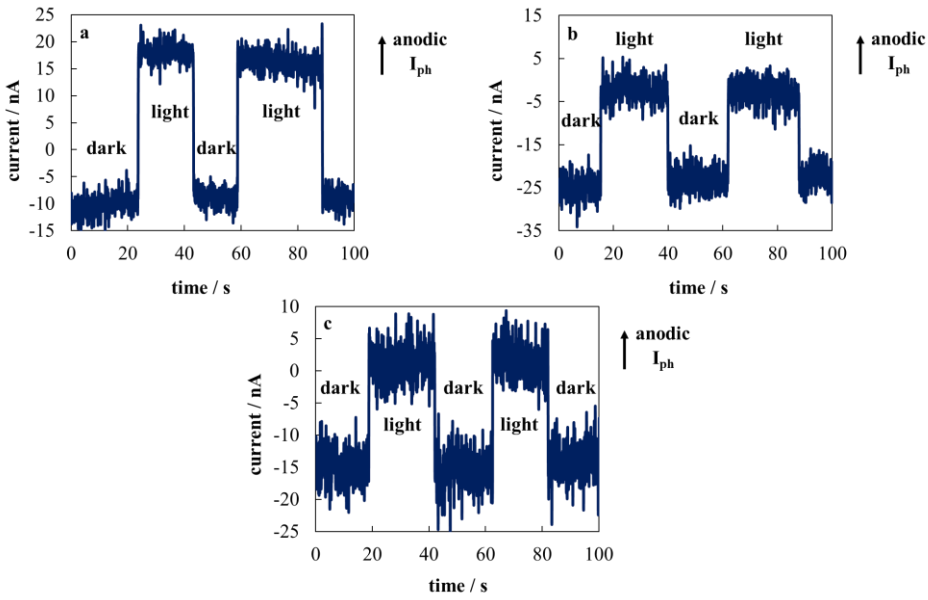

Fig. 6-4. Current vs time curves recorded at U_{OC} ~ 0 V vs Ag/AgCl in 0.1 M ABE solution (pH ~ 8) for passive grown on a) 304L, b) 316L and c) duplex stainless steel at λ = 300 nm after 2 h at 70°C and 238 h at 40°C of immersion in artificial tap water (pH 7.5).

Table 6-1. Band gap values for passive films grown on as supplied SSs by air exposure and after passivation in food simulant solutions estimated by recording photocurrent spectra at U_{OC} ~ 0 V vs. Ag/AgCl for native oxides and at U_E = 0.1 V vs. Ag/AgCl for passivated samples both in 0.1 M ABE.

Passivation treatment	SS	E_g / eV (as supplied)	E_g / eV (after 2 h at 70°C)	E_g / eV (after 2 h at 70°C and 24 h at 40°C)	E_g / eV (after 2 h at 70°C and 238 h at 40°C)
Acidic Food	304L	2.9	2.9	2.9	2.9
	316L	3.4	3.4	3.4	3.4
	Duplex	3.3	3.3	3.3	3.3
Fatty Food	304L	2.1	2.3	2.3	2.1
	316L	2.4	2.4	2.3	2.4
	Duplex	3.3	3.3	3.4	3.3

6.1.2 *Inductively Coupled Plasma – Optical Emission Spectroscopy*

Released amount of Fe, Cr, Ni, Mn and Mo (if present) for as supplied 304L, 316L and duplex stainless steel after immersion in both acidic (pH ~ 2.4) and artificial tap water (pH ~ 7.5) solutions are respectively reported in Table 6-2 and Table 6-3 (see also Fig. 6-5 and Fig. 6-6). According to the experimental results, the total amount of metal ions dissolved during the immersion tests is significantly higher in 5 g L^{-1} citric acid than that reported after immersion in fatty food environment (i.e. artificial tap water). However, the overall measured concentrations released from the surface of the oxide layer for all SS grades under investigation after 240 h of immersion in both simulating solutions are lower with respect to the SRL limits reported in the CoE protocol, as already reported in the literature for austenitic SSs of similar composition and for a lean duplex grade[196].

After immersion in acidic solution, most of the release is due to Fe dissolution for all stainless steel grades. Moreover, the total released amount of ions increases by decreasing Cr bulk content. In addition to Fe, the dissolved amounts of Cr, Mn, Ni and Mo during 316L immersion are significantly higher than those reported for both 304L and duplex. The released amount of Fe, Ni and Mn reported for duplex are lower than those estimated for austenitic 304L, while the amount of Cr dissolution is lower for the latter. The higher extent of dissolved Mo in the case of duplex stainless steel could be explained considering the higher bulk content of the latter if compared with that of 316L (see Fig. 6-5).

Table 6-2. Released amount of metals during 2 h at 70 °C (A), 2 h at 70°C (B) and 24 h at 40°C and 2 h at 70°C and 238 h at 40°C (C) of immersion in 5 gL^{-1} citric acid (pH 2.4), according to the CoE protocol.

			304L		
Passivation conditions	**Fe / ppb**	**Cr / ppb**	**Ni / ppb**	**Mn / ppb**	**Mo / ppb**
A	1388	62.66	63.17	24.57	N/A
B	1575	79.84	68.57	28.52	N/A
C	1805	127.2	77.09	29.4	N/A
			316L		
A	1617	90.07	41.67	20.83	6.24
B	1766	88.69	46.44	23.26	5.25
C	2394	167.2	80.95	32.85	11.08
			Duplex		
A	842.8	80.96	12.65	4.39	9.50
B	921.2	84.17	13.97	6.39	10.39
C	1514	168.8	32.41	8.58	22.38

The immersion in fatty food electrolyte does not bring to iron dissolution, since concentration of iron ions in the electrolyte after the immersion steps at 70°C and 40°C is below the detection limits even at the end of CoE protocol. Conversely, it possible to detect chromium, nickel, manganese and molybdenum (if present in the SS) ions even if in concentration significantly lower than that measured in citric acid. Notably, the detected concentration of manganese ions for 304L is higher than that measured for the other SS grades (see Fig. 6-6).

Table 6-3. Released amount of metals during 2 h at 70 °C (A), 2 h at 70°C (B) and 24 h at 40°C and 2 h at 70°C and 238 h at 40°C (C) of immersion in artificial tap water (pH 7.5), according to the CoE protocol.

			304L		
Passivation conditions	**Fe / ppb**	**Cr / ppb**	**Ni / ppb**	**Mn / ppb**	**Mo / ppb**
A	< LOD	1.87	1.59	2.07	N/A
B	< LOD	2.05	2.17	10.81	N/A
C	< LOD	2.06	2.53	11.00	N/A
			316L		
A	< LOD	1.87	1.45	1.38	0.67
B	< LOD	1.98	1.76	1.34	0.59
C	< LOD	2.27	1.80	0.96	1.24
			Duplex		
A	< LOD	2.26	1.65	0.84	1.90
B	< LOD	2.29	1.63	0.92	1.87
C	< LOD	2.39	1.44	0.83	2.44

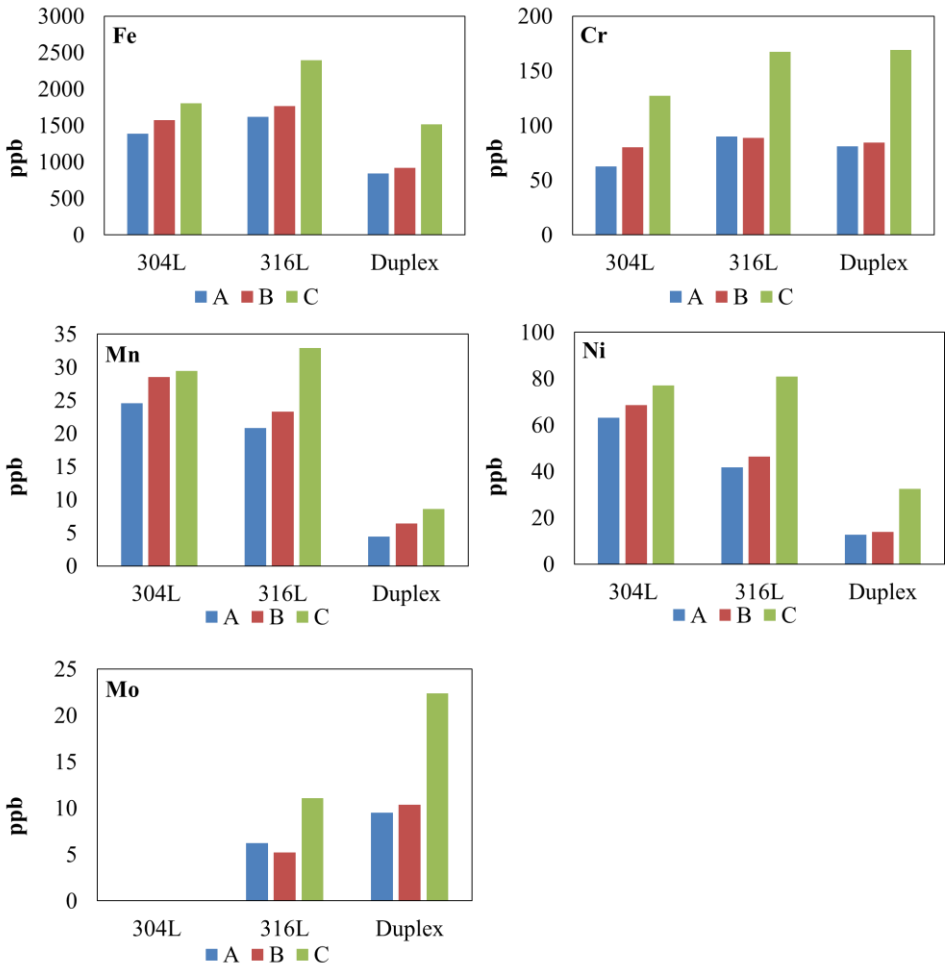

Fig. 6-5. Total amount of released ions for different stainless steel grades after immersion in acidic food simulant environment, according to the CoE protocol.

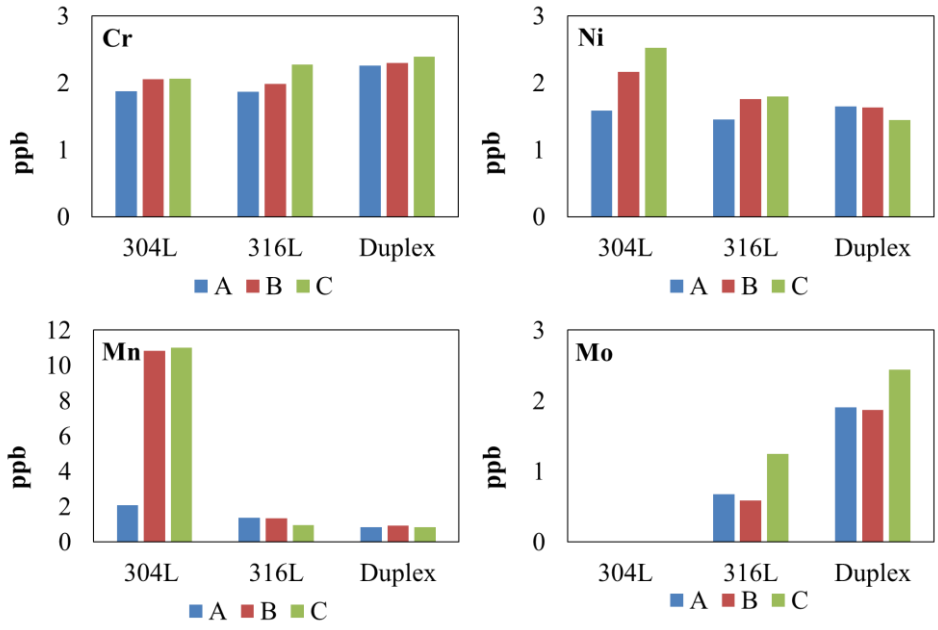

Fig. 6-6. Total amount of released ions for different stainless steel grades after immersion in artificial tap water simulant environment, according to the CoE protocol.

The results collected from the release experiments were used to estimate the thinning of the SSs during immersion in both citric acid and tap water assuming uniform corrosion. The SS density and the volume of oxidized steel can be linked to the total metal ion release by the following eq.

$$\rho_{SS} = \frac{\sum_i m_i}{V_{M_x}} \qquad (6.1)$$

where V_{Mx} is the volume of the surface metal (cm^3), m_i is the amount of the corresponding ion released after 240 h of immersion (g) and ρ is the density of SS ($g\ cm^{-3}$). Since the densities of the main metals are quite similar, the density of Fe was used for the estimation of the consumed metal thickness, *h*, as follow:

$$h = \frac{\sum C_i V_{sol}}{\rho_{SS} A_{SS}} \cdot 10^7 \qquad (6.2)$$

where V_{sol} (ml) is the volume of simulating solutions during the immersion tests and C_i the concentration of the corresponding ion released after 240 h of immersion (µg ml^{-1}). Moreover, considering that the ratio between the exposed surface area and the volume of simulating solutions was kept constant during the migration tests (0.5 cm^2 ml^{-1}), Eq. 6.2 can be written as reported below:

$$h = \frac{\sum C_i}{\rho_{SS}} \cdot 2 \cdot 10^7 \qquad (6.3)$$

According to Eq. 6.3, the alloy thickness reduction is significant in the case of immersion in acidic food environment ranging from 4.5 for duplex SS to 6.9 nm for 316L SS, while is almost negligible in tap water (0.02 nm).

6.1.3 *In – situ OCP and EIS measurements*

Fig. 6-7 shows the OCP vs time curves recorded during immersion in food stimulants at 70°C. The immersion in citric acid removes the air formed film of the surface of all the investigated SSs, as suggested by the rapid shift toward more negative values of the corrosion potential. Notably, in the case of 316L the OCP slightly increases reaching an almost constant value, while for 304L and Duplex SSs the open circuit potential raises monotonically (see Fig. 6-7a).

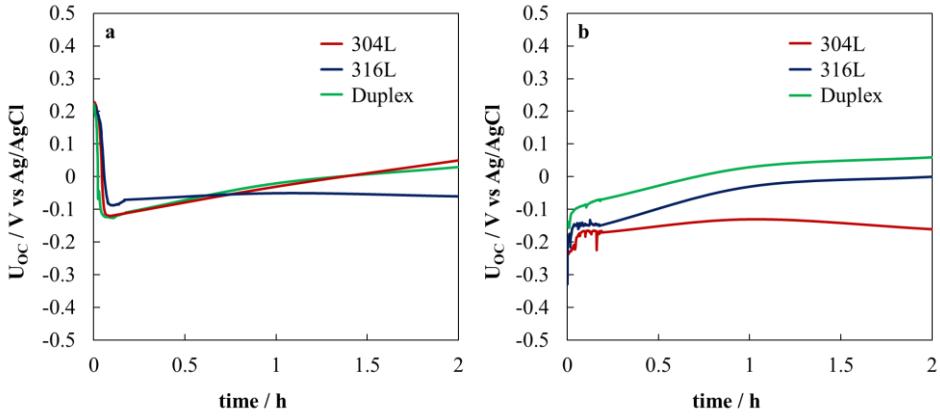

Fig. 6-7. *In-situ* open circuit potential recorded for 2 h of immersion at 70°C in a) 5 gL^{-1} (pH 2.4) and b) artificial tap water (pH 7.5) for different stainless steel grades.

EIS spectra in the Nyquist representation recorded during immersion at the OCP at room temperature and at 70°C are reported in Fig. 6-8. They are portions of depressed semicircles, that can be easily fitted with the very simple equivalent circuit of Fig. 4-12. The fitting parameters reported in Table 6-4 suggest that R_P decreases soon after immersion in 70°C citric acid solution for all the SSs, but it remains almost constant for 316L, while it raises to higher values for 304L and duplex SS.

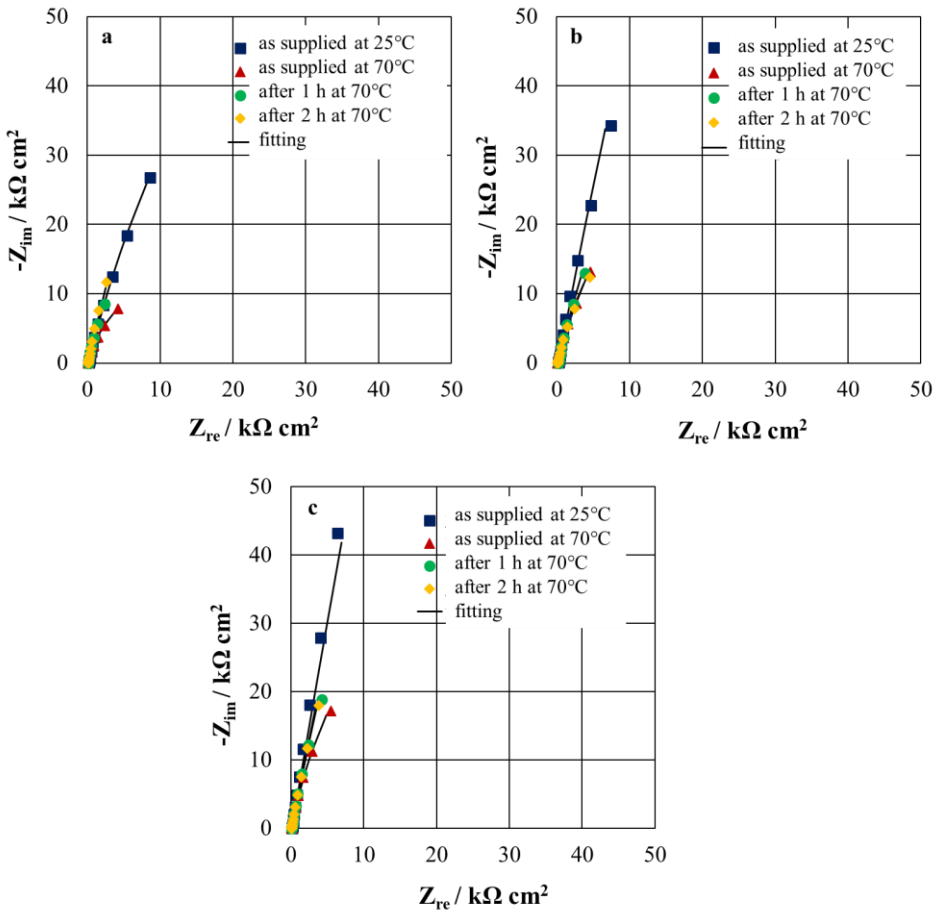

Fig. 6-8. *In-situ* EIS spectra in the Nyquist representation recorded at the corresponding open circuit potential reported in Fig. 6-7 for passive films grown on a) 304L, b) 316L and c) duplex stainless steel after immersion in 5 gL^{-1} citric acid solution (pH 2.4).

Moreover, the best fitting exponent of the constant phase element, α, is lower than 1, as already reported in previous works for passive films on steel[55,170]. This behaviour can be explained by assuming the formation of passive film with a not constant resistivity on going from the metal/oxide to the oxide/electrolyte interface. In order to estimate the thickness of passive films grown on different stainless steel grades at different immersion time in food simulants, the power law model analysis[170,171] was applied to CPE parameters provided in Table 6-4,

by assuming ε = 12 (close to the value reported for hematite and for chromium oxide) and limiting value of resistivity of 500 Ohm cm. Oxide thickness are reported in Table 6-4.

Table 6-4. Fitting parameters of *in-situ* EIS spectra recorded after different immersion time at 70°C in acidic food simulating solutions obtained by employing the equivalent circuit reported in Fig. 4-12. Fitting parameters of as supplied samples recorded at 25°C are also reported.

5 g L^{-1} citric acid						
Passivation conditions	**R_{el} Ω cm^2**	**R_p Ω cm^2**	**Q_{CPE} S s^{α} cm^{-2}**	**α**	**χ^2**	**δ nm**
			304L			
As supplied at 25°C	210	$3.5 \cdot 10^{5}$	$5.11 \cdot 10^{-5}$	0.86	$2.75 \cdot 10^{-3}$	3.96
As supplied at 70°C	134	$3.5 \cdot 10^{4}$	$1.63 \cdot 10^{-4}$	0.86	$1.19 \cdot 10^{-3}$	1.29
After 1 h at 70°C	106	$6.1 \cdot 10^{5}$	$1.78 \cdot 10^{-4}$	0.86	$1.75 \cdot 10^{-3}$	1.06
After 2 h at 70°C	115	$7.0 \cdot 10^{6}$	$1.35 \cdot 10^{-4}$	0.87	$3.08 \cdot 10^{-3}$	1.29
			316L			
As supplied at 25°C	231	$2.6 \cdot 10^{6}$	$4.38 \cdot 10^{-5}$	0.89	$2.45 \cdot 10^{-3}$	2.59
As supplied at 70°C	153	$1.0 \cdot 10^{5}$	$1.13 \cdot 10^{-4}$	0.88	$1.36 \cdot 10^{-3}$	1.11
After 1 h at 70°C	215	$2.9 \cdot 10^{5}$	$1.16 \cdot 10^{-4}$	0.87	$1.12 \cdot 10^{-3}$	1.40
After 2 h at 70°C	127	$1.4 \cdot 10^{5}$	$1.23 \cdot 10^{-4}$	0.86	$2.28 \cdot 10^{-3}$	1.61
			Duplex			
As supplied at 25°C	167	$7.0 \cdot 10^{6}$	$3.59 \cdot 10^{-5}$	0.90	$4.41 \cdot 10^{-3}$	2.42
As supplied at 70°C	129	$1.5 \cdot 10^{5}$	$8.57 \cdot 10^{-5}$	0.90	$1.05 \cdot 10^{-3}$	1.11
After 1 h at 70°C	112	$7.8 \cdot 10^{5}$	$8.17 \cdot 10^{-5}$	0.89	$1.26 \cdot 10^{-3}$	1.29
After 2 h at 70°C	99	$3.1 \cdot 10^{6}$	$8.62 \cdot 10^{-5}$	0.89	$1.51 \cdot 10^{-3}$	1.37

During the immersion in citric acid the oxide thickness keeps almost constant around 1.3 nm, thus thin enough to allow electron tunnel to feed the half cell cathodic process (i.e. oxygen reduction). Moreover, this implies that during the immersion in 70°C citric acid the oxide formation current is balanced by a dissolution current responsible for the ion release revealed by ICP-OES. These findings were also confirmed by fitting EIS spectra recorded in not aggressive room temperature electrolyte where dissolution phenomena should be blocked (see Fig. 6-9 and Table 6-5). The estimated passive films thicknesses are in agreement with the values estimated according to the power law model from fitting parameters of EIS spectra recorded in citric acid solution.

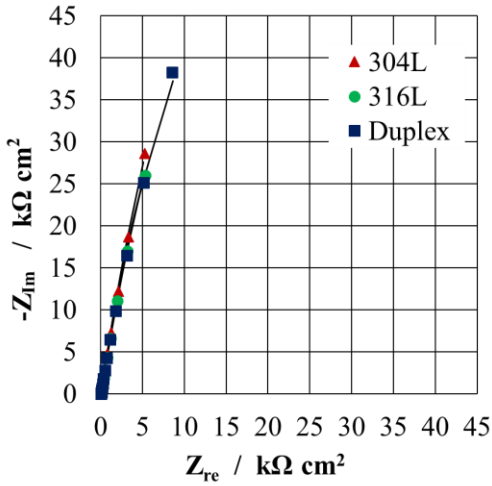

Fig. 6-9. *Ex-situ* EIS spectra in the Nyquist representation recorded at U_{OC} ~ 0.1 V vs SSC in 0.1 M ABE (pH ~ 8) for passive films grown after 240 of immersion in 5 g/L citric acid solution.

Table 6-5. Fitting parameters of *ex-situ* EIS spectra recorded at U_{OC} ~ 0.1 V vs SSC in 0.1 M ABE for passive films grown in 5 g/L citric acidic solution according to the CoE protocol. The equivalent circuit reported in Fig. 4-12 was employed.

5 g L^{-1} citric acid							
SSs	**time**	**R_{el}**	**R_{ox}**	**Q_{CPE}**	**α**	**χ^2**	**δ**
	h	**Ω cm^2**	**Ω cm^2**	**S s$^{\alpha}$ cm^{-2}**			**nm**
304L	**0**	39	$2.0 \cdot 10^{7}$	$2.70 \cdot 10^{-5}$	0.94	$9.1 \cdot 10^{-4}$	1.41
	2	67	$1.8 \cdot 10^{5}$	$4.48 \cdot 10^{-5}$	0.90	$4.0 \cdot 10^{-4}$	1.89
	26	62	$8.0 \cdot 10^{6}$	$5.80 \cdot 10^{-5}$	0.91	$1.3 \cdot 10^{-3}$	1.33
	240	63	$6.7 \cdot 10^{5}$	$5.41 \cdot 10^{-5}$	0.91	$6.6 \cdot 10^{-4}$	1.30
316L	**0**	99	$3.7 \cdot 10^{5}$	$3.40 \cdot 10^{-5}$	0.91	$4.0 \cdot 10^{-4}$	2.11
	2	79	$1.4 \cdot 10^{5}$	$4.75 \cdot 10^{-5}$	0.91	$3.6 \cdot 10^{-4}$	1.41
	26	60	$4.5 \cdot 10^{5}$	$5.64 \cdot 10^{-5}$	0.90	$7.1 \cdot 10^{-4}$	1.75
	240	59	$6.0 \cdot 10^{5}$	$5.97 \cdot 10^{-5}$	0.90	$9.5 \cdot 10^{-4}$	1.39
Duplex	**0**	81	$4.4 \cdot 10^{5}$	$2.90 \cdot 10^{-5}$	0.93	$1.9 \cdot 10^{-3}$	1.62
	2	67	$1.2 \cdot 10^{6}$	$2.96 \cdot 10^{-5}$	0.94	$7.0 \cdot 10^{-4}$	1.41
	26	63	$2.3 \cdot 10^{5}$	$4.16 \cdot 10^{-5}$	0.91	$5.6 \cdot 10^{-4}$	1.80
	240	67	$4.0 \cdot 10^{5}$	$3.94 \cdot 10^{-5}$	0.92	$7.5 \cdot 10^{-4}$	1.59

A different behaviour was shown in tap water, where OCP values slightly increasing toward more positive values were recorded for 316L and duplex SSs, while an almost constant more negative value was recorded for 304L (see Fig. 6-7b).

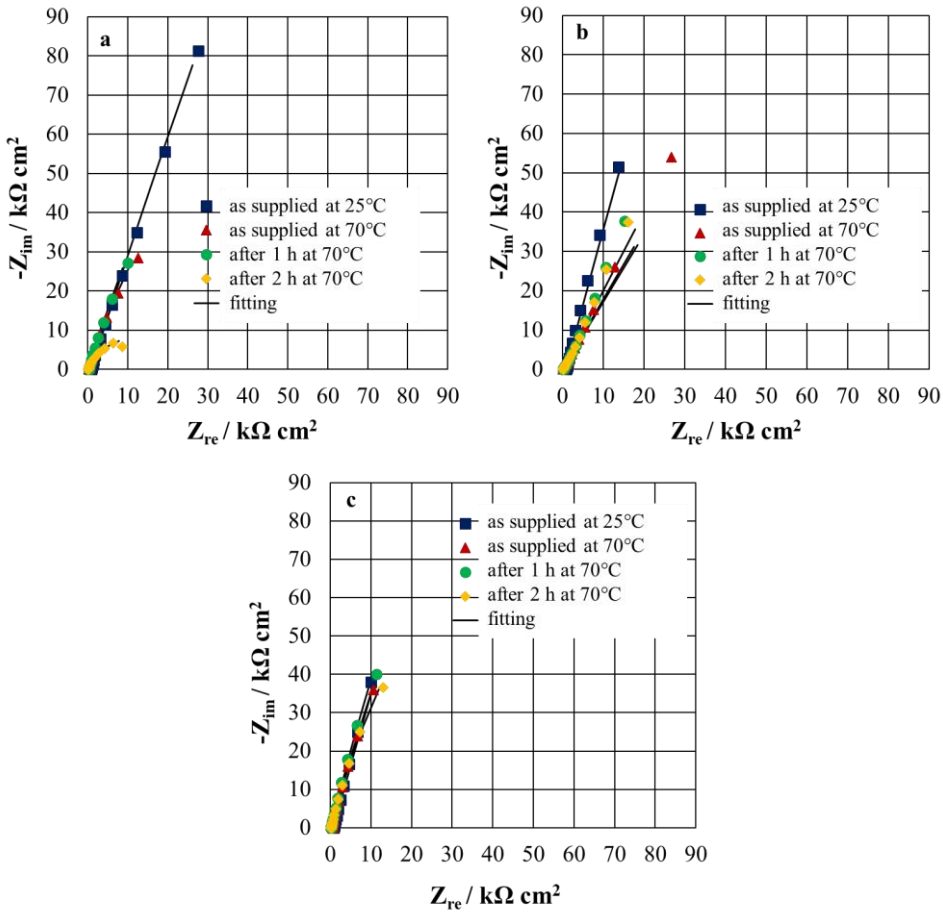

Fig. 6-10. *In-situ* EIS spectra in Nyquist representation recorded at the corresponding open circuit potential reported in Fig. 6-7 for passive films grown on a) 304L, b) 316L and c) duplex stainless steel after immersion in artificial tap water solution (pH 7.5).

Moreover, the polarization resistance derived by fitting the EIS are very high for 316L and duplex SS, while lower values were obtained for 304L (one order of magnitude lower than that estimated in citric acid), thus suggesting the occurring of corrosion phenomena in spite the very low concentration of released ions. Notably, the fitting quality of the EIS spectra is very poor, since it seems that an equivalent circuit more complex than that reported in Fig. 4-12 is necessary to describe the behaviour of 304L/passive film/electrolyte interface.

Table 6-6. Fitting parameters of *in-situ* EIS spectra recorded after different immersion time at 70°C in fatty food simulating solutions. Fitting parameters of as supplied samples recorded at 25°C are also reported. The equivalent circuit reported in Fig. 4-12 was employed.

	Artificial Tap Water					
Passivation conditions	**R_{el} Ω cm^2**	**R_p Ω cm^2**	**Q_{CPE} S s$^{\alpha}$ cm^{-2}**	**α**	**χ^2**	**δ nm**
			304L			
As supplied at 25°C	727	$5.1 \cdot 10^{6}$	$1.77 \cdot 10^{-5}$	0.81	$1.08 \cdot 10^{-3}$	34
As supplied at 70°C	282	$3.6 \cdot 10^{5}$	$4.86 \cdot 10^{-5}$	0.81	$2.38 \cdot 10^{-3}$	11
After 1 h at 70°C	220	$7.5 \cdot 10^{5}$	$5.33 \cdot 10^{-5}$	0.82	$1.51 \cdot 10^{-3}$	8.5
After 2 h at 70°C	113	$2.4 \cdot 10^{4}$	$9.92 \cdot 10^{-5}$	0.75	$1.12 \cdot 10^{-1}$	19
			316L			
As supplied at 25°C	892	$6.5 \cdot 10^{6}$	$2.87 \cdot 10^{-5}$	0.84	$3.58 \cdot 10^{-3}$	10
As supplied at 70°C	221	$3.0 \cdot 10^{6}$	$3.49 \cdot 10^{-5}$	0.72	$2.11 \cdot 10^{-2}$	117
After 1 h at 70°C	141	$6.0 \cdot 10^{6}$	$3.72 \cdot 10^{-5}$	0.67	$1.52 \cdot 10^{-2}$	273
After 2 h at 70°C	124	$4.0 \cdot 10^{6}$	$3.83 \cdot 10^{-5}$	0.68	$4.98 \cdot 10^{-3}$	212
			Duplex			
As supplied at 25°C	789	$4.0 \cdot 10^{6}$	$3.92 \cdot 10^{-5}$	0.84	$2.32 \cdot 10^{-3}$	7.7
As supplied at 70°C	554	$7.9 \cdot 10^{5}$	$4.02 \cdot 10^{-5}$	0.86	$3.71 \cdot 10^{-4}$	5.1
After 1 h at 70°C	186	$1.3 \cdot 10^{6}$	$3.64 \cdot 10^{-5}$	0.86	$6.29 \cdot 10^{-4}$	5.6
After 2 h at 70°C	231	$4.0 \cdot 10^{5}$	$3.80 \cdot 10^{-5}$	0.86	$5.44 \cdot 10^{-4}$	5.5

Moreover, the use of a variable resistivity to account for the non-ideal capacitance of these passive films provides not reliable thickness. EIS spectra recorded in not aggressive solution (0.1 M ABE) at room temperature were

fitted using a R(RQ) circuit and the thickness of the film estimated according to the power law model resulted to be meaningful (see Fig. 6-11 and Table 6-7).

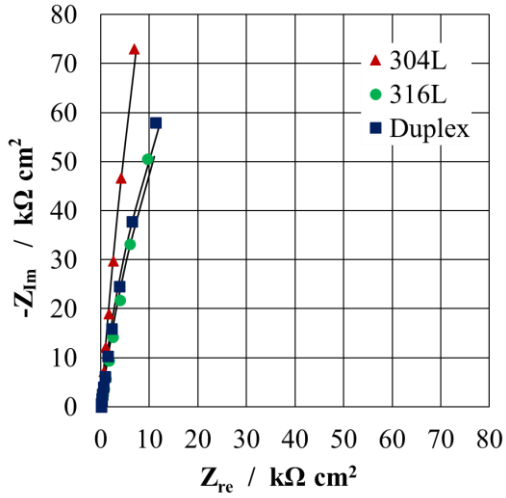

Fig. 6-11. *Ex – situ* EIS spectra in the Nyquist representation recorded at U_{OC} ~ 0.1 V vs SSC in 0.1 M ABE (pH ~ 8) for passive films grown after 240 of immersion in tap water solution.

Table 6-7. Fitting parameters of *ex-situ* EIS spectra recorded at U_{OC} ~ 0.1 V vs SSC in 0.1 M ABE for passive films grown in tap water solution according to the CoE protocol. The equivalent circuit reported in Fig. 4-12 was employed.

Artificial Tap Water							
SSs	**time**	$\mathbf{R_{el}}$	$\mathbf{R_{ox}}$	$\mathbf{Q_{CPE}}$	**n**	χ^2	**δ**
	h	**Ω cm²**	**Ω cm²**	**S sⁿ cm⁻²**			**nm**
304L	**0**	39	$2.0 \cdot 10^{7}$	$2.70 \cdot 10^{-5}$	0.94	$9.1 \cdot 10^{-4}$	1.41
	2	55	$6.8 \cdot 10^{5}$	$2.32 \cdot 10^{-5}$	0.95	$4.8 \cdot 10^{-4}$	1.39
	26	50	$7.5 \cdot 10^{5}$	$2.31 \cdot 10^{-5}$	0.94	$4.3 \cdot 10^{-4}$	1.49
	240	64	$2.5 \cdot 10^{6}$	$2.16 \cdot 10^{-5}$	0.96	$6.3 \cdot 10^{-4}$	1.28
316L	**0**	99	$3.7 \cdot 10^{5}$	$3.40 \cdot 10^{-5}$	0.91	$4.0 \cdot 10^{-4}$	2.11
	2	57	$6.5 \cdot 10^{5}$	$2.83 \cdot 10^{-5}$	0.92	$4.9 \cdot 10^{-4}$	2.06
	26	58	$5.6 \cdot 10^{5}$	$3.10 \cdot 10^{-5}$	0.92	$4.5 \cdot 10^{-4}$	1.90
	240	73	$5.9 \cdot 10^{5}$	$2.89 \cdot 10^{-5}$	0.92	$5.8 \cdot 10^{-4}$	1.93
Duplex	**0**	81	$4.4 \cdot 10^{5}$	$2.90 \cdot 10^{-5}$	0.93	$1.9 \cdot 10^{-3}$	1.62
	2	66	$2.4 \cdot 10^{5}$	$2.87 \cdot 10^{-5}$	0.92	$8.3 \cdot 10^{-4}$	2.17
	26	84	$2.4 \cdot 10^{5}$	$2.83 \cdot 10^{-5}$	0.92	$6.9 \cdot 10^{-4}$	2.21
	240	67	$5.7 \cdot 10^{5}$	$2.58 \cdot 10^{-5}$	0.94	$5.1 \cdot 10^{-4}$	1.52

In order to better understand the phenomena occurring during immersion in food simulants, polarization curves were recorded for all the SS in citric acid and tap water at 70°C after 2h of immersion (see Fig. 6-12). The curves are almost overlapped for 304L, 316L and duplex SSs in citric acid where the passivity current densities are almost coincident. Conversely, the polarization curves recorded in tap water strongly depends on the SS grade. The passivity current for 304L is four times higher than that measured with 316L and duplex SSs, and some significant oscillations appear at 0.2 V (Ag/AgCl). Current oscillations are also present for the other SS grades but they are less pronounced and/or at higher potential (as in the case of duplex). In spite the very low chloride concentration

these oscillations suggest the formation of metastable pits and thus, possible onset of localized corrosion especially for 304L.

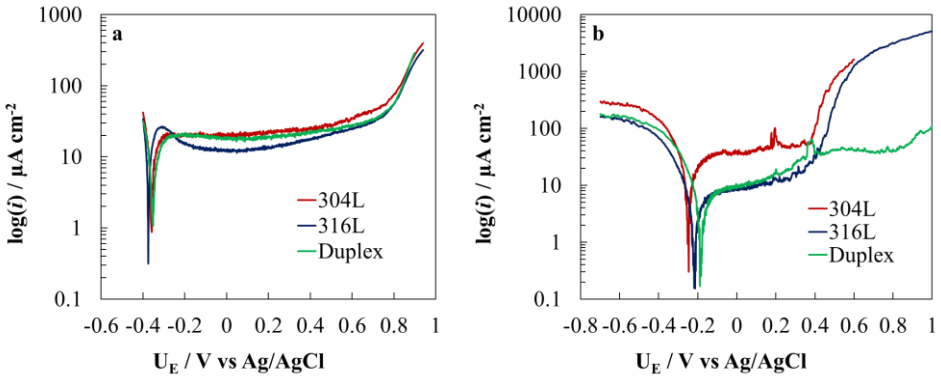

Fig. 6-12. *In-situ* polarization curves recorded for different stainless steel grades after 2 h of immersion at 70°C in a) 5 gL^{-1} citric acid (pH 2.4) and b) artificial tap water (pH 7.5) solutions.

By considering the high concentration of released manganese ions during the first 2h of immersion, it is likely that such phenomena can be linked to the presence of MnS inclusions. In fact, as widely reported in the literature, over the course of the past century corrosion pits in austenitic stainless steels have been associated with manganese sulfide (MnS) inclusions[12,24,30,31]. According to the SEM pictures reported below (Fig. 6-13,Fig. 6-14 and Fig. 6-15), they usually appear mottled in texture and recessed from the surface

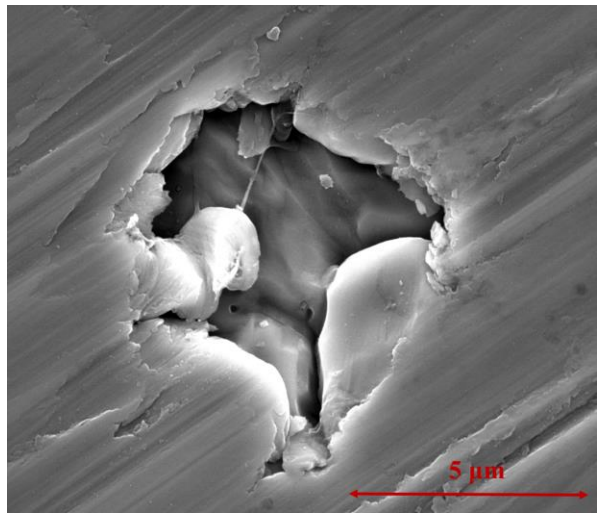

Fig. 6-13. SEM picture related to MnS inclusion on austenitic 304L SS obtained at 20 000x.

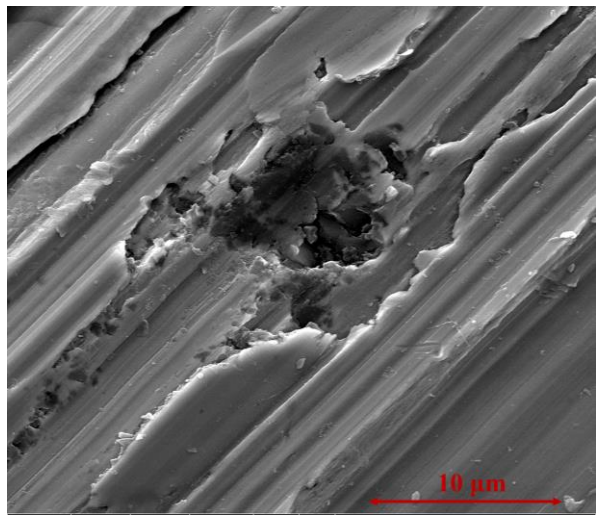

Fig. 6-14. SEM picture related to MnS inclusion on austenitic 316L SS obtained at 8 000x.

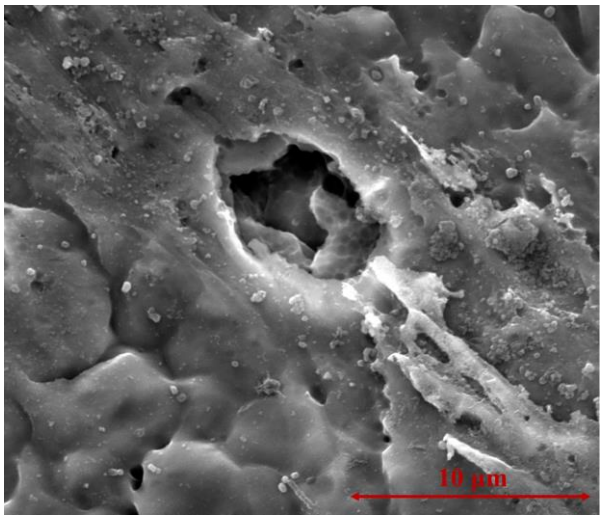

Fig. 6-15. SEM picture related to MnS inclusion on duplex SS obtained at 10 000x.

Passive films on austenitic and duplex SSs grown during immersion in electrolyte simulating acidic food are iron containing Cr_2O_3 according to the estimated band gap values and to previous results reported in literature[196]. The immersion in high temperature citric acid dissolves the air formed passive films (as suggested by the sudden drop of the open circuit potential soon after immersion) followed by a repassivation. During the first 2h of immersion at 70°C the corrosion potential keeps almost constant for AISI 316L, while it rises to higher values for both AISI 304L and duplex SSs. The shift to more noble value of the corrosion potential suggests the formation of a more stable passive film, in agreement with the lower dissolution rate proved by the ICP-OES measurements. The highest dissolution rate is measured for 316L, thus resulting the less resistant toward generalized corrosion in acidic food. Notably, the lowest corrosion rate was measured for duplex SS. However, polarization resistance estimated by fitting the EIS spectra recorded in citric acid at 70°C do not change appreciably and are very high for all the SSs (in the order of 10^5 – 10^6 Ω cm^2). Hence, during immersion in citric acid SSs are covered by a thin

passive film with a high band gap (3 – 3 eV) anodically polarized with respect to its flat band potential and thus blocking toward anodic processes other than films growth. During immersion the formation current is balanced by the dissolution current accounting for the ions release, according to the scheme reported in Fig. 6-16.

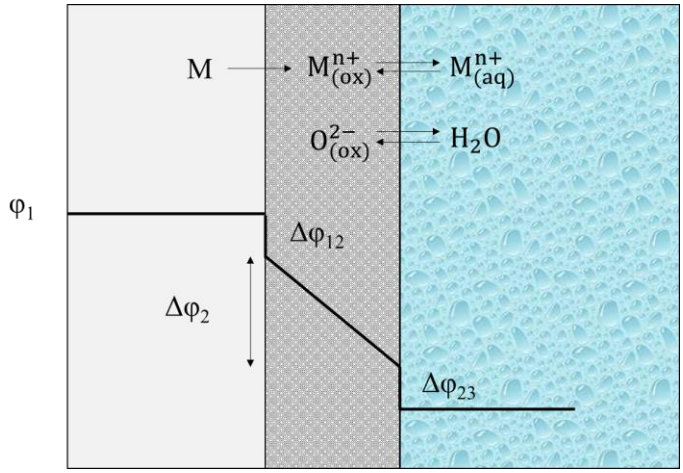

Fig. 6-16. Schematic representation of the variation of potential across a passive film.

The behaviour of SSs during immersion in fatty food simulant is completely different. The photoelectrochemical results show that passive films on austenitic SSs have a band gap close to the value expected for Fe_2O_3, while significantly higher value was measured for the passive film on duplex SS, i.e. 3.4 eV coincident with the band gap value reported for Cr_2O_3. Notably, the dissolution rate in this environment is almost negligible according to the ICP-OES findings. Indeed, there is no potential drop (see Fig. 6-7) soon after immersion in the electrolyte and the potential keeps constant for 304L while it raises to more positive values for 316L and duplex SSs. However, the dependence of polarization resistances of passive films estimated from the EIS spectra for 304L is completely different than that for 316L and duplex SS. In spite the very low metal ions release the polarization resistance decreases of more than two orders of magnitude for 304L and the exponent α of the constant phase element is

significantly lower than 1. Matching this information with high release of manganese revealed for 304L as well as with the polarization curves of Fig. 6-12, it seems that the corrosion resistance of 304L is strongly affected by MnS inclusions.

According to the literature[11,105,202–206], the dissolution of such inclusions produces S species (e.g. thiosulfate ions) and exposes the bare surface of steel matrix, resulting in high pitting susceptibility near the incursions in highly concentrated chloride containing solutions. Tap water contains a very low concentration of Cl^- ions and considering the very high PREN of the SSs of this work the occurrence of pitting seems unlikely. However, taking into account the high temperature of the electrolyte (70°C in the first 2 h and 40°C for 238 h) and the local conditions induced by MnS inclusions (low pH and Cr^{3+} release) pit initiation can occur. As displayed in Fig. 6-17, the initiation step can be followed by the formation of metastable pits and repassivation, or by pit growth close to the trench formed as a consequence of MnS oxidation.

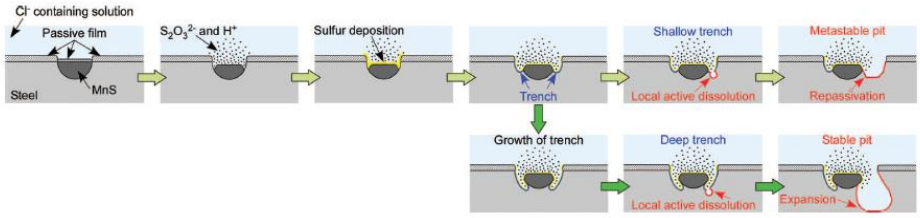

Fig. 6-17. Schematic illustration of the pit initiation mechanism at MnS inclusion in stainless steel[105].

The transition from metastable to stable pits is strongly affected by the presence of molybdenum in the alloy since, according to ref.[11], in spite the presence of trench there is no evidence of pit formation for Mo containing SSs even at high Cl^- concentration (0.1 M NaCl) and at high potential, since repassivation is promoted by molybdenum species. This explain why 316L and duplex SSs do not show significant reduction of the polarization resistance during immersion in

Tap water in contrast to the behaviour of 304L. The oscillation in the polarization curves of Fig. 6-12 are more evident than in the case of duplex and 316L. Thus, in spite the concentration of chloride species is very low the use of 304L for fatty food can bring to sever damage of the metal.

6.2 Passive films on SS after immersion in Hot Purified Water

As discussed in section 2.4, high purity water is widely employed in food and beverage plant since it is used as raw material for the preparation of cleaning solutions or as service fluid. For this reason, in order to assess the effect of high temperature water on corrosion resistance of SSs, passive films were grown at the open circuit potential by immersion in purified water (with conductivity lower than 1.3 μS/cm at 25°C) at 60 °C. Austenitic 304L and 316L and Duplex SSs were immersed for 15 h, 24 h and 168 h.

According to raw photocurrent spectra recorded at 0.15 V vs SSC in 0.1 M ABE for passive films grown on different SSs grades after 168 h of immersion, reported in Fig. 6-18, a long photocurrent tail was registered al low photon energy even using a 400 nm cut off filter (see Fig. 6-18b). Indeed, a non direct optical transition of ~ 2.1 eV, very close to that reported for Fe_2O_3, was estimated for passive films grown on austenitic stainless steels suggesting a strong chromium dissolution after 168 h of immersion in HPW. Conversely, 2.9 eV was estimated for passive film on duplex SS suggesting that the oxide is still rich in chromium even after 168 h of immersion in HPW. Finally, according to the current transient reported in Fig. 6-19, passive films under investigation are n-type SC and anodic spikes were recorded in the case of austenitic SSs, in agreement with the formation of Fe_2O_3.

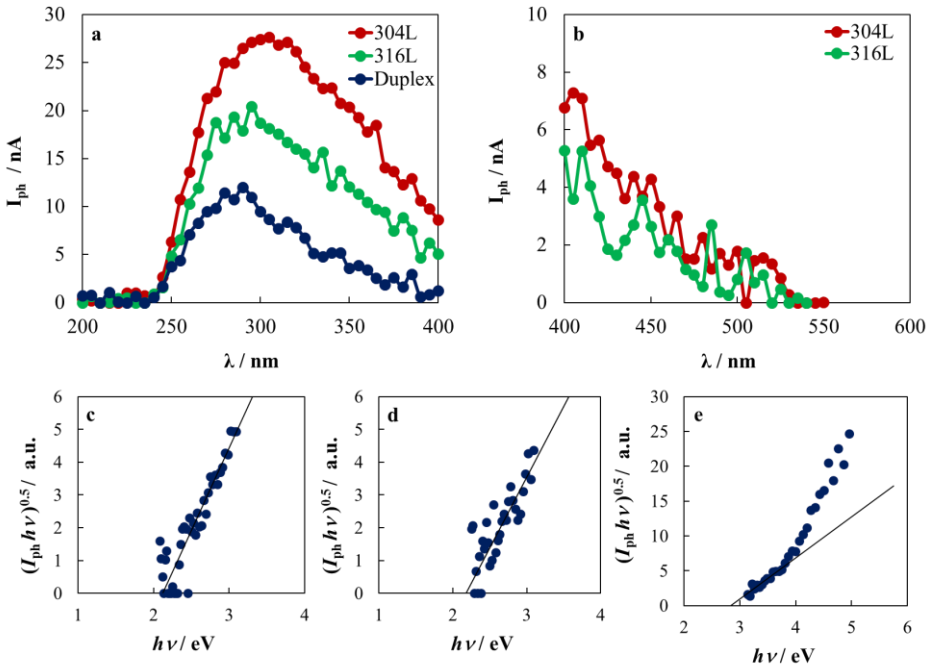

Fig. 6-18. Raw photocurrent spectra recorded at 0.15 V vs SSC in 0.1 M ABE (pH ~ 8) for passive films grown after 168 h of immersion in HPW at 60°C on different stainless steel grades. $(Q_{ph}\ h\nu)^{0.5}$ vs hν plots are reported for passive films grown on c) 304L, d) 316L and e) Duplex SS.

In Table 6-8, the optical band gap values related to passive films grown after different immersion time in HPW are reported. Notably, passive films grown on 304L and 316L SS display a strong chromium depletion since 15 h of immersion, while in the case of Duplex E_g decreases slowly.

Table 6-8. Optical band gap values for passive films grown on different stainless steel grades at 0.15 V vs SSC by different immersion time in HPW at 60°C. E_g of the corresponding as supplied samples are also reported.

Passivation treatment	SS	E_g / eV (as supplied)	E_g / eV (after15 h)	E_g / eV (after 24 h)	E_g / eV (after 168 h)
Hot Purified Water at 60 °C	304L	2.9	2.3	2.3	2.1
	316L	3.1	2.3	2.4	2.2
	Duplex	3.3	3.3	3.2	2.8

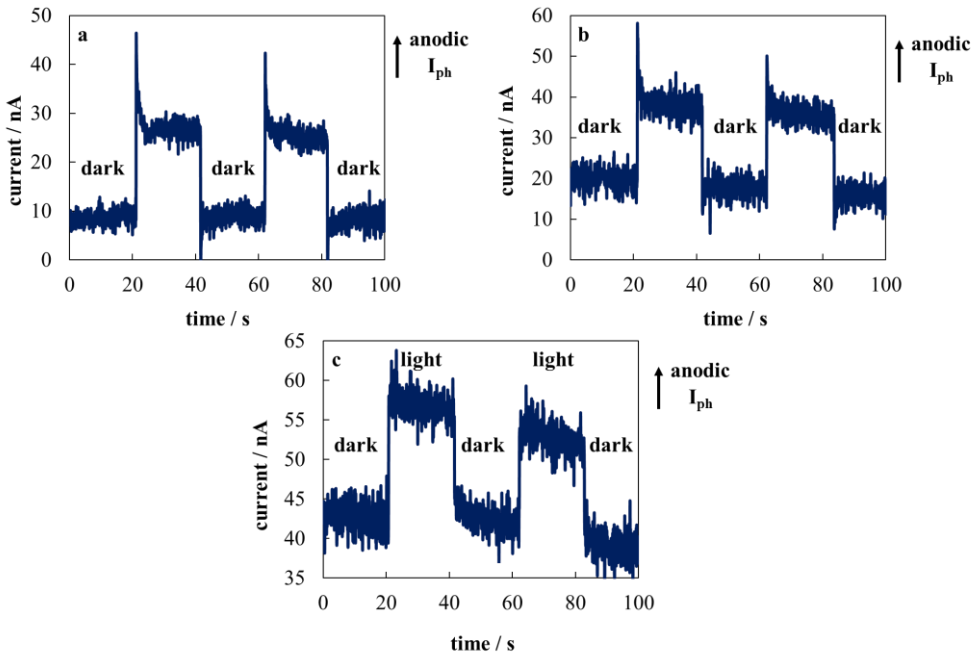

Fig. 6-19. Current vs time curves recorded under illumination (on) and dark conditions (off) at λ = 300 nm at U_E = 0.15 V vs SSC in 0.1 M ABE solution (pH ~ 8) for passive grown after 168 h of immersion in HPW at 60 °C on a) 304L, b) 316L and c) Duplex SSs.

EIS spectra were also recorded in order to estimate the resistance of passive films grown after different immersion time. In Fig. 6-20 EIS spectra recorded at the open circuit potential (U_{OC} ~ 0 V vs SSC) in 0.1 M ABE for passive films grown after 168 h of immersion in HPW at 60°C are reported in the Nyquist representation.

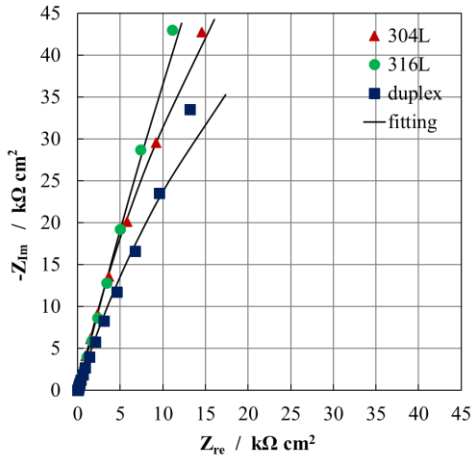

Fig. 6-20. EIS spectra in Nyquist representation recorded at the open circuit potential (~ 0 V vs SSC) in 0.1 M ABE (pH ~ 8) for passive films grown on different stainless steel grades after 168 h of immersion in HPW.

Impedance data were finally fitted according to the equivalent circuit displayed in Fig. 4-12. Although the strong chromium depletion of passive films, the best fitting parameters suggest that the corresponding oxide resistance (R_{ox}) is still high even after 168 h of immersion in HPW, while α is slightly lower than that estimated for the corresponding as supplied samples due to a not constant resistivity along the thickness of passive films as a consequence of dissolution phenomena. In order to estimate the thickness of passive films grown on different stainless steel grades at different immersion time in HPW, the power law model analysis[170,171] was applied to CPE parameters provided in Table 6-9, by assuming ε = 12 (close to the value reported for hematite and for chromium oxide) and limiting value of resistivity of 500 Ohm cm. According to the values

reported in Table 6-9, passive films grown on SS samples after different immersion time are thicker than those grown on as supplied samples. Notably, thickening occurs by increasing the immersion time in HPW.

Table 6-9. Fitting parameters of EIS spectra recorded at the open circuit potential (U_{OC} ~ 0 V vs SSC) in 0.1 M ABE solution for passive films grown on different stainless steel grades after 168 h of immersion in HPW at 60°C. the equivalent circuit reported in Fig. 4-12 was employed.

SSs	time	R_{el}	R_{ox}	Q_{CPE}	α	χ^2	d
	h	Ω cm^2	Ω cm^2	S s$^{\alpha}$ cm^{-2}			nm
304L	**0**	39	$2.0 \cdot 10^{7}$	$2.7 \cdot 10^{-5}$	0.94	$9.1 \cdot 10^{-4}$	1.41
	15	24	$6.0 \cdot 10^{6}$	$2.3 \cdot 10^{-5}$	0.91	$1.1 \cdot 10^{-3}$	2.86
	24	25	$3.3 \cdot 10^{5}$	$3.1 \cdot 10^{-5}$	0.87	$1.2 \cdot 10^{-3}$	5.19
	168	22	$3.5 \cdot 10^{5}$	$3.1 \cdot 10^{-5}$	0.86	$8.1 \cdot 10^{-4}$	6.19
316L	**0**	99	$3.7 \cdot 10^{5}$	$3.4 \cdot 10^{-5}$	0.91	$4.0 \cdot 10^{-4}$	2.11
	15	25	$3.8 \cdot 10^{5}$	$3.2 \cdot 10^{-5}$	0.83	$2.8 \cdot 10^{-3}$	11.25
	24	31	$4.3 \cdot 10^{5}$	$3.0 \cdot 10^{-5}$	0.85	$1.5 \cdot 10^{-3}$	8.21
	168	27	$1.5 \cdot 10^{6}$	$3.2 \cdot 10^{-5}$	0.85	$7.9 \cdot 10^{-4}$	8.40
Duplex	**0**	81	$4.4 \cdot 10^{5}$	$2.9 \cdot 10^{-5}$	0.93	$1.9 \cdot 10^{-3}$	1.62
	15	21	$3.8 \cdot 10^{5}$	$3.5 \cdot 10^{-5}$	0.86	$1.2 \cdot 10^{-3}$	6.13
	24	20	$6.8 \cdot 10^{5}$	$2.9 \cdot 10^{-5}$	0.85	$5.3 \cdot 10^{-4}$	8.44
	168	19	$2.3 \cdot 10^{5}$	$3.5 \cdot 10^{-5}$	0.82	$2.1 \cdot 10^{-3}$	14.76

6.3 Passive films on SSs after immersion in Cleaning solution

Different 304L, 316L and duplex SSs coupons were immersed in 0.25 M NaOH at 82°C in order to assess the effect Cleaning In Place (CIP). Fig. 6-21 shows the photocurrent spectra recorded in 0.1 M ABE at 0.15 V vs Ag/AgCl after 7 days of immersion. The effect of hot alkaline solution is significant for 304L and 316L SSs, since a long photocurrent tail appears at low photon energy, even using a 400 nm cut off filter (see Fig. 6-21b), corresponding to indirect optical transitions close to 2.2 eV (see Fig. 6-21c-d). The latter value is very close to the band gap reported for Fe_2O_3. This finding suggests that immersion in hot purified water induces the preferential dissolution of Cr and the consequent formation of an iron oxide passive film. In contrast, the band gap of passive films on duplex SS is higher (E_g = 3.0 eV), suggesting that in spite the immersion in hot NaOH the layer is still rich in chromium. In Table 6-10 the band gap values as a function of immersion time (15 h, 24 h and 168 h) for the investigated SSs are summarized.

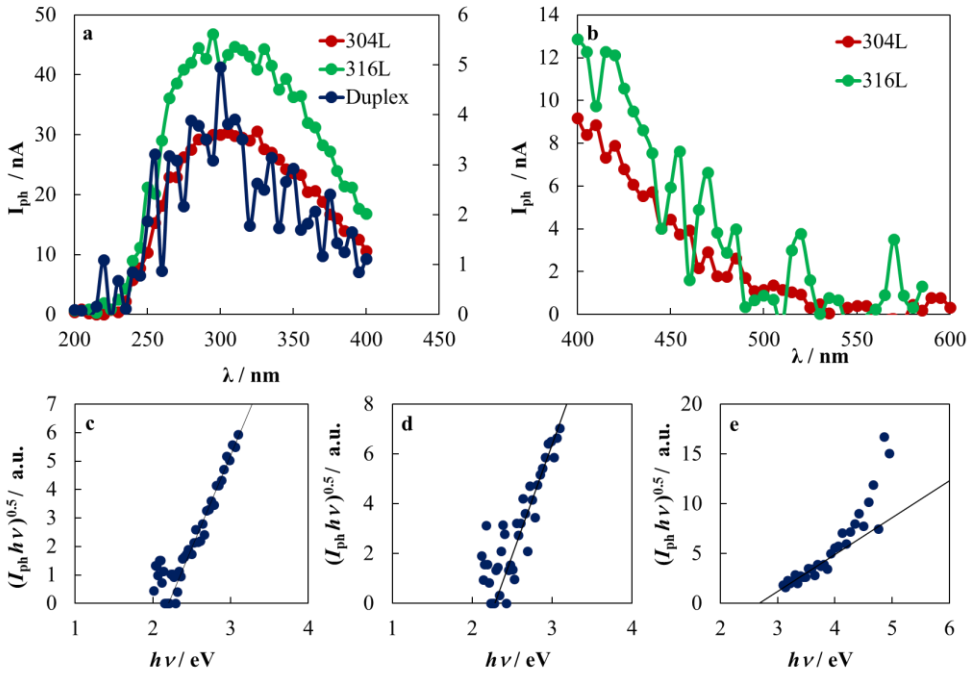

Fig. 6-21. Raw photocurrent spectra recorded at 0.15 V vs SSC in 0.1 M ABE (pH ~ 8) for passive films grown after 168 h of immersion in 0.25 M NaOH at 82 °C on different stainless steel grades. $(Q_{ph}\ h\nu)^{0.5}$ vs hν plots are reported for passive films grown on c) 304L, d) 316L and e) Duplex SS.

Table 6-10. Optical band gap values for passive films grown on different stainless steel grades at 0.15 V vs SSC by different immersion time in 0.25 M NaOH at 82°C. E_g of the corresponding as supplied samples are also reported.

Passivation treatment	SS	E_g / eV (as supplied)	E_g / eV (after15 h)	E_g / eV (after 24 h)	E_g / eV (after 168 h)
Hot NaOH at 82 °C	304L	2.9	2.2	2.3	2.2
	316L	3.1	2.5	2.3	2.3
	Duplex	3.3	2.9	3.0	3.0

According to the current transients reported in Fig. 6-22, the passive films on the investigated SSs are all n-type SC with very high anodic photocurrent. It is

important to stress that for the passive films grown on 304L and 316L the presence of anodic photocurrent spikes confirms the formation of Fe_2O_3[115].

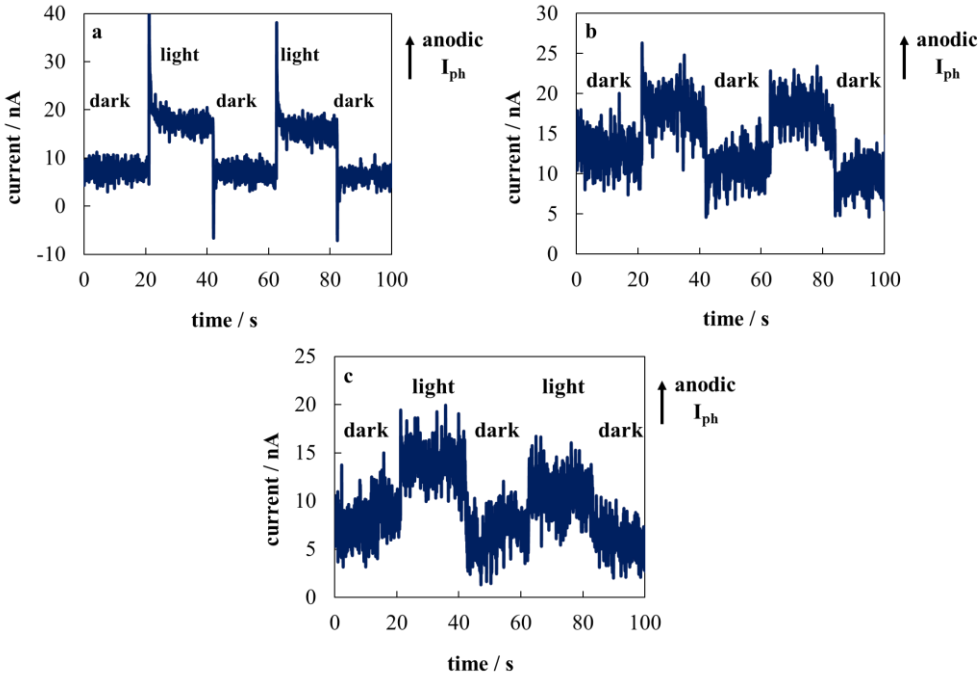

Fig. 6-22. Current vs time curves recorded under illumination (on) and dark conditions (off) at λ = 300 nm at U_E = 0.15 V vs SSC in 0.1 M ABE solution (pH ~ 8) for passive grown after 168 h of immersion in 0.25 M NaOH solution at 82 °C on a) 304L, b) 316L and c) Duplex SSs.

In Fig. 6-23 the impedance spectra in the Nyquist representation for passive films grown after 7 days of immersion in hot soda are reported. They can be simulated by the equivalent circuit of Fig. 4-12 and the best fitting parameters are reported in Table 6-11.

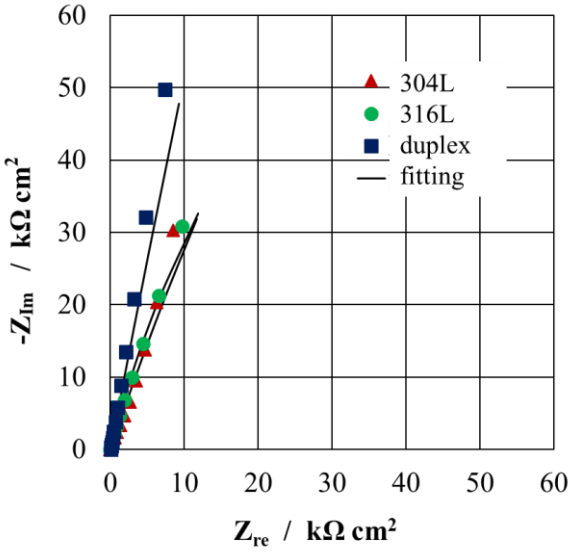

Fig. 6-23. EIS spectra in Nyquist representation recorded at the open circuit potential (~ 0 V vs SSC) in 0.1 M ABE (pH ~ 8) for passive films grown on different stainless steel grades after 168 h of immersion in 0.25 M NaOH at 82°C.

According to the fitting parameters, R_{OX} is very high and α is slightly lower than those measured for as supplied samples. This can be due to a not constant resistivity of the passive films along the thickness as a consequence of the dissolution phenomena. In spite the films are chromium depleted, the corresponding oxide resistance is very high according to impedance measurements. Finally, the thickness of passive films grown on different stainless steel grades at different immersion time in hot soda were estimated according to the power law model analysis[170,171] by assuming ε = 12 and ρ_d equals to 500 Ohm cm. The values reported in Table 6-11 suggest passive film thickening by increasing the immersion time in cleaning solution.

Table 6-11. Fitting parameters of EIS spectra recorded at the open circuit potential (U_{OC} ~ 0 V vs SSC) in 0.1 M ABE solution for passive films grown on different stainless steel grades after 168 h of immersion in 0.25 M NaOH at 82°C. The equivalent circuit reported in Fig. 4-12 was employed.

SSs	time	R_{el}	R_{ox}	Q_{CPE}	α	χ^2	δ
	h	Ω cm^2	Ω cm^2	S s$^{\alpha}$ cm^{-2}			nm
304L	**0**	39	$2.0 \cdot 10^{7}$	$2.7 \cdot 10^{-5}$	0.94	$9.1 \cdot 10^{-4}$	1.41
	15	19	$1.3 \cdot 10^{7}$	$2.9 \cdot 10^{-5}$	0.92	$1.6 \cdot 10^{-3}$	2.06
	24	21	$3.1 \cdot 10^{5}$	$3.7 \cdot 10^{-5}$	0.86	$1.1 \cdot 10^{-3}$	5.16
	168	20	$8.1 \cdot 10^{5}$	$4.2 \cdot 10^{-5}$	0.80	$5.2 \cdot 10^{-3}$	16.3
316L	**0**	99	$3.7 \cdot 10^{5}$	$3.4 \cdot 10^{-5}$	0.91	$4.0 \cdot 10^{-4}$	2.11
	15	20	$1.1 \cdot 10^{6}$	$3.6 \cdot 10^{-5}$	0.91	$7.0 \cdot 10^{-4}$	1.99
	24	14	$2.3 \cdot 10^{6}$	$5.0 \cdot 10^{-5}$	0.88	$4.5 \cdot 10^{-4}$	2.84
	168	21	$3.0 \cdot 10^{5}$	$4.1 \cdot 10^{-5}$	0.85	$1.2 \cdot 10^{-3}$	6.13
Duplex	**0**	81	$4.4 \cdot 10^{5}$	$2.9 \cdot 10^{-5}$	0.93	$1.9 \cdot 10^{-3}$	1.62
	15	15	$2.0 \cdot 10^{7}$	$3.6 \cdot 10^{-5}$	0.92	$1.9 \cdot 10^{-3}$	1.76
	24	17	$2.2 \cdot 10^{5}$	$4.3 \cdot 10^{-5}$	0.88	$1.4 \cdot 10^{-3}$	3.09
	168	17	$8.8 \cdot 10^{4}$	$4.7 \cdot 10^{-5}$	0.80	$1.3 \cdot 10^{-2}$	14.8

6.4 Passivation in Disinfection solutions

Due to their mechanical properties and corrosion resistance, stainless steels are the most employed materials in food and pharmaceutical industries, where severe regulations relating to contamination of processed fluids and a highly awareness regarding health and safety of consumers are required. In order to avoid contaminations due to the occurrence of corrosion phenomena and to eliminate bacteria, viruses and spoilage microorganisms from surfaces and equipment, *Cleaning*, *Disinfection* and *Sanitization* operations are usually employed thanks to the physical action of high velocity flow jet spray, agitation and chemical action of cleaning agents enhanced by high temperature[58]. On the other hand, prolonged exposure to cleaning solutions can induce modifications on composition and therefore on electronic properties of passive films due to the onset of corrosion phenomena (i.e. rouging) during disinfection and/or cleaning processes[55].

Sodium hypochlorite is the most widely used chemical in the food industry for the removal of organic soils (cleaning) and control of microbes (disinfection) in a single process. According to the literature[89,91–93,207], the disinfection is due to the penetration of HClO into microbial cell across their wall and membrane inhibiting the enzyme activity essential to the growth and damaging the membrane and DNA. The cleaning action of sodium hypochlorite is based on the synergism of the oxidizing power of ClO^- and the ability of OH^- to dissolve organic soils. A role is also played by the temperature[85,208,209].

The concentration of un-dissociated HClO and ClO^- are pH dependent according to the following relationships:

$$HClO = ClO^- + H^+$$

$$\log [ClO^-]/[HClO] = - 7.49 + pH$$

Thus, [HClO] << [ClO^-] in alkaline solution. The concentration of NaClO has a direct impact on the pH of the solution but also on the possible disinfection activity. This explains why there are several works investigating the effect of NaClO solution with different concentration on their cleaning and disinfection activity. In spite the large interest of these aspects, there are just a few works focusing on the effect of NaClO solution on the corrosion resistance of stainless steel[59,210–212].

Typically, stainless steel 316L grade is the most employed material for the construction of equipment used directly in food processing, such as tank, process vessels, fermenters, homogenizers, evaporators and packaging machines, as well as for the realization of the components of CIP system due to its superior corrosion resistance[58]. On the other hand, only some guidelines are reported regarding the operating conditions involved during disinfection process in terms of NaClO concentration, temperature and time contact. Moreover, there is a lack on the knowledge of the suitable amount of NaClO in order to gain a good compromise between cleaning/disinfection efficiencies and corrosion resistance of the employed materials. In spite low NaClO concentrated solutions are recommended according to the prescription reported in the literature, the present work aims to study corrosion resistance of 316L/EN 1.4404 in chlorine based solutions as a function of NaClO concentration, pH and temperature, in order to simulate disinfection processes. Passive films were grown at open circuit potential by immersion of 316L stainless steel in the solutions under investigation. Samples were passivated in 60 mg L^{-1} (~ 8.1 10^{-4} M, pH ~ 8.5), 6 g L^{-1} (~ 8.1 10^{-2} M, pH ~ 10.8), and 60 g L^{-1} (~ 0.81 M, pH ~ 11.4) NaClO containing solutions for different immersion time (15 h, 24 h and 168 h) at room temperature and 45 °C. The aforementioned solutions were prepared by diluting a pure ~ 10% NaClO solution. Due to the high hygienic standards in terms of surface roughness in food and bioprocessing, 316L SS coupons were mechanically treated as described in section 3.

6.4.1 *In-situ OCP Measurements*

To monitor the passive film properties as a function of the immersion time, AISI 316L coupons were immersed in NaClO solutions of different concentrations at room temperature and at 45°C. Fig. 6-24 shows the open circuit potential vs immersion time plots recorded for 316L samples immersed in hypochlorite solution of different NaClO concentrations (and thus pH). At room temperature (see Fig. 6-24a) an open circuit potential close to ~ 0.2 V vs. Ag/AgCl was measured in 60 mg L^{-1} solution (pH ~ 8.5) after 168 h of immersion. More anodic values were measured in 6 g L^{-1} (pH ~ 10.8) and 60 g L^{-1} (pH ~ 11.4) solutions reaching 0.45 and 0.62 V vs. Ag/AgCl, respectively, after 168 h of immersion.

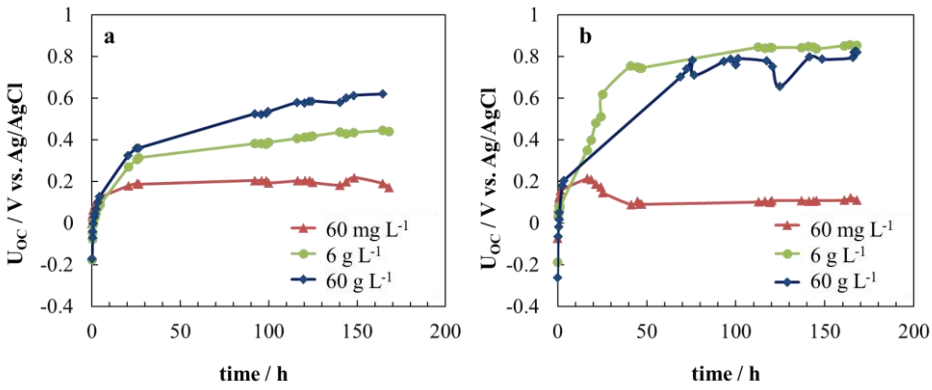

Fig. 6-24. Potential vs. time curves recorded for 30 minutes in 60 mgL^{-1} (pH ~ 8.4) (red line), 6 gL^{-1} (pH ~ 10.8) (green line) and 60 gL^{-1} (pH ~ 11.4) (blue line) at a) room temperature and b) 45°C.

This experimental finding could be explained considering the very high oxidizing potential of highly concentrated NaClO solution. Indeed, in aerated ClO^- containing solution the possible cathodic processes can be:

$$ClO^- + 2H^+ + 2e^- = Cl^- + H_2O \qquad (1a)$$

$$U_{eq} = 1.715 - 0.0591pH + 0.0295\log (ClO^-/Cl^-) \quad (V \text{ vs. SHE})$$

$$2ClO^- + 4H^+ + 2e^- = Cl_2 + 2H_2O \quad (1b)$$

$$U_{eq} = 2.036 - 0.1182pH + 0.0295\log((ClO^-)^2/(Cl_2)) \quad (V \text{ vs. SHE})$$

$$O_2 + 2H_2O + 4e^- = 4OH^- \quad (1c)$$

$$U_{eq} = 1.23 - 0.059pH \quad (V \text{ vs. SHE})$$

According to the equilibrium potentials reported in Table 6-12, hypochlorite reduction is thermodynamically favourable with respect to O_2 reduction and therefore the corrosion potential will be shifted toward more anodic values with respect to those measured at the same pH in ClO^- free solution. According to[117,201], corrosion potentials of 0 V vs. Ag/AgCl at pH ~ 8.4 and of - 0.5 V/AgAgCl at pH ~ 13 were measured for 316L samples.

Table 6-12. Equilibrium potentials for the three possible cathodic processes in the NaClO solutions at the corresponding pH.

	E_0 / V vs Ag/AgCl		
	pH 8.4	**pH 10.8**	**pH 11.4**
(1a) ClO^- / Cl^-	1.104	1.023	1.017
(1b) ClO^- / Cl_2	0.838	0.672	0.660
(1c) O_2 / OH^-	0.534	0.393	0.357

At the lowest ClO^- concentration (i.e. 60 mg L^{-1} and pH ~ 8.5), the resulting E_{corr} falls in the passive region according to Fig. 6-25, while at higher hypochlorite concentration the corrosion potentials are very close or higher than the equilibrium potential for Cr_2O_3 oxidation to chromate ions, since the early stage of immersion with consequent dissolution of Cr species from the passive film (see Table 6-13). For the latter, E_{corr} increases monotonically with immersion time, so that also O_2 evolution becomes thermodynamically possible after 168 hours of immersion.

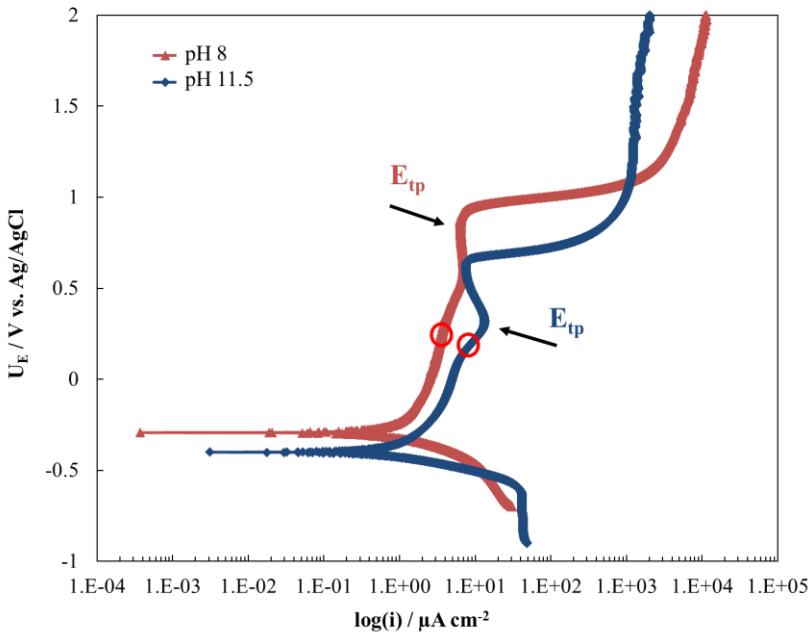

Fig. 6-25. Polarization curves recorded in a) 0.1 M ABE at pH 8 (red line) and b) 0.01 M NaOH pH 11.5 (blue line).

According to Fig. 6-24b, at 45°C a slightly lower corrosion potential is measured in 60 mg L^{-1} solution, while more anodic values (up to 0.8 V vs Ag/AgCl) were measured in 6 and 60 g L^{-1} solutions with respect to those obtained at room temperature. The equilibrium potential for 1a, 1b and 1c at 45°C are not far from those at room temperature, since very low temperature coefficient can be estimated for the corresponding reactions[213]. Thus, E_{corr} is significantly higher than the chromate formation potential and, for long immersion time, for oxygen reduction.

Table 6-13. Equilibrium potentials for Cr oxidation to chromate ions at the corresponding pH.

	E_0 / V vs Ag/AgCl		
Cr_2O_3 / CrO_4^{2-}	**pH 8.4**	**pH 10.8**	**pH 11.4**
$E_0 = 1.386 – 0.0985pH + 0.0197log(CrO_4^{2-})$	0.24	0	-0.06
$E_0 = 1.311 – 0.0985pH + 0.0197log(CrO_4^{2-})$	0.17	-0.07	-0.13
$E_0 = 1.244 – 0.0985pH + 0.0197log(CrO_4^{2-})$	0.10	-0.14	-0.197

6.4.2 *XPS measurements*

Fig. 6-26 and Fig. 6-27 show Fe $2p_{3/2}$, Cr $2p_{3/2}$ and O 1s core level spectra after 168 h of immersion time in all passivating solutions at room temperature and at 45 °C. For the samples immersed at room temperature in 60 mg L^{-1} and 6 g L^{-1} of NaClO solution the Fe $2p_{3/2}$ core level spectra exhibit a peak at ~ 710 eV associated to Fe^{3+} in the surface oxide layer[214]. In the case of sample immersed in 60 g L^{-1} of NaClO solution, a shift of this peak toward higher binding energy (~712 eV) is evident and can be associated to the presence of Fe^{3+} hydroxide in the surface oxide layer[214]. It is important to mention that for the sample after 168 h of immersion in 60 mg L^{-1} of NaClO solution, a weak peak at ~ 707 eV related to metallic Fe is detected[214]. This experimental finding suggests the formation of a very thin passive film that does not allow to fully attenuating the photoelectrons emitted by the substrate. Cr $2p_{3/2}$ core level spectra exhibit a peak at ~ 576 eV related to the Cr^{3+} in the surface oxide layer. No Cr^{+6} peaks are detected. For 60 g L^{-1} of NaClO solution a reduction of the peak intensity occurs, associated to a reduction of chromium content in the surface oxide layer. O 1s core level spectra exhibit one peak at ~ 530 eV that is related to O^{2-} and one peak at ~ 532 eV that is related to OH^-. For the samples immersed in 60 mg L^{-1} and 6 g L^{-1} of NaClO solution, the O^{2-} peak is higher with respect to OH^-. In the case of 60 g L^{-1} of NaClO solution, an increase of the OH^- with respect to O^{2-}

peak is evident, relating to an increase of hydroxide content in the surface oxide layer in agreement with the Fe $2p_{3/2}$ core level spectra evidence.

The same peaks are present for the samples immersed in 60 mg L^{-1} and 6 g L^{-1} of NaClO solution at 45°C. In the case of 60 g L^{-1} of NaClO solution at 45°C, it is important to stress the absence of peak related to Cr^{3+} in the surface oxide layer and the increase of OH^- peak suggesting the hydration of the iron oxide on the surface.

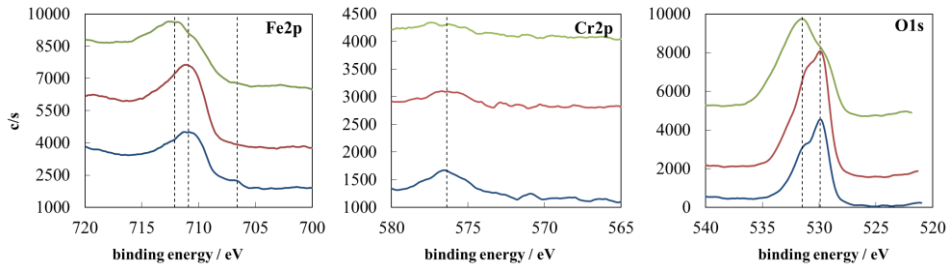

Fig. 6-26. Fe $2p_{3/2}$, Cr $2p_{3/2}$ and O 1s core level spectra after 168 h exposure at room temperature in 60 mg L^{-1} (blue line), 6 g L^{-1} (red line) and 60 g L^{-1} (green line) NaClO containing solutions.

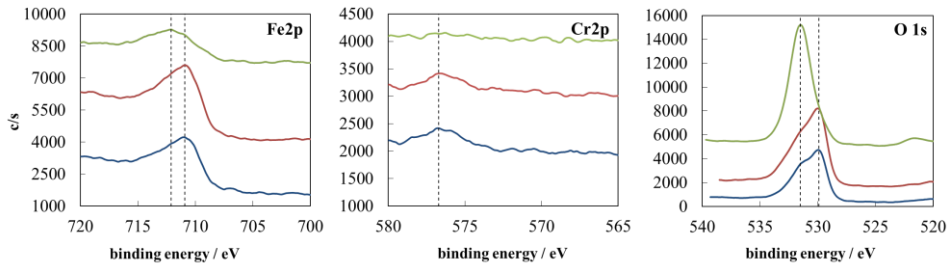

Fig. 6-27. Fe $2p_{3/2}$, Cr $2p_{3/2}$ and O 1s core level spectra after 168 h exposure at 45 °C in 60 mg L^{-1} (blue line), 6 g L^{-1} (red line) and 60 g L^{-1} (green line) NaClO containing solutions.

Due to the knowledge of the atomic composition, the intensity ratio between the main peaks corresponding to the presence of Cr and Fe was calculated. According to the values reported in Table 6-14, Cr amount in passive films

drastically decreases in highly chlorine concentrated solutions at both temperatures suggesting an iron enrichment due to chromium dissolution phenomena after high exposure time to disinfectant solutions. Experimental results are in agreement with the formation of iron oxi/hydroxide passive layers whose hydroxide content increase by increasing NaClO content.

Table 6-14. Atomic composition of passive layers grown after 168 h of exposure in chlorine containing disinfection solutions at room temperature and at 45 °C. Cr / Fe atomic ratio is also reported as a function of passivation conditions.

atomic percent (at. %)							
Room Temperature							
	N 1s	**O 1s**	**Cr 2p**	**Fe 2p**	**Ni 2p**	**Mo 3d**	**Cr / Fe**
60 mg L^{-1}	0.77	32.05	1.57	6.32	2.07	0.27	0.25
6 g L^{-1}	1.24	54.6	1.2	11.23	0	0.17	0.11
60 g L^{-1}	0.21	49.85	0.78	8.1	0.58	0.06	0.10
45 °C							
	N 1s	**O 1s**	**Cr 2p**	**Fe 2p**	**Ni 2p**	**Mo 3d**	**Cr / Fe**
60 mg L^{-1}	0.1	31.73	4.38	19.19	3.66	0.2	0.24
6 g L^{-1}	0.58	47.73	0.97	8.7	0.15	0.07	0.11
60 g L^{-1}	0.34	54.85	0.53	4.64	0	0.09	0.11

6.4.3 *Polarization curves*

Soon after immersion in NaClO solution, polarization curves were recorded in no aggressive solution (0.1 M ABE), in order to get further information on the passive film formed during the immersion in disinfection solutions. The passivity current is not strongly influenced by immersion time for 60 mg L^{-1} NaClO solution even at 45°C (see Fig. 6-28), and the effect is also negligible for 6 g L^{-1} solution at room temperature (see Fig. 6-29a). Conversely, at 45°C in 6 g L^{-1} and for 60 g L^{-1} solution at room temperature and 45°C, the passivity current is very low. Moreover, the peak current corresponding to Cr dissolution as Cr(VI) for passive film formed after 168 h in 60 g L^{-1} solution at 45°C becomes almost negligible suggesting a strong chromium depletion in the film (see Fig. 6-30b).

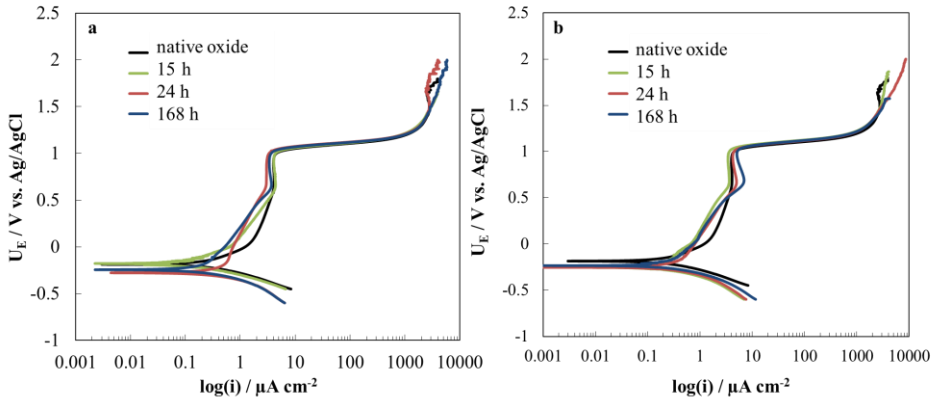

Fig. 6-28. Polarization curves recorded at 1 mV s^{-1} in 0.1 M ABE (pH ~ 8) after passivation at the open circuit potential in 60 mg L^{-1} NaClO at a) room temperature and b) 45°C.

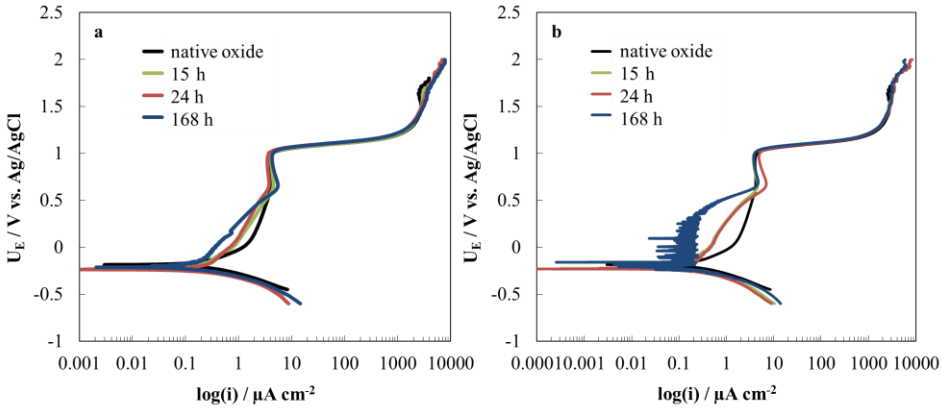

Fig. 6-29. Polarization curves recorded at 1 mV s^{-1} in 0.1 M ABE (pH ~ 8) after passivation at the open circuit potential in 6 g L^{-1} NaClO at a) room temperature and b) 45°C.

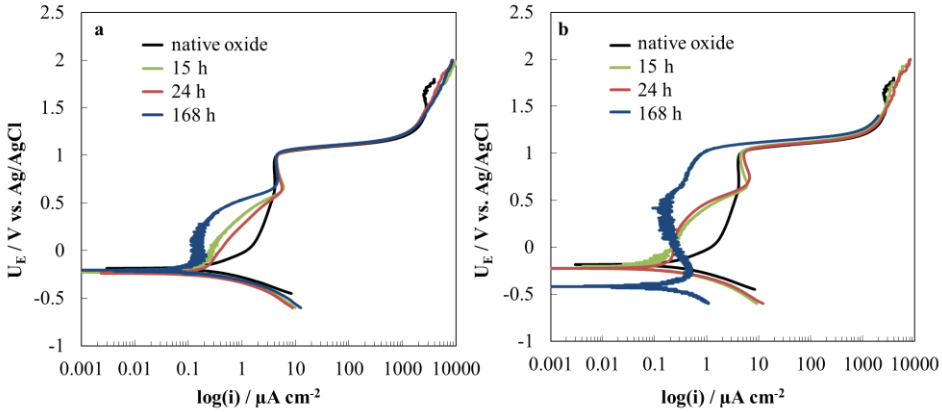

Fig. 6-30. Polarization curves recorded at 1 mV s^{-1} in 0.1 M ABE (pH ~ 8) after passivation at the open circuit potential in 60 g L^{-1} NaClO at a) room temperature and b) 45°C.

6.4.4 *Photoelectrochemical measurements*

In order to study passive films composition and their electronic properties (band gap, conductivity type), photoelectrochemical measurements were carried out in 0.1 M ABE solution (pH ~ 8) where, according to the Pourbaix diagram at this potential and at this pH, the chromium oxide is thermodynamically stable[150]. Photoelectrochemical spectra recorded in an exploited potential range close to the open circuit potential in order to avoid modifications of passive film properties (U_E = 0.15 V vs. SSC) for passive films grown after 168 h of immersion in the disinfectant solution are reported in Fig. 6-31. A redshift in the optical emission threshold is also present for passive films grown in 6 gL^{-1} and 60 gL^{-1} NaClO containing solutions. According to Eq. 3.10, by assuming a no direct optical transition, E_g have been estimated, as reported in Fig. 6-31c-e.

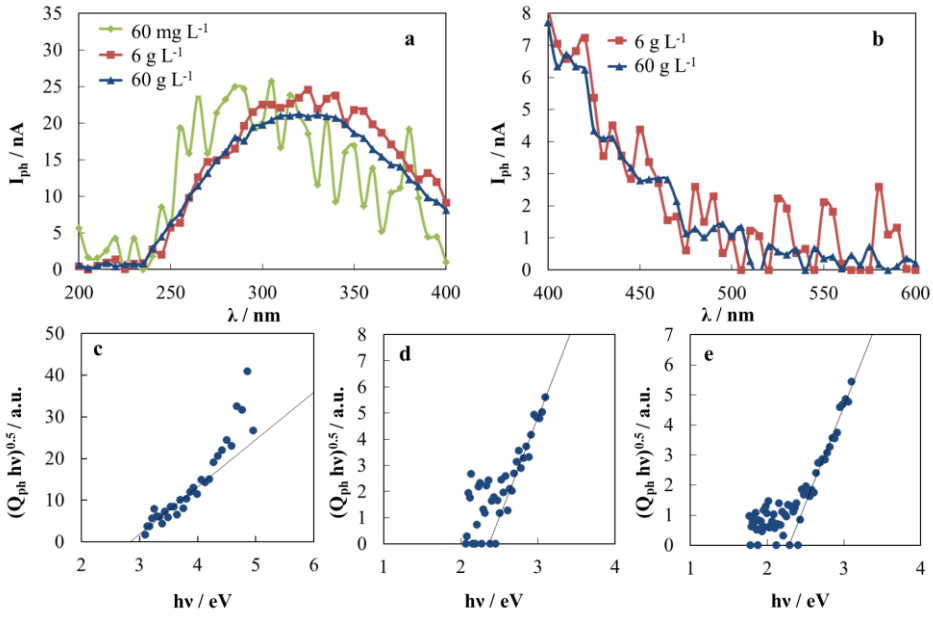

Fig. 6-31. Raw photocurrent spectra related to passive films grown on 316L SS with a mirror surface finishing after 168 h of immersion at room temperature in disinfection solutions by polarizing samples in ABE solution (pH ~ 8) at U_E = 0.15 V vs. Ag/AgCl for (a) 200 nm < λ < 400 nm and (b) λ ≥ 400nm. (c) $(Q_{ph}\ h\nu)^{0.5}$ vs hν for passive film grown after 168 h of immersion in 60 mgL^{-1} NaClO, (d) $(Q_{ph}\ h\nu)^{0.5}$ vs hν for passive film grown after 168h of immersion in 6 gL^{-1} NaClO and (e) $(Q_{ph}\ h\nu)^{0.5}$ vs hν for passive film grown after 168h of immersion in 60 gL^{-1} NaClO.

The same photoelectrochemical investigation was carried out for passive films grown on 316L in the solutions under investigation at 45°C. According to the photocurrent spectra reported in Fig. 6-32a-b, passive films grown in 6 g L^{-1} and 60 g L^{-1} are more photoactive if compared with those grown at room temperature and a redshift of the light absorption threshold is measured for oxide layers grown at pH 10.8 and 11.4.

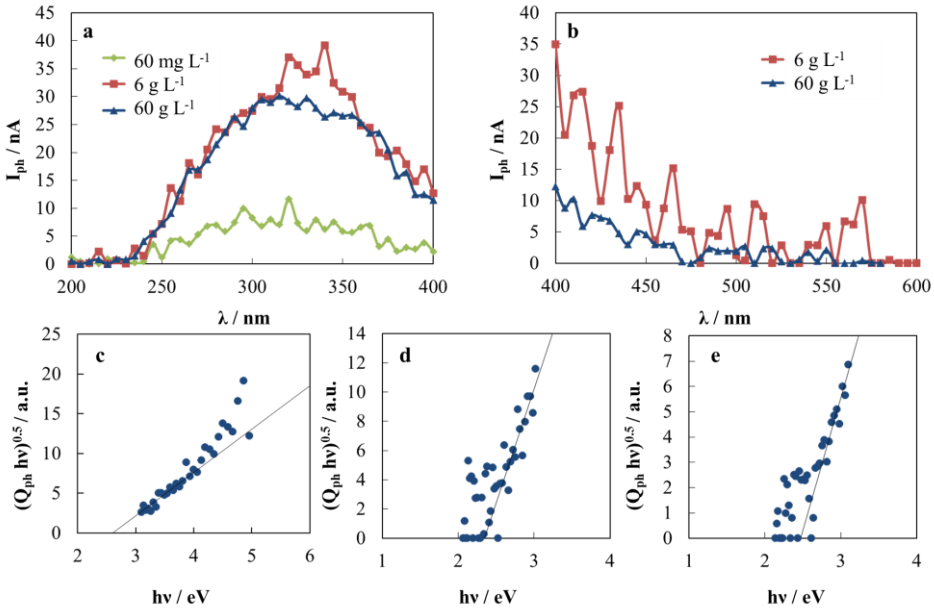

Fig. 6-32. Raw photocurrent spectra related to passive films grown on 316L SS with a mirror surface finishing after 168 h of immersion at 45 °C in disinfection solutions by polarizing samples in ABE solution (pH ~ 8) at U_E = 0.15 V vs. Ag/AgCl for (a) 200 nm < λ < 400 nm and (b) λ ≥ 400nm. (c) $(Q_{ph}\ h\nu)^{0.5}$ vs hν for passive film grown after 168 h of immersion in 60 mgL^{-1} NaClO, (d) $(Q_{ph}\ h\nu)^{0.5}$ vs hν for passive film grown after 168h of immersion in 6 gL^{-1} NaClO and (e) $(Q_{ph}\ h\nu)^{0.5}$ vs hν for passive film grown after 168h of immersion in 60 gL^{-1} NaClO.

Optical band gap estimated for passive films grown on 316L by immersion in the mimicking solutions under investigation after different immersion time at room temperature and 45°C are reported in Table 6-15. The E_g values reported are lower with respect to that reported for the native oxide film grown on 316L by air exposure as well as with respect to that estimated for Cr_2O_3[55,117,201] (E_g close to 3.0 eV). Moreover, for passive films grown in 60 mg L^{-1} at room

temperature a E_g ~ 2.85 eV was estimated that is not affected by the immersion time in agreement with the formation of an iron containing chromium oxide[201]. Conversely, slightly lower values were obtained after passivation in 45°C in the same solution suggesting the formation of a more hydrate passive film in agreement with the XPS measurements.

For highly concentrated solutions passivation at both room temperature and 45°C lead to the formation of passive films whose estimated optical band gap values are significantly lower, in agreement with the formation of iron rich oxide layer. In fact, a band gap value close to that reported for FeOOH[160] and band gap value ranging from 1.9 to 2.2 eV are reported for Fe_2O_3[55,115].

Table 6-15. Band gap values for passive films grown on 316L SSs with a mirror surface finishing at the open circuit potential by immersion for 15 h, 24 h and 168 h in different NaClO containing solutions both at Room Temperature and 45 °C.

	E_g / eV					
Passivation conditions	**Room Temperature**			**45 °C**		
	15 h	**24 h**	**168 h**	**15 h**	**24 h**	**168 h**
60 mg L^{-1}	2.86	2.86	2.84	2.61	2.6	2.54
6 g L^{-1}	2.54	2.53	2.37	2.38	2.36	2.35
60 g L^{-1}	2.39	2.32	2.29	2.47	2.35	2.4

In order to check the real sing of photocurrent and the n-type or p-type conductivity behavior, current vs. time curves have been recorded at U_E = 0.15 V vs SSC in ABE solution by manually chopping sample irradiation under monochromatic light (λ = 280 nm) for passive films grown in the solutions under investigations at both temperatures. According to the current transient, reported in Fig. 6-33, passive films grown on 316L behaves like n-type

semiconductor and anodic spikes were also recorded as expect for iron oxide films[55].

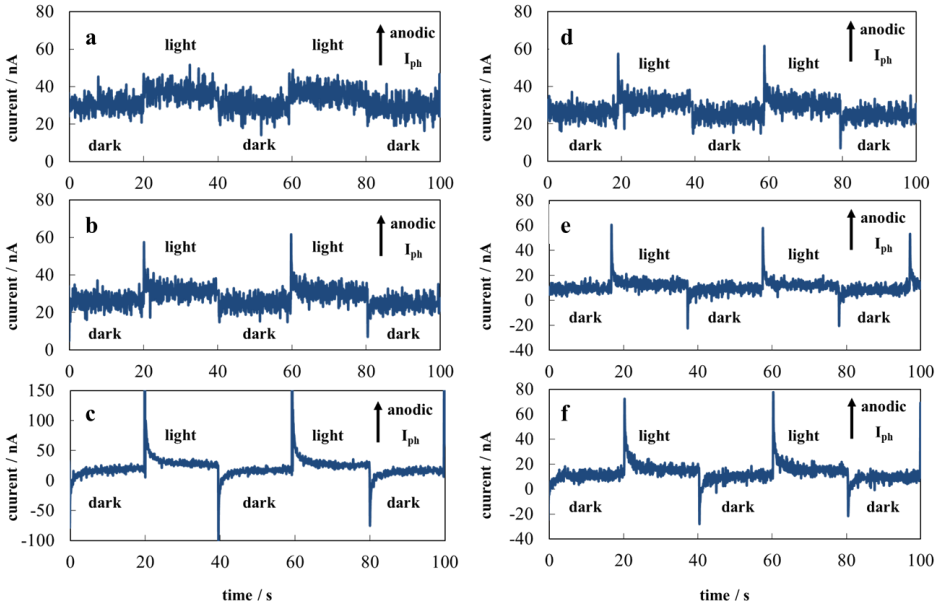

Fig. 6-33. Current vs time curves recorded under illumination (on) and dark conditions (off) at λ = 280 nm at U_E = 0.15 V vs SSC in 0.1 M ABE solution (pH ~ 8) for passive grown on 316 SS mechanically treated after 168 h of immersion in a) 60 mgL^{-1} NaClO at room temperature, b) 6 gL^{-1} NaClO at room temperature and c) 60 gL^{-1} NaClO at room temperature d) 60 mgL^{-1} NaClO at 45°C, e) 6 gL^{-1} NaClO at 45°C and f) 60 gL^{-1} at 45°C NaClO disinfectant solutions.

6.4.5 *Impedance measurements*

In Fig. 6-34, impedance spectra recorded in 0.1 M ABE (pH ~ 8) at the open circuit potential (U_{OC} ~ 0.1 V vs. SSC) are reported in the Nyquist representation (i.e. imaginary part vs. real part of the overall impedance) as a function of NaClO concentration.

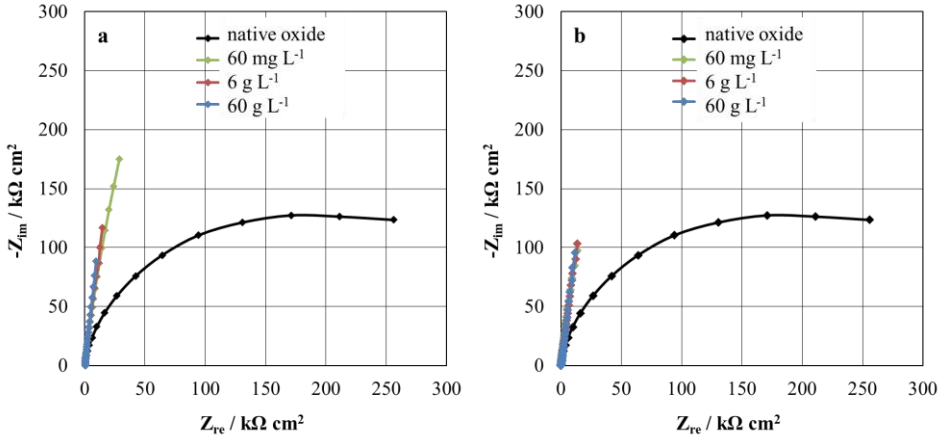

Fig. 6-34. EIS spectra in Nyquist representation for passive films grown on 316L SS after passivation at open circuit potential at a) room temperature and b) 45 °C, recorded in 0.1 M ABE (pH ~ 8) at the open circuit potential (U_{OC} ~ 0.1 V vs SSC).

EIS spectra of native oxide grown on 316L by air exposure has been also recorded in order to have a reference. Fitting parameters of the latter are reported in Table 6-16. The dependence of the imaginary impedance component on real component is describe by a portion of a slightly depressed semicircle. In order to get a rough estimation of the corresponding oxide resistance (R_{ox}), EIS spectra were finally fitted according to the equivalent circuit reported in Fig. 4-12. According to the fitting parameters reported in Table 6-17 and Table 6-18, R_{ox} is higher than that obtained for the native oxide grown by air exposure (see Table 6-16) and their values increase by increasing both immersion time and NaClO amount in simulating solutions.

Table 6-16. Fitting parameters of EIS spectra on passive films grown by air exposure on 316L SS with a mirror surface finishing according to the equivalent circuit reported in Fig. 4-12.

native oxide				
R_{sol} Ω cm^2	R_{ox} Ω cm^2	Q_{CPE} S s$^{\alpha}$ cm^{-2}	α	δ nm
48.87	$1.94 \cdot 10^{5}$	$1.46 \cdot 10^{-5}$	0.931	3.18

Table 6-17. Fitting parameters of EIS spectra on passive films grown on 316L SS with a mirror surface finishing at the open circuit potential by immersion in disinfectant solutions under investigation at room temperature according to the equivalent circuit reported in Fig. 4-12. Thickness values estimated according to the power law model are also reported.

Passivation condition		R_{sol} Ω cm^2	R_{ox} Ω cm^2	Q_{CPE} S s$^{\alpha}$ cm^{-2}	α	δ nm
60 mg L^{-1}	**15 h**	60.76	$5.14 \cdot 10^{5}$	$1.14 \cdot 10^{-5}$	0.940	3.49
	24 h	49.63	$1.96 \cdot 10^{6}$	$6.39 \cdot 10^{-6}$	0.904	6
	168 h	46.61	$2.50 \cdot 10^{6}$	$8.54 \cdot 10^{-6}$	0.936	4.51
6 g L^{-1}	**15 h**	52.97	$8.55 \cdot 10^{5}$	$1.61 \cdot 10^{-5}$	0.940	2.40
	24 h	58.27	$2.13 \cdot 10^{6}$	$7.69 \cdot 10^{-6}$	0.932	6.17
	168 h	56.23	$3.00 \cdot 10^{6}$	$1.30 \cdot 10^{-5}$	0.940	2.95
60 g L^{-1}	**15 h**	55.81	$9.11 \cdot 10^{6}$	$1.89 \cdot 10^{-5}$	0.946	1.63
	24 h	64.09	$9.50 \cdot 10^{6}$	$1.78 \cdot 10^{-5}$	0.940	2.13
	168 h	58.36	$1.76 \cdot 10^{7}$	$1.75 \cdot 10^{-5}$	0.935	2.79

Table 6-18. Fitting parameters of EIS spectra on passive films grown on 316L SS with a mirror surface finishing at the open circuit potential by immersion in disinfectant solutions under investigation at 45 °C according to the equivalent circuit reported in Fig. 4-12. Thickness values estimated according to the power law model are also reported.

Passivation condition		R_{sol} Ω cm^2	R_{ox} Ω cm^2	Q_{CPE} S s$^{\alpha}$ cm^{-2}	α	δ nm
60 mg L^{-1}	15 h	61.43	$8.19 \cdot 10^5$	$6.28 \cdot 10^{-6}$	0.920	9.32
	24 h	59.46	$1.65 \cdot 10^6$	$1.07 \cdot 10^{-5}$	0.942	3.59
	168 h	57.11	$2.52 \cdot 10^6$	$1.56 \cdot 10^{-5}$	0.940	2.40
6 g L^{-1}	15 h	54.93	$1.41 \cdot 10^6$	$1.13 \cdot 10^{-5}$	0.940	3.49
	24 h	54.26	$2.01 \cdot 10^6$	$1.49 \cdot 10^{-5}$	0.942	2.56
	168 h	54.49	$3.96 \cdot 10^6$	$1.45 \cdot 10^{-5}$	0.931	3.17
60 g L^{-1}	15 h	60.79	$1.22 \cdot 10^7$	$1.76 \cdot 10^{-5}$	0.929	2.64
	24 h	55.26	$1.60 \cdot 10^7$	$1.97 \cdot 10^{-5}$	0.937	2.08
	168 h	53.78	$2.60 \cdot 10^7$	$1.62 \cdot 10^{-5}$	0.902	5.61

In order to estimate the thickness of passive films grown after immersion in the disinfectant solutions, the power law model analysis[170,171] was applied to CPE parameters provided in Table 6-17 and Table 6-18 by assuming $\varepsilon = 12$ and limiting value of resistivity of 450 Ohm cm taken from calibration of Fe17Cr stainless steel[170]. According to the power-law approach, passive films grown in 60 mg L^{-1} solution are thicker than those grown at higher NaClO concentrations (see Table 6-17 and Table 6-18), in contrast to the results provided by the XPS analyses. However, since the latter are n-type semiconductors with a very low Cr concentration, it is likely that the power law formula provides the space charge region width instead of the entire film thickness.

In this experimental work the effect of chlorine concentration, exposure time and

temperature on corrosion resistance of passive films grown during disinfection processes was investigated. According to the photoelectrochemical characterization, long time exposure to disinfectant solutions lead to the formation of iron-chromium mixed oxide films with an iron content that increase by increasing exposure time to aggressive environments. Moreover, the estimated band gap decreases by increasing immersion time and NaClO concentration up to values corresponding to the formation of a hydrated iron oxide film. This experimental finding is also supported by XPS data and PCS measurements. According to the experimental results, highly concentrated NaClO solution can lead to a strong chromium depletion of the passive film with consequent onset of Class II rouging phenomena. In fact, passive film loses chromium during immersion in 6 and 60 g L^{-1} NaClO solution with consequent formation of an iron rich hydrated oxide, which is a n-type semiconductor but under very high anodic potential (as those measured in this electrolyte) is under Fermi level pinning with consequent onset of a potential dependent current dissolution (see scheme of Fig. 6-35). Moreover, since the reduction of ClO^- ions produces chloride ions, a localized attack (i.e. pitting) can occur on the surface of the SS, whose pitting resistance is less than expected due to the chromium depletion. This phenomenon can be enhanced by using a higher temperature (namely 45°C), due to a higher chromium dissolution rate as well as to a reduction of pitting potential[215]. When the disinfection is carried out at pH 8.5 the film is a n-type semiconductor under reverse bias regime with a low passivation current balanced by the dissolution at the metal/film interface, thus accounting for a constant film thickness.

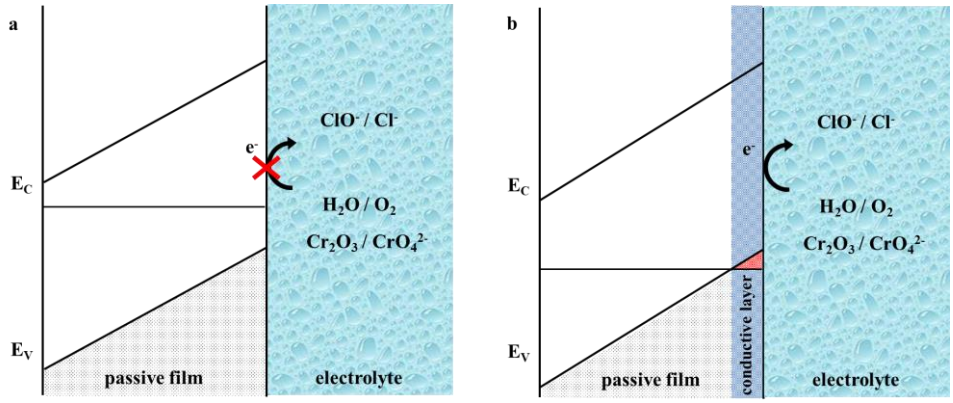

Fig. 6-35. Scheme relating to passive film/electrolyte interface a) under anodic potential and b) under Fermi level pinning where allowed electronic states are reported in red.

According to *Novoa et al.*[209] the passive films on SS grown during immersion in NaClO solutions are described by a topotactic model with chromium rich regions behaving like insulator or semiconductor and iron rich regions characterized by the presence of magnetite with a high conductivity and, thus, where no charge accumulation is possible. The model accounts for a very high capacitance estimated from the impedance spectra corresponding to a film thickness without any physical meaning. However, the experimental findings of this work suggest a different model for the passive films grown in the disinfection solution. In fact, the EIS spectra can be easily fitted with just one time constant and the corresponding capacitance, estimated using the power law[170,171], provides physically reasonable thickness. Moreover, the corrosion potential reached during the immersion in 6 and 60 gL^{-1} NaClO solutions is so positive that the presence of magnetite is not likely.

6.5 Concluding remarks

Passive films on different SS grades (namely 304L, 316L and Duplex) were grown by immersion at open circuit potential in solutions mimicking the environments typical of food and beverage industry according to the CoE protocol.

In high temperature citric acid (i.e. acidic food processing conditions) the SSs are subjected to a generalized corrosion with metal ions release in concentration roughly proportional to the composition of the steel. The highest dissolution rate was estimated for 316L, resulting the less resistant than 304L and duplex SSs. The passive films formed in these conditions are iron containing chromium oxide behaving as n-type semiconductors according to their band gap values (~ 3.1 – 3.2 eV) and to the corresponding photocurrent transients showing anodic photocurrent. The fitting parameters of the EIS spectra suggest a very slow corrosion process (high polarization resistance) due to the presence of passive films, whose thickness is between 1-2 nm according to the power law model accounting for a not constant resistivity.

In high temperature tap water (i.e. fatty food processing conditions) the release ions concentrations are significantly lower. However, the photoelectrochemical results suggest that the band gap of passive films on 304L and 316L grown during immersion in high temperature tap water becomes lower than that formed under air exposure, as a consequence of iron stability and chromium dissolution. Conversely, passive films on duplex maintain a band gap close to that reported for Cr_2O_3. In spite the very low metal ions release during immersion in tap water the EIS spectra suggest the occurrence of localized corrosion due to the presence of MnS inclusions and to the formation of trenches around them that can bring to the onset of pitting phenomena in spite the very low concentration of chloride species.

According to the photoelectrochemical results, passivation at the open circuit potential after immersion in HPW and CIP solutions induce the formation of almost pure hematite on austenitic grades, while iron doped chromium oxide films are formed on duplex stainless steel. In spite strong chromium depletion, the corresponding oxide layers are n-type semiconductors, thus highly resistant towards corrosion phenomena. Finally, the power low analysis suggests that thickness of passive films grown on different stainless steel grades increases by increasing the immersion time in simulating solutions.

Passivation at open circuit potential was carried out by immersion in different NaClO containing solutions in order to simulate disinfection processes. The effect of chlorine concentration, exposure time and temperature on passivation kinetics was studied. According to the photoelectrochemical characterization of passive films grown on 316L SS, it was found that long time exposure to disinfectant solutions lead to the formation of iron-chromium mixed oxide films with an iron content that increases by increasing exposure time to aggressive environment, as suggested by XPS data. This experimental finding is also supported by PCS measurements. Estimated band gap decreases by increasing immersion time and NaClO concentration down to values corresponding to the formation of a hydrated iron oxide film. According to the photocurrent transients, passive films grown after immersion in simulating solutions are n-type semiconductor, and therefore more resistant toward anodic dissolution processes. In spite of their very low chromium content, the oxide resistance of passive films, estimated by fitting of EIS spectra, is very high even after long exposure time to highly chlorine containing environment.

It is important to stress that the prolonged exposure of SSs to corrosive industrial environments typically employed in food processing significantly affect their composition and electronic properties and thus their corrosion resistance. The variation of Cr content, if any, within passive films should be taken into account by manufacturers when cleaning and disinfection protocols have to be

employed. In fact, according to the experimental results, the prolonged exposure to acidic environments induce thinning of the metal phase and Fe selective dissolution with the formation of Cr rich passive films that can be in turn affected by the exposure to alkaline solutions (i.e. cleaning). On the other hand, fatty and alcoholic food induce strong chromium depletion on austenitic grades with consequent iron enrichment of passive films. This means that the exposure to acidic or chlorine containing solutions (i.e. chlorine based disinfectants) can induce selective dissolution phenomena (i.e. pitting). These experimental findings suggest that cleaning and disinfection solutions need to be carefully handled in term of temperature, concentration and contact time with industrial equipment in order to avoid deterioration of circuit's material.

7 Biofilm Growth

Biofouling on food contact surfaces, such as heat exchangers, work tables and conveyors, represents one of the major concerns in food processing since it has a significant impact on operating efficiency and on food product quality due to the proliferation of food borne pathogens. Biofouling represents a worldwide, costly and eco-aggressive issue common in all food industries, especially in diary processing, since it can induce shortens runtimes due to maintenance operations, reduction of operating efficiency and environmental impact due to the large use of chemical detergents and sanitizers typically employed for cleaning operations. Stainless steels are the most frequently used material for construction of vessels, piping, valves and various types of equipment used in food processing due to their high mechanical and corrosion resistance combined to antibacterial and antifouling properties[216–218]. On the other hand, electrochemical reactions are involved during bacteria proliferation and maturation that can in turn modify the physico-chemical properties of passive films covering SS surface. Moreover, as reported in the literature, severe pitting corrosion can be caused by bacterial proliferation on their surfaces[219,220].

In the present work corrosion resistance of duplex and austenitic 316L stainless steel after biofilm growth was studied. In order to mimic the real growth conditions, a fed-batch fermenter for the production of heterologous recombinant proteins (*Col G*) in *Escherichia Coli* was used. In order to investigate the effect of surface roughness on bacteria attachment and growth, 316L with different surface finishing, whose roughness are reported in Table 7-1, were also studied.

Table 7-1. Surface finishing and average surface roughness R_a of duplex and 316L stainless steel used for bacterial growth and sterilization cycles.

Samples	Finishing	Roughness, R_a / (μm)
316L	2B G220	0.19
316L	2B G600	< 0.19
316L	BA	0.03 – 0.1
Duplex	2E	< 1.2

7.1 Simulation of Sterilization In Place

Since sterilization is performed prior bacteria fermentation, a physico-chemical characterization of passive films grown after different sterilization cycles (20 min of exposure at 121°C in VE series Systec Autoclave) on 316L and duplex stainless steel was carried out by Photoelectrochemical and Impedance measurements. In Fig. 7-1, photocurrent spectra recorded at U_E = 0.15 V vs SSC in 0.1 M ABE (pH ~ 8) for passive films grown after different SIP cycles on 316L 2B G220 are reported. It is important to evidence the presence of a red shift in the light absorption threshold for $\lambda > 400$ nm since after the first SIP cycle corresponding to optical transitions at 2.39 eV. Slightly lower values were obtained after 10 and 30 SIP cycles. The same findings were obtained for 316L 2B G660 and 316L BA. Conversely, no photocurrent was measured in the case of duplex SS after 10 and 30 SIP cycles suggesting thinning of passive film by increasing the exposure time to high temperature vapor. In Table 7-2 the E_g values for both austenitic and duplex stainless steel after different sterilization cycles are reported.

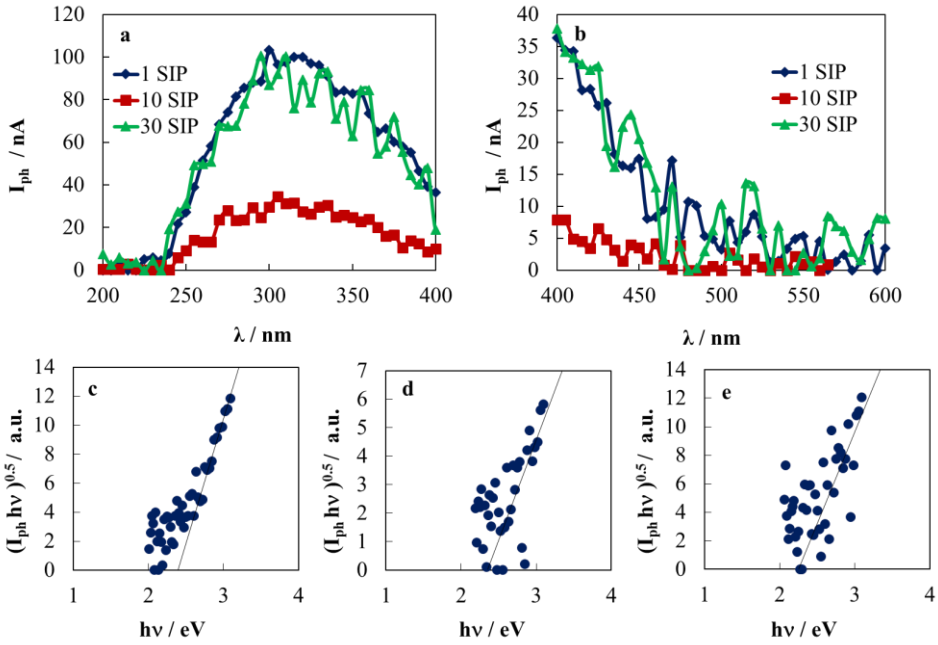

Fig. 7-1. Raw photocurrent spectra recorded at U_E = 0.15 V vs Ag/AgCl in 0.1 M ABE solution (pH ~ 8) for a) 0 < λ < 400 nm and b) λ > 400 nm for passive films grown on 316L 2B G220 stainless steel. $(Q_{ph}\,h\nu)^{0.5}$ vs hν plot for passive grown after c) 1 SIP, d) 10 SIP and e) 30 SIP cycles.

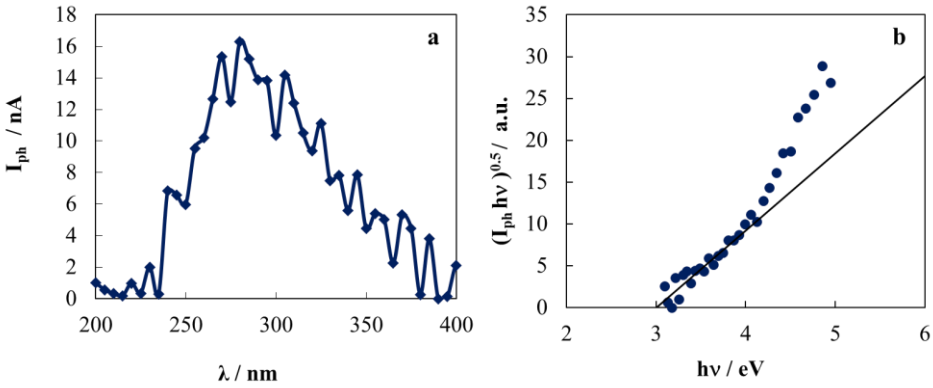

Fig. 7-2. a) Raw photocurrent spectra recorded at U_E = 0.15 V vs Ag/AgCl in 0.1 M ABE solution (pH ~ 8) for passive films grown on duplex stainless steel after 1 SIP cycle and b) $(Q_{ph}\,h\nu)^{0.5}$ vs hν plot.

Table 7-2. Band gap values for passive films grown on 316L with different surface finishing and on duplex stainless steel after 1, 10 and 30 SIP cycles.

Passivation condition	316L G220	316L G600	316L BA	Duplex
1 SIP	2.39	2.35	2.39	3
10 SIP	2.35	2.33	2.42	-
30 SIP	2.25	2.3	2.44	-

Experimental results are in agreement with the formation of iron rich passive films suggesting a strong chromium depletion since from the first sterilization step. The same findings were obtained for 316L with different R_a. Conversely, the optical band gap value reported for duplex SS is 3.0 eV, in agreement with the formation of chromium rich oxide layer.

According to the current transients, recorded under constant irradiating wavelength (λ = 280 nm) showed in Fig. 7-3 and Fig. 7-4, the measured photocurrent is anodic, confirming that the passive films grown on duplex and 316L SS after different sterilization cycles behave as n-type SC. Anodic spikes were also recorded for passive films grown austenitic 316L suggesting a strong recombination of the photogenerated charge carriers, as usually occurs with iron oxide electrodes[115], while no spikes were recorded for passive film on DSS confirming that the latter is a chromium rich oxide layer.

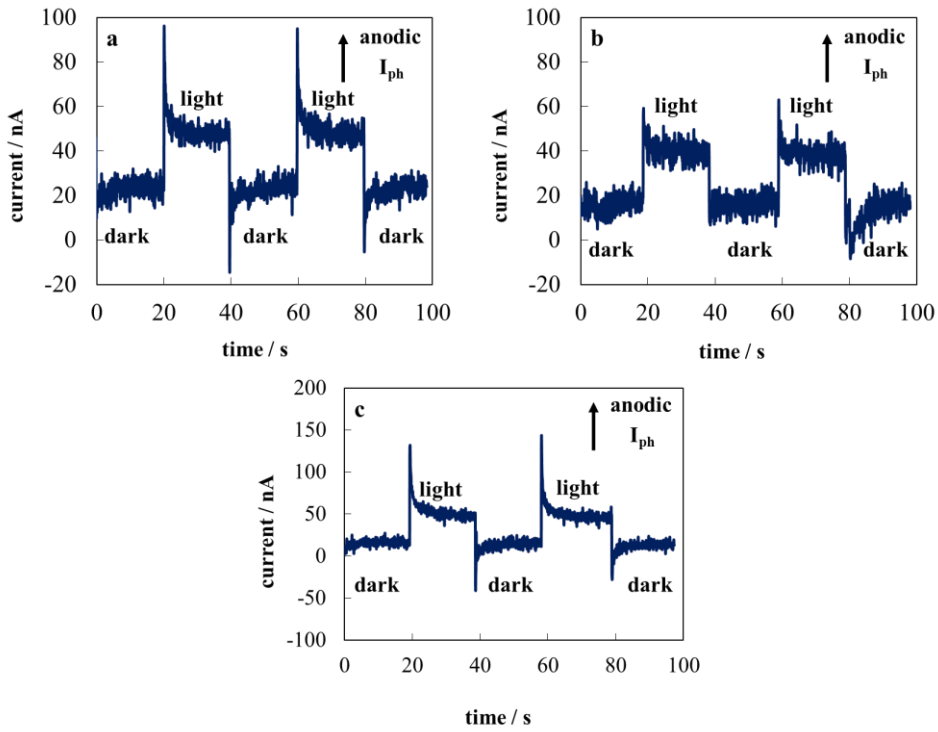

Fig. 7-3. Current vs time curves recorded under illumination (on) and dark conditions (off) at λ = 280 nm at U_E = 0.15 V vs SSC in 0.1 M ABE solution (pH ~ 8) for passive grown on 316 SS 2B G220 after a) 1 SIP, b) 10 SIP and c) 30 SIP cycles.

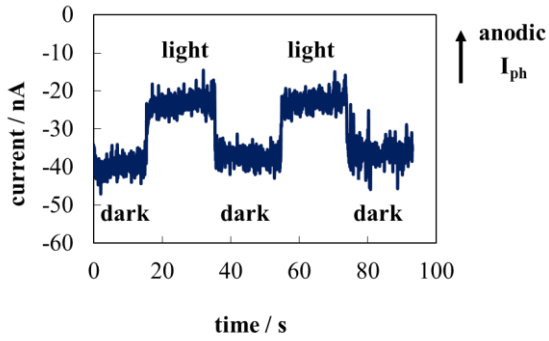

Fig. 7-4. Current vs time curves recorded under illumination (on) and dark conditions (off) at λ = 280 nm at U_E = 0.15 V vs SSC in 0.1 M ABE solution (pH ~ 8) for passive grown on duplex SS after 1 SIP cycle.

In order to get more insight into the resistance of passive films grown after SIP cycles, impedance measurements were also carried out in 0.1 M ABE (pH ~ 8)

at the open circuit potential (U_{OC} ~ 0.1 V vs SS). As displayed by the EIS spectra reported in Fig. 7-5 for austenitic 316L 2B G220, the dependence of the imaginary impedance component on real component is describe by a portion of a slightly depressed semicircle. The same findings were obtained for the other samples.

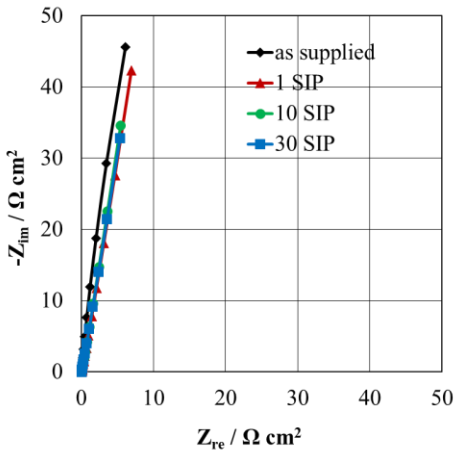

Fig. 7-5. EIS spectra in Nyquist representation recorded in 0.1 M ABE (pH ~ 8) at the open circuit potential (U_{OC} ~ 0.1 V vs SSC) for passive films grown on 316L 2B G220 after different sterilization cycles.

EIS data were finally fitted by employing the equivalent circuit reported in Fig. 4-12. According to the values reported in Table 7-3, passive films grown after several SIP cycles display higher oxide resistance compared to that reported for the corresponding as supplied samples, although the strong Cr depletion. Finally, estimation of the thickness of passive films grown after different SIP cycles was also performed according to the power law model analysis[170,171] applied to CPE parameters provided in Table 7-3 by assuming ε = 12 and limiting value of resistivity of 500 Ohm cm taken from calibration of Fe17Cr stainless steel[170]. According to the estimated values, passive films grown after sterilization process are thicker than those grown on as supplied samples by air exposure.

Table 7-3. Fitting parameters of EIS spectra recorded at the open circuit potential (U_{OC} ~ 0 V vs Ag/AgCl) in 0.1 M ABE (pH ~ 8) on passive films grown on duplex and on 316L with different surface finishing after 1, 10 and 30 SIP cycles according to the equivalent circuit reported in Fig. 4-12.

316L 2B G220						
Passivation conditions	**R_{el} Ω cm²**	**R_{ox} Ω cm²**	**Q_{CPE} S s^{α} cm^{-2}**	**α**	**χ^2**	**δ nm**
As supplied	52	$2.0 \cdot 10^{6}$	$3.4 \cdot 10^{-5}$	0.94	$1.12 \cdot 10^{-2}$	1.2
1 SIP	87	$5.0 \cdot 10^{6}$	$3.5 \cdot 10^{-5}$	0.88	$2.91 \cdot 10^{-3}$	3.7
10 SIP	39	$7.0 \cdot 10^{6}$	$4.4 \cdot 10^{-5}$	0.87	$1.78 \cdot 10^{-3}$	3.6
30 SIP	43	$1.0 \cdot 10^{7}$	$4.6 \cdot 10^{-5}$	0.88	$6.85 \cdot 10^{-4}$	2.7
316L 2B G600						
As supplied	47	$1.0 \cdot 10^{6}$	$3.2 \cdot 10^{-5}$	0.95	$1.01 \cdot 10^{-3}$	1.1
1 SIP	43	$5.0 \cdot 10^{6}$	$3.0 \cdot 10^{-5}$	0.92	$2.16 \cdot 10^{-3}$	1.9
10 SIP	42	$6.0 \cdot 10^{6}$	$4.6 \cdot 10^{-5}$	0.89	$3.69 \cdot 10^{-3}$	2.6
30 SIP	46	$6.0 \cdot 10^{6}$	$4.4 \cdot 10^{-5}$	0.87	$2.81 \cdot 10^{-3}$	4.0
316L BA						
As supplied	43	$1.1 \cdot 10^{6}$	$3.9 \cdot 10^{-5}$	0.95	$1.50 \cdot 10^{-3}$	0.8
1 SIP	82	$6.0 \cdot 10^{6}$	$4.1 \cdot 10^{-5}$	0.87	$2.95 \cdot 10^{-3}$	3.9
10 SIP	47	$6.0 \cdot 10^{6}$	$5.7 \cdot 10^{-5}$	0.90	$7.00 \cdot 10^{-3}$	1.5
30 SIP	45	$5.0 \cdot 10^{6}$	$6.0 \cdot 10^{-5}$	0.89	$3.27 \cdot 10^{-3}$	1.8
Duplex						
As supplied	30	$2.0 \cdot 10^{5}$	$4.1 \cdot 10^{-5}$	0.93	$4.77 \cdot 10^{-3}$	1.2
1 SIP	63	$9.0 \cdot 10^{6}$	$2.5 \cdot 10^{-5}$	0.87	$2.34 \cdot 10^{-3}$	6.0
10 SIP	71	$7.0 \cdot 10^{6}$	$3.4 \cdot 10^{-5}$	0.90	$2.20 \cdot 10^{-3}$	2.7
30 SIP	37	$1.0 \cdot 10^{7}$	$3.4 \cdot 10^{-5}$	0.90	$1.02 \cdot 10^{-3}$	2.8

7.2 Bacteria Growth

E. Coli growth on duplex and 316L with different surface finishing (2B G220, 2B G600, BA and mirror) stainless steel samples was carried out in a fed-batch fermenter, whose schematic representation in reported in Fig. 7-6. According to the experimental set-up, fed-batch fermentation consists on a not closed system where one or more specific nutrients are fed into the vessel during the process allowing cell to proliferate at a specific growth rate thanks to it is possible to obtain both high cell densities and product concentration minimizing by-product excretion at the same time[214].

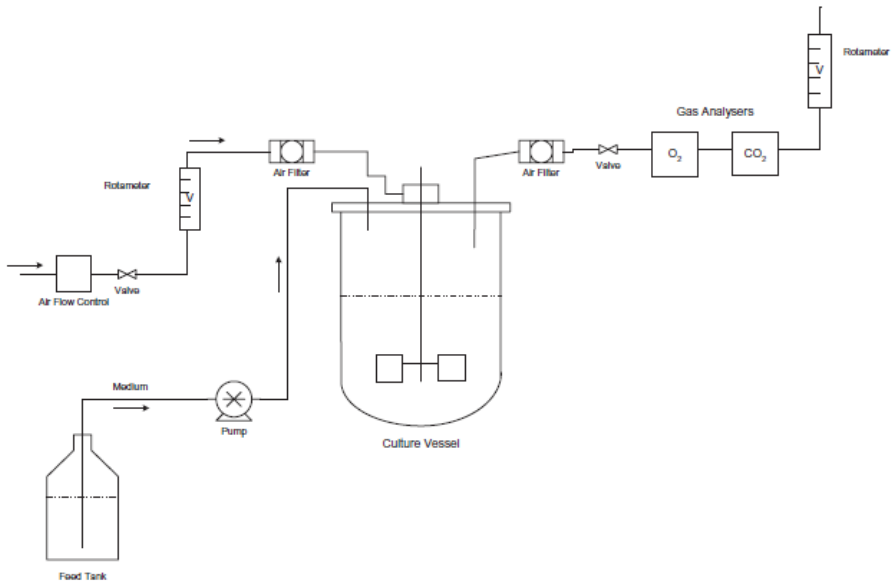

Fig. 7-6. Schematic representation of a fed-batch fermentation process[214].

Prior fermentation, the inoculum and two different culture medium are prepared. Inoculum is arranged by adding the antibiotic and the Col G (*E. coli*) to the Vegetal LB and, after that, it is incubated at 37°C for 8 h at 240 rpm in an orbital shake incubator. The first culture medium is prepared by adding Trypton and Yeast Extract (i.e. nitrogen source), MQ water and glycerol, that is injected soon

after the sterilization as a carbon source for bacteria metabolism. The second culture medium consist on a buffer solution (consisting of K_2HPO_4 and KH_2PO_4) used in order to maintain constant the pH. While the inoculum is prepared, SS samples are loaded on the baffles of the fermenter though Teflon made supports in order to avoid galvanic coupling with the samples, as reported below in Fig. 7-7.

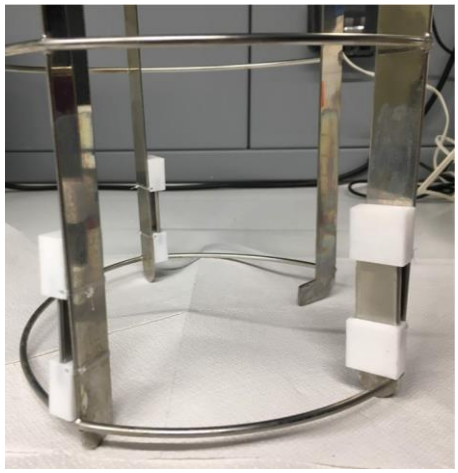

Fig. 7-7. Representation of sample assembly within the fed-batch fermenter.

After samples assembly into the fermenter, the two culture medium solutions are injected in the fermenter by a pump. Three probes are also loaded in order to monitor temperature, pH and OD (i.e. dissolved oxygen). The fermenter is then loaded in autoclave in order to perform SIP step at 121°C for 20 min. During fermentation, the temperature is kept constant at ~ 37°C and antibiotic and antifoam agent are usually added to the seeding culture in order to remove the extent of inactive bacteria and to allow oxygen to flow during fermentation respectively. Soon after the injection of the inoculum, bacteria start to growth. Monitoring of biofilm growth is carried out by absorbance (i.e OD 600 nm)

measurements every 30 minutes and fermentation is stopped when OD decrease down to a critical value at which the onset of anaerobic fermentation occurs[214].

The evaluation of biofilm adhesion and the estimation of the extent of bacteria attachment was performed by SEM. Samples were prepared by fixing them with 4% glutheraldeyde in culture medium for about 5 minutes at room temperature and were finally washed with 15% ethanol for three minutes. In the Fig. 7-8, reported below, bacteria adhesion on 316L 2B G600 is reported compared with the corresponding as supplied sample.

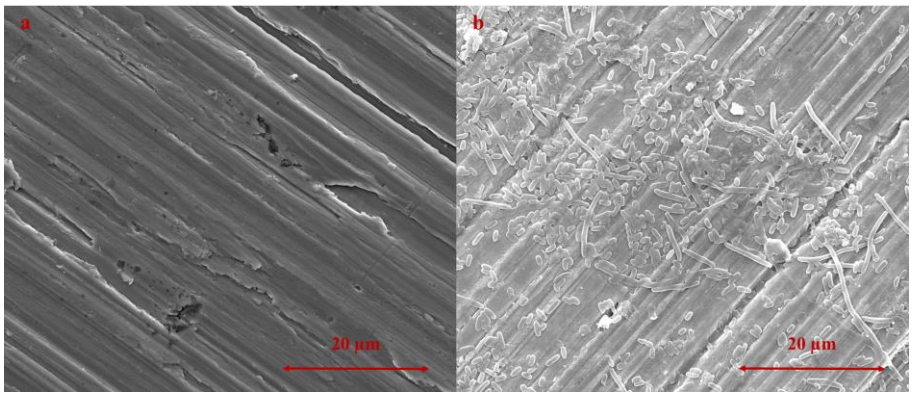

Fig. 7-8. SEM picture related to austenitic 316L 2B G600 surface finishing a) before and b) after fermentation obtained at 4 000x magnification.

In Fig. 7-9 it is reported a rough dimensioning of the *E. coli* bacterium. The estimated values are in agreement with those reported in the literature[221].

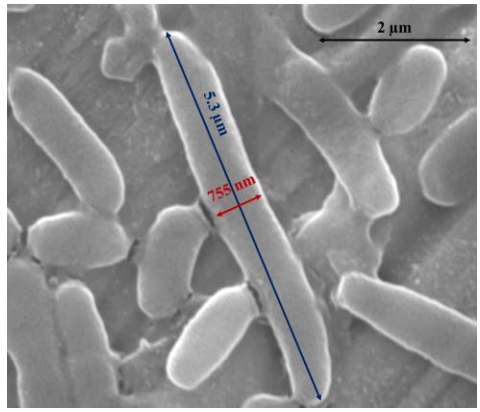

Fig. 7-9. SEM picture of a E. coli bacterium attached on austenitic 316L 2B G600 surface finishing obtained at 40 000x magnification. A rough estimation of bacteria dimension was also reported.

Notably, as it is possible to see in Fig. 7-10, bacteria attachment is strongly influenced by the surface roughness since the coverage degree of SSs surfaces increase by increasing R_a.

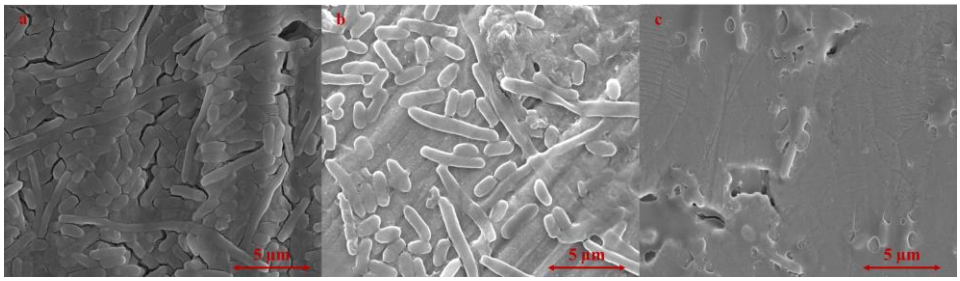

Fig. 7-10. SEM pictures of biofilm grown on austenitic 316 2B a) G220, b) G600 and d) BA obtained at 14 000x magnification.

7.3 Electrochemical Impedance Spectroscopy

In order to gain more insight into corrosion resistance of passive films after bacteria attachment, electrochemical measurements were performed. In particular, OCP monitoring and impedance measurements were carried out in order to estimate the corrosion potential (E_{corr}) and polarization resistance (R_p) of SS samples.

The open circuit potential was measured in 0.1 M ABE (pH ~ 8) soon after fermentation in order to be sure that bacteria are still alive and to avoid the onset of degradation mechanism of living microorganism. The same electrochemical investigation was carried out for the corresponding as supplied samples in order to have a reference. Electrochemical measurements of 316L after 1 SIP cycle are also reported in order to take into account of sterilization step employed prior fermentation. According to the potential vs. time curves reported in Fig. 7-11 for austenitic 316L with different surface finishing and in Fig. 7-12 for Duplex SS, corrosion potential increase after sterilization, suggesting the formation of more stable passive films than those grown on the corresponding as supplied SSs. Conversely, when fermentation is performed, the OCP decreases toward more negative potential values. Notably, the decrease of corrosion potential is strongly affected by the surface roughness, since the more cathodic value is obtained for 316L 2B G220, while no appreciable differences were obtained in the 316L BA.

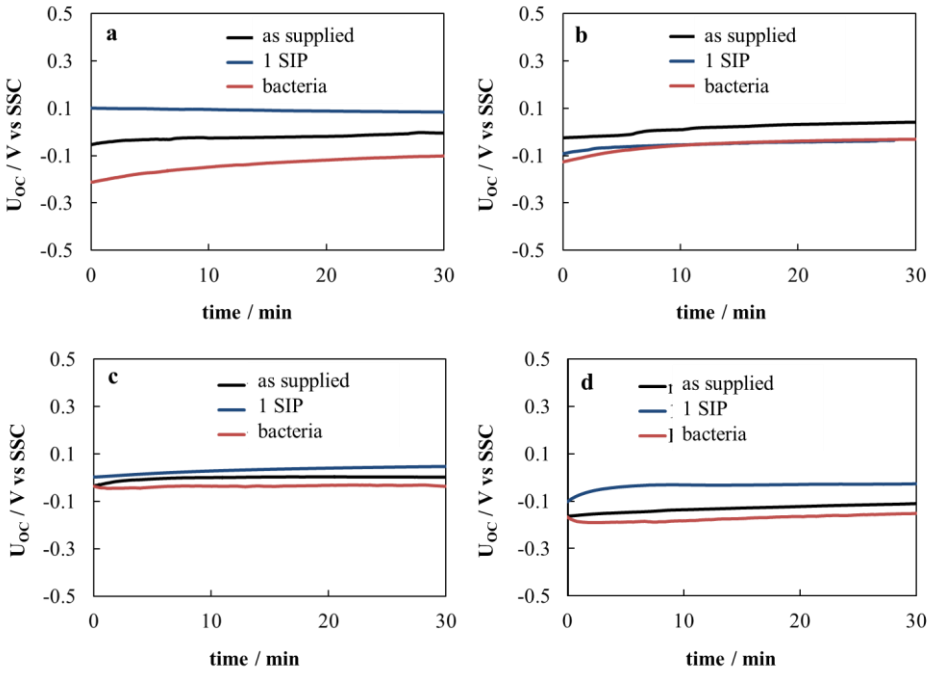

Fig. 7-11. Potential vs. time curves recorded for 30 minutes in 0.1 M ABE (pH ~ 8) after bacteria addiction on a) 316L 2B G220, b) 316L 2B G600 and c) 316L BA and d) 316L mechanically treated stainless steels.

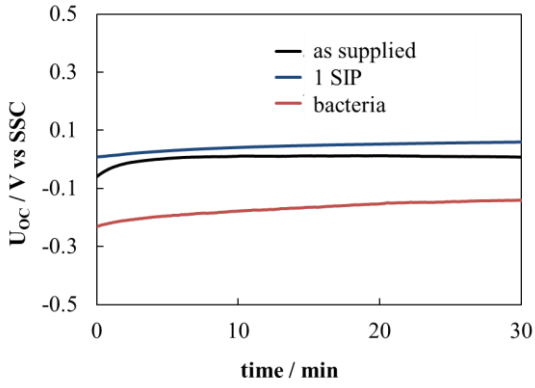

Fig. 7-12. Potential vs. time curves recorded for 30 minutes in 0.1 M ABE (pH ~ 8) after bacteria addiction on duplex stainless steel.

Impedance measurements were finally carried out in 0.1 M ABE (pH ~ 8) solution at the corresponding open circuit potentials (see Fig. 7-11 and Fig. 7-12) in order to study *metal/passive film/biofilm/electrolyte* interfaces. According to EIS reported in Fig. 7-13Fig. 7-14Fig. 7-17 in the Bode and Nyquist representation, the overall impedance increases after the exposure to vapor at high temperature (i.e. sterilization cycle) with respect to the as supplied samples. Conversely it decreases after bacteria addiction.

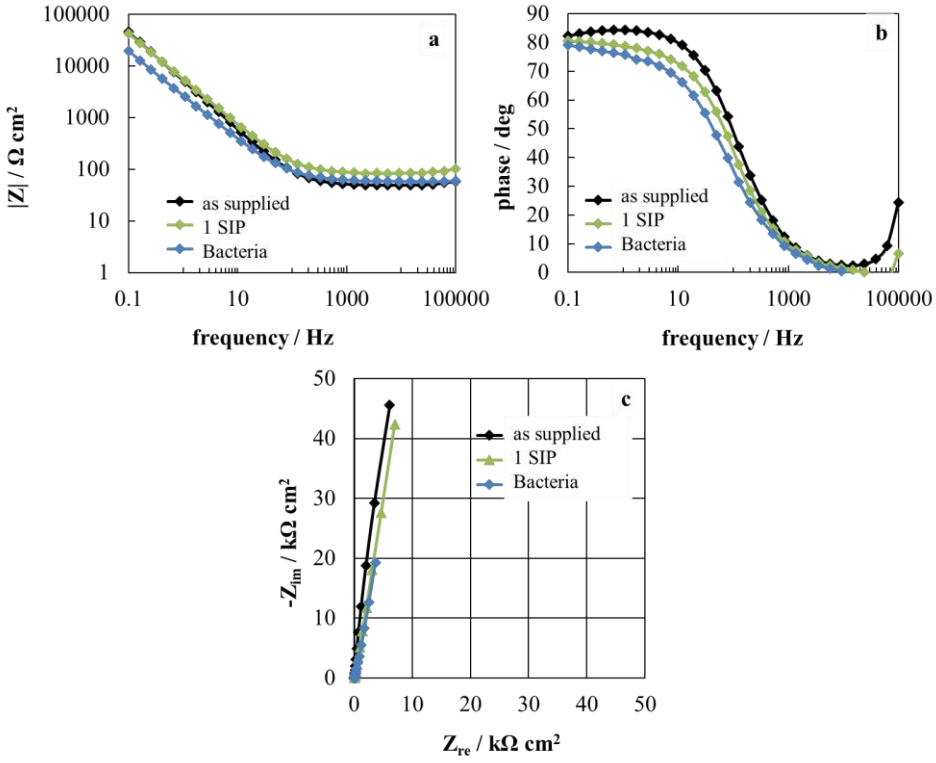

Fig. 7-13. EIS spectra reported in the Bode and Nyquist representation recorded in 0.1 M ABE (pH ~ 8) for 316L 2B G 220 stainless steel.

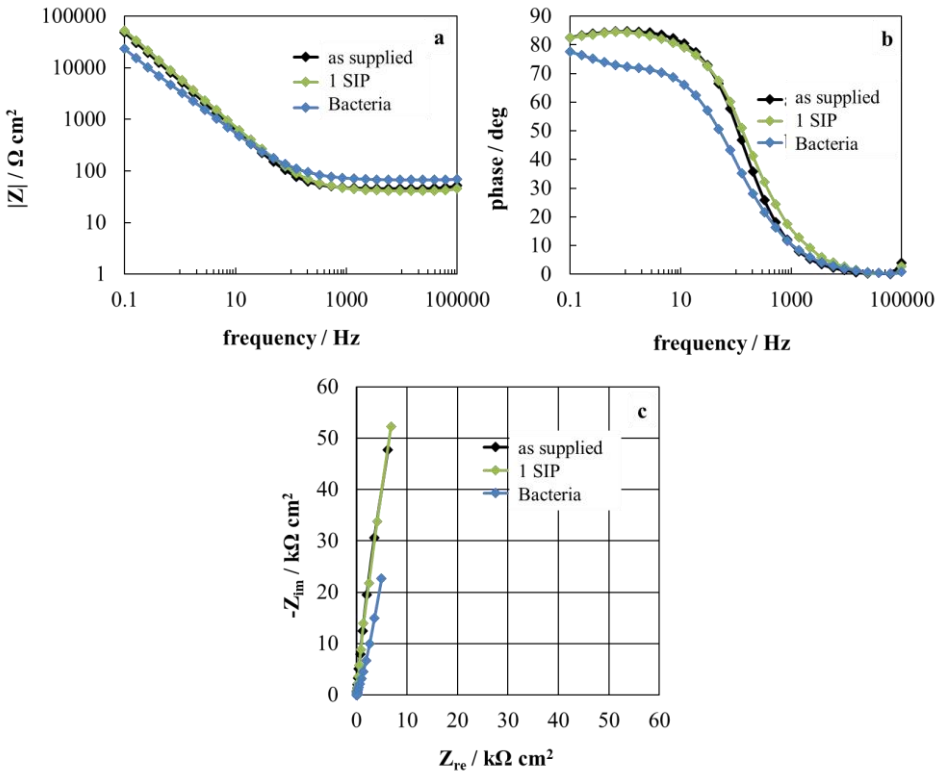

Fig. 7-14. EIS spectra reported in the Bode and Nyquist representation recorded in 0.1 M ABE (pH ~ 8) for 316L 2B G 600 stainless steel.

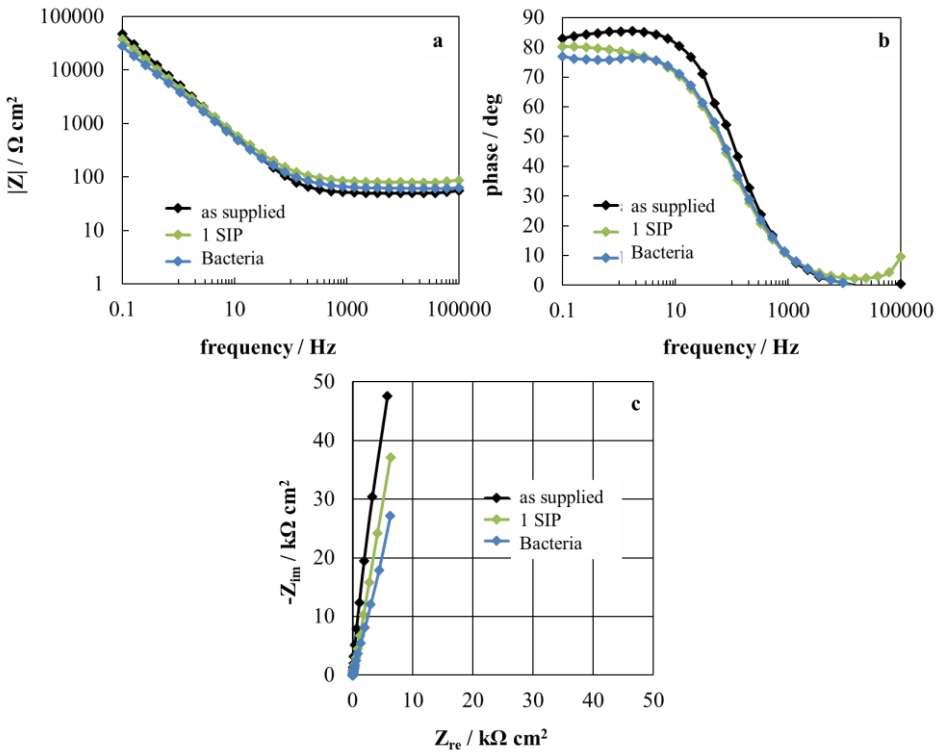

Fig. 7-15. EIS spectra reported in the Bode and Nyquist representation recorded in 0.1 M ABE (pH ~ 8) for 316L BA stainless steel.

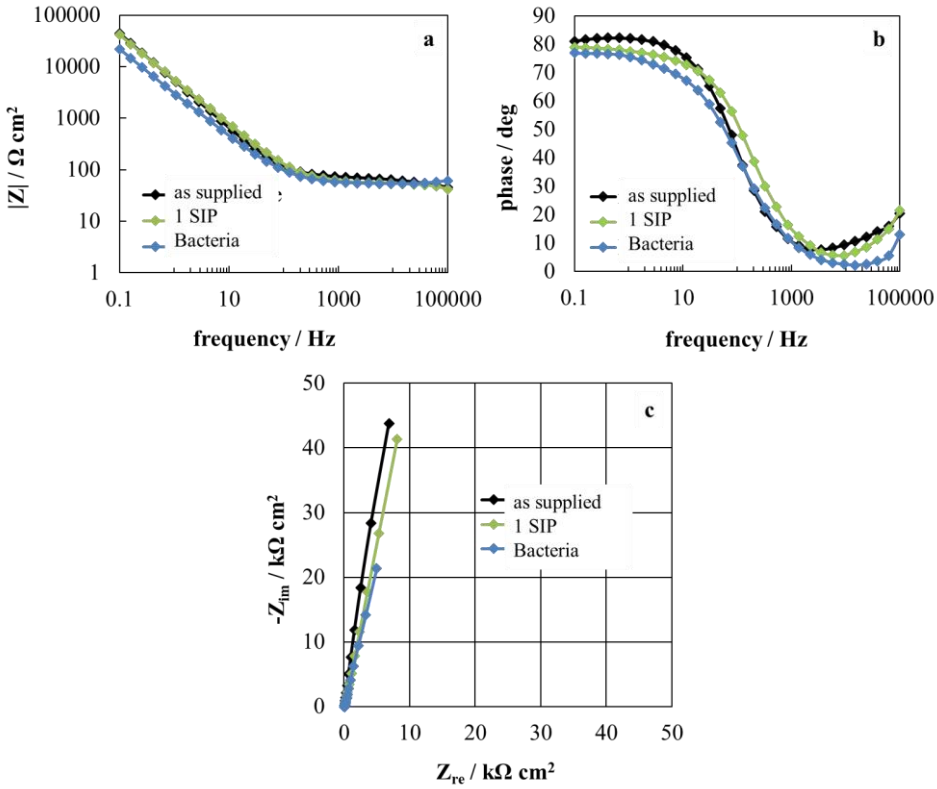

Fig. 7-16. EIS spectra reported in the Bode and Nyquist representation recorded in 0.1 M ABE (pH ~ 8) for 316L mechanically treated stainless steel.

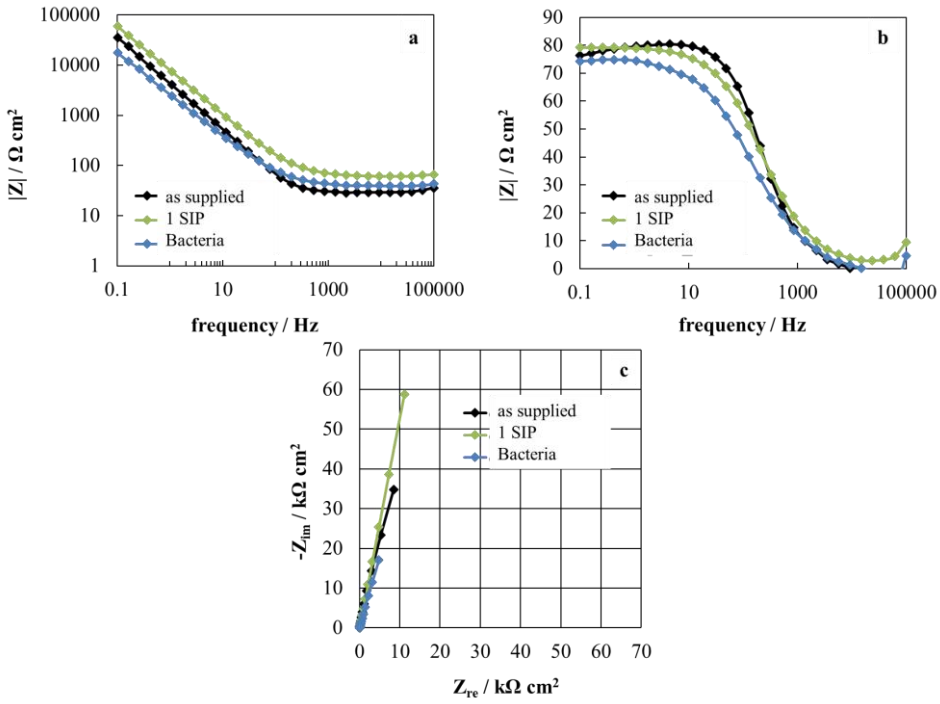

Fig. 7-17. EIS spectra reported in the Bode and Nyquist representation recorded in 0.1 M ABE (pH ~ 8) for Duplex stainless steel

According to the physical model reported in Fig. 7-18, the change in the electrochemical behavior between abiotic (i.e. without bacteria) and biotic (i.e. in the presence of living microorganism) condition can be explained considering that the presence of bacteria colonies induces local oxygen depletion at the metal surface in the areas covered by biofilm, combined with a higher oxygen concentration where the metal surface is exposed to the bulk aqueous phase. The situation is more complex considering that bacteria metabolism adds new chemical compounds at the metal/liquid interface such as acids, phosphate, chlorine compounds, nutrients and EPSs products that can be adsorbed or incorporated onto the metal surface changing the electronic properties of passive film. Since colonies of microorganism are randomly distributed, differential

aeration cells establish on the surface of SS, where the cathodic regions are the areas not covered by bacteria while the areas under biofilm behave as anodic sites where consequent local corrosion rate intensification occurs[221,222].

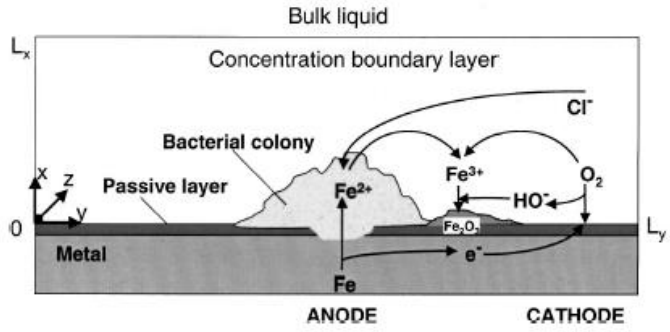

Fig. 7-18. Schematic representation of the physical model[222].

Notably, no localized corrosion attacks underneath the biofilm was observed due to the very low amount of aggressive species in the system under investigation. Nevertheless, the experimental finding suggests that a more complex equivalent circuit should be employed for the estimation of polarization resistance in order to take into account the several phenomena that are involved at the metal/electrolyte interface. The electrochemical equilibria that have to be considered at the metal surface, are the iron dissolution, as anodic process with the formation of ferrous cations or iron oxides depending on the environmental conditions, and the oxygen reduction that can induce local pH increase, as reported below:

a) $Fe \rightarrow Fe^{2+} + 2e^-$ (7.1)

b) $O_2 + 2H_2O + 4e^- \rightarrow 4OH^-$ (7.2)

The equivalent circuit providing the impedance response for the system under investigation is reported in Fig. 7-19, where two parallel impedances for both the anodic and the cathodic processes (see Eq. 7.1 and 7.2) are displayed. Notably,

the charge transfer resistance for the oxygen reduction reaction is coupled with a mass transfer impedance in order to model decrease of oxygen content on the surface.

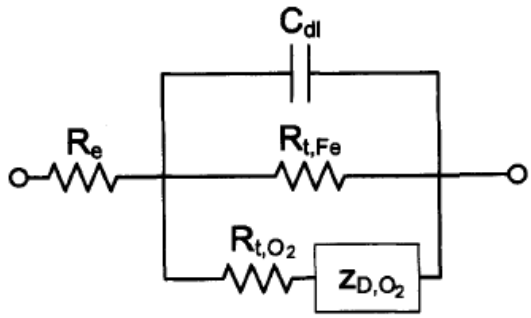

Fig. 7-19. Electrical circuit providing the impedance response for iron dissolution and oxygen reduction[125].

The steady state anodic current density for iron dissolution process, under charge transfer kinetic control, can be written as follow:

$$i_{Fe} = K_{Fe}^{*} exp(b_{Fe}(V - V_{0,Fe}) \qquad (7.3)$$

where K_{Fe}^{*} is equal to $n_{Fe}Fk_{Fe}$ with the units of current density and b_{Fe} is $\alpha_{Fe}n_{Fe}F/RT$ where n_{Fe} is the number of electrons transferred per mole of reaction species in iron dissolution reaction, F is the Faraday's constant (96487 Coulombs/equivalent), k_{Fe} is the rate constant for the reaction, α_{Fe} is the symmetry factor, R is the universal gas constant (8.3147 J/mol K), T is the temperature in absolute units, V is the interfacial and $V_{0,Fe}$ represents the interfacial equilibrium potential. By incorporating the interfacial equilibrium potential into the effective rate constant it is possible to write the Eq. 7.3 as follow:

$$i_{Fe} = K_{Fe} exp(b_{Fe} V) \quad (7.4)$$

where K_{Fe} is equal to K_{Fe}^{*} exp ($-b_{Fe} V_{0,Fe}$). Thus, the Faradic current response to a potential perturbation can be expressed as reported below:

$$\tilde{\imath}_{Fe} = K_{Fe} exp(b_{Fe} V) b_{Fe} \tilde{V} \quad (7.5)$$

The same can be written for the cathodic reaction considering that the latter is also influenced by the rate of transport of reactants (i.e. oxygen diffusion toward the metal surface). Thus the steady state current density is given by:

$$i_{O_2} = -K_{O_2} C_{O_2,0} exp(-b_{O_2} V) \quad (7.6)$$

where K_{O2} is equal to $n_{O2} F k_{O2} \exp(-b_{O2} V_{0,O2})$ and $K_{O2} C_{O2,0}$ has the units of a current density.

The oscillating form of the cathodic current density is given by:

$$\tilde{\imath}_{O\,2} = K_{O_2} C_{O_2,0} b_{O_2}\, exp\left(-b_{O_2} V\right) \tilde{V} - K_{O_2}\, exp\left(-b_{O_2} V\right) \tilde{C}_{O_2,0} \quad (7.7)$$

At the corrosion potential the external current density is zero:

$$i_{Fe} + i_{O_2} = 0 \quad (7.8)$$

and the overall oscillating component of the latter is given by:

$$\tilde{\imath} = \tilde{\imath}_{Fe} + \tilde{\imath}_{O_2} \quad (7.9)$$

Thus the steady potential and the oscillating potential are the same for both reactions, providing:

$$\frac{\tilde{\imath}}{\tilde{V}} = \frac{\tilde{\imath}_{Fe}}{\tilde{V}} + \frac{\tilde{\imath}_{O\,2}}{\tilde{V}} \quad (7.10)$$

or with the impedance notation:

$$Z^{-1} = Z_{O_2}^{-1} + Z_{Fe}^{-1} \quad (7.11)$$

where the impedance for the oxygen reduction can be written as:

$$Z_{O_2} = R_{t,O_2} + Z_{D,O_2} \quad (7.12)$$

while the impedance for the iron can be expressed as:

$$Z_{Fe} = R_{t,Fe} \quad (7.13)$$

According to the proposed equivalent circuit reported in Fig. 7-19, the overall impedance for the system under investigation is given by[125]:

$$Z_T(\omega) = R_e + \frac{Z(\omega)}{1 + j\omega Z(\omega) C_{dl}} \quad (7.14)$$

It is important to stress that the development of anodic and cathodic areas onto metal surface depends on the environmental conditions that strongly differ from those in the bulk in terms of pH, oxygen concentration and presence of foreign species due to bacteria metabolism. In fact, both iron dissolution and oxygen reduction reactions can occur on the metal surface depending on the corresponding rates. Since the system dynamically changes due to transitions between anodic and cathodic areas, the determination of the physical meaning of the R_p in not straightforward. Nevertheless, a rough estimation of the polarization resistance can be carried out by employing the very simple equivalent circuit reported in Fig. 4-12. Notably, according to the fitting parameters reported in Table 7-4, the best fitting exponent of the constant phase element, α, is lower than that of passive films grown on as supplied SSs in agreement with the formation of a non-homogeneous film on SS surface after bacteria adhesion. For all passive films, the corresponding estimated Q_{CPE} after biofilm growth is higher than that estimated for the corresponding as supplied

samples, suggesting the presence of additional charge contribution on the metal/electrolyte interface.

Table 7-4. Fitting parameters of EIS spectra recorded in 0.1 M ABE (pH ~ 8) at the open circuit potentials reported in Fig. 7-11 and Fig. 7-12 on different stainless steel grades after bacteria addiction. Fitting parameters of as supplied samples are also reported. The equivalent circuit reported in Fig. 4-12 was employed

	As supplied				
	R_{el} $\Omega\ cm^2$	R_p $\Omega\ cm^2$	Q_{CPE} $S\ s^{\alpha}\ cm^{-2}$	α	χ^2
316L 2B G220	52	$2.1 \cdot 10^6$	$3.38 \cdot 10^{-5}$	0.94	$1.12 \cdot 10^{-3}$
316L 2B G600	47	$1.3 \cdot 10^6$	$3.20 \cdot 10^{-5}$	0.95	$1.01 \cdot 10^{-3}$
316L 2B BA	43	$1.1 \cdot 10^6$	$3.88 \cdot 10^{-5}$	0.95	$1.50 \cdot 10^{-3}$
316L mirror	66	$4.0 \cdot 10^6$	$3.54 \cdot 10^{-5}$	0.90	$2.26 \cdot 10^{-2}$
Duplex	30	$2.1 \cdot 10^5$	$4.14 \cdot 10^{-5}$	0.93	$4.77 \cdot 10^{-3}$
	Bacteria				
	R_{el} $\Omega\ cm^2$	R_p $\Omega\ cm^2$	Q_{CPE} $S\ s^{\alpha}\ cm^{-2}$	α	χ^2
316L 2B G220	59	$4.0 \cdot 10^6$	$7.77 \cdot 10^{-5}$	0.85	$2.70 \cdot 10^{-3}$
316L 2B G600	68	$5.0 \cdot 10^6$	$6.41 \cdot 10^{-5}$	0.82	$9.04 \cdot 10^{-4}$
316L 2B BA	62	$1.8 \cdot 10^6$	$5.25 \cdot 10^{-5}$	0.86	$2.32 \cdot 10^{-3}$
316L mirror	56	$7.3 \cdot 10^5$	$6.50 \cdot 10^{-5}$	0.86	$6.01 \cdot 10^{-3}$
Duplex	40	$3.0 \cdot 10^6$	$8.36 \cdot 10^{-5}$	0.83	$2.32 \cdot 10^{-3}$

7.4 Disinfection protocols

In order to assess the effectiveness of NaClO in bacteria removal and to investigate how the coupling of processes (autoclaving, biofilm grown and disinfection) may effect corrosion resistance of SS under investigation, disinfection protocols were employed. Since a detailed regulations regarding the use of disinfectant is not available, the effect of temperature and contact time were also investigated in order to find a good compromise between bacteria detachment and corrosion resistance of SS. Bacteria removal was carried out by using 60 mgL^{-1} NaClO at both room temperature and 45°C for 30 minutes and 24 h. Low containing NaClO solution is used since E_{corr} falls in the passive region, as discussed in section 6.4.1. 316L with a mirror surface finishing was used.

In Fig. 7-20, potential vs. time curves related to biofilm attachment and removal with 60 mgL^{-1} NaClO at room temperature and 45°C for both 30 minutes and 24 h are reported.

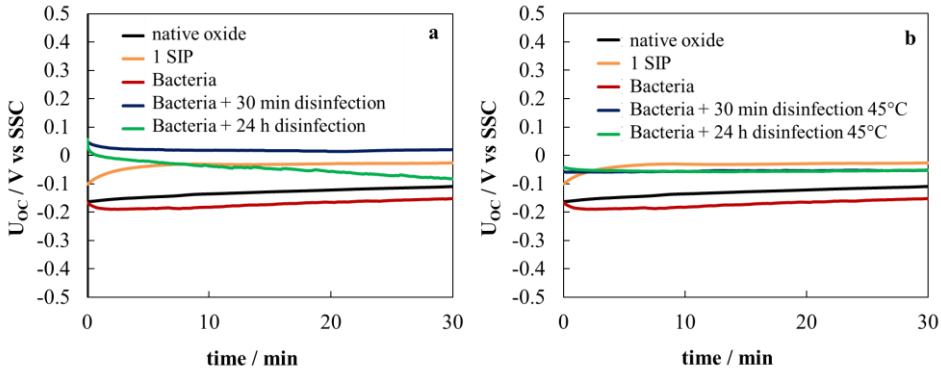

Fig. 7-20. Potential vs. time curves recorded for 316L with a mirror surface finishing after different biofilm removal steps performed with 60 mgL^{-1} NaClO solution at a) room temperature and b) 45°C for different immersion time.

According to the potential vs. time curves reported in Fig. 7-20a, disinfection with 60 mgL^{-1} NaClO at room temperature shifts the corrosion potential toward more anodic value than that recorded after bacteria addiction. This finding suggests that bacteria removal with sodium hypochlorite induce also repassivation of stainless steel surface and the formation of a more stable passive film even better than that obtained after sterilization process. On the other hand, prolonged exposure time to NaClO solution induce a decrease on the recorded open circuit potential probably due to the onset of dissolution phenomena. Indeed, as already discussed in section 6.4.4, a slightly decrease of the band gap (~2.86 eV) occurs after 24 h of passivation at the open circuit potential at the same temperature, in agreement with the formation of an iron-chromium mixed oxide film. When sanitization is performed at 45°C, corrosion potential increases if compared to that recorded in the case of bacteria attachment on SS surface (as well as after disinfection at room temperature). Nevertheless, the recorded potentials after both 30 minutes and 24 h of immersion in 60 mgL^{-1} NaClO are lower than those obtained in the same solution at room temperature. Notably, the immersion time does not affect corrosion potential since the measured OCP are almost the same.

Finally, in order to estimate the polarization resistance of passive films grown after disinfection treatments, EIS spectra, reported in Fig. 7-21, were recorded in 0.1 M ABE (pH ~ 9) at the open circuit potentials. For comparison, the EIS spectrum of the native oxide grown on mechanically treated 316L was also reported. According to the strong influence on the measured capacitance of frequency (as already founded for passive films grown on SSs) the dependence of the imaginary impedance component on the real one is described by a portion of a depressed semicircle. Impedance spectra were finally fitted according to the equivalent circuit reported in Fig. 4-12. The fitting parameters, derived from the best fitting procedure, by employing the equivalent circuit reported in Fig. 4-12, are reported in Table 7-5.

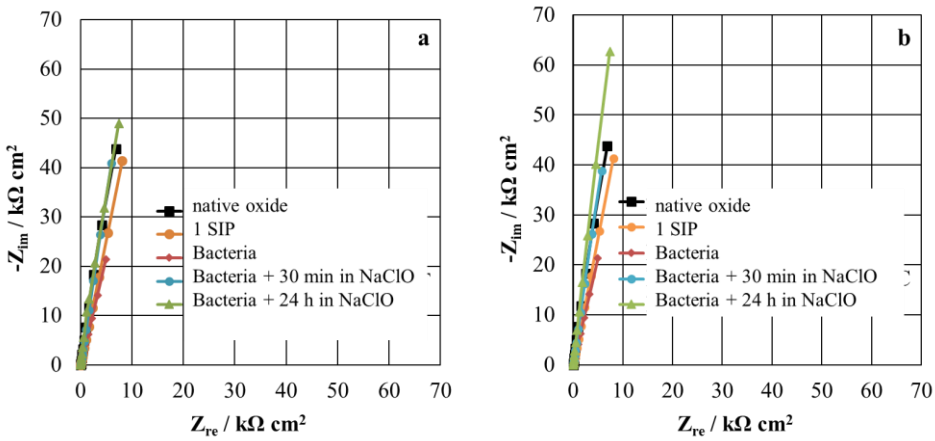

Fig. 7-21. EIS spectra in the Nyquist representation of mechanically treated 316L SS after disinfection processes.

Table 7-5. Fitting parameters of EIS spectra recorded in 0.1 M ABE (pH ~ 8) at the open circuit potentials reported in Fig. 7-20 after disinfection processes on mechanically treated 316L SS samples after bacteria addiction. The equivalent circuit reported in Fig. 4-12 was employed.

Passivation treatment	**R_{sol} Ω cm²**	**R_p Ω cm²**	**Q_{CPE} S s^{α} cm^{-2}**	**α**	**χ^2**
Native oxide	66	$4.0 \cdot 10^{6}$	$3.5 \cdot 10^{-5}$	0.90	$2.3 \cdot 10^{-2}$
Bacteria	56	$7.3 \cdot 10^{5}$	$6.5 \cdot 10^{-5}$	0.86	$6.0 \cdot 10^{-3}$
30 min in 60 mgL^{-1} at RT	68	$6.0 \cdot 10^{6}$	$3.8 \cdot 10^{-5}$	0.89	$2.2 \cdot 10^{-3}$
24 h in 60 mgL^{-1} at RT	49	$1.3 \cdot 10^{6}$	$3.0 \cdot 10^{-5}$	0.93	$1.4 \cdot 10^{-2}$
30 min in 60 mgL^{-1} at 45°C	52	$4.0 \cdot 10^{6}$	$3.9 \cdot 10^{-5}$	0.90	$3.0 \cdot 10^{-3}$
24 h in 60 mgL^{-1} at 45°C	68	$6.0 \cdot 10^{6}$	$3.8 \cdot 10^{-5}$	0.89	$2.2 \cdot 10^{-3}$

Notably, the lowest polarization resistance was obtained for SS samples characterized by the presence of bacteria, in agreement with the decrease in the overall impedance discussed in section 7.3. Concerning the constant phase element, the exponential factor α, increases after disinfection for all samples under investigation, in agreement with the formation of a more stable passive film.

7.5 Concluding remarks

In this experimental work the effect of bacteria growth on corrosion resistance of austenitic 316L and duplex stainless steels was studied. In order to assess the effect of surface roughness on bacteria adhesion, 316L with different surface finishing were also studied. The investigation of the interaction between aerobic biofilm and metal surface and the understanding of environmental conditions that can induce localized dissolution phenomena were carried out by simulating biofilm growth into a fed-batch fermenter, devoted to the production of recombinant protein via *E. coli* bacteria. Since sterilization is typically carried out in food processing in order to destroy all the living microorganism present onto the interior wall of reactors, fermenters and piping, the effect of *Sterilization in Place* was studied by performing different SIP cycles with vapor at 121°C for about 20 min. According to the photoelectrochemical results, a band gap value of about 2.4 eV was estimated for passive films on 316L even after the first SIP cycles suggesting strong iron enrichment on passive films, as also confirmed by the presence of anodic spikes. Conversely, 3.0 eV was reported after passivation of DSS in agreement with higher chromium content within the oxide compared to those grown on austenitic 316L. Notably, by increasing the number of SIP cycles, no photocurrent was measured. According to the current transients, passive films grown after different SIP cycles are n-type SC thus highly resistant toward dissolution phenomena, although the strong variation on oxide composition.

Parameters such as dissolved oxygen in the culture medium, pH and nutrients concentration strongly affect the growth efficiency of bacteria, and thus their adhesion on metal surfaces. Indeed, according to the experimental results, more negative corrosion potentials were measured, after biofilm growth with respect to those measured on as supplied samples. This finding can be explained considering the formation of a non-homogeneous layer on metallic surfaces due to random dispersion of bacteria micro-colonies where oxygen aeration differs

leading to the onset of localized dissolution phenomena where microorganisms are attached. Notably, according to SEM pictures, the extent of bacteria attachments strongly depends on SS surface roughness.

Biofilm removal by employing chlorine based disinfectant (i.e. NaClO) effectively remove bacteria and induce the formation of a more stable and protective passive film due to the higher corrosion potentials measured than those obtained when bacteria are attached on the surfaces. On the other hand, prolonged exposure time to NaClO containing solution (i.e. 24 h) at room temperature shifts the open circuit potential to more cathodic values with respect to 30 minutes contact times. On the other hand, slightly lower corrosion potentials are recorded after disinfection treatments at 45°C with respect to room temperature processes while the effect of time is negligible, suggesting that lower contact time are sufficient in order to effective remove bacteria.

8 Conclusions and perspectives

This Ph.D. work aimed to make a ranking of different stainless steel grades typically employed in food and beverage industry based on the study of their corrosion resistance in selected simulating solutions able to model aggressive environments encountered in food processing.

The first part of the research activity was mainly focused on the study of the physico-chemical properties of passive films electrochemically grown on two austenitic grades and on duplex stainless steels in the attempt to link their electronic properties to their corrosion resistance. For this purpose, passive films were grown on different stainless steel grades by anodic polarization in acidic (pH ~ 2), quasi neutral (pH ~ 7) and alkaline (pH ~ 13) solutions. Moreover, in order to get more insight into the mechanism of rouging, electrochemical conditions inducing dissolution phenomena on the surface of stainless steel were investigated. A critical assessment on the role of Mo and on the effect of surface roughness (R_a) on passive films growth kinetic was also carried out. Since the corrosion resistance of stainless steel markedly depends on the formation of a few nanometers thick chromium oxide protective layer, growth kinetic and corrosion resistance of passive films on pure sputtered chromium were also studied. *In-situ* techniques, such as Photocurrent Spectroscopy and Electrochemical Impedance Spectroscopy were used in the attempt to gain more insight into solid state properties (i.e. band gap and conductivity type) and corrosion resistance (i.e. corrosion potential and polarization resistance) of passive films. According to the experimental measurements, potentiostatic polarization of pure chromium induces the formation of thin passive films behaving as p-type semiconductor or insulator with a very high flat band potential, and thus poorly resistant towards anodic dissolution. Conversely, in spite the differences on SSs composition, surface roughness and electrolytes employed for passive films growth, experimental results are in agreement with

the formation of Fe-Cr mixed oxide films behaving as n-type semiconductor, and thus more stable toward corrosion phenomena.

The second part of the research activity was devoted to the study of corrosion resistance of passive films grown on both austenitic and duplex stainless steels by immersion at the open circuit potential in solutions prepared by following to the protocols and prescriptions reported in the literature. According to the PCS measurements, iron-chromium mixed oxide films are formed after immersion at the open circuit potential, whose chromium content strongly depends on the alloy bulk composition and on the mimicking solutions. Nevertheless, the corresponding oxide layers are n-type semiconductor, thus highly resistant towards anodic dissolution. Total concentration of released non precipitates ions from the oxide surface, determined by ICP-OES, suggests that the extend of dissolution is significant after the early immersion stage. In addition, the prolonged exposure to acidic solution seems to be worse for austenitic grades if compared with duplex stainless steel due to the higher thinning rate of the metal phase. In spite ion release is negligible in the case of immersion in tap water solution, selective dissolution phenomena and consequent decrease of polarization resistance occur on 304L (not containing Mo) due to MnS inclusions dissolution, even at low concentration of chloride species. Nevertheless, the released heavy metal ions after simulation tests are under the specific release limit (SRL) values, but it is not possible to exclude the SS failure during prolonged working conditions.

The last part of the research activity aimed to investigate the effect of biofilm growth on different stainless steel grades as a function of bulk composition and surface roughness. Disinfection protocols were also employed in order to assess the effect of sanitization processes on corrosion resistance of passive films. For this reason, disinfection, sterilization and biofilm growth were first studied separately. The experimental results suggest that bacteria attachment and proliferation strongly depend on surface roughness. In addition, according to the

electrochemical investigation, in the early growth stage, bacteria adhesion induces the formation of dispersed micro-colonies onto the metal surface and thus oxygen differential aeration can promote the onset of localized corrosion phenomena in the anodic areas covered by bacteria. The conclusion of this experimental work was also focused on the application of disinfection protocols by employing chlorine based disinfectant (i.e. NaClO) in order to find a good compromise between effectiveness on biofilm removal and corrosion resistance of stainless steel as a function of pH, temperature and contact time of the employed solutions. In particular, impedance measurements suggest that low concentrated sodium hypochlorite disinfectants remove bacteria and promote also re-passivation of SSs. Nevertheless, it does not exist a cleaning or disinfection protocol suitable for all processing environments, therefore further studies and investigations should be carried out in order to optimize cleaning efficiency without degradation of circuit's material due to the occurrence of corrosion phenomena.

It is important to stress that the prediction of corrosion behavior of stainless steels employed in food processing is not straightforward as well as the estimation of the equipment working life. In fact, SSs usually come in contact with several kinds of processed media and the involved processing conditions are extremely different in terms of pH, temperature, chemical composition and flow rate of the employed solutions. Moreover, it is not possible to determine uniquely which kind of material may be the best choice able to replace all the other materials. Conversely, in the attempt to minimize the maintenance costs and increase materials useful lifetime, some preliminary considerations can be made for the selection of the more appropriate SS grade for equipment manufacturing and installing considering the environments that SSs face in food and beverage industry within storage, cleaning and processing sections of the plant.

List of Figures

Bibliography

1. SSINA: Stainless Steel: Corrosion. Available at: http://www.ssina.com/corrosion/crevice-pitting.html. (Accessed: 2nd November 2019)

2. Breda, M., Pezzato, L., Pizzo, M. & Calliari, I. Effect of cold rolling on pitting resistance in duplex stainless steels. *Metall. Ital.* **106**, 15–19 (2014).

3. Stainless, A. M., Cherubini, L. & Cdx, L. A. P. S. DUPLEX STAINLESS STEELS, A REVIEW AFTER DSS '07 held in GRADO. Dr. J.CHARLES. 1–22 (2007).

4. Boniardi, M., Casaroli, A. & Dipartimento Di Meccanica, P. di M. Stainless steels Gruppo Lucefin Research & Development. 10–20 (2014).

5. Davis, J. R. Alloy Digest Sourcebook: Stainless Steels. *ASM Int.* **27**, 624–635 (1999).

6. Mott, N. F. *Mechanical properties of metals*. *Physica* **15**, (1949).

7. Covert, R. A. & Tuthill, A. H. Stainless Steels : An Introduction to Their Metallurgy and Corrosion Resistance. *Dairy, Food Environ. Sanit.* **20**, 506–517 (2000).

8. Cunat, P. and Other Chromium-Containing Alloys. 1–24 (2004).

9. Song, D. *et al.* Corrosion behavior and mechanism of Cr–Mo alloyed steel: Role of ferrite/bainite duplex microstructure. *J. Alloys Compd.* **809**, 151787 (2019).

10. Baldissin, D. & Battezzati, L. Multicomponent phase selection theory applied to high nitrogen and high manganese stainless steels. *Scr. Mater.* **55**, 839–842 (2006).

11. Nishimoto, M., Muto, I., Sugawara, Y. & Hara, N. Morphological Characteristics of Trenching around MnS Inclusions in Type 316 Stainless Steel: The Role of Molybdenum in Pitting Corrosion Resistance. *J. Electrochem. Soc.* **166**, C3081–C3089 (2019).

12. Kobayashi, Y., Virtanen, S. & Böhni, H. Microelectrochemical studies on the influence of Cr and Mo on nucleation events of pitting corrosion. *J. Electrochem. Soc.* **147**, 155–159 (2000).

13. Ilevbare, G. O. & Burstein, G. T. Role of alloyed molybdenum in the inhibition of pitting corrosion in stainless steels. *Corros. Sci.* **43**, 485–

513 (2001).

14. Tobler, W. J. & Virtanen, S. Effect of Mo species on metastable pitting of Fe18Cr alloys-A current transient analysis. *Corros. Sci.* **48**, 1585–1607 (2006).

15. Maurice, V. *et al.* Effects of molybdenum on the composition and nanoscale morphology of passivated austenitic stainless steel surfaces. *Faraday Discuss.* **180**, 151–170 (2015).

16. Hashimoto, K., Asami, K., Kawashima, A., Habazaki, H. & Akiyama, E. The role of corrosion-resistant alloying elements in passivity. *Corros. Sci.* **49**, 42–52 (2007).

17. Isaacs, H. S. & Huang, S. M. Behavior of dissolved molybdenum during localized corrosion of austenitic stainless steel. *J. Electrochem. Soc.* **143**, 277–279 (1996).

18. Laycock, N. J. & Newman, R. C. Localised dissolution kinetics, salt films and pitting potentials. *Corros. Sci.* **39**, 1771–1790 (1997).

19. Newman, R. C. The dissolution and passivation kinetics of stainless alloys containing molybdenum-II. Dissolution kinetics in artificial pits. *Corros. Sci.* **25**, 341–350 (1985).

20. Newman, R. C. The dissolution and passivation kinetics of stainless alloys containing molybdenum-1. Coulometric studies of FeCr and FeCrMo alloys. *Corros. Sci.* **25**, 331–339 (1985).

21. Sugimoto, K. & Sawada, Y. The role of molybdenum additions to austenitic stainless steels in the inhibition of pitting in acid chloride solutions. *Corros. Sci.* **17**, 425–445 (1977).

22. Stott, F. H., Wei, F. I. & Enahoro, C. A. The influence of manganese on the High-temperature oxidation of iron-chromium alloys. *Mater. Corros.* **40**, 198–205 (1989).

23. Suutala, N. Effect of Manganese and Nitrogen on the Solidification Mode in Austenitic Stainless Steel Welds. *Metall. Trans. A, Phys. Metall. Mater. Sci.* **13 A**, 2121–2130 (1982).

24. Nilsson, E. A. A., Pettersson, L. & Antti, M. L. Mn, Si and Ti in cast stainless steel at elevated temperature. *Ironmak. Steelmak.* **9233**, 1–11 (2017).

25. Leffler, B. High performance stainless steel, http://www.outokumpu.com/. (2017).

26. Tanure, L. *et al.* Microstructural characterization and mechanical

behavior during recrystallization annealing of Nb-stabilized type ASTM 430 and Nb-Ti-stabilized ASTM 439 ferritic stainless steels. *J. Mater. Res. Technol.* **8**, 4048–4065 (2019).

27. Yan, H., Bi, H., Li, X. & Xu, Z. Microstructure and texture of Nb + Ti stabilized ferritic stainless steel. *Mater. Charact.* **59**, 1741–1746 (2008).

28. Cavazos, J. L. Characterization of precipitates formed in a ferritic stainless steel stabilized with Zr and Ti additions. *Mater. Charact.* **56**, 96–101 (2006).

29. Mehrazi, S., Moran, A. J., Arnold, J. L., Buchheit, R. G. & Lillard, R. S. The electrochemistry of copper release from stainless steels and its role in localized corrosion. *J. Electrochem. Soc.* **165**, C860–C868 (2018).

30. Lillard, R. S., Kashfipour, M. A. & Niu, W. Pit propagation at the boundary between manganese sulfide inclusions and austenitic stainless steel 303 and the role of copper. *J. Electrochem. Soc.* **163**, C440–C451 (2016).

31. Abd El Meguid, E. A., Mahmoud, N. A. & Abd El Rehim, S. S. Effect of some sulphur compounds on the pitting corrosion of type 304 stainless steel. *Mater. Chem. Phys.* **63**, 67–74 (2000).

32. Seo, M., Hultquist, G., Leygraf, C. & Sato, N. The influence of minor alloying elements (Nb, Ti and Cu) on the corrosion resistivity of ferritic stainless steel in sulfuric acid solution. *Corros. Sci.* **26**, (1986).

33. Hultquist, G., Seo, M., Leitner, T., Leygraf, C. & Sato, N. The dissolution behaviour of iron, chromium, molybdenum and copper from pure metals and from ferritic stainless steels. *Corros. Sci.* **27**, 937–946 (1987).

34. Jeon, S. H., Kim, H. J., Kong, K. H. & Park, Y. S. Effects of copper addition on the passivity and corrosion behavior of 27Cr-7Ni hyper duplex stainless steels in sulfuric acid solution. *Mater. Trans.* **56**, 78–84 (2014).

35. Luo, H., Dong, C., Xiao, K. & Li, X. The passive behaviour of ferritic stainless steel containing alloyed tin in acidic media. *RSC Adv.* **6**, 9940–9949 (2016).

36. De Lima, H. M. L. F., Tavares, S. S. M., Martins, M. & Araújo, W. S. The effect of copper addition on the corrosion resistance of cast duplex stainless steel. *J. Mater. Res. Technol.* **8**, 2107–2119 (2019).

37. Chaudhuri, S. Heat treatment of stainless steels types. (2002).

38. Steels, A. The Atlas Steels Technical Handbook of Stainless Steels Atlas Steels Technical Department. (2013).

39. Olsson, J. & Snis, M. Duplex - A new generation of stainless steels for desalination plants. *Desalination* **205**, 104–113 (2007).

40. Zhang, B. *et al.* Chloride attack on the passive film of duplex alloy. *Corros. Sci.* **154**, 123–128 (2019).

41. Dillon, C., Rahoi, D. & Tuthill, a. Stainless steel in bioprocessing; Part1: Materials Selection. *Biopharm 5* 38–42 (1992).

42. Santos, T. F. A., Torres, E. A., Lippold, J. C. & Ramirez, A. J. Detailed Microstructural Characterization and Restoration Mechanisms of Duplex and Superduplex Stainless Steel Friction-Stir-Welded Joints. *J. Mater. Eng. Perform.* **25**, 5173–5188 (2016).

43. Landolt, D. *Corrosion and surface chemistry of metals*. *Corrosion and Surface Chemistry of Metals* (2007). doi:10.5860/choice.45-0897

44. Escher, F. Handbook of food processing equipment. *LWT - Food Sci. Technol.* **38**, 108–109 (2005).

45. Activating Your Ideas Stainless steel for the food & drink industry Let us inspire you ahead . We have been serving the food & drink industry for decades .

46. Bellezze, T. *et al.* Corrosion behaviour of austenitic and duplex stainless steels in an industrial strongly acidic solution. *Mater. Corros.* **67**, 831–838 (2016).

47. Colombo, A. & Trasatti, S. P. Corrosion of an UNS S31803 distillation column for acetic acid recovery. *Eng. Fail. Anal.* **55**, 317–326 (2015).

48. Pečar, D., Slemnik, M. & Goršek, A. Testing the corrosion resistance of stainless steels during the fermentation of probiotic drink. *J. Sci. Food Agric.* **91**, 1293–1297 (2011).

49. Ram, C., Sharma, C. & Singh, A. K. In-Plant Corrosion Study of Steels in Distillery Effluent Treatment Plant. *J. Mater. Eng. Perform.* **24**, 1841–1847 (2015).

50. Partington, E. Stainless Steel in the Food and Beverage Industry. *Mater. Appl. Ser.* **7**, 28 (2006).

51. Dong, X., Iacocca, R. G., Bustard, B. L. & Kemp, C. A. J. Investigation of stainless steel corrosion in ultrahigh-purity water and steam systems by surface analytical techniques. *J. Mater. Eng. Perform.* **19**, 135–141 (2010).

52. Mathiesen, J. E. F. T. Effects of Gas Atmosphere and Surface Quality on Rouging of Three Stainless Steels in WFI. **1**, 1–10 (2003).

53. Troels Methiesen & Elkjaer Frantsten, J. Rouging of Stainless Steel In wfi systems. *NACE Corros.* 2–6 (2007).

54. Sandle, B. T. Peer Reviewed : Water Quality. (2015).

55. Di Franco, F., Santamaria, M., Massaro, G. & Di Quarto, F. Photoelectrochemical monitoring of rouging and de-rouging on AISI 316L. *Corros. Sci.* **116**, 74–87 (2017).

56. Klapper, H. S., Göllner, J., Heyn, A. & Burkert, A. Relevance of the cathodic process on the passivation of stainless steels - An approximation to the origin of the rouging phenomenon. *Mater. Corros.* **63**, 54–58 (2012).

57. Gonzalez, M. M. Rouge: The intrinsic phenomenon in 316L stainless steel - A key material for biopharmaceutical facilities. *Pharm. Eng.* **32**, 64–72 (2012).

58. Chisti, Y. *Process Hygiene: Modern Systems of Plant Cleaning*. *Encyclopedia of Food Microbiology: Second Edition* **3**, (Elsevier, 2014).

59. Martin, J. G. P. *et al.* Efficiency of a cleaning protocol for the removal of enterotoxigenic Staphylococcus aureus strains in dairy plants. *Int. J. Food Microbiol.* **238**, 295–301 (2016).

60. Ortega, M. P., Hagiwara, T., Watanabe, H. & Sakiyama, T. Adhesion behavior and removability of Escherichia coli on stainless steel surface. *Food Control* **21**, 573–578 (2010).

61. Shi, X. & Zhu, X. Biofilm formation and food safety in food industries. *Trends Food Sci. Technol.* **20**, 407–413 (2009).

62. Carniello, V., Peterson, B. W., van der Mei, H. C. & Busscher, H. J. Physico-chemistry from initial bacterial adhesion to surface-programmed biofilm growth. *Adv. Colloid Interface Sci.* **261**, 1–14 (2018).

63. Moradi, M. & Tajik, H. Biofilm removal potential of neutral electrolysed water on pathogen and spoilage bacteria in dairy model systems. *J. Appl. Microbiol.* **123**, 1429–1437 (2017).

64. Møretrø, T. & Langsrud, S. Residential Bacteria on Surfaces in the Food Industry and Their Implications for Food Safety and Quality. *Compr. Rev. Food Sci. Food Saf.* **16**, 1022–1041 (2017).

65. Myszka, K. & Czaczyk, K. Bacterial Biofilms on Food Contact Surfaces - a Review. *Polish J. Food Nutr. Sci.* **61**, 173–180 (2011).

66. Galié, S., García-Gutiérrez, C., Miguélez, E. M., Villar, C. J. & Lombó, F. Biofilms in the food industry: Health aspects and control methods. *Front. Microbiol.* **9**, 1–18 (2018).

67. Chmielewski, R. A. N. & Frank, J. F. Biofilm formation and control in food processing facilities. *Compr. Rev. Food Sci. Food Saf.* **2**, 22–32 (2003).

68. Poulsen, L. V. Review: Article Microbial Biofilm in Food Processing. *Rev. Lit. Arts Am.* **326**, 321–326 (1999).

69. Awad, T. S., Asker, D. & Hatton, B. D. Food-Safe Modification of Stainless Steel Food-Processing Surfaces to Reduce Bacterial Biofilms. *ACS Appl. Mater. Interfaces* **10**, 22902–22912 (2018).

70. Eds, S. L., Shirtliff, M. & Leid, J. The Role of Biofilms in Device-Related. 13–34 (2008). doi:10.1007/7142

71. Council of Europe. Council of Europe's Policy Statements Concering Materials and Articles Intended to come into contact with foodstuffs. (2002).

72. Cederberg, D. L. *et al. Food contact materials – metals and alloys*. *Food contact materials – metals and alloys* (2015). doi:10.6027/tn2015-522

73. Mazinanian, N., Odnevall Wallinder, I. & Hedberg, Y. Comparison of the influence of citric acid and acetic acid as simulant for acidic food on the release of alloy constituents from stainless steel AISI 201. *J. Food Eng.* **145**, 51–63 (2015).

74. Result details. Available at: https://search.coe.int/cm/Pages/result_details.aspx?ObjectID=09000016805c8094. (Accessed: 18th October 2019)

75. Mazinanian, N., Wallinder, I. O. & Hedberg, Y. Final report, December 2014. (2014).

76. Directorate, E. *Metals / Alloys – Aerospace*. (2013).

77. Soccol, C. R., Vandenberghe, L. P. S., Rodrigues, C. & Pandey, A. New perspectives for citric acid production and application. *Food Technol. Biotechnol.* **44**, 141–149 (2006).

78. Rajeswari, V., Padma Suresh, L. & Rajeshwari, Y. Water storage and distribution system for pharmaceuticals using PLC and SCADA. *Proc. IEEE Int. Conf. Circuit, Power Comput. Technol. ICCPCT 2013* 79–86 (2013). doi:10.1109/ICCPCT.2013.6528951

79. Inside Water for Injection - Poducing WFI, I.V. Fluids and Parenterals.

Available at: https://www.wfi-waterforinjection.com/. (Accessed: 2nd November 2019)

80. SPX. CIP and Sanitation of Process Plant. *Schneider Electr. White Pap. PX* 1–24 (2013).

81. Garcaa & Daaz, L. M. Cleaning in Place. *Compr. Biotechnol.* (2008).

82. Goode, K. R., Asteriadou, K., Robbins, P. T. & Fryer, P. J. Fouling and cleaning studies in the food and beverage industry classified by cleaning type. *Compr. Rev. Food Sci. Food Saf.* **12**, 121–143 (2013).

83. Bremer, P. J., Fillery, S. & McQuillan, A. J. Laboratory scale Clean-In-Place (CIP) studies on the effectiveness of different caustic and acid wash steps on the removal of dairy biofilms. *Int. J. Food Microbiol.* **106**, 254–262 (2006).

84. Maris, P. Modes of action of disinfectants. *Rev. Sci. Tech.* **14**, 47–55 (1995).

85. Schmidt, R. H. Basic Elements of Equipment Cleaning and Sanitizing in. 1–11 (1997).

86. De Freitas Cunha Lins, V. *et al.* Corrosion resistance of AISI 304 and 444 stainless steel pipes in sanitizing solutions of clean-in-place proCess. *Mater. Res.* **19**, 333–338 (2016).

87. Meireles, A., Ferreira, C., Melo, L. & Simões, M. Comparative stability and efficacy of selected chlorine-based biocides against Escherichia coli in planktonic and biofilm states. *Food Res. Int.* **102**, 511–518 (2017).

88. Centers for Disease Control and Prevention. Guideline for Disinfection and Sterilization in Healthcare Facilities, 2008; Miscellaneous Inactivating Agents. *CDC website* 9–13 (2013). doi:1

89. Fukuzaki, S. Mechanisms of actions of sodium hypochlorite in cleaning and disinfection processes. *Biocontrol Sci.* **11**, 147–57 (2006).

90. Stoica, M., Brumă, M. & Cârâc, G. Electrochemical study of AISI 304 stainless steel during the exposure at the disinfectant solutions with fungal suspensions. *Mater. Corros.* **61**, 1017–1025 (2010).

91. Urano, H. & Fukuzaki, S. The Mode ofvAction of Sodium Hypodhlrite in the Cleaning Process. *Biocontrol Sci.* **10**, 21–29 (2005).

92. Gomes, I. B., Simões, M. & Simões, L. C. The effects of sodium hypochlorite against selected drinking water-isolated bacteria in planktonic and sessile states. *Sci. Total Environ.* **565**, 40–48 (2016).

93. Qi, Y. *et al.* Chemical additives affect sulfate reducing bacteria biofilm properties adsorbed on stainless steel 316L surface in circulating cooling water system. *Front. Environ. Sci. Eng.* **11**, 1–14 (2017).

94. Dion, M. & Parker, W. Steam sterilization principles. *Pharm. Eng.* **33**, 60–69 (2013).

95. van Doornmalen, J. & Kopinga, K. Review of surface steam sterilization for validation purposes. *Am. J. Infect. Control* **36**, 86–92 (2008).

96. Shih, C. C., Su, Y. Y., Chen, L. C., Shih, C. M. & Lin, S. J. Degradation of 316L stainless steel sternal wire by steam sterilization. *Acta Biomater.* **6**, 2322–2328 (2010).

97. Roy, K., Undey, C., Mistretta, T., Naugle, G. & Sodhi, M. Multivariate statistical monitoring as applied to clean-in-place (CIP) and steam-in-place (SIP) operations in biopharmaceutical manufacturing. *Biotechnol. Prog.* **30**, 505–515 (2014).

98. Outokumpu Surface Contents a world that.

99. Euro Inox. Roughness measurements of stainless steel surfaces. 1–7 (2014).

100. La Mantia, F., Habazaki, H., Santamaria, M. & Di Quarto, F. A critical assessment of the Mott-Schottky analysis for the characterisation of passive film-electrolyte junctions. *Russ. J. Electrochem.* **46**, 1306–1322 (2010).

101. Academy, T., Academy, R. & Trakt, S. S. Handbook of Thin Film Materials. *Appl. Phys. A* **73**, 1–21

102. Marcus, P. & Mansfeld, F. *Analytical Methods in Corrosion Science and Engineering*. *International Journal of Microstructure and Materials Properties* **2**, (2007).

103. Maurice, V. & Marcus, P. *Modern Aspects of Electrochemistry*. (2009).

104. Di Quarto, F., Sunseri, C., Piazza, S. & Romano, M. C. Semiempirical Correlation between Optical Band Gap Values of Oxides and the Difference of Electronegativity of the Elements. Its Importance for a Quantitative Use of Photocurrent Spectroscopy in Corrosion Studies. *J. Phys. Chem. B* **101**, 2519–2525 (1997).

105. Chiba, A., Muto, I., Sugawara, Y. & Hara, N. Pit Initiation Mechanism at MnS Inclusions in Stainless Steel: Synergistic Effect of Elemental Sulfür and Chloride Ions. *J. Electrochem. Soc.* **160**, C511–C520 (2013).

106. Scott, L. Vi = 1.5,. **62**, 136–145 (1950).

107. Press, S. P., Britain, G. & Istituto, M. a Relation the Between the in Binding Energy and Band-Gap Energy Semiconductors Structure or Zinc-Blende. **20**, 268–273 (1961).

108. Santamaria, M., Huerta, D., Piazza, S., Sunseri, C. & Di Quarto, F. Influence of the electronic properties of passive films on the corrosion resistance of Mo-Ta alloys a photoelectrochemical study. *J. Electrochem. Soc.* **147**, 1366–1375 (2000).

109. Di Quarto, F., Santamaria, M., Skeldon, P. & Thompson, G. E. Photocurrent spectroscopy study of passive films on hafnium and hafnium-tungsten sputtered alloys. *Electrochim. Acta* **48**, 1143–1156 (2003).

110. Santamaria, M., Di Quarto, F., Skeldon, P. & Thompson, G. E. Effect of composition on the photoelectrochemical behavior of anodic oxides on binary aluminum alloys. *J. Electrochem. Soc.* **153**, 518–526 (2006).

111. Santamaria, M., Di Quarto, F. & Habazaki, H. Influences of structure and composition on the photoelectrochemical behaviour of anodic films on Zr and Zr-20 at.%Ti. *Electrochim. Acta* **53**, 2272–2280 (2008).

112. Santamaria, M., Di Quarto, F. & Habazaki, H. Photocurrent spectroscopy applied to the characterization of passive films on sputter-deposited Ti-Zr alloys. *Corros. Sci.* **50**, 2012–2020 (2008).

113. Di Franco, F., Zampardi, G., Santamaria, M., Di Quarto, F. & Habazaki, H. Characterization of the solid state properties of anodic oxides on magnetron sputtered Ta, Nb and Ta-Nb alloys. *J. Electrochem. Soc.* **159**, 33–39 (2012).

114. Santamaria, M., Di Franco, F., Di Quarto, F., Skeldon, P. & Thompson, G. E. Tailoring of the solid state properties of Al-Nb mixed oxides: A photoelectrochemical study. *J. Phys. Chem. C* **117**, 4201–4210 (2013).

115. Santamaria, M., Terracina, S., Konno, Y., Habazaki, H. & Di Quarto, F. Physicochemical characterization and photoelectrochemical analysis of iron oxide films. *J. Solid State Electrochem.* **17**, 3005–3014 (2013).

116. Zaffora, A., Di Franco, F., Santamaria, M., Habazaki, H. & Di Quarto, F. The influence of composition on band gap and dielectric constant of anodic Al-Ta mixed oxides. *Electrochim. Acta* **180**, 666–678 (2015).

117. Santamaria, M. *et al.* Photoelectrochemical and XPS characterisation of oxide layers on 316L stainless steel grown in high-temperature water. *J. Solid State Electrochem.* **19**, 3511–3519 (2015).

118. Di Quarto, F., Zaffora, A., Di Franco, F. & Santamaria, M. Review -

Photocurrent spectroscopy in corrosion and passivity studies: A critical assessment of the use of band gap value to estimate the oxide film composition. *J. Electrochem. Soc.* (2017).

119. Pauling, L. *The Nature of Chemical Bond*. (Cornell University Press, 1960).

120. Mazinanian, N. & Hedberg, Y. S. Metal release mechanisms for passive stainless steel in citric acid at Weakly Acidic pH. *J. Electrochem. Soc.* **163**, C686–C693 (2016).

121. Hedberg, Y. S. & Odnevall Wallinder, I. Metal release from stainless steel in biological environments: A review. *Biointerphases* **11**, 018901 (2016).

122. Sivula, K., Le Formal, F. & Grätzel, M. Solar water splitting: Progress using hematite (α-Fe 2O3) photoelectrodes. *ChemSusChem* **4**, 432–449 (2011).

123. Di Quarto, F., La Mantia, F. & Santamaria, M. Physicochemical characterization of passive films on niobium by admittance and electrochemical impedance spectroscopy studies. *Electrochim. Acta* **50**, 5090–5102 (2005).

124. Bard, A. J. & Faulkner, L. R. *Fundamentals and Fundamentals and Applications*. (2001). doi:10.1016/B978-0-08-098353-0.00003-8

125. Tribollet, M. E. O. & B. *Electrochemical Impedance Spectroscopy*. (2008).

126. Mantia, F. La *et al.* Assessment on the use of the amorphous semiconductor theory for the analysis of oxide films. *Electrochim. Acta* **179**, 460–468 (2015).

127. Life, P. & Sciences, A. Concepts-of-ICP-OES-Booklet. (2004). doi:005446B

128. Fassel, V. A. & Kniseley, R. N. Inductively Coupled Plasma-Optical Emission Spectroscopy. *Anal. Chem.* **46**, 1110A-1120A (1974).

129. Moulder, J. F., Stickle, W. F., Sobol, P. E. & Bomben, K. D. XPS Handbook.pdf. 1–261 (1995).

130. Desimoni, E. & Brunetti, B. X-ray Photoelectron Spectroscopic characterization of chemically modified electrodes used as chemical sensors and biosensors: A review. *Chemosensors* **3**, 70–117 (2015).

131. Smart, R., Mcintyre, S. & Bello, I. Lab excercise Ma4_XPS1. *Surf. Sci.*

132. Franinović, M. http://mafija.fmf.uni-lj.si/seminar/files/2013_2014/XPS024.pdf. (2012).

133. Muthuvel, M. ABC's of Electrochemistry: X-Ray Photoelectron Spectroscopy (XPS). (2011).

134. Hakiki, N. E. Comparative study of structural and semiconducting properties of passive films and thermally grown oxides on AISI 304 stainless steel. *Corros. Sci.* **53**, 2688–2699 (2011).

135. Robertson, J. Corrosion Science,. **32**, 443–465 (1991).

136. Massoud, T., Maurice, V., Klein, L. H., Seyeux, A. & Marcus, P. Nanostructure and local properties of oxide layers grown on stainless steel in simulated pressurized water reactor environment. *Corros. Sci.* **84**, 198–203 (2014).

137. Tardio, S., Abel, M.-L., Carr, R. H., Castle, J. E. & Watts, J. F. Comparative study of the native oxide on 316L stainless steel by XPS and ToF-SIMS. *J. Vac. Sci. Technol. A Vacuum, Surfaces, Film.* **33**, 05E122 (2015).

138. Haupt, S. & Strehblow, H. H. The formation of the passive layer on Cr in 0.5 M H2SO4 A combined electrochemical and surface analytical study. *J. Electroanal. Chem.* **228**, 365–392 (1987).

139. Sunseri, C., Piazza, S. & Di Quarto, F. Photocurrent Spectroscopic Investigations of Passive Films on Chromium. *J. Electrochem. Soc.* **137**, 2411–2417 (1990).

140. Moffat, T. P. & Latanision, R. M. An Electrochemical and X-Ray Photoelectron Spectroscopy Study of the Passive State of Chromium. *J. Electrochem. Soc.* **139**, 1869–1879 (1992).

141. Maurice, V., Yang, W. P. & Marcus, P. XPS and STM Investigation of the Passive Film Formed on Cr(110) Single-Crystal Surfaces. *J. Electrochem. Soc.* **141**, 3016–3027 (1994).

142. Bojinov, M., Fabricius, G., Laitinen, T., Saario, T. & Sundholm, G. Conduction mechanism of the anodic film on chromium in acidic sulphate solutions. *Electrochim. Acta* **44**, 247–261 (1998).

143. Zuili, D., Maurice, V. & Marcus, P. In situ scanning tunneling microscopy study of the structure of the hydroxylated anodic oxide film formed on Cr(110) single-crystal surfaces. *J. Phys. Chem. B* **103**, 7896–7905 (1999).

144. Kim, J. S., Cho, E. A. & Kwon, H. S. Photo-electrochemical analysis of

passive film formed on Cr in pH 8.5 buffer solution. *Electrochim. Acta* **47**, 415–421 (2001).

145. Tsuchiya, H., Fujimoto, S., Chihara, O. & Shibata, T. Semiconductive behavior of passive films formed on pure Cr and Fe-Cr alloys in sulfuric acid solution. *Electrochim. Acta* **47**, 4357–4366 (2002).

146. Mito, Y., Ueda, M. & Ohtsuka, T. Photo-luminescence from passive oxide films on nickel and chromium by photo-excitation of UV light. *Corros. Sci.* **51**, 1540–1544 (2009).

147. Lebreau, F., Islam, M. M., Diawara, B. & Marcus, P. Structural, magnetic, electronic, defect, and diffusion properties of Cr2O3: A DFT+ U study. *J. Phys. Chem. C* **118**, 18133–18145 (2014).

148. Marcelin, S., Ter-Ovanessian, B. & Normand, B. Electronic properties of passive films from the multi-frequency Mott-Schottky and power-law coupled approach. *Electrochem. commun.* **66**, 62–65 (2016).

149. Miller, N. *et al.* Hole transport and photoluminescence in Mg-doped InN. *J. Appl. Phys.* **107**, (2010).

150. Pourbaix, M. *Atlas of Electrochemical Equilibria in Aqueous Solutions*. (Pergamon Press: Oxford, UK, 1966).

151. Macdonald, D. D. The Point Defect Model for the Passive State. *J. Electrochem. Soc.* **139**, 3434–3449 (1992).

152. MacDonald, D. D. The history of the Point Defect Model for the passive state: A brief review of film growth aspects. *Electrochim. Acta* **56**, 1761–1772 (2011).

153. Seyeux, A., Maurice, V. & Marcus, P. Oxide film growth kinetics on metals and alloys i. physical model. *J. Electrochem. Soc.* **160**, (2013).

154. Habazaki, H., Konno, Y., Aoki, Y., Skeldon, P. & Thompson, G. E. Galvanostatic growth of nanoporous anodic films on iron in ammonium fluoride-ethylene glycol electrolytes with different water contents. *J. Phys. Chem. C* **114**, 18853–18859 (2010).

155. Kure, K. *et al.* Formation of self-organized nanoporous anodic films on Type 304 stainless steel. *Electrochem. commun.* **21**, 1–4 (2012).

156. Hao, L., Zhang, S., Dong, J. & Ke, W. Atmospheric corrosion resistance of MnCuP weathering steel in simulated environments. *Corros. Sci.* **53**, 4187–4192 (2011).

157. Morcillo, M., Díaz, I., Chico, B., Cano, H. & de la Fuente, D. Weathering steels: From empirical development to scientific design. A

review. *Corros. Sci.* **83**, 6–31 (2014).

158. Morcillo, M., Díaz, I., Cano, H., Chico, B. & de la Fuente, D. Atmospheric corrosion of weathering steels. Overview for engineers. Part I: Basic concepts. *Constr. Build. Mater.* **213**, 723–737 (2019).

159. Song, L., Chen, Z. & Hou, B. The role of the photovoltaic effect of γ-FeOOH and β-FeOOH on the corrosion of 09CuPCrNi weathering steel under visible light. *Corros. Sci.* **93**, 191–200 (2015).

160. Song, L., Ma, X., Chen, Z. & Hou, B. The role of UV illumination on the initial atmospheric corrosion of 09CuPCrNi weathering steel in the presence of NaCl particles. *Corros. Sci.* **87**, 427–437 (2014).

161. Song, L. Y. *et al.* UV illumination on the atmospheric corrosion of Q450 weathering steel depositing with NH4Cl. *Mater. Corros.* **69**, 29–36 (2018).

162. Qiu, X., Li, J. & Liu, Z. Corrosion of weathering steel under light illumination and simulated atmospheric conditions. *Int. J. Electrochem. Sci.* **14**, 3236–3244 (2019).

163. Qiu, P. *et al.* The transformation of corrosion products on weathering steel by visible-light illumination under simulated marine atmospheric condition. *Int. J. Electrochem. Sci.* **11**, 10498–10510 (2016).

164. Norio Sato. *Electrochemistry at Metal and Semiconductor Electrodes*. **66**, (1998).

165. Alcántara, J. *et al.* An attempt to classify the morphologies presented by different rust phases formed during the exposure of carbon steel to marine atmospheres. *Mater. Charact.* **118**, 65–78 (2016).

166. Li, Z. liang *et al.* Atmospheric corrosion behavior of low-alloy steels in a tropical marine environment. *J. Iron Steel Res. Int.* **26**, 1315–1328 (2019).

167. Qian, Y., Ma, C., Niu, D., Xu, J. & Li, M. Influence of alloyed chromium on the atmospheric corrosion resistance of weathering steels. *Corros. Sci.* **74**, 424–429 (2013).

168. Alaoui Mouayd, A., Orazem, M. E., Sutter, E. M. M., Tribollet, B. & Koltsov, A. Contribution of electrochemical dissolution during pickling of low carbon steel in acidic solutions. *Corros. Sci.* **82**, 362–368 (2014).

169. Musiani, M., Orazem, M. E., Pébère, N., Tribollet, B. & Vivier, V. Constant-phase-element behavior caused by coupled resistivity and permittivity distributions in films. *J. Electrochem. Soc.* **158**, 424–428

(2011).

170. Orazem, M. E. *et al.* Dielectric properties of materials showing constant-phase-element (CPE) impedance response. *J. Electrochem. Soc.* **160**, 215–225 (2013).

171. Transactions, E. C. S. & Society, T. E. in Films. **28**, 77–94 (2010).

172. Tsuchiya, H., Fujimoto, S. & Shibata, T. Semiconductive behavior of passive films formed on Fe-Cr alloy. *J. Electroceramics* **16**, 49–54 (2006).

173. Stratmann, M. & Müller, J. The mechanism of the oxygen reduction on rust-covered metal substrates. *Corros. Sci.* **36**, 327–359 (1994).

174. Tewary, N. K., Kundu, A., Nandi, R., Saha, J. K. & Ghosh, S. K. Microstructural characterisation and corrosion performance of old railway girder bridge steel and modern weathering structural steel. *Corros. Sci.* **113**, 57–63 (2016).

175. Guedes, I. C. *et al.* The influence of copper and chromium on the semiconducting behaviour of passive films formed on weathering steels. *Thin Solid Films* **515**, 2167–2172 (2006).

176. Watanabe, M. Faraday Discussions. *J. Japanese Assoc. Cryst. Growth* **34**, 240–241 (2008).

177. Maurice, V., Yang, W. P. & Marcus, P. X-ray photoelectron spectroscopy and scanning tunneling microscopy study of passive films formed on (100) Fe-18Cr-13Ni single-crystal surfaces. *J. Electrochem. Soc.* **145**, 909–920 (1998).

178. Di Quarto, F., Sunseri, C., Piazza, S. & Romano, M. C. Semiempirical correlation between optical band gap values of oxides and the difference of electronegativity of the elements. Its importance for a quantitative use of photocurrent spectroscopy in corrosion studies. *J. Phys. Chem. B* **101**, 2519–2525 (1997).

179. Betova, I. *et al.* The transpassive dissolution mechanism of highly alloyed stainless steels I. Experimental results and modelling procedure. *Corros. Sci.* **44**, 2675–2697 (2002).

180. Bojinov, M., Fabricius, G., Laitinen, T. & Saario, T. Transpassivity mechanism of iron-chromium-molybdenum alloys studied by AC impedance, DC resistance and RRDE measurements. *Electrochim. Acta* **44**, 4331–4343 (1999).

181. Bojinov, M. *et al.* Influence of molybdenum on the conduction

mechanism in passive films on iron-chromium alloys in sulphuric acid solution. *Electrochim. Acta* **46**, 1339–1358 (2001).

182. Fattah-alhosseini, A., Saatchi, A., Golozar, M. A. & Raeissi, K. The transpassive dissolution mechanism of 316L stainless steel. *Electrochim. Acta* **54**, 3645–3650 (2009).

183. Betova, I. *et al.* The transpassive dissolution mechanism of highly alloyed stainless steels II. Effect of pH and solution anion on the kinetics. *Corros. Sci.* **44**, 2699–2723 (2002).

184. Santamaria, M. *et al.* Photoelectrochemical and XPS characterisation of oxide layers on 316L stainless steel grown in high-temperature water. *J. Solid State Electrochem.* **19**, 3511–3519 (2015).

185. Tranchida, G., Clesi, M., Di Franco, F., Di Quarto, F. & Santamaria, M. Electronic properties and corrosion resistance of passive films on austenitic and duplex stainless steels. *Electrochim. Acta* **273**, (2018).

186. Ha, H. Y., Lee, T. H. & Kim, S. J. Role of nitrogen in the active-passive transition behavior of binary Fe-Cr alloy system. *Electrochim. Acta* **80**, 432–439 (2012).

187. Mesquita, T. J., Chauveau, E., Mantel, M. & Nogueira, R. P. A XPS study of the Mo effect on passivation behaviors for highly controlled stainless steels in neutral and alkaline conditions. *Appl. Surf. Sci.* **270**, 90–97 (2013).

188. Bandy, R. & Newman, R. C. Surface Enrichment of Nitrogen during Passivation of a Highly Resistant Stainless Steel. *J. Electrochem. Soc.* **130**, 1774–1776 (1983).

189. Olsson, C. O. A. The influence of nitrogen and molybdenum on passive films formed on the austenoferritic stainless steel 2205 studied by AES and XPS. *Corros. Sci.* **37**, 467–479 (1995).

190. Garfias-Mesias, L. F., Sykes, J. M. & Tuck, C. D. S. The effect of phase compositions on the pitting corrosion of 25 Cr duplex stainless steel in chloride solutions. *Corros. Sci.* **38**, 1319–1330 (1996).

191. Femenia, M., Pan, J., Leygraf, C. & Luukkonen, P. In situ study of selective dissolution of duplex stainless steel 2205 by electrochemical scanning tunnelling microscopy. *Corros. Sci.* **43**, 1939–1951 (2001).

192. Perren, R. A. *et al.* Corrosion resistance of super duplex stainless steels in chloride ion containing environments: Investigations by means of a new microelectrochemical method. II. Influence of precipitates. *Corros. Sci.* **43**, 727–745 (2001).

193. Herting, G., Odnevall Wallinder, I. & Leygraf, C. Corrosion-induced release of chromium and iron from ferritic stainless steel grade AISI 430 in simulated food contact. *J. Food Eng.* **87**, 291–300 (2008).

194. Herting, G., Lindström, D., Wallinder, I. O. & Leygraf, C. Multi-analytical investigation of stainless steel grade AISI 420 in simulated food contact. *J. Food Eng.* **93**, 23–31 (2009).

195. Dalipi, R. *et al.* Study of metal release from stainless steels in simulated food contact by means of total reflection X-ray fluorescence. *J. Food Eng.* **173**, 85–91 (2016).

196. Mazinanian, N. Metal Release and Corrosion of Stainless Steel in Simulated Food Contact. *Corrosion* **72**, 775–790 (2016).

197. Schorr, M. & Valdez, B. The phosphoric acid industry: Equipment, materials, and corrosion. *Corros. Rev.* **34**, 85–102 (2016).

198. Ram, C., Sharma, C. & Singh, A. K. In-Plant Corrosion Study of Steels in Distillery Effluent Treatment Plant. *J. Mater. Eng. Perform.* **24**, 1841–1847 (2015).

199. Chiavari, C. *et al.* Influence of low-temperature carburising on metal release from AISI316L austenitic stainless steel in acetic acid. *J. Food Eng.* **137**, 7–15 (2014).

200. Batista, L., Monteiro, S., Loureiro, V. B., Teixeira, A. R. & Ferreira, R. B. Protein haze formation in wines revisited. The stabilising effect of organic acids. *Food Chem.* **122**, 1067–1075 (2010).

201. Tranchida, G., Clesi, M., Franco, F. Di, Quarto, F. Di & Santamaria, M. Electrochimica Acta Electronic properties and corrosion resistance of passive fi lms on austenitic and duplex stainless steels. *Electrochim. Acta* **273**, 412–423 (2018).

202. Levet, F., Granier, X. & Schlick, C. Pr E-P Rin. *Lect. Notes Comput. Sci.* **4073**, 114–125 (2006).

203. Bai, G., Lu, S., Li, D. & Li, Y. Effects of boron on microstructure and metastable pitting corrosion behavior of Super304H austenitic stainless steel. *J. Electrochem. Soc.* **162**, C473–C481 (2015).

204. Bai, G., Lu, S., Li, D. & Li, Y. Influences of niobium and solution treatment temperature on pitting corrosion behaviour of stabilised austenitic stainless steels. *Corros. Sci.* **108**, 111–124 (2016).

205. Man, C., Dong, C., Xiao, K., Yu, Q. & Li, X. The Combined Effect of Chemical and Structural Factors on Pitting Corrosion Induced by MnS-

(Cr, Mn, Al)O Duplex Inclusions. *Corrosion* **74**, 312–325 (2018).

206. Li, J. *et al.* Enhancing Pitting Corrosion Resistance of Severely Cold-Worked High Nitrogen Austenitic Stainless Steel by Nitric Acid Passivation. *J. Electrochem. Soc.* **166**, C365–C374 (2019).

207. Wang, X. *et al.* Reinvestigation of membrane cleaning mechanisms using NaOCl: Role of reagent diffusion. *J. Memb. Sci.* **550**, 278–285 (2018).

208. Sirtes, G., Waltimo, T., Schaetzle, M. & Zehnder, M. The effects of temperature on sodium hypochlorite short-term stability, pulp dissolution capacity, and antimicrobial efficacy. *J. Endod.* **31**, 669–671 (2005).

209. Guitián, B., Nóvoa, X. R. & Puga, B. Electrochemical Impedance Spectroscopy as a tool for materials selection: Water for haemodialysis. *Electrochim. Acta* **56**, 7772–7779 (2011).

210. Chen, X. & Hung, Y. C. Effects of organic load, sanitizer pH and initial chlorine concentration of chlorine-based sanitizers on chlorine demand of fresh produce wash waters. *Food Control* **77**, 96–101 (2017).

211. Rosado de Castro, M., da Silva Fernandes, M., Kabuki, D. Y. & Kuaye, A. Y. Biofilm formation on stainless steel as a function of time and temperature and control through sanitizers. *Int. Dairy J.* **68**, 9–16 (2017).

212. Vázquez-Sánchez, D., Cabo, M. L., Ibusquiza, P. S. & Rodríguez-Herrera, J. J. Biofilm-forming ability and resistance to industrial disinfectants of staphylococcus aureus isolated from fishery products. *Food Control* **39**, 8–16 (2014).

213. J, A., Licht, T. S. & Swendeman, N. The Temperature Coefficients of Electrode Potentials The Isothermal and Thermal CoefficientsmThe Standard Ionic Entropy of Electrochemical. 616–625

214. Volpe, L., Salamone, M., Giardina, A. & Ghersi, G. Optimization of a Biotechnological Process for Production and Purification of Two Recombinant Proteins: Col G and Col H. *Chem. Eng. Trans.* **49**, 61–66 (2016).

215. L.L. Shreir, R. A. J. & G. T. B. Metal/ Environment . Reactions. *John Wiley Sons Inc* **vol.1**, 1432 (1994).

216. Arnold, J. W. & Bailey, G. W. Surface finishes on stainless steel reduce bacterial attachment and early biofilm formation: Scanning electron and atomic force microscopy study. *Poult. Sci.* **79**, 1839–1845 (2000).

217. Barish, J. A. & Goddard, J. M. Anti-fouling surface modified stainless steel for food processing. *Food Bioprod. Process.* **91**, 352–361 (2013).

218. Zouaghi, S. *et al.* Atmospheric pressure plasma spraying of silane-based coatings targeting whey protein fouling and bacterial adhesion management. *Appl. Surf. Sci.* **455**, 392–402 (2018).

219. Liu, H., Sharma, M., Wang, J., Cheng, Y. F. & Liu, H. Microbiologically influenced corrosion of 316L stainless steel in the presence of Chlorella vulgaris. *Int. Biodeterior. Biodegrad.* **129**, 209–216 (2018).

220. Jin, Y. *et al.* Sharing riboflavin as an electron shuttle enhances the corrosivity of a mixed consortium of Shewanella oneidensis and Bacillus licheniformis against 316L stainless steel. *Electrochim. Acta* **316**, 93–104 (2019).

221. Nguyen, T. M. P., Sheng, X., Ting, Y. P. & Pehkonen, S. O. Biocorrosion of AISI 304 stainless steel by desulfo vibrio desulfuricans in seawater. *Ind. Eng. Chem. Res.* **47**, 4703–4711 (2008).

222. Picioreanu, C. & Van Loosdrecht, M. C. M. A mathematical model for initiation of microbiologically influenced corrosion by differential aeration. *J. Electrochem. Soc.* **149**, (2002).

Scientific output

Publications in International Journals

1. G. Tranchida, M. Clesi, F. Di Franco, F. Di Quarto, M. Santamaria, *Electronic Properties and Corrosion Resistance of Passive Films on Austenitic and Duplex Stainless Steel.*
   Electrochim. Acta 273 (2018) 412-423
   https://doi.org/10.1016/j.electacta.2018.04.058

2. G. Tranchida, F. Di Franco, S. Virtanen, M. Santamaria
   Effect of NaClO disinfection/cleaning on passive film on AISI 316L.
   Corros. Sci.
   https://doi.org/10.1016/j.corsci.2019.108415

3. G. Tranchida, B. Megna, F. Di Franco, M. Santamaria
   Study of Corrosion Resistance of SSs For Food and Beverage Industry.
   La metallurgia Italiana.

4. A. Zaffora, G. Tranchida, F. Di Franco, M. Santamaria, F. Di Quarto
   Recent advances in using Photocurrent Spectroscopy for the Characterization of Passive Films on Metals and Metallic Alloys.
   La metallurgia Italiana.

Publications in International Journals "Under Review"

1. G. Tranchida, F. Di Franco, M. Santamaria
   Corrosion Resistance of Passive Films on Different Stainless Steel Grades for Food and Beverage Industry.
   Submitted to "Corrosion Science".

Papers "Under preparation"

1. G. Tranchida, F. Di Franco, M. Santamaria
   Effect of Mo on corrosion resistance of passive films grown on different stainless steel grades.

2. G. Tranchida, F. Di Franco, M. Santamaria
   Monitoring of passive film growth on Weathering Steel by EIS and PCS measurements.

3. G. Tranchida, F. Di Franco, G. Ghersi, P. Cinà, M. Santamaria
Effect of Biofilm Growth on Corrosion Resistance of Stainless Steel Used in Pharmaceutical Industry.

Conference Paper

1. G. Tranchida, F. Di Franco, B. Megna, M. Santamaria
Studio della Resistenza alla Corrosione di Acciai Impiegati nell'Industria Alimentare e delle Bevande
Giornate Nazionali sulla Corrosione e Protezione – GNC 2019, July 3rd – 5th, 2019.

National Conference Contributions

1. **(Presenting Author)** G. Tranchida, H. E. Pituccio, F. Di Franco, F. Di Quarto, M. Santamaria, *Growth and Characterization of Atmospheric and Anodic Oxide Films on Weathering Steels*, XXVI Congresso Nazionale della Società chimica Italiana - SCI 2017, September 10th – 14th, 2017, Paestum, SA (Oral Communication).

2. G. Tranchida, M. Clesi, F. Di Franco, F. Di Quarto, M. Santamaria, *Corrosion Resistance of Stainless Steel for Food and Beverage Industry*, XXVIII Annual Meeting, Società Chimica Italiana GEI 2018, 21st – 25th gennaio, 2018, Sestriere, TO. (Oral Communication).

3. **(Presenting Author)** G. Tranchida, F. Di Franco, B. Megna, M. Santamaria, *Studio della resistenza alla Corrosione di Acciai Impiegati nell'Industria Alimentare e delle Bevande*, XIII edizione delle Giornate Nazionali sulla Corrosione e Protezione - GNC 2019, 3rd – 5th luglio, Palermo, PA. (Oral Communication).

4. **(Presenting Author)** G. Tranchida, F. Di Franco, M. Santamaria, *Corrosion Resistance of Different Stainless Steel grades in Cleaning Industrial Environments*, XXVIII Annual Meeting, Società Chimica Italiana GEI 2019, 8th – 12th settembre, SCI, Padova, PD. (Oral Communication).

International Conference Contributions

1. G. Tranchida, M. Clesi, F. Di Franco, F. Di Quarto, M. Santamaria, *Electronic Properties and Corrosion Resistance of Passive Films on Austenitic and Duplex Stainless Steels*, The 68th Annual Meeting of the International Society of Electrochemistry - ISE 2017, August 27th – September 1st ,2017, Providence (USA). (Oral Communication).

2. **(Presenting Author)** G. Tranchida, M. Clesi, F. Di Franco, M. Santamaria, Corrosion Resistance of Stainless Steel for Food and Beverage Industry, The 68th Annual Meeting of the International Society of Electrochemistry - ISE 2018, September 2nd – 7th, 2018, Bologna, BO. (Poster contribution).

Ph.D. School

1. 1st ISSE International Spring School of Electrochemistry - Smart Materials For and From Electrochemistry, May 19th – 23rd, 2019, Castellammare del Golfo (TP).

Secondment

1. Visiting Ph.D. Student at the "Institute for Surface Science and Corrosion", Department of Materials Science, Friedrich Alexander University Erlangen-Nuremberg, Germany, February 1st – July 31st, 2018. Supervisor Prof. Dr. Sannakaisa Virtanen.

Followed lectures

1. "*Nanoscale Surface Characterization and Structures"*, (3 ects), Lecturer Dr. Manuela Killian, WW & Schmuki group, *Department of Materials Science*, Friedrich Alexander University Erlangen-Nuremberg, April 17th – July 10th, 2018.

2. "*Corrosion in Biological Environment"*, Lecturer Prof. Ing. Monica Santamaria, Engineering Department, University of Palermo, Palermo Corso (6 cfu), March 4th – May 10th, 2019.

3. "*How to write great research paper-tips & tricks and what not to do*", March 14th, 2017.

4. Corso di formazione, "*Comunicazione in pubblico*", April 19th – 20th, 2017

5. "*Spin-off accademico: fare impresa all'Università di Palermo*", March 29th, 2017.

6. "*Materials by Design: multiscale molecular modeling of nanostructured materials*", November 30th, 2017.

7. "*Ricerca e terza missione all'Università di Palermo: dove siamo*", Responsabile: Prof. Livan Fratini, Trainer: Livan Fratini, January 28th, 2019.

8. "*La Comunicazione attraverso i Media*", Relatori: Vera Martinella, Carmelo Nicolosi, Discussant: Antonio Russo, February 4th, 2019.

9. "*From start – up to accelerator: the complexity of innovation in multinationals*", Responsabile: prof.ssa Eleonora Riva Sanseverino, Trainers: Prof. Livan Fratini, Prof.Umberto La Commare, Prof. Giovanni Perrone, Prof. Marcantonio Ruisi, Ing. Roberto candela Prysmian S.p.A., February 26th, 2019.

10. "*Modelli Matematici nella Vita Quotidiana*", Relatori: Fabio Bagarello, Discussant: Francesco Oliveri, March 4th, 2019.

11. "*Supramolecular chemistry and catalysis with metal nanoparticles*", Dr. Bastien Léger, University of Artois (France), June 4th – 5th, 2019.